

Dissertation
submitted to the
Combined Faculties for the Natural Sciences and Mathematics
of the Ruperto-Carola-University of Heidelberg, Germany
for the degree of
Doctor of Natural Sciences

Put forward by
Dipl.-Phys. Daniel Weber
born in Malsch (District of Karlsruhe)

Oral examination: November 2nd, 2011

Nanogaps for Nanoantenna-Assisted Infrared Spectroscopy

Referees: Prof. Dr. Annemarie Pucci
Prof. Dr. Albrecht Winnacker

Nanogaps for Nanoantenna-Assisted Infrared Spectroscopy

Lithographically prepared gold nanorods, showing antenna-like plasmon resonances in the infrared (IR) spectral range, are able to strongly enhance local electromagnetic fields. This can be exploited for nanoantenna-assisted IR spectroscopy (NAIRS), a sensing application allowing detection of very small amounts of molecules (attomol). Since near-field coupling between nanorods over small gaps considerably increases the field enhancement, the main focus of the thesis was the characterization and preparation of gaps in the sub-10 nm range. Therefore, two approaches were applied: the narrowing of lithographically prepared gaps (20 – 50 nm) by chemically induced metal deposition, on the one hand, and the milling of long rods by focused ion beams (FIB) on the other hand. IR optical investigations of the grown or milled nanorods allowed non-destructive assessment of the fabrication quality. In regard to the chemical method, gaps in the range of 10 nm were presumably prepared, whereas FIB milling resulted in gaps down to 20 nm. In addition, near-field and far-field coupling effects in nanorod arrays were analyzed to determine the optimal rod arrangement for NAIRS. Finally, the probe molecule mercaptoundecanoic acid was spectroscopically investigated with the help of gold nanoantennas and enhancement factors up to 48 000 were estimated.

Nanolücken für Nanoantennen-unterstützte Infrarot-Spektroskopie

Lithographisch hergestellte Gold-Nanodrähte weisen antennenartige Plasmonenresonanzen im infraroten (IR) Spektralbereich auf und sind in der Lage, lokale elektromagnetische Felder beträchtlich zu verstärken. Dies kann für Nanoantennen-unterstützte Infrarot-Spektroskopie (NAIRS), eine Sensoranwendung welche die Detektion kleinster Mengen an Molekülen (attomol) erlaubt, ausgenutzt werden. Da Nahfeldkopplung über Lücken zwischen Nanodrähten die Feldverstärkung bedeutend vergrößert, lag der Hauptaugenmerk der Arbeit auf der Charakterisierung und Herstellung von Lücken im Bereich kleiner als 10 nm. Dazu wurden zwei Vorgehensweisen angewandt: zum einen das Verengen von lithographisch hergestellten Lücken (20 – 50 nm) durch chemisch induzierte Metallabscheidung und zum anderen das fokussierte Ionenstrahl (FIB)-Ätzen von langen Drähten. IR optische Untersuchungen der gewachsenen bzw. geätzten Nanodrähte ließen Rückschlüsse auf die Herstellungsqualität zu. Mit der chemischen Methode wurden Lücken im Bereich von vermutlich 10 nm hergestellt, wohingegen FIB-Ätzen zu Lücken bis zu 20 nm Größe führte. Desweiteren wurden Nah- und Fernfeldkopplungseffekte in Nanodraht-Feldern analysiert, um die optimale Anordnung der Drähte für NAIRS zu bestimmen. Schließlich wurde das Testmolekül Mercaptoundekansäure mithilfe von Gold-Nanoantennen spektroskopisch untersucht und Verstärkungsfaktoren bis zu 48 000 abgeschätzt.

Contents

List of Figures	v
List of Tables	ix
1. Introduction	1
2. Fundamentals	3
2.1. Infrared Spectroscopy	3
2.2. Metal Optics	5
2.3. Plasmon-Polaritons	7
2.4. Individual Nanoantennas	11
2.4.1. Spectral Resonance Position	11
2.4.2. Electromagnetic Field Enhancement	13
2.4.3. Higher Order Modes	15
2.5. Interaction between Nanoantennas	16
2.6. Phonon-Polaritons	19
2.6.1. Excitations in Thin Dielectric Layers	22
2.7. Surface-Enhanced Infrared Absorption	22
3. Materials & Methods	25
3.1. Lithographic Gold Nanorods	25
3.1.1. Measurement of Rod Height	27
3.1.2. Measurement of Rod Length and Width	28
3.1.3. Overview on Investigated Samples	31
3.2. Microscopic Infrared Spectroscopy	31
3.2.1. Experimental Set-Up	31
3.2.2. Measurement Principle	33
3.3. Substrates	34
3.3.1. Thermally Oxidized Silicon	36
3.4. Alkanethiol-Based Self-Assembled Monolayers	37
3.4.1. Mercaptoundecanoic Acid	38
3.5. Surface-Enhanced Infrared Spectroscopy Using Nanoantennas	41

3.5.1.	Octadecanethiol as Probe Molecule	41
3.5.2.	Antenna Sensing of Phonon-Polaritons	45
3.6.	Finite-Difference Time-Domain Simulations	47
4.	Individual Nanoantennas Arranged in Arrays	49
4.1.	Nanorod Arrays on Natural Oxide Covered Silicon	49
4.1.1.	Resonance Parameters and General Properties	49
4.1.2.	Comparison with FDTD Simulations	55
4.1.3.	Reproducibility of Lithographic Preparation	57
4.1.4.	Influence of the Adhesion Layer	61
4.2.	Nanorod Arrays on Thermally Oxidized Silicon	61
4.3.	Influence of the Supporting Substrate	66
4.3.1.	Spectral Resonance Position	66
4.3.2.	Quality Factor	70
4.3.3.	Extinction Cross-Section	70
4.3.4.	Higher Order Modes	71
4.3.5.	Summary	73
4.4.	Important Findings	74
5.	Interaction Effects in Nanoantenna Arrays	75
5.1.	Transverse Interaction	76
5.1.1.	Comparison with FDTD Simulations	78
5.1.2.	Spectral Resonance Position	78
5.1.3.	Quality Factor and Extinction	81
5.1.4.	Investigation of the Near-Field	81
5.2.	Longitudinal Interaction	83
5.2.1.	Spectral Resonance Position	84
5.2.2.	Quality Factor and Extinction	84
5.3.	Mixed Interaction	86
5.4.	Conclusion	88
5.5.	Important findings	89
6.	Characterization and Preparation of Nanogaps	91
6.1.	Wet-Chemical Metal Deposition	92
6.1.1.	Principle	92
6.1.2.	Measurement Process	92
6.1.3.	Results	92
6.2.	Photo-Induced Metal Deposition	96
6.2.1.	Principle	96

6.2.2.	Nanorod Arrays on Silicon Substrates	96
6.2.2.1.	Measurement Process	96
6.2.2.2.	Results of Sample Wa2	97
6.2.2.3.	Results of Sample Wb3	99
6.2.2.4.	Conclusion	101
6.2.3.	Nanorod Dimers on Calcium Fluoride Substrates	101
6.2.3.1.	Measurement Process	102
6.2.3.2.	Sample Layout	103
6.2.3.3.	IR Optical Characterization before Metal Deposition	105
6.2.3.4.	Results of Antenna#18	106
6.2.3.5.	Results of Antenna#19	113
6.2.3.6.	Mode Assignment	117
6.3.	Focused Ion Beam milling	120
6.3.1.	FIB Sample Preparation and Layout	120
6.3.2.	Transmission Electron Microscopic Analysis	121
6.3.3.	Results - Natural Oxide Covered Silicon	123
6.3.3.1.	Effect of FIB Imaging	123
6.3.3.2.	FIB and SEM Characterization	124
6.3.3.3.	IR Optical Characterization	125
6.3.3.4.	TEM and EDX Characterization	128
6.3.3.5.	Conclusion	130
6.3.4.	Results - Thermally Oxidized Silicon	131
6.3.4.1.	Effect of FIB Imaging and Milling	132
6.3.4.2.	IR Optical Characterization	134
6.3.4.3.	TEM and EDX Characterization	134
6.3.4.4.	Conclusion	138
6.4.	Important Findings	138
7.	Sensing of Mercaptoundecanoic Acid	139
7.1.	Infrared Reflection Absorption Spectroscopy	139
7.1.1.	Sample Preparation	140
7.1.2.	Measurement Principle	140
7.1.3.	Results	142
7.2.	Nanoantenna-Assisted Infrared Spectroscopy	144
7.2.1.	Oxygen Plasma Cleaning	144
7.2.2.	Identifying the Spectral Signature of MUA	145
7.2.3.	Changing the Carboxyl Configuration	148
7.2.4.	Destroying the Adsorbate by Plasma Cleaning	148
7.2.5.	Estimation of an Enhancement Factor	150

7.3. Important Findings	154
8. Summary	155
9. Outlook	159
Bibliography	161
A. Experimental Details	191
A.1. Lithographic Preparation at NIMS	191
A.2. Scanning Electron Microscopy	192
A.2.1. Carbon Contamination	192
A.2.2. Brightness and Contrast	194
A.2.3. Comparison between Different Microscopes	196
A.3. Microscopic Infrared Spectroscopy	197
A.3.1. Set-Up of the IR Microscope	197
A.3.2. Schwarzschild Objective	197
A.3.3. Non-Linearity of the MCT Detector	200
A.3.4. Measurement Time of the MCT Detector	201
A.3.5. Influence of Different Aperture Sizes	201
A.3.6. Stability of the Apparatus	203
A.3.7. CO ₂ Concentration Inside the Purging Box	206
A.4. Argon-Sputtering	207
A.5. Measurement Stability of IRRAS	208
B. Various Spectra and Tables	211
C. List of Publications	215
D. Acknowledgments	217
E. List of Abbreviations	219
Index	221

List of Figures

2.1. Schematic diagram of a FT-IR spectrometer	4
2.2. Bulk dielectric function of gold	6
2.3. Dispersion relation of volume and surface plasmon-polaritons	8
2.4. Quasi-static calculation of far-field spectra of prolate ellipsoids	10
2.5. Relation $\lambda_{\text{res}}(L)$ for nanorods featuring different R (BEM simulations) . . .	12
2.6. Near-field distribution of gold nanoantennas (BEM simulations)	14
2.7. Defect-induced activation of second order antenna resonance	15
2.8. FDTD simulations of near- and far-field spectra of nanorod dimers	17
2.9. Dielectric function and dispersion relation of a dielectric solid	20
2.10. Dispersion relations of surface phonon-polaritons in a three-layer-system . .	21
3.1. Schematic drawing of gold nanorods with their characteristic dimensions . .	26
3.2. AFM height profiles of gold nanorods	27
3.3. SEM images of gold nanorods on silicon	29
3.4. Optical beam path for microscopic IR transmittance measurements	32
3.5. Principle of relative transmittance	33
3.6. Relative transmittance spectra of all investigated substrates	35
3.7. Rel. transmittance spectrum of thermally oxidized silicon versus silicon . .	36
3.8. Ordered structure of an AT-SAM on a Au(111) surface	38
3.9. Structure of mercaptoundecanoic acid	39
3.10. PM-IRRAS spectrum of a MUA monolayer adsorbed on gold	40
3.11. Examples of nanoantenna-assisted infrared spectroscopy	42
3.12. SEIRS enhancement factors of electrochemic and lithographic nanorods . .	44
3.13. Experimental and theoretical Fano-like line shapes	46
4.1. Relative transmittance spectra of gold nanorod arrays on silicon	50
4.2. Determination of characteristic resonance parameters	51
4.3. General behavior of characteristic resonance parameters	52
4.4. Comparison between $\sigma_{\text{ext}}(\tilde{\nu})/\sigma_{\text{geo}}$ and σ_{ext} (FDTD simulations)	53
4.5. Comparison between transmittance and reflectance measurements	54
4.6. Comparison between arrays (experiment) and isolated rods (simulation) . .	55
4.7. Simulation of nanorod in effective medium vs. nanorod on substrate	56

List of Figures

4.8. Homogeneity within one nanorod array	57
4.9. $\lambda_{\text{res}}(L)$ for different samples of the same preparation series	58
4.10. Comparison of extinction spectra between different preparation series	59
4.11. $\lambda_{\text{res}}(L)$ and $Q(\lambda_{\text{res}})$ of three samples from different preparation series	60
4.12. Influence of titanium adhesion layer on antenna resonance	61
4.13. Relative transmittance spectra of nanorod arrays on 106 nm SiO_2 / Si	62
4.14. Simulation of nanorod on silicon dioxide with and without oscillator	63
4.15. Comparison between silicon, quartz glass, and oxide covered silicon	64
4.16. Extinction spectra of nanorod arrays on 106 nm SiO_2 / Si	65
4.17. $\lambda_{\text{res}}(L)$ for non-interacting nanorod arrays on different substrates	67
4.18. Dispersion relation of nanorod arrays on different substrates	69
4.19. Q and $\sigma_{\text{ext}}(\tilde{\nu}_{\text{res}})/\sigma_{\text{geo}}$ of nanorod arrays on different substrates	70
4.20. Appearance of higher order modes in relative transmittance spectra	71
4.21. Light refraction at the interfaces of the substrate	73
5.1. SEM image of a typical gold nanoantenna array	75
5.2. Relative transmittance spectra of nanorod arrays featuring different d_y	76
5.3. Experimental and simulated extinction spectra for different d_y	77
5.4. Constructive interference condition in transverse direction	79
5.5. Relative changes of λ_{res} , Q , and $\sigma_{\text{ext}}(\tilde{\nu}_{\text{res}})/\sigma_{\text{geo}}$ for different d_y	80
5.6. $\sigma_{\text{ext}}(\tilde{\nu}_{\text{res}})/\sigma_{\text{geo}}$ versus $\lambda_{\text{res}}/(n_{\text{Si}}d_y)$ in double logarithmic representation	81
5.7. Experimental and simulated near-field mappings for different d_y	82
5.8. Experimental spectra for different d_x and behavior of λ_{res}	83
5.9. Constructive interference condition in longitudinal direction	84
5.10. Relative changes of Q and $\sigma_{\text{ext}}(\tilde{\nu}_{\text{res}})/\sigma_{\text{geo}}$ for different d_x	85
5.11. Extinction spectra (mixed interaction)	86
5.12. Evolution of Q for different interacting arrays on silicon	87
6.1. Different approaches to nanogap formation.	91
6.2. Reflectance spectra before and after wet-chemical metal deposition	93
6.3. SEM images of nanorods after wet-chemical metal deposition	94
6.4. Histogram of an array after wet-chemical metal deposition	95
6.5. Schematic drawing of the photo-induced metal deposition process	96
6.6. Photo-induced metal deposition on sample Wa2 (IR spectra)	97
6.7. Photo-induced metal deposition on sample Wa2 (SEM images)	98
6.8. Photo-induced metal deposition on sample Wb3 (IR spectra)	99
6.9. Photo-induced metal deposition on sample Wb3 (SEM images)	100
6.10. Inverted microscopic set-up used for photo-induced metal deposition	102
6.11. Arrangement of sets and patterns on samples Antenna#18 and #19	104

6.12. IR spectra of dimers with decreasing gap size	105
6.13. Histogram of $\tilde{\nu}_{\text{res}}$ and $\Delta\lambda_{\text{res}}/\lambda_{\text{res}}$ versus g_x for nanorod dimers	106
6.14. Influence of the carbon layer on relative transmittance spectra	107
6.15. Correlation between SEM and IR spectra (SEM images)	108
6.16. Correlation between SEM and IR spectra (IR spectra)	109
6.17. Defects of nanorod dimers and their influence on the IR spectra	111
6.18. Transverse and longitudinal antenna resonances for nanorod dimers	112
6.19. Explanation of the blue-shift of the transverse mode with decreasing g_x	113
6.20. Analysis of non-illuminated and illuminated single rods of Antenna#19	114
6.21. Analysis of illuminated dimers of Antenna#19	115
6.22. Activation of dark modes at oblique incidence and simulations	117
6.23. Schematic representation of possible mode couplings in a nanorod dimer	118
6.24. Behavior of all assigned modes of nanorod dimers	119
6.25. Schematic drawings of arrays intended for nanogap formation	120
6.26. Preparation of TEM samples	122
6.27. Example of a TEM measurement	123
6.28. Effect of FIB imaging on natural oxide covered silicon	124
6.29. FIB and SEM images of FIB-milled nanorods	125
6.30. Normalized relative transmittance spectra	126
6.31. Comparison between optical properties of D_{I} - and D_{II} -milled nanorods	127
6.32. TEM and EDX images of D_{I} - and D_{II} -milled nanorods	129
6.33. EDX spectra of gap area milled by D_{II}	130
6.34. Effect of FIB imaging on 106nm thick oxide covered silicon	132
6.35. Effect of FIB milling on 106nm thick oxide covered silicon	133
6.36. Optical characterization of nanorods milled by $D_{\text{III}} - D_{\text{V}}$	135
6.37. TEM analyses for rods milled by $D_{\text{III}} - D_{\text{V}}$	136
6.38. EDX spectra for nanorods milled by D_{III}	137
7.1. Surface selection rule	139
7.2. Schematic IRRAS set-up	141
7.3. IRRAS spectra of MUA (baseline corrected)	143
7.4. Influence of oxygen plasma cleaning on antenna resonance	145
7.5. NAIRS of MUA, relative transmittance and first derivative spectra	146
7.6. Fano profiles and their derivatives	147
7.7. Effect of plasma cleaning on a MUA monolayer on gold nanoantennas	149
7.8. NAIRS signal strength estimation of the 1465cm^{-1} band	151
7.9. Comparison of enhancement factors of ODT and MUA	153
A.1. Lithographic nanorod preparation	191

List of Figures

A.2. Carbon contamination during SEM measurements	193
A.3. Influence of brightness and contrast in SEM images	195
A.4. Comparison between different SEMs	196
A.5. Schematic drawing of the beam path inside the IR microscope	198
A.6. Schematic drawing of a Schwarzschild objective	200
A.7. Non-linearity of the MCT detector	201
A.8. MCT measurement time and influence of different apertures	202
A.9. Measurement of a 100%-line	203
A.10.CO ₂ and water ice absorption in single channel spectrum	204
A.11.Influence of non-linearity correction on measurement stability	205
A.12.Evolution of CO ₂ intensity depending on purging	206
A.13.Influence of argon-sputtering	207
A.14.Stability of the relative reflectance measurement in IRRAS	208
A.15.IRRAS spectra of MUA (raw data)	209
B.1. Substrate inhomogeneity	212
B.2. Behavior of the characteristic resonance parameters for different d_x	212
B.3. Mixed interaction. Relative reflectance spectra and $\lambda_{\text{res}}(L)$ relation	213
B.4. Comparison between measurements of different resolution	213
B.5. Evolution of the combined $l = 1$ and $l = 2$ modes (spectra)	214

List of Tables

3.1. Characteristic parameters of the gold nanorod samples	30
3.2. Refractive indices of the substrates	34
3.3. Vibrational frequencies of MUA adsorbed on gold	41
4.1. Reproducibility of lithographic preparation	58
4.2. Fitting results of the relation $\lambda_{\text{res}}(L)$ for different substrates	68
4.3. Linear fits of the relations $\lambda_{\text{res}}(L)$ of higher order modes	72
6.1. Different FIB parameters for nanogap preparation	121
7.1. Frequencies and mode assignments of MUA (IRRAS)	143
A.1. Explanation of the components of the IR microscope	199
B.1. Results of the spectral fit of thermally oxidized silicon (spectrum of Fig. 3.7)	211

1. Introduction

Infrared (IR) spectroscopy [1] is a well-known analytical method in life sciences. Since nearly every specimen (gaseous molecules, liquids, solid states) features characteristic absorption bands (“fingerprints”) in the IR spectral range [1], IR spectroscopy can be used for the identification and quantification (Lambert-Beer law [2]) of known compounds [3]. Furthermore, information about composition, structure, and configuration of, preferentially, organic molecules can be derived. Advantages of IR spectroscopy include label-free, non-destructive, and *in situ* investigations, applied for example to analyze the secondary structure of proteins [4, 5].

Unfortunately, IR as well as the complementary Raman spectroscopy [6] suffer from very low scattering cross-sections ($10^{-20} - 10^{-30} \text{ cm}^2$) [7], limiting the detection of very small amounts of molecules. However, this problem can be overcome by the use of field-enhanced vibrational spectroscopies based on surface-enhanced Raman scattering (SERS) [8, 9] and its counterpart, surface-enhanced infrared absorption (SEIRA) [10, 11]. Besides the chemical contribution (formation of charge transfer complexes, first layer effect, see e.g. [12–15]), the main part of the signal enhancement originates from the excitation of surface plasmon resonances (collective electron oscillations) at metal surfaces, resulting in considerable electromagnetic field enhancement in the vicinity of metal surfaces [16, 17]. Furthermore, it was found that resonant excitation of *localized* surface plasmon resonances in metal nanoparticles by light yields huge local electromagnetic near-field enhancement [18, 19]. And due to the rapid evolution of new nanostructure preparation techniques (e.g. electron beam lithography, ion beam milling, self assembly), an own field of research, *plasmonics* [20, 21], developed which can be considered as “*merging photonics and electronics at nanoscale dimensions* [22]“.

While first SEIRA experiments were carried out on rough [10, 23] or island-like metal films [24–27], the sensitivity of the method was improved by employing regularly arranged metal nanoparticles [28]. One advantage of metal nanoparticles over random-like island structures is the possible tuning of the particles’ optical properties by varying size and shape [18]. In this context, metal nanorods with lengths in the micron range are of special interest since their resonance position

1. Introduction

in the IR can be adjusted by mainly changing the rod length [29–31]. In analogy to radio frequency antennas, nanorods are referred to as “nanoantennas” to reflect their ability to concentrate electromagnetic radiation. Recently, gold nanorods have been applied to the sensing of adsorbed molecules [32–34], pushing the detection limit towards zeptomolar¹ sensitivity. In addition, near-field interaction over narrow gaps between the tip ends of parallel aligned nanoantennas promises additional enhancement of the electromagnetic field [30, 35].

The present thesis deals with lithographically prepared gold nanorods which show antenna-like plasmon resonances in the IR. Nanorods arranged in regular arrays are better suited for potential sensing applications compared to individual nanorods since shorter measurement times are possible due to higher signal-to-noise ratio. For this reason, one aim of the thesis was to investigate the dependency of the nanorods’ optical properties on the rod arrangement within an array. The obtained findings set path for an optimal design of nanoantenna arrays suited for nanoantenna-assisted infrared spectroscopy (NAIRS) [33, 34]. Moreover, the main objective was to increase near-field coupling between nanorods by preparing nanogaps between their tip ends in the range of less than 20 nm. To this end, two different approaches to nanogap fabrication were applied and investigated: the narrowing of lithographically prepared gaps (20 – 50 nm) by chemically induced metal deposition [36, 37], on the one hand, and the milling of long rods by focused ion beams (FIB) [38] on the other hand. Furthermore, the probe molecule mercaptoundecanoic acid was used to demonstrate the sensing application of NAIRS.

The structure of the thesis is as follows: Chapters 2 and 3 briefly present fundamentals, materials, and methods, which are necessary for the understanding of the experimental results in Chaps. 4 to 7. Whereas Chap. 4 focuses on the optical properties of arrays consisting of non-interacting nanorods, Chap. 5 investigates the separation-dependency of the nanorods’ optical response within arrays. The main part, the characterization and preparation of nanogaps, is discussed in Chap. 6. Furthermore, first results of NAIRS of mercaptoundecanoic acid are shown in Chap. 7 and compared to former experiments with octadecanethiol [34]. Finally, summary and outlook can be found in Chap. 8 and 9, respectively.

¹One zeptomol corresponds to 10^{-21} mol.

2. Fundamentals

The chapter starts with an introduction on infrared spectroscopy (Sec. 2.1), explaining the basic principles of Fourier transform infrared spectroscopy. After a brief overview on metal optics (Sec. 2.2), plasmon-polaritons are introduced in Sec. 2.3. Furthermore, Sec. 2.4 deals with the optical properties of individual nanoantennas, whereas interaction effects between several particles is shortly reviewed in Sec. 2.5. Subsequently, Sec. 2.6 focuses on the interaction of light and phonons in dielectric media. Finally, the effect of surface-enhanced infrared absorption, which is the basis of nanoantenna-assisted infrared spectroscopy, is covered in Sec. 2.7.

2.1. Infrared Spectroscopy

The present section is based on the description given in [1]. In general, spectroscopy deals with interaction of electromagnetic waves and matter. A sample is illuminated by a certain radiation source and the energy of the transmitted or reflected light is analyzed. Since frequencies of molecular vibrations are located in the IR regime, IR spectroscopy is commonly used to investigate the vibrational spectrum of solid, liquid or even gaseous species¹. Besides molecular vibrations, also other excitations, such as plasmon- (Sec. 2.3) or phonon-polaritons (Sec. 2.6), can be probed by IR spectroscopy, in which light is usually characterized by the quantity wavenumber² [1]

$$\tilde{\nu} = \frac{1}{\lambda} = \frac{E}{hc}. \quad (2.1)$$

Here, λ , E , and c are the wavelength, energy, and speed of the light, respectively, and h is Planck's constant. The relevant spectral region in this work ranges from approximately $\tilde{\nu} = 600 \text{ cm}^{-1}$ to $\tilde{\nu} = 7000 \text{ cm}^{-1}$ and belongs to the mid-infrared (MIR).

¹Note that only molecular vibrations which feature a transition dipole moment can be excited by IR light [1].

²The wavenumber is sometimes referred to as "frequency". It must not be mixed up with the frequency $\nu = c/\lambda$.

2. Fundamentals

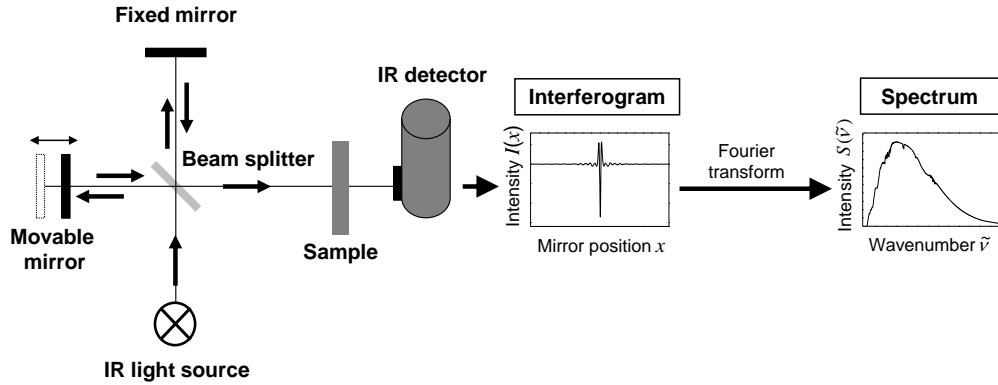


Figure 2.1.: Schematic diagram [39] of a FT-IR spectrometer consisting of a IR light source, a classical Michelson interferometer, and an IR detector. By Fourier transforming the measured interferogram $I(x)$, the actual spectrum $S(\tilde{\nu})$ is obtained (see text).

In contrast to dispersive spectroscopy, where spectral dispersion of light is achieved by gratings or prisms, the Fourier transform infrared (FT-IR) technique performs the spectral splitting with the help of an interferometer, allowing wavelength dependent radiation modulation. The simplest type is the classical Michelson interferometer, consisting of a movable and a fixed mirror (see Fig. 2.1). Coming from the IR light source, the IR beam is divided by a beam splitter into two partial beams, which are reflected on mirrors back to the beam splitter where they recombine and interfere. After passing the sample, the light is collected by an IR detector (see Sec. 3.2.1 for the different types). Any shifting of the movable mirror changes the optical path length, leading to a varying interference amplitude. Thus, the detected signal intensity is a function of the mirror position and is called *interferogram*.

As a simple example, moving the mirror in case of a monochromatic light source (e.g. laser) of frequency $\tilde{\nu}_0$ leads to a cosine signal of the measured intensity I as a function of the optical path difference x [1]:

$$I(x) = \frac{S_0}{2} \{1 + \cos(2\pi\tilde{\nu}_0x)\}, \quad (2.2)$$

where S_0 is the initial beam intensity. In the case of a broadband light source with spectral intensity $S(\tilde{\nu})$, an integration over all frequencies $\tilde{\nu}$ has to be performed to obtain the interferogram $I(x)$ [1]:

$$I(x) = \int_0^{\infty} S(\tilde{\nu}) \{1 + \cos(2\pi\tilde{\nu}x)\} d(2\pi\tilde{\nu}). \quad (2.3)$$

While the first part of the integrand is a constant which depends on the beam profile, detector, etc., the second part represents the Fourier transform of the spectral intensity $S(\tilde{\nu})$. By calculating the inverse Fourier transform, $S(\tilde{\nu})$ can be determined [1]:

$$S(\tilde{\nu}) = \int_{-\infty}^{\infty} I(x) \cos(2\pi\tilde{\nu}x) dx. \quad (2.4)$$

Note that the spectrum $S(\tilde{\nu})$ calculated by Eq. (2.4) features spectral characteristics of the apparatus (beam profile, beam splitter, polarizer, detector, etc.), which can be eliminated by normalizing the spectrum of the sample to a reference spectrum (see Sec. 3.2.2).

2.2. Metal Optics

The general dispersion relation of electromagnetic waves inside non-magnetic media can be derived from Maxwell's equations in matter [40] and is given by [41]

$$|\vec{k}|^2 = \epsilon(\omega) \frac{\omega^2}{c^2}. \quad (2.5)$$

Here, \vec{k} and $\omega = 2\pi c\tilde{\nu}$ denote the wave vector and the angular frequency of the electromagnetic wave, respectively. Hence, the propagation behavior of the wave is determined by the medium's dielectric function ϵ which is, in most cases, a complex function of ω [42]:

$$\epsilon(\omega) = \epsilon_1(\omega) + i\epsilon_2(\omega), \quad (2.6)$$

featuring a real ($\Re\{\epsilon\} = \epsilon_1$) and imaginary part ($\Im\{\epsilon\} = \epsilon_2$). Furthermore, the complex refractive index \tilde{N} is defined according to [42, 43]

$$\tilde{N} = n + i\kappa = \sqrt{\epsilon} = \sqrt{\epsilon_1 + i\epsilon_2}. \quad (2.7)$$

Its real and imaginary part are referred to as refractive index n and extinction coefficient κ . The real part n determines the propagation velocity of the electromagnetic wave inside the medium, whereas the imaginary part κ leads to an exponential decay of the electric field vector which is called absorption [41].

2. Fundamentals

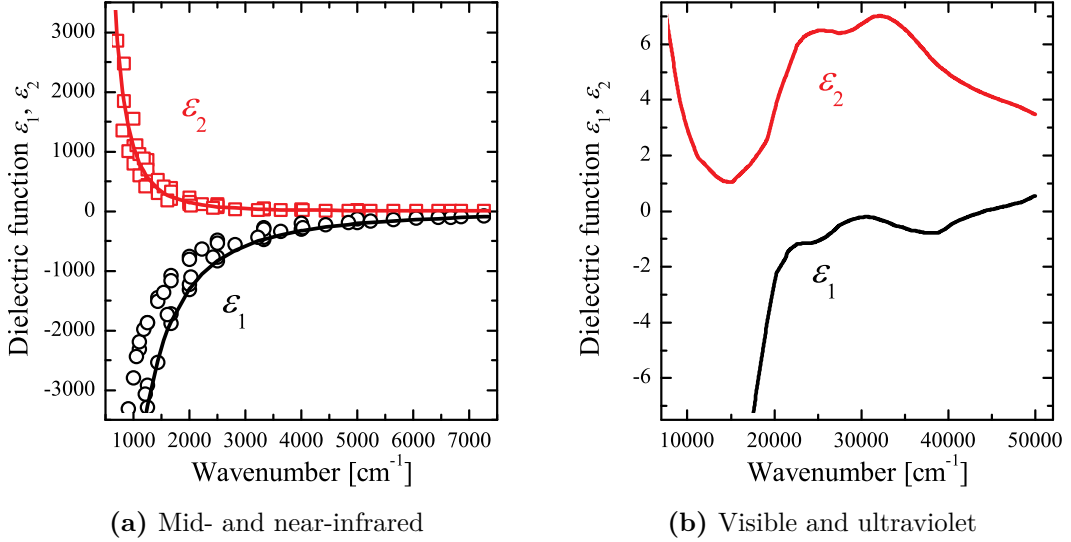


Figure 2.2.: Real (ϵ_1) and imaginary part (ϵ_2) of the bulk dielectric function of gold in the (a) IR and (b) visible/UV range. In (a), the open symbols represent experimental data from ORDAL *et al.* [44]. In addition, calculations of ϵ_1 and ϵ_2 according to the Drude model ($\omega_p/2\pi c = 72500 \text{ cm}^{-1}$ and $\omega_\tau/2\pi c = 216 \text{ cm}^{-1}$) are shown as solid lines. The curves in (b) originate from experimental data of JOHNSON & CHRISTY [45], which is taken from the SCOUT database [46].

In general, the dielectric function of a metal can be written as [47]

$$\epsilon(\omega) = 1 + \chi_{\text{free}}(\omega) + \chi_{\text{IB}}(\omega), \quad (2.8)$$

considering the susceptibilities χ_{free} and χ_{IB} of free electrons and interband transitions, respectively. Over a wide frequency range, the metal optical properties can be described by the model of P. DRUDE [48], where a gas of free electrons moves against a fixed background of positive core ions. In this model, the metal dielectric function is given by [20, 41]

$$\epsilon(\omega) = \epsilon_\infty - \frac{\omega_p^2}{\omega^2 + i\omega\omega_\tau}, \quad (2.9)$$

with the two Drude parameters plasma frequency ω_p and scattering rate ω_τ . In addition, the dielectric constant ϵ_∞ describes the effect of a residual polarization caused by the positive background of the core ions and is usually in the range between 1 and 10. For a detailed description of the Drude model, the reader is referred to the literature [42, 49–51].

Figure 2.2 shows the bulk dielectric function of gold from the MIR to the ultraviolet (UV) spectral range. In the IR (Fig. 2.2a), the Drude dielectric function of Eq. (2.9) provides a good approximation for ϵ_1 and ϵ_2 . They show the typical behavior of metals: the absolute values of ϵ_1 and ϵ_2 monotonically increase with decreasing wavenumber. Since ϵ_1 features high negative values, electromagnetic waves cannot propagate through the metal and are therefore reflected. However, they can penetrate into the metal for a certain distance, the skin depth δ_{skin} , which is about 22 nm for gold in the IR [52]. In the visible and UV spectral range (Fig. 2.2b), the onset of interband transitions at around 19000 cm^{-1} [53] leads to an increase of ϵ_2 . Furthermore, ϵ_1 becomes positive for $\omega/2\pi c \gtrsim 44000 \text{ cm}^{-1}$, causing the UV transparency of gold.

2.3. Plasmon-Polaritons

In general, *plasmons* are collective charge carrier oscillations in a free electron gas. In the following, the properties of bulk and surface plasmon modes as well as localized particle plasmons are briefly discussed.

The optical properties of an *ideal metal* can be described within the Drude model, neglecting the damping term ω_τ and setting the background polarizability $\epsilon_\infty = 1$. Consequently, Eq. (2.9) yields the simple form

$$\epsilon(\omega) = 1 - \left(\frac{\omega_p}{\omega}\right)^2. \quad (2.10)$$

Considering an infinite three-dimensional (3D) metal, two different types of electromagnetic modes exist [17]. The first types of modes, *volume plasmons* (VPs), are longitudinal modes which do not couple to transverse electromagnetic waves [20]. The second types of modes, *volume plasmon-polaritons* (VPPs), are transverse modes similar to photons except that their optical properties are modified by interaction with electrons of the metal. The VPP dispersion relation,

$$k(\omega) = \frac{\sqrt{\omega^2 - \omega_p^2}}{c}, \quad (2.11)$$

follows from Eq. (2.5) by using $\epsilon(\omega)$ of Eq. (2.10). As illustrated in Fig. 2.3a, it asymptotically approaches the ones of the photon [$\omega(k) = c \cdot k$] and the VP [$\omega(k) = \omega_p$] in the limit of very large and very small wave vectors, respectively. Hence, the expression *polariton* always describes a mixture of a photonic and another elementary excitation (compare to *phonon-polaritons* in Sec. 2.6).

2. Fundamentals

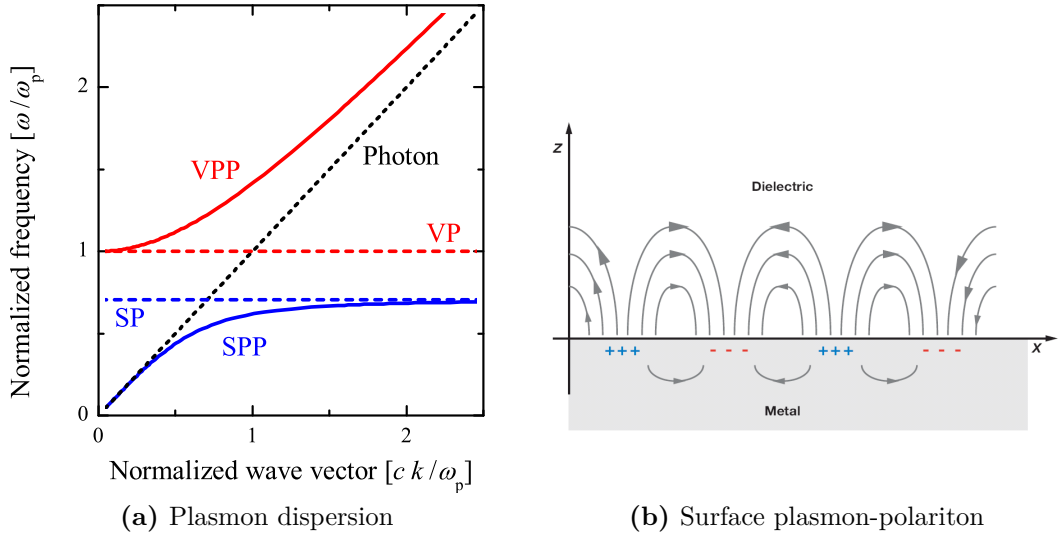


Figure 2.3.: (a) Dispersion curves of the volume [Eq. (2.11)] and surface plasmon-polariton [Eq. (2.12)] with $\epsilon(\omega)$ according to Eq. (2.10) and $\epsilon_d = 1$, respectively. The frequencies of volume (ω_p) and surface plasmon ($\omega_p/\sqrt{2}$) follow from Eq. (2.10) and the conditions $\epsilon(\omega) = 0$ (VP) and $\epsilon(\omega) = -1$ (SP) [17]. (b) Schematic representation of a surface plasmon-polariton propagating in x -direction [54].

No bulk modes exist for frequencies below ω_p due to the negative dielectric function [see Eq. (2.10)]. However, electromagnetic surface waves are possible in presence of an interface between metal and dielectric medium [20]. In analogy to the 3D case, *surface plasmons* (SP) and *surface plasmon-polaritons* (SPPs) are the two different types of modes. The dispersion relation of the SPP is derived by solving Maxwell's equations, considering the continuity conditions for electromagnetic fields at interfaces [55]:

$$k_{\parallel}(\omega) = \frac{\omega}{c} \sqrt{\frac{\epsilon(\omega)\epsilon_d}{\epsilon(\omega) + \epsilon_d}}, \quad (2.12)$$

where ϵ_d is the dielectric constant of the dielectric medium. The solid blue curve in Fig. 2.3a illustrates the dispersion relation of Eq. (2.12), which approximates the light line for small wave vectors and the SP frequency for large wave vectors. Moreover, Eq. (2.12) describes a longitudinal electron surface wave, propagating in the direction parallel to the surface (see Fig. 2.3b). Since its electric field intensity perpendicular to the interface exponentially decays, the wave is bound to the surface [56].

Localized Surface Plasmon Resonances

Electrons in metal nanoparticles exhibit plasma oscillations similar to those of surface plasmon-polaritons. However, the term *localized* surface plasmon-polariton is used since the propagation of these modes is restricted to the geometry of the particle in contrast to the propagating bulk and surface modes. Under certain conditions, localized surface plasmon resonances (LSPRs) can be directly excited by light as briefly discussed in the following.

The scattering of electromagnetic waves by spherical particles can be solved analytically according to Mie's theory [57]. Moreover, if the nanoparticle is much smaller than the wavelength λ of the exciting radiation, the scattering problem can be described in the *quasi-static* approximation [16, 17]. Here, retardation is neglected since the phase of the electromagnetic wave is nearly constant over the dimensions of the particle. Furthermore, only dipolar resonances are considered. In this model, the polarizability $\alpha(\omega)$ of a spherical metal nanoparticle with radius R , surrounded by a medium with dielectric constant ϵ_d , is given by [17]

$$\alpha(\omega) = 4\pi\epsilon_0\epsilon_d R^3 \frac{\epsilon(\omega) - \epsilon_d}{\epsilon(\omega) + 2\epsilon_d}, \quad (2.13)$$

where $\epsilon(\omega)$ describes the metal dielectric function and ϵ_0 is the vacuum permittivity. In case of weak damping ($\epsilon_2 \ll 1$), the induced polarization inside the particle shows resonant behavior at the frequency ω_{res} matching the equation

$$\epsilon_1(\omega_{\text{res}}) = -2\epsilon_d. \quad (2.14)$$

The spectral position of the LSPR depends on material properties of the metal via $\epsilon(\omega)$ as well as on the polarizability of the surrounding medium via ϵ_d . As an example, gold nanospheres in vacuum ($\epsilon_d = 1$) show resonances for $\lambda_{\text{res}} = 2\pi c/\omega_{\text{res}} \approx 484 \text{ nm}$, whereas resonances for silver nanospheres occur at $\lambda_{\text{res}} \approx 354 \text{ nm}$ [58].

Another consequence of Eq. (2.14) is that a surrounding medium with $\epsilon_d > 1$ shifts the LSPR to longer wavelengths. This behavior, which is commonly termed *red-shift*, is due to the monotonic decrease of $\epsilon_1(\omega)$ towards lower frequencies (compare to Sec. 2.2). Moreover, if $\epsilon_1(\omega)$ can be described by Eq. (2.10), the resonance condition of Eq. (2.14) yields

$$\omega_{\text{res}} = \frac{\omega_p}{\sqrt{1 + 2\epsilon_d}}. \quad (2.15)$$

2. Fundamentals

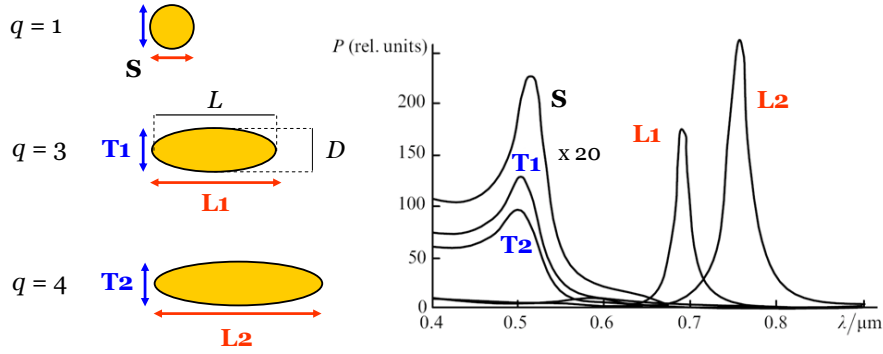


Figure 2.4.: Quasi-static calculation of the absorbed radiation power of gold nanoparticles ($L \ll \lambda$) surrounded by water ($\epsilon_d = 1.77$) [60]. For non-spherical particles, longitudinal (L1 and L2) and transverse (T1 and T2) modes exist which become spectrally more separated as the aspect ratio q increases. The scale of curves S, T1 and T2 over the ordinate is magnified by a factor of 20.

Note that the quasi-static model is only an approximation and that the LSPR also depends on the size and shape of the nanoparticle [54]. For example, the LSPR shifts to longer wavelengths in case of a nanosphere with increasing sphere radius R [17, 59].

The quasi-static model is not restricted to spherical particles and also holds for ellipsoids [19, 61]. In the following, prolate ellipsoids will be considered since their shape resembles the one of nanorods. Figure 2.4 shows quasi-static calculations of a sphere and two different ellipsoids [60], which are characterized by their aspect ratio

$$q = \frac{L}{D}, \quad (2.16)$$

where L denotes the length and D the diameter of the particle. While the sphere ($q = 1$) features a single resonance, the absorption behavior of the elongated particles depends on the polarization of the incident light. *Transverse* (T1 and T2) and *longitudinal* (L1 and L2) modes³ exist for light polarized perpendicular or parallel to the long axis, respectively. While the transverse modes exhibit a small blue-shift of the LSPR with increasing q , a strong red-shift accompanied by increasing intensity is observed for the longitudinal modes. Further augmentation of q would yield resonances in the IR range. However, if the sizes of L and λ become comparable, the quasi-static approximation becomes invalid since retardation has to be considered.

³“Transverse” and “longitudinal” refer to the orientation of the electron oscillation relative to the long particle axis. Note that the electron oscillations are of longitudinal nature in both cases.

2.4. Individual Nanoantennas

The model of the ideal antenna is useful to gain insight into the optical properties of nanoantennas. “Ideal” in this context means that the cylindrical antenna of diameter D , being much smaller than the antenna length L , consists of a perfectly conducting metal⁴. Consequently, light is not able to penetrate into the metal ($\delta_{\text{skin}} = 0$). In this model, the optical properties are obtained by classical scattering theory of electromagnetic waves including retardation. As a result, antenna resonances occur if L matches multiples of one half of the incident wavelength [62]:

$$L = l \cdot \frac{\lambda_{\text{res}}}{2n_s}, \quad l \in \mathbb{N}. \quad (2.17)$$

In this equation, the influence of a surrounding dielectric medium is taken into account via its refractive index n_s . As discussed in Sec. 2.4.1, this relation does not hold for nanosized metal antennas. Furthermore, Sec. 2.4.2 deals with the field enhancing properties of nanoantennas. Finally, Eq. (2.17) indicates that also higher order excitations ($l > 1$) are possible additional to the fundamental resonance ($l = 1$). This topic is addressed in Sec. 2.4.3.

2.4.1. Spectral Resonance Position

In the model of the ideal antenna, the spectral resonance position λ_{res} only depends on the antenna length L and the refractive index of the surrounding medium n_s [Eq. (2.17)]. Considering real metal nanoantennas, this behavior changes as illustrated by the BEM⁵ simulations of Fig. 2.5. Here, the far-field resonance position λ_{res} is plotted versus the total rod length $L_{\text{total}} = L_{\text{rod}} + 2R$ of cylindrically shaped nanorods with hemispherical tip ends (see sketch in Fig. 2.5). The solid green line represents the relation of an ideal antenna in vacuum, which obviously differs from the simulated relations. One reason for this discrepancy is that sharp tip ends inhibit full charge build up for small R , suppressing half-wavelength charge oscillations that have maximum charge density at the rod ends [29]. Furthermore, the metal cannot be treated as a perfect conductor in the IR and, hence, the skin depth δ_{skin} (Sec. 2.2) cannot be neglected [65]. Since δ_{skin} of gold is in the range of 15 – 30 nm at optical and

⁴It is $\epsilon_1 \rightarrow -\infty$ and $\epsilon_2 \rightarrow 0$ for an ideal conductor.

⁵The **boundary element method** [63, 64] is a simulation technique, allowing the exact calculation of the optical response of a nanoobject, including retardation [29].

2. Fundamentals

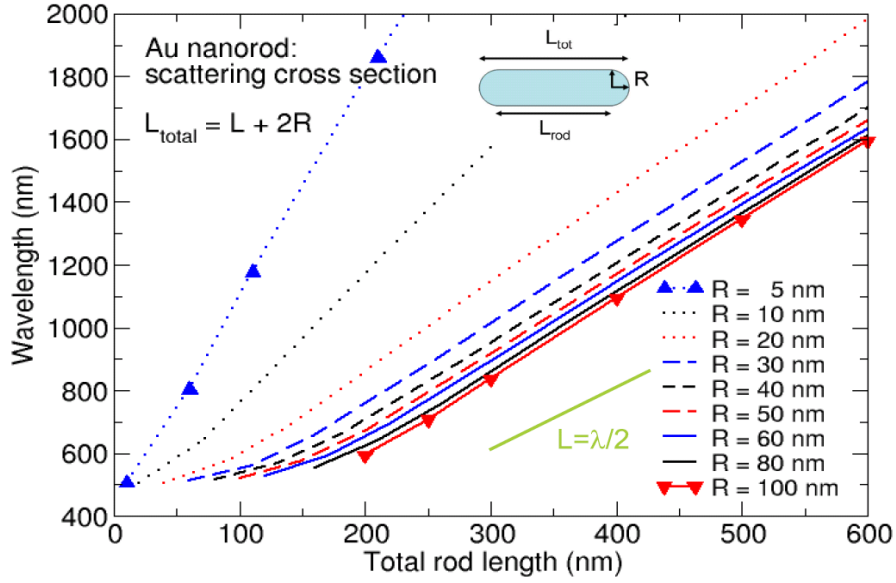


Figure 2.5.: Resonant wavelength versus total antenna length for different diameters (BEM simulations). The schematic representation of the nanorod as well as the ideal antenna relation ($L = \lambda/2$) were subsequently inserted into the figure, which is taken from [29].

infrared frequencies [29, 52], the diameter $D = 2R$ becomes increasingly important and, hence, the position of λ_{res} depends on R for fixed L_{total} . The influence of R is rather strong for R in the range of δ_{skin} , whereas only small changes of $\lambda_{\text{res}}(L_{\text{total}})$ are observed in Fig. 2.5 for $R \gg \delta_{\text{skin}}$.

Concerning the L_{total} -dependency of λ_{res} , a linear relation exists for sufficiently long rods. In 2007, NOVOTNY proposed an analytic approximation [65] which allows the calculation of an *effective wavelength* λ_{eff} inside a thin antenna ($L \gg R$):

$$\lambda_{\text{eff}}(\lambda; \epsilon_s, R, \lambda_p, \epsilon_\infty) = \frac{\lambda}{\sqrt{\epsilon_s}} \sqrt{\frac{4\pi^2 \epsilon_s \left[\frac{R}{\lambda} \cdot \tilde{z}(\lambda; \lambda_p, \epsilon_\infty, \epsilon_s) \right]^2}{1 + 4\pi^2 \epsilon_s \left[\frac{R}{\lambda} \cdot \tilde{z}(\lambda; \lambda_p, \epsilon_\infty, \epsilon_s) \right]^2} - 4R}. \quad (2.18)$$

In this equation, λ denotes the wavelength of the incident radiation and ϵ_s the dielectric constant of a homogeneous surrounding medium. Furthermore, $\tilde{z}(\lambda; \lambda_p, \epsilon_\infty, \epsilon_s)$ is a function of λ featuring the three parameters λ_p (plasma wavelength of the metal), ϵ_∞ , and ϵ_s . The reader may be referred to [65] for the exact expression of \tilde{z} . Basic assumption in this model is that the metal can be described by a Drude dielectric function neglecting the scattering rate ω_τ [Eq. (2.9) with $\omega_\tau = 0$]. In this thesis,

Eq. (2.18) is used to describe the relation between λ_{res} and L of gold nanorods. To this end, the function

$$L(\lambda_{\text{res}}) = \lambda_{\text{eff}}(\lambda_{\text{res}}; \epsilon_{\text{s}}, R, \lambda_{\text{p}} = 138 \text{ nm}, \epsilon_{\infty} = 1) / 2 \quad (2.19)$$

is fitted to the experimental data with the only fitting parameter ϵ_{s} . The radius R of cuboid-shaped rods is calculated by converting the rectangular cross-section into a circular one of same area ($R = \sqrt{w \cdot h / \pi}$ with rod width w and height h).

The surrounding medium also influences the spectral resonance position besides the geometrical parameters L and R . As indicated in Eq. (2.17), any value of $n_{\text{s}} > 1$ leads to a shift of the resonance to longer wavelengths, which is also true for nanoantennas [7]. This can be explained by electric induction charges of opposite sign that are formed inside the dielectric. In media with high polarizability (high refractive index n_{s}), more induction charges arise, attenuating the intra-rod restoring force.

The influence of the three parameters L , $D = 2R$, and n_{s} on the spectral resonance position can be summarized as follows:

- longer L leads to a red-shift of λ_{res} for fixed D and n_{s} ,
- larger D leads to a blue-shift of λ_{res} for fixed L and n_{s} ,
- higher n_{s} leads to a red-shift of λ_{res} for fixed L and D .

2.4.2. Electromagnetic Field Enhancement

Metal nanostructures, in particular metal nanoantennas, are able to strongly enhance the local electric field (near-field) in the vicinity of the metal surface when excited resonantly by light [7, 17, 20]. As shown by simulations [30], the local-field at the vicinity of the tip end of a nanorod can be considerably enhanced compared to the incident electric field. The electric field enhancement is notably strong for plasmonic excitations [7] due to the typically large negative value of ϵ_1 of metals (compare to Sec. 2.2). Moreover, the *lightning rod effect* [67], which is exclusively determined by the structure's geometry, additionally contributes to the field enhancement. While the local field is symmetrically distributed on spherical surfaces, it is rather concentrated at the tip ends of prolate ellipsoids. This leads to increasing field enhancement for nanorods with high aspect ratio, as illustrated in Fig. 2.6. Here, mappings of the local electric field E normalized to the incident electric field E_0 are shown for two

2. Fundamentals

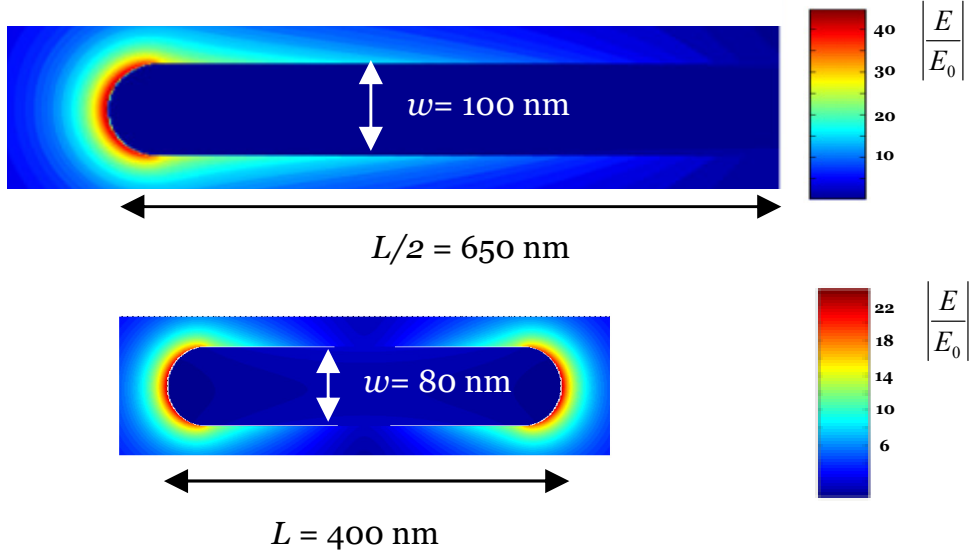


Figure 2.6.: BEM simulated near-field distribution [66] of two cylindrically-shaped, resonant gold nanoantennas in vacuum featuring different length L and width w . Note the different color scale for the two plots, quantifying the ratio between the local electric field E and the incident field E_0 .

different gold nanoantennas at resonance. Obviously, the longer rod ($q = 13$) features higher values of $|E/E_0|$ at the vicinity of the tip ends (note the different color scale) compared to the shorter rod ($q = 5$). Moreover, as shown in [30], the near-field intensity at the vicinity of the rod tip

- increases for longer rod length L at fixed rod radius R ,
- increases for smaller R at fixed L .

However, the second point does not hold for very small R , since the simulations of [30] do not consider a size-dependent scattering rate ω_τ of the dielectric function of gold. For small dimensions, additional scattering of the electrons counteracts with the lightning rod effect, leading to an optimal rod diameter for the field enhancement. Moreover, the tip end morphology also plays an important role: the sharper the tip, the higher the electric field enhancement [68, 69].

In summary, the characteristic behavior of the metal dielectric function (monotonic decrease of ϵ_1 with increasing wavelength, see Sec. 2.2) and the lightning rod effect are responsible for the higher electric field enhancement of nanorods resonant in the IR compared to those being resonant in the visible spectral range.

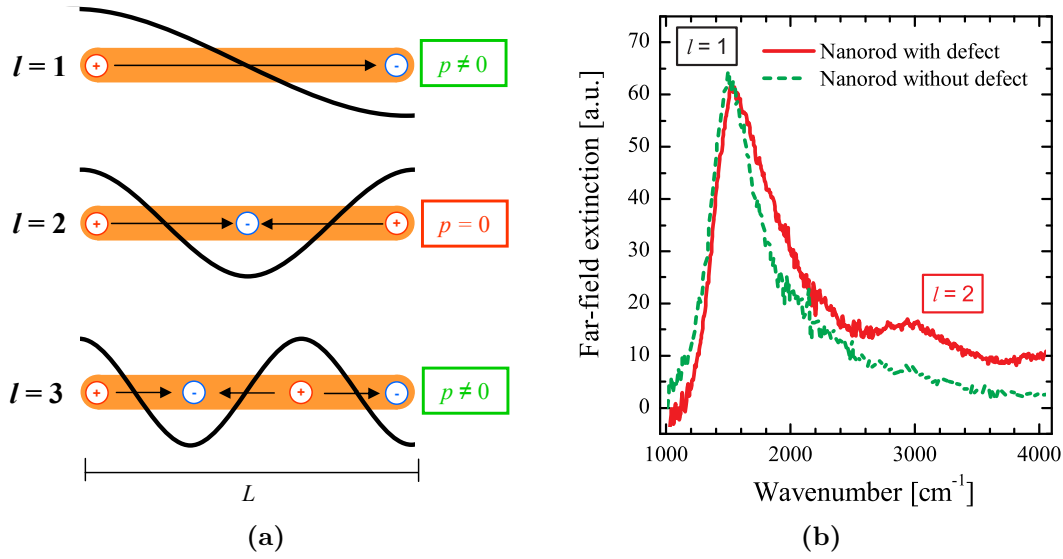


Figure 2.7.: (a) Charge distributions of the first three resonance modes of an antenna with length L . Due to the separation of charges, dipole moments are formed and indicated by arrows. (b) Far-field extinction spectra of two individual, lithographically prepared nanorods ($L \approx 1.5 \mu\text{m}$, $w \approx 60 \text{nm}$, $h \approx 100 \text{nm}$) on ZnS [70]. The second order resonance ($l = 2$) is only observed for the nanorod with a structural defect.

2.4.3. Higher Order Modes

This section is partly adopted from [71]. Besides the strong fundamental mode ($l = 1$), nanoantennas also exhibit multipolar ($l > 1$) resonances at roughly λ_{res}/l [70]. It is known from classical antenna theory [40] that only multipolar modes with an antisymmetric charge distribution (odd l) can be excited at normal incidence of light [72, 73] due to their non-vanishing total dipole moment p , as illustrated in Fig. 2.7a. In contrast to these *bright modes*, the excitation of centrosymmetric charge distributions (*dark modes*, even l) is not possible at normal incidence of light.

However, dark modes can be enabled by symmetry-breaking [74], e.g. oblique incidence of light [75, 76] or structural defect of the nanorod [70]. Latter is illustrated in Fig. 2.7b, where far-field extinction spectra of two individual nanorods are shown. The even order resonance $l = 2$ only occurs for the imperfectly prepared nanorod, whereas it is not detected for the intact nanorod (see [70] for details). In addition, numerical simulations support that dark modes can be activated at normal incidence when the excited nanostructure features asymmetric shape [70]. Structural defects may be induced by inhomogeneities of the substrate's surface (e.g. scratches) or imperfections arising from the lithographic preparation of the nanorods.

2.5. Interaction between Nanoantennas

The present section is partly adopted from [77]. Interaction between particles in multimers and in arrays of nanoantennas affects the optical properties of the system which therefore strongly depend on the separation distances, especially between nearest neighbor particles. Interaction effects were broadly analyzed experimentally and theoretically for different kinds of arrangements and shapes of particles. In addition to the investigation of coupling in dimers consisting of e.g. ellipsoids [78], spheres [74, 79], nanodisks [80], nanorods [81, 82], or nanoantennas [83, 84], also many-particle systems like nanorod assemblies [59], linear arrays of nanocylinders [85], or two-dimensional (2D) nanoparticle arrays [86–91] have been subject of studies. It is important to note that all these studies focused on the visible spectral range while there are only a few dealing with the IR [30, 32, 92], where retardation can no more be neglected since an electromagnetic wave needs a not negligible time to travel from one rod end to the other. Because the rod lengths are similar to the wavelength, the Rayleigh limit is no more applicable to Mie scattering and extinction at resonance arises from absorption and scattering. Thus, the line shape of the resonance curve is due to both the contributions, absorption and scattering, and we deal with the problem of resonant Mie scattering and asymmetric lines.

Two regimes of interaction between the antennas can be distinguished: the direct dipolar interaction in the near-field, which features a $1/d^3$ dependence on the particle separation d , and the radiative coupling in the far-field, which varies as $\exp(ikd)/d$ [85, 89] with k being the wave vector of the emitted radiation that depends on the refractive index n_s of the surrounding medium. The near-field interaction regime is relevant for very small d , whereas the long-range radiative coupling becomes important for d in the range of the wavelength in the surrounding medium. Therefore, in a system with nanoparticles on a substrate, its refractive index clearly determines the transition between near-field and radiative coupling.

Near-Field Dipolar Coupling

Regarding the dipolar near-field coupling, a reduction of d between two spherical particles, for example, results in a strong red-shift of the resonance if the incident light is polarized parallel to the dimer axis. On the other hand, perpendicular polarization of the light leads to a moderate blue-shift for decreasing d [74, 79, 94]. This can be understood within the plasmon hybridization model [74] where an analogy to the formation of bonding and antibonding atomic orbitals exists. Similar behavior is

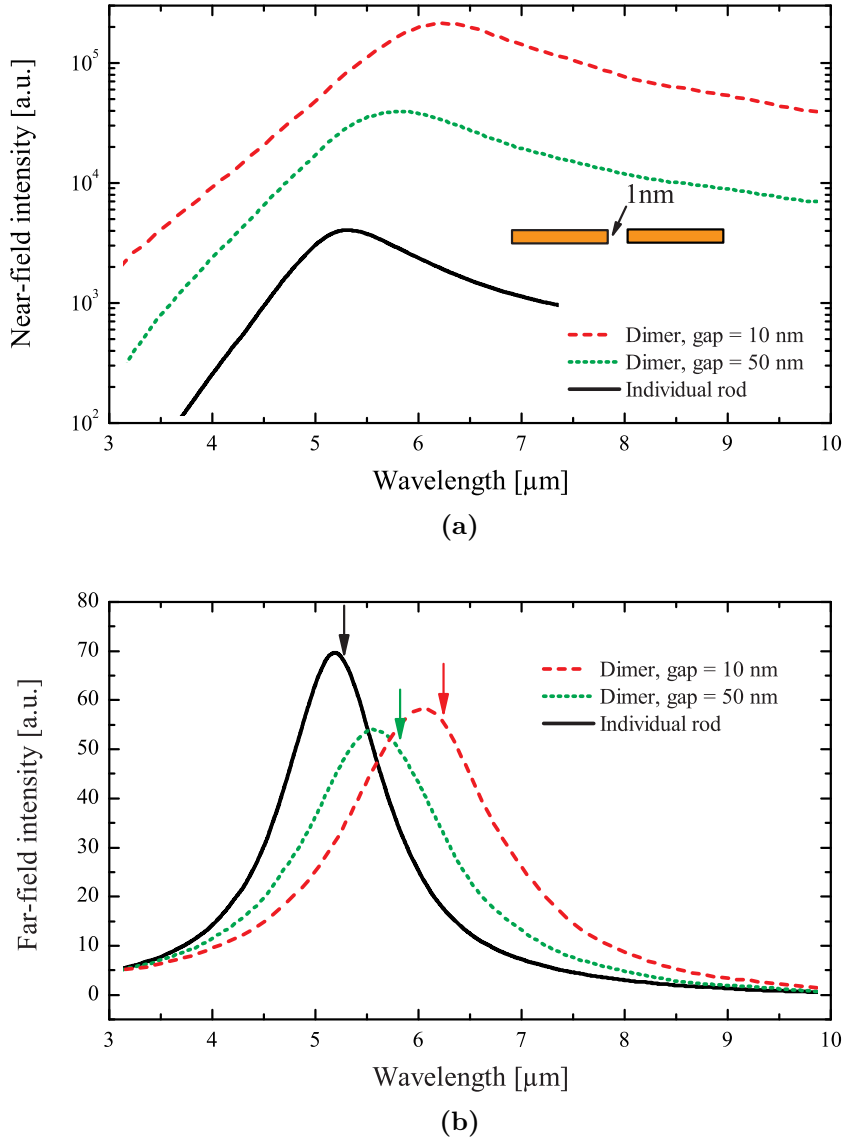


Figure 2.8.: FDTD simulations [93] of cuboid-shaped gold nanorods ($L = 1410\text{nm}$, quadratic cross-section of $40 \times 40\text{nm}^2$) supported by a CaF_2 substrate. (a) and (b) show the near- and far-field responses, respectively, of an individual gold nanorod as well as those of nanorod dimers with gaps of 50 nm and 10 nm. In (a), the near-field spectrum is calculated at a position located 1 nm away from one tip end inside the gap in case of the dimers (see schematic drawing). In (b), the far-field extinction values are normalized to the response of one nanorod. Additionally, the resonance positions of the near-field spectra in (a) are indicated by arrows in (b).

2. Fundamentals

observed for the longitudinal plasmon resonances of nanorod dimers: if the distance between the tip ends is reduced, a strong red-shift of the resonance occurs while a decrease of the distance perpendicular to the long rod axis results in a small shift of the resonance to shorter wavelengths [81, 82]. In addition, it was found for elliptical dimers that the observed red-shift exponentially declines with increasing d and finally vanishes for d larger than approximately 2.5 times the short axis length [78]. This exponential decay is described as a plasmon ruler [80] and can be used to measure inter-particle distances in the presence of biological substances [95].

For elongated particles like nanorods, the tip-to-tip configuration yields very high electromagnetic field enhancements since the field is confined in a very small gap between the tip ends [30, 35]. This is illustrated in Fig. 2.8a, where finite-difference time-domain (FDTD) simulations (see Sec. 3.6) of an individual gold nanoantenna (solid black spectrum) and of nanoantenna dimers are shown. The spectra show the near-field intensity 1 nm away from the tip end of the rods (see sketch). Obviously, with decreasing gap, huge enhancement is achieved which exceeds that of an individual rod by two orders of magnitude in case of the 10 nm gap. In Fig. 2.8b, far-field extinction spectra of the same nanoantennas as in Fig. 2.8a are plotted. Note that the nanorod dimers feature *smaller far-field extinction values* at resonance compared to the individual one, indicating that a lower amount of light is scattered out of the incident photon wave vector direction. The reduced far-field values as well as the spectral red-shift of the resonance for small gaps can be understood by looking at a coupled dipole model including retardation [30, 34]. Moreover, note that the resonance position in the near-field is slightly red-shifted to the one observed in the far-field (compare Figs. 2.8a and 2.8b) due to retardation effects [29].

Far-Field Radiative Coupling

The retarded radiative dipolar coupling, which depends on the phase shift between excitations of different particles, becomes especially important in ordered particle ensembles [91, 96]. Calculations for 2D square arrays of nanoparticles with one characteristic lattice constant in both lateral directions showed plasmon resonance blue-shifts with decreasing lattice constant as long as it is in the range of λ_{res} [88]. In addition, a narrowing of the collective plasmon resonance compared to that of a single particle is observed which is optimal for λ_{res} slightly bigger than the lattice constant [32, 86, 88]. This can be explained by the diffractive coupling (constructive interferences of emitted fields) of the particles and the resulting suppression of the radiation damping due to the collective scattering process [32]. Moreover, the

appearance of sharp spectral features was theoretically [97, 98] and experimentally [85, 92, 96, 99] analyzed and attributed to diffraction resulting from scattering by the periodic arrangement of the particles. However, when the nanoparticles are supported by a substrate, the long-range nature of the inter-particle interaction is suppressed, preventing the existence of lattice resonances that are otherwise present in the symmetric configuration of a homogeneous dielectric background [96, 100].

2.6. Phonon-Polaritons

In polar dielectric solids, collective oscillations of atoms are possible which are called *phonons* [42]. For crystals featuring a basis with more than one atom, different phonon branches exist: the lower energetic acoustic branch with a linear relation between frequency ω and wave vector k for small k and the optical branch at higher energies [42]. Each of these branches consists of transverse and longitudinal modes. Due to conservation of energy and momentum and due to the transverse nature of electromagnetic waves, light can only couple to transverse optical (TO) phonons [101]. Since light features a comparably low momentum, only the TO phonon modes at $k \approx 0$ are of interest for possible coupling. In this range, the TO phonon branch can be approximated with the constant value ω_{TO} , the natural vibrational frequency of the TO mode at $k = 0$ in the absence of an external light field [101]. Furthermore, the interaction between the light wave and the TO phonon can be modeled by solving the equations of motion of a linear chain consisting of positive and negative ions. This calculation yields the dielectric function in the classical oscillator model [101]:

$$\epsilon(\omega) = \epsilon_{\infty} + (\epsilon_{\text{st}} - \epsilon_{\infty}) \frac{\omega_{\text{TO}}^2}{\omega_{\text{TO}}^2 - \omega^2 - i\gamma\omega}. \quad (2.20)$$

In this equation, ϵ_{st} and ϵ_{∞} denote the static ($\omega = 0$) and high frequency ($\omega \rightarrow \infty$) dielectric constants, respectively, whereas γ represents the damping rate. Figure 2.9a shows the real and imaginary part of $\epsilon(\omega)$, calculated for typical values of ϵ_{st} , ϵ_{∞} , and γ . The imaginary part ϵ_2 features a maximum at the frequency ω_{TO} of the TO phonon whereas ϵ_1 becomes negative between the frequencies ω_{TO} and $\omega_{\text{LO}} = \sqrt{\epsilon_{\text{st}}/\epsilon_{\infty}} \omega_{\text{TO}}$ [101], the longitudinal optical (LO) frequency. This frequency range, which is shaded in blue in Fig. 2.9a, is referred to as *reststrahlen* band.

Light can propagate through polar dielectric solids for frequencies smaller than ω_{LO} and higher than ω_{TO} . The coupled phonon-photon waves in this frequency range

2. Fundamentals

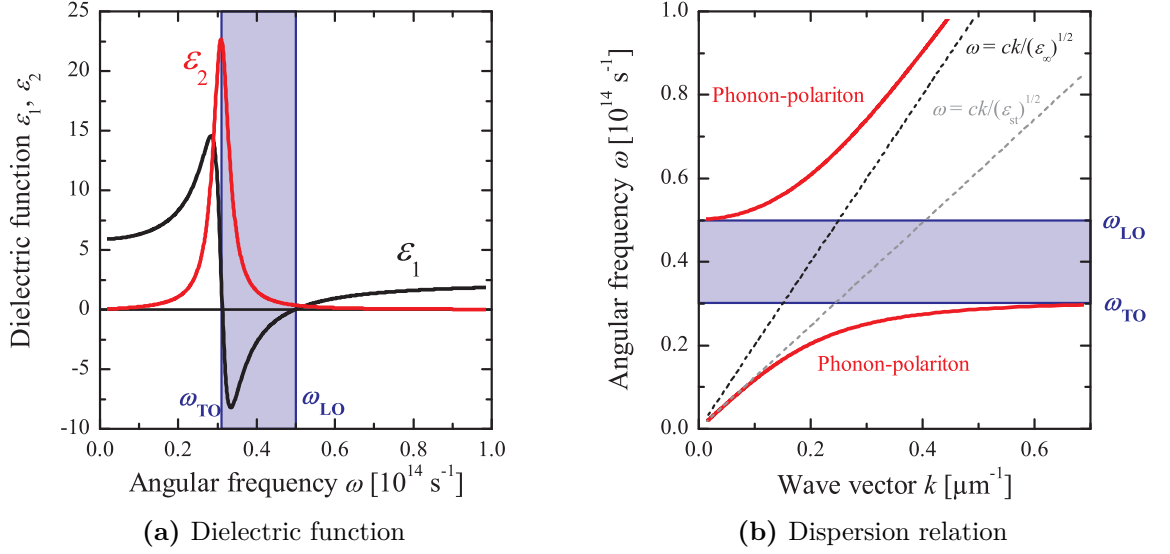


Figure 2.9.: (a) Calculated real (ϵ_1) and imaginary part (ϵ_2) according to Eq. (2.20) using the values $\epsilon_{\infty} = 2.25$, $\epsilon_{\text{st}} = 5.9$, $\omega_t = 3.1 \times 10^{13} \text{ s}^{-1}$, and $\gamma = 1 \times 10^{13} \text{ s}^{-1}$ [42]. (b) Calculated dispersion relation according to Eq. (2.21) using the same values as in (a). Note that damping is neglected in Eq. (2.21), i.e. $\gamma = 0$.

are called *volume phonon-polaritons* and are mixed modes which have characteristics of both polarization waves (the TO phonons) and photons [101]. Considering an interface between a polar dielectric and vacuum, the dispersion relation between frequency ω and wave vector k for these bulk phonon-polariton modes is given by:

$$k(\omega) = \frac{\omega}{c} \cdot \sqrt{\epsilon_{\infty} + \frac{\omega_{\text{TO}}^2 (\epsilon_{\text{st}} - \epsilon_{\infty})}{\omega_{\text{TO}}^2 - \omega^2}}, \quad (2.21)$$

which follows from Eq. (2.5) by using $\epsilon(\omega)$ of Eq. (2.20), disregarding damping (i.e. $\gamma = 0$). The solid red curves in Fig. 2.9b show the two dispersion branches which asymptotically approach the light lines in a medium with dielectric constant ϵ_{∞} for high frequencies and accordingly a medium with ϵ_{st} for low frequencies. Obviously, no bulk modes exist in the *reststrahlen* band due to the negative values of ϵ_1 in this range (see Fig. 2.9a). However, in analogy to plasmon-polaritons, *surface phonon-polariton* modes can be excited in the “forbidden” frequency range.

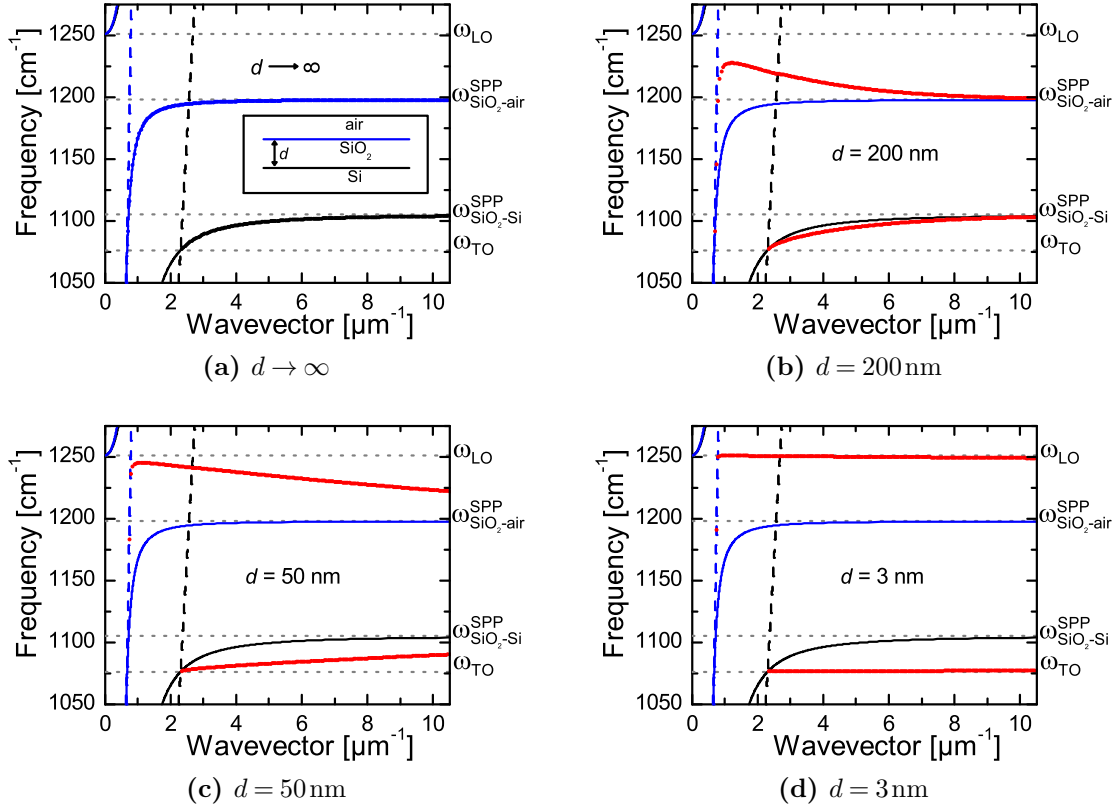


Figure 2.10.: Dispersion relations of SPP modes in a three-layer-system of air, silicon dioxide and silicon [102]. For an infinitely thick SiO₂ layer (a), two SPP modes at the corresponding interface exist which are marked in blue and black in all figures. With decreasing SiO₂ layer thickness, the SPP modes interact and new types of mixed (Fuchs-Kliwer) modes emerge which are shown in red in (b) to (d). Note that the blue and black curves in (b) to (d) are only shown for comparison and do only exist for $d \rightarrow \infty$.

2.6.1. Excitations in Thin Dielectric Layers

Considering more than one interface, multiple types of surface phonon-polariton (SPP⁶) modes are possible. In the following, we will consider a three-layer-system consisting of two semi-infinite half spaces of silicon and air surrounding a layer of silicon dioxide with defined thickness d (see inset of Fig. 2.10a). For simplicity, the dielectric function of SiO₂ is approximated with a harmonic oscillator without damping, featuring a pole at $\omega_{\text{TO}} = 1065 \text{ cm}^{-1}$ and a root at $\omega_{\text{LO}} = 1251 \text{ cm}^{-1}$ (literature values of GUNDE [103]). In Fig. 2.10, the values of ω_{TO} and ω_{LO} mark the possible propagation range of the SPP modes, the *reststrahlen* band. If the thickness of the silicon dioxide layer is very large ($d \rightarrow \infty$, see Fig. 2.10a), two independent surface modes at the respective interfaces of air/SiO₂ (solid blue) and SiO₂/Si (solid black) exist. For large wave vectors, both relations approach the frequency of the corresponding surface phonon, $\omega_{\text{SiO}_2\text{-air}}^{\text{SPP}}$ and $\omega_{\text{SiO}_2\text{-Si}}^{\text{SPP}}$, respectively, whereas for small wave vectors, they follow the light lines in air (dashed blue) and silicon (dashed black). However, if the thickness of the dielectric layer becomes smaller, the two SPP modes increasingly interact. As a result, mixed modes, referred to as Fuchs-Kliwer (FK) modes [104, 105], emerge which are shown in solid red for three different d in Figs. 2.10b to 2.10d. With decreasing d , the higher energetic FK⁺ mode approximates the LO frequency of SiO₂ for large wave vectors while the frequency of the lower energetic FK⁻ mode becomes similar to the TO frequency. Note that the purpose of Fig. 2.10 is to show that mixed SPP modes exist and that they depend on the thickness of the silicon dioxide layer. Since many simplifications and approximations were made, the curves do not represent the exact behavior of a real three-layer-system, but only show a trend.

2.7. Surface-Enhanced Infrared Absorption

Major parts of the present section are adopted from [34]. Surface-enhanced IR absorption is a phenomenon similar to that of surface-enhanced Raman scattering [9, 13, 14] and was first discovered in 1980, when HARTSTEIN *et al.* found that the IR absorption of molecules chemisorbed on metal films can be substantially enhanced [10]. For molecules adsorbed on noble metal island films, enhancement factors⁷ up to

⁶Note that the abbreviation SPP is in general used for both surface *plasmon*-polariton and surface *phonon*-polariton modes. The actual meaning has to be concluded out of context.

⁷The enhancement factor is defined as the ratio between signal strength of the enhanced case normalized to the non-enhanced case.

10^3 were reported [16, 25, 27]. It is generally believed that two effects contribute to the enormous enhancement of SEIRA as well as SERS: chemical or first layer effects [15], on the one hand, and electromagnetic effects [17] on the other hand. The first one will be neglected within this work since the functional groups of the investigated adsorbates are not in direct contact with the metal surface. Concerning the electromagnetic enhancement effect, it is assumed that the local enhancement of an adsorbate's vibration can be estimated with [7]

$$\left| \frac{E_{\text{loc}}(\lambda_{\text{vib}})}{E_0(\lambda_{\text{vib}})} \right|^2. \quad (2.22)$$

In this equation, E_{loc} and E_0 denote the local electric field strength in the vicinity of the molecule and the incident electric field strength, respectively, at the wavelength λ_{vib} of the IR active vibration. It is known from SEIRA studies of molecules on metal island films that the enhancement of the IR absorption depends on the material as well as on the morphology of the film [24, 25]. The material properties are directly connected to the dielectric function and hence, their influence on the field enhancement is obvious (compare to Sec. 2.4.2). To understand the influence of the film morphology, the islands are considered as individual metal particles in a simple approximation. These particles feature localized surface plasmon resonances (Sec. 2.3) in the visible which come along with an enhancement of the electromagnetic field. Due to different size and shape of the large amount of islands, the LSPR becomes broadened. In addition, interaction between the individual islands leads to a shift of the resonance of lower energies accompanied by additional broadening (see Sec. 2.5). Thus, broad resonances of metal island films are possible in the infrared spectral range. Furthermore, maximal enhancement is achieved slightly before the islands start to merge (percolation threshold) [24]. In addition, asymmetric line shapes of the adsorbate vibration are found, which can be explained by effective medium theories [106, 107].

3. Materials & Methods

The chapter starts with the geometrical properties of the lithographically prepared gold nanorods (Sec. 3.1). After explaining the main measurement technique, the microscopic IR spectroscopy (Sec. 3.2), the IR optical properties of the substrates are presented in Sec. 3.3. Furthermore, the adsorbate molecule mercaptoundecanoic acid, which is used for nanoantenna-assisted IR spectroscopy in Chap. 7, is introduced in Sec. 3.4. In addition, a brief overview on the state of the art of NAIRS is given in Sec. 3.5. The chapter ends with a short description of the FDTD simulation technique, the results of which are compared to experimental findings throughout the thesis.

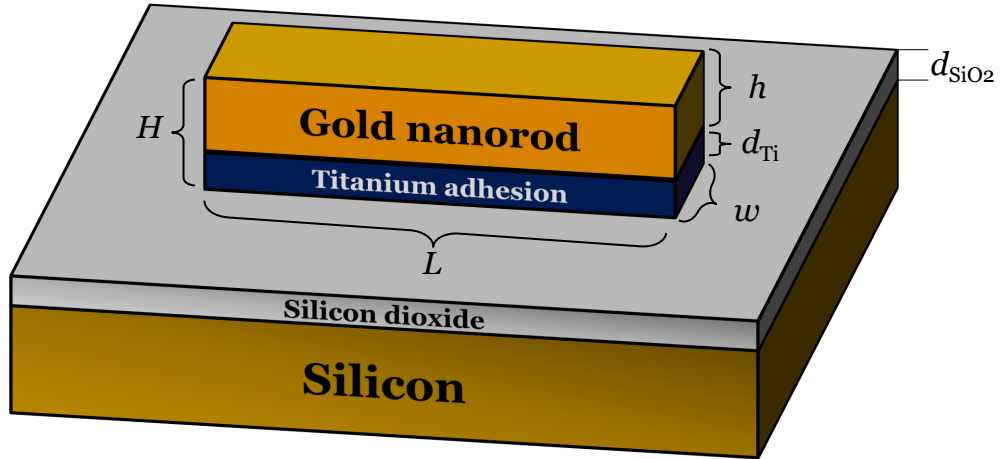
3.1. Lithographic Gold Nanorods

Within this thesis, the IR optical properties of lithographically prepared gold nanorods on various substrates (silicon, quartz glass, zinc sulphide, calcium fluoride) are shown. All samples were prepared by standard electron beam lithography (EBL) [7, 34, 70, 77, 108–110]. The main results originate from nanorods fabricated at the National Institute for Materials Science (NIMS) in Tsukuba, Japan, on silicon (111) wafers (see Sec. A.1 for fabrication process).

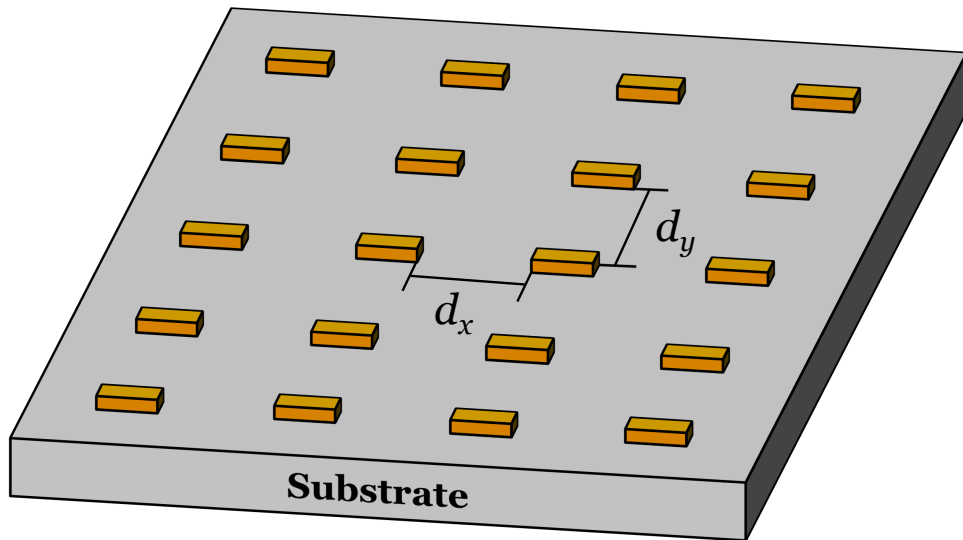
The gold nanorods feature a cuboid-like shape with length L , height h and width w and are connected to the substrate's surface via a thin titanium adhesion layer of thickness d_{Ti} (see Fig. 3.1a). Furthermore, rods of the same length L are regularly arranged in arrays with characteristic separation distances parallel (d_x) and perpendicular (d_y) to the long rod axis (see Fig. 3.1b). As an abbreviation, they will be referred to as longitudinal (d_x) and transverse (d_y) separation distances in the remainder of the text.

The following two sections deal with the experimental determination of the rod height by atomic force microscopy (AFM, Sec. 3.1.1) and the rod length and width by scanning electron microscopy (SEM, Sec. 3.1.2). Finally, Sec. 3.1.3 gives an overview on all samples that have been investigated by IR spectroscopy.

3. Materials & Methods



(a) Side view



(b) Top view

Figure 3.1.: (a) Schematic view on a cuboid-like gold nanorod with length L , height h , and width w prepared on an oxide (d_{SiO_2}) covered silicon substrate. The titanium layer (d_{Ti}) acts as adhesion promoter. The total rod height H is the sum of the actual rod height h and d_{Ti} . (b) Schematic view on a small part of a nanorod array (typical dimensions of $50 \times 50 \mu\text{m}^2$) with its characteristic separation distances in longitudinal (d_x) and transverse (d_y) direction.

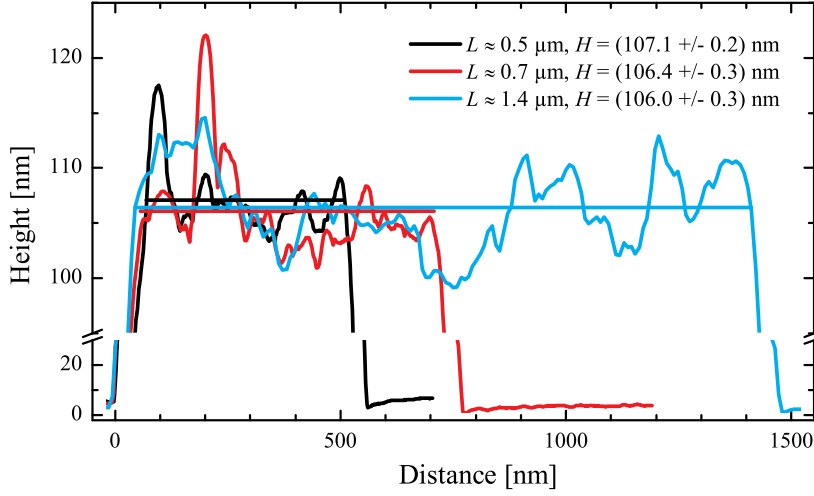


Figure 3.2.: AFM height profiles of three nanorods. The cross-sections were performed parallel to the long rod axis, approximately in the middle of the short rod axis. To determine the average height, the profiles were fitted to a constant, resulting in the values of $H = h + d_{Ti}$ given in the figure.

3.1.1. Measurement of Rod Height

The AFM measurements were performed at ambient conditions at the Kirchhoff Institute for Physics using the multimode instrument MMAFM-2 fabricated by DIGITAL INSTRUMENTS. All images were recorded in tapping mode with tips featuring radii of curvature of about 10 nm and resonance frequencies of about 330 kHz (VEECO, MPP-11100). A detailed explanation of the AFM's functional principle can be found in literature [111, 112].

Figure 3.2 shows measured height profiles of three nanorods on natural oxide covered silicon with a presumably 5 nm thick titanium adhesion layer. Obviously, the nanorods feature a very rough surface with height differences in the order of 10 nm. To characterize the surface roughness, the root mean squared (R_{RMS})-value of a defined area A is calculated according to [113]

$$R_{RMS} = \sqrt{\frac{1}{n} \sum_{i=1}^n y_i^2}. \quad (3.1)$$

Here, the roughness profile contains n data points within A and y_i denotes the vertical distance from the mean line to the i^{th} data point. The R_{RMS} -values of ten rods of sample Wb1 (see Sec. 3.1.3) have been determined using the software NANOSCOPE. As a result, values between $R_{RMS} \approx 4$ nm and $R_{RMS} \approx 8$ nm have been

3. Materials & Methods

obtained, considering the whole surface of the respective nanorod. For comparison, the values of the bare substrate range between $R_{\text{RMS}} \approx 0.2\text{nm}$ and $R_{\text{RMS}} \approx 0.3\text{nm}$, indicating a very smooth substrate surface.

Furthermore, the absolute height H of the rods (see Fig. 3.1a) was determined for those ten rods of sample Wb1 by fitting the AFM height profiles to a constant (see Fig. 3.2). The average of all measurements was calculated to be $H = (106 \pm 3)\text{nm}$, taking into account the standard deviation of the mean. This nicely fits to the projected values of $h = 100\text{nm}$ and $d_{\text{Ti}} = 5\text{nm}$. In addition, six rods of sample Wc1 ($h = 100\text{nm}$, $d_{\text{Ti}} = 10\text{nm}$) were investigated by AFM and an average value of $H = (109 \pm 4)\text{nm}$ was obtained, confirming that the evaporation of titanium and gold during the sample preparation are well and reproducibly controlled. Thus, AFM analyses of other samples were omitted.

3.1.2. Measurement of Rod Length and Width

Nearly all SEM measurements were performed with the LEO-1530 SEM at the Institute of Applied Physical Chemistry. Since silicon features a sufficiently high conductivity, covering the silicon samples with a conductive layer was not necessary. However, carbon contaminations on the sample surface can be formed by the focused electron beam due to carbon hydride residues in the gas phase [114, 115], which is illustrated in Sec. A.2.1. The base pressure in the sample compartment was at least $1 \times 10^{-6}\text{mbar}$ and acceleration voltages of $U_{\text{acc}} = 3 - 5\text{kV}$ were applied.

The LEO-1530 is equipped with two detectors: an In-lens detector, placed in the electron column, and an EVERHART-THORNLEY detector [116], referred to as SE2 detector in the remainder of the text, which is located on the side of the sample stage. Both detectors collect secondary electrons that escape from the sample due to the primary electron beam irradiation. While the In-lens detector is suited for high resolution topographic imaging due to its good contrast at high magnification, the SE2 detector is rather used for general purpose imaging [117]. Besides topographic information, also material contrast can be achieved because of local variations of the secondary electron yield [118]. However, this material contrast, which is more pronounced for the In-lens detector owing to its very high surface sensitivity [119], is not as high as the one of a back scattered electron (BSE) detector. Here, the electron yield depends on the atomic number of the specimen [118] and hence, heavier atoms appear brighter in the BSE detector image. The reader may be referred to the literature [118, 120, 121] for a detailed consideration of the SEM working principle.

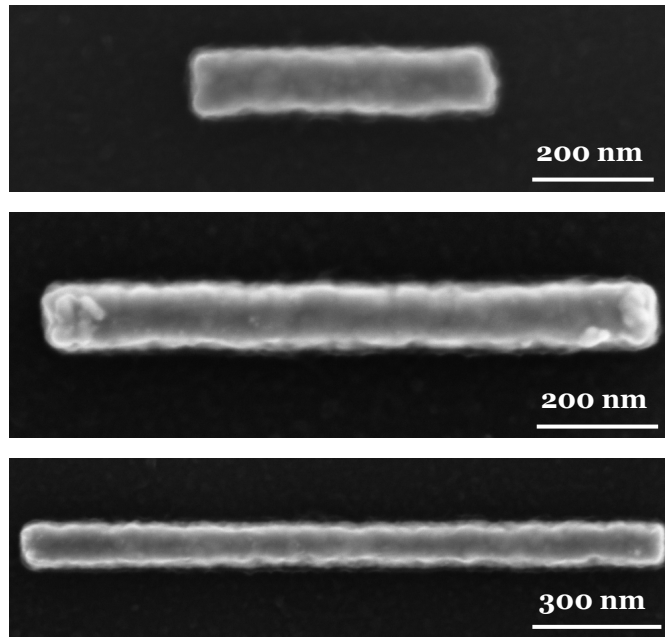


Figure 3.3.: SEM images of three nanorods of sample Wb3. All images were recorded with the In-lens detector at an acceleration voltage of $U_{\text{acc}} = 5 \text{ keV}$.

Figure 3.3 shows a selection of SEM images of nanorods with different lengths. Note that it is important to choose brightness and contrast (B&C) of the images in a way, that textures of the nanorod are visible. Furthermore, the edges of the rods should appear brighter for optimal settings of B&C due to the increasing number of secondary electrons leaving the specimen at the edge [118]. Moreover, it is apparent from the images shown in Fig. 3.3, that the nanorods feature a rather cuboid-like shape with blunt tip ends.

Length L and width w of the rods in the arrays were determined by measuring at least three rods at different locations within the array. Note that the variation of L between several measurements was below the error caused by different adjustments of B&C ($\Delta L = 30 \text{ nm}$, see Sec. A.2.2). Hence, the length distribution within the arrays is very narrow. Supportingly, no deviations of the resonance frequency (which inversely depends on L , see Sec. 2.4.1) were observed for IR measurements at different positions within one array (see Fig. 4.8). Finally, it should be mentioned that the calibration of the used SEM was checked with the help of a test sample with defined structures, see Sec. A.2.3.

3. Materials & Methods

Series	Samples	Remarks / objectives
A	Wa1 - Wa4	Rough back side, WCMD (6.1) and PIMD (6.2)
B	Wb1 -Wb3	Interaction (5), PIMD (6.2)
C	Wc1, Wc2	FIB milling (6.3)
E	Wef1, Wef2	Transverse interaction (5.1)
H	Wh1	106 nm oxide layer, FIB milling (6.3)
CaF ₂	Antenna#2	NAIRS (7)
	Antenna#15	Arrays of dimers, comparison data for PIMD (6.2)
	Antenna#18, #19	PIMD (6.2)

(a)

Sample	w [nm]	h [nm]	d_{Ti} [nm]	d_x [μm]	d_y [μm]
Wa1-Wa4	40 ± 5	60	5	1, 0.04 – 0.06	1
Wb1	95 ± 10	101 ± 3	5	5	5
Wb2	115 ± 10	100	10	5	5
Wb3	120 ± 9	100	5	5 – 0.04	5 – 1
Wc1	110 ± 8	99 ± 4	10	10	10
Wc2	108 ± 9	100	10	10	10
Wef1	93 ± 7	100	5	5	5 – 0.1
Wef2	95 ± 9	100	5	5	5 – 0.1
Wh1	85 ± 10	60	5	10	10
Antenna#2	60	60	CaF ₂	5	5
Antenna#15	60	60	CaF ₂	5	8
Antenna#18, #19	60	60	CaF ₂	30	30

(b)

Table 3.1.: (a) Overview on all preparation series. Series A to E were prepared on natural oxide covered silicon wafers. The abbreviations WCMD and PIMD stand for wet-chemical and photo-induced metal deposition, respectively, whereas FIB and NAIRS denote focused ion beam milling and nanoantenna-assisted infrared spectroscopy. The numbers in brackets give the sections / chapters in which the results of the corresponding experiments can be found. (b) Geometric parameters of all samples investigated in this thesis. The values with error are results from AFM or SEM measurements, respectively. Here, the error represents the standard deviation of the mean.

3.1.3. Overview on Investigated Samples

All silicon substrate samples fabricated at the MANA foundry station are grouped into different preparation series (A-H). Natural oxide covered silicon wafers ($d_{\text{SiO}_2} \approx 3 \text{ nm}$, measured by ellipsometry [122]) were used for the samples of series A to E, whereas in series H, gold nanorods were prepared on thermally oxidized silicon wafers ($d_{\text{SiO}_2} \approx 106 \text{ nm}$ [123]). Moreover, various samples exist within each series. Here, the notation Wb3, for example, refers to sample number three of preparation series B (W stands for wafer). Note that series E and F (not used in this thesis) were prepared on the same sample which is therefore called Wef1.

Besides the silicon substrate samples, gold nanorod arrays were also fabricated on CaF_2 substrates at the Italian Institute of Technology in Genoa, Italy. Table 3.1a gives an overview on the different preparation series. In addition, the geometric dimensions of the rods and arrays are summarized in Tab. 3.1b. Note that the rod width w of the rods on the CaF_2 samples was not directly measured by SEM, but a value of $w = (60 \pm 10) \text{ nm}$ can be assumed based on SEM investigations of similarly prepared samples [124].

3.2. Microscopic Infrared Spectroscopy

Microscopic IR spectroscopy was applied to investigate the optical properties of the nanorods. A microscope is necessary to locate the nanostructures on the substrate and to focus the light onto the nanorods for a sufficiently high signal-to-noise ratio. The experimental set-up (Sec. 3.2.1) and the measurement principle (Sec. 3.2.2) are described in the following sections. An elaborate investigation of the measurement stability can be found in Sec. A.3.6.

3.2.1. Experimental Set-Up

The IR optical characterization of the nanorods was performed at the Kirchhoff Institute for Physics using a commercial IR microscope (BRUKER HYPERION 1000) coupled to a FT-IR spectrometer (BRUKER TENSOR 27, functional principle see Sec. 2.1). The IR light source, which is located inside the spectrometer, is a direct current heated piece of silicon carbide (“globar”). The modulated IR light is guided with mirrors into the microscope, where a transmittance and a reflectance mode exist. The optical beam path inside the microscope differs depending on the chosen mode (see Sec. A.3.1 for a detailed description).

3. Materials & Methods

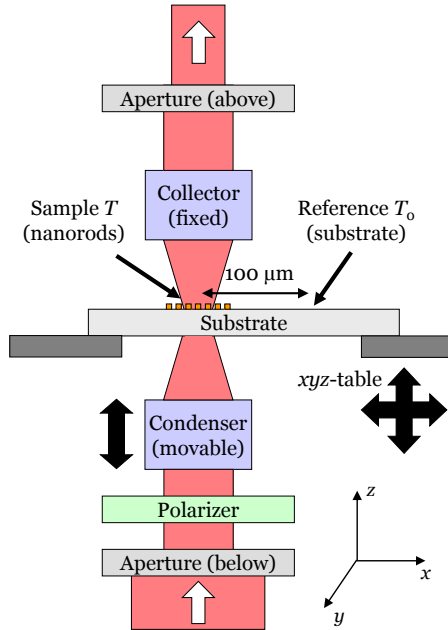


Figure 3.4: Optical beam path for microscopic IR transmittance measurements (see text). Sample (T) and reference (T_0) positions (see Sec. 3.2.2) are defined by moving the sample in the xy -plane. The typical distance between the two measurement positions is about $100\mu\text{m}$.

Figure 3.4 shows a scheme of the (IR) transmittance geometry, which was used for nearly all measurements. Here, the IR light is focused onto the substrate’s surface with the help of an objective¹ (condenser) and a circular aperture. The sample is located on a movable xyz -table that can be electronically positioned in the xy -plane (accuracy of $1\mu\text{m}$). After passing the sample, the light is collected by another objective (collector) and detected by a liquid nitrogen cooled mercury cadmium telluride (MCT) detector², allowing measurement times of about 20h (see Sec. A.3.4). Circular apertures below and above the sample can be brought into the beam path to select a certain measurement spot in the focal plane. Here, different aperture diameters (in the focal plane) can be chosen between 8.3 and $104\mu\text{m}$ (see Sec. A.3.5 for the influence of different aperture sizes). Additionally, an IR polarizer can be inserted for polarization-dependent measurements. Moreover, when operating in reflectance mode, the sample is illuminated from above and the upper objective serves both as condenser and collector. The possible positions of apertures and IR polarizer are described in Sec. A.3.1.

¹Since conventional, refractive type objectives are non-transparent for IR light, a Schwarzschild objective (36-fold magnification, numerical aperture $NA = 0.5$) is used which focuses the light by mirrors (see Sec. A.3.2 for details).

²The principle of this type of semiconductor detector is based on the photoelectric effect [1]. Although MCT detectors are faster and more sensitive compared to pyroelectric detectors [e.g. deuterated triglycine sulfate (DTGS) detectors] [1], they exhibit the disadvantage of non-linearity, i.e. a non-linear relation between the detected signal and the light intensity exists [125–127], see Sec. A.3.3 for more details.

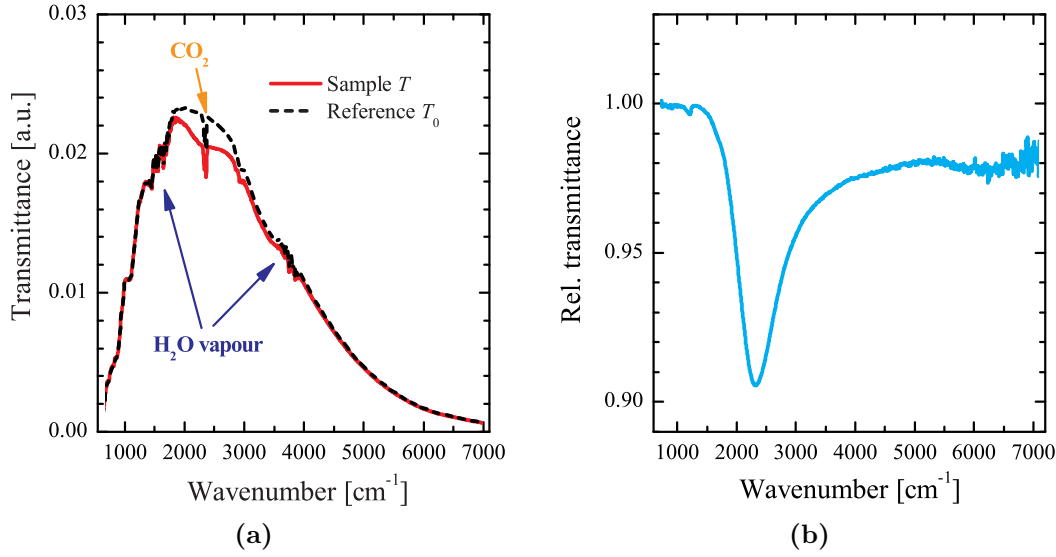


Figure 3.5.: Principle of relative transmittance. In (a), examples of single channel spectra of a sample (gold nanorods on silicon) and a reference measurement (bare silicon) are shown. The atmospheric absorptions of water vapour and carbon dioxide are indicated. The quotient of these two spectra is the blue solid curve in (b).

Besides the IR mode, the microscope can also be operated in the visible mode which allows the precise localization of the nanorods and the definition of the measurement positions (see Sec. 3.2.2). In this case, the optical image is either recorded by a CCD³ camera or directly observed through a binocular eyepiece.

3.2.2. Measurement Principle

As mentioned in Sec. 2.1, any measured spectrum is afflicted with external features. For this reason, the spectrum T of the nanorods (sample position, see Fig. 3.4) is always normalized to a spectrum T_0 of the bare substrate (reference position), resulting in the relative transmittance spectrum $T_{\text{rel}}(\tilde{\nu})$:

$$T_{\text{rel}}(\tilde{\nu}) = \frac{T(\tilde{\nu})}{T_0(\tilde{\nu})}. \quad (3.2)$$

In case of reflectance measurements, an analogue procedure leads to the relative reflectance spectrum $R_{\text{rel}}(\tilde{\nu})$. Figure 3.5a shows typical examples of single channel spectra T (nanorods on silicon) and T_0 (bare silicon); atmospheric absorptions of water vapor and carbon dioxide are indicated. The solid blue curve in Fig. 3.5b represents

³Charge coupled device

3. Materials & Methods

Substrate	n_{sub}
Calcium fluoride	1.41 [128]
Quartz glass	1.44 – 1.45 [129]
Zinc sulphide	2.2 [128]
Silicon	3.42 [128]

Table 3.2.: Literature values of the refractive indices n_s of all substrates used in this work.

the calculated relative transmittance spectrum, showing a typical antenna resonance at around 2300 cm^{-1} . Note that the noise in Fig. 3.5b increases for $\tilde{\nu} < 1000\text{ cm}^{-1}$ and $\tilde{\nu} > 5000\text{ cm}^{-1}$ due to low signal intensity (see Fig. 3.5a).

Measurement Parameters

Recording one spectrum corresponds to one periodic movement of the interferometer’s mirror (see Sec. 2.1) and is therefore referred to as one *scan*. In general, the spectral noise decreases by a factor of \sqrt{N} , where N is the number of scans [1]. Hence, many scans are recorded and the average is formed to improve the signal-to-noise ratio. Furthermore, it is beneficial to continuously switch between sample and reference measurement to reduce any influences of instabilities (see Sec. A.3.6).

The spectral resolution $\Delta\tilde{\nu}$ is another important measurement parameter. If relatively broad excitations such as plasmonic resonances are investigated, a resolution of $4 - 8\text{ cm}^{-1}$ is sufficient. In contrast, the exact determination of vibrational frequencies of adsorbates requires a resolution of at least 2 cm^{-1} . However, the choice of a better resolution $\Delta\tilde{\nu}$ leads to an increase of the spectral noise, which is inversely proportional to $\Delta\tilde{\nu}$ for fixed N and aperture size [1]. In addition, recording a spectrum with a better resolution requires more measurement time for constant N [1]. Taking all together, a compromise between a good resolution and an acceptable measurement time has to be made for every measurement.

3.3. Substrates

Figure 3.6 shows relative transmittance spectra of various substrates. Quartz glass (SiO_2) and calcium fluoride feature the highest transmittance values of all substrates due to their relatively small refractive indices (see Tab. 3.2). From this point of view, they are best suited for relative transmittance measurements of gold nanorods

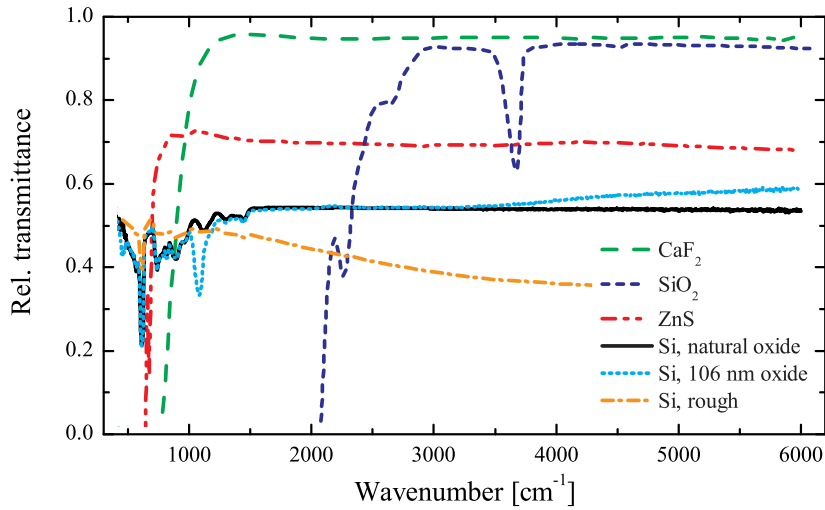


Figure 3.6.: Relative transmittance spectra of different substrates (reference vacuum). The measurements (resolution of at least 8 cm^{-1}) were performed in the sample compartment (5 mbar) of a BRUKER IFS66 v/s FT-IR spectrometer using a DTGS detector. In each case, different positions on the sample were measured and an average was generated.

since only weak image charges in the substrate are induced, leading to more intense antenna resonances. However, quartz glass cannot be used for measurements in the MIR spectral range due to its non-transparency below 2000 cm^{-1} . In addition, a strong absorption band at around 3670 cm^{-1} is present which originates from hydroxyl (OH) groups⁴ chemically bound to the silica network [130].

Zinc sulphide shows nearly constant transmittance beginning from around 1000 cm^{-1} . However, very smooth surfaces are difficult to prepare and scratches on the surface are hard to avoid, leading to imperfections in the nanorod preparation [70].

Finally, silicon exhibits the lowest transmittance of all substrates due to high reflection losses. Nevertheless, it is suited for transmittance measurements despite its complete non-transparency in the visible range. One of its advantages is that the preparation of very smooth surfaces and the lithographic fabrication of metal structures is well-known from semiconductor industries. As can be seen in Fig. 3.6, the silicon substrate with a rough backside features a decline of the transmittance towards higher wavenumbers. This can be explained by increased light scattering out of the normal transmittance direction; a process that is proportional to $\tilde{\nu}^4$ [42]. Besides the nearly constant transmittance in the range above 1500 cm^{-1} in case of smooth silicon, there are several absorption peaks in the low wavenumber region. Nearly all

⁴Some moisture is always present during the manufacturing process, leading to these unavoidable impurities.

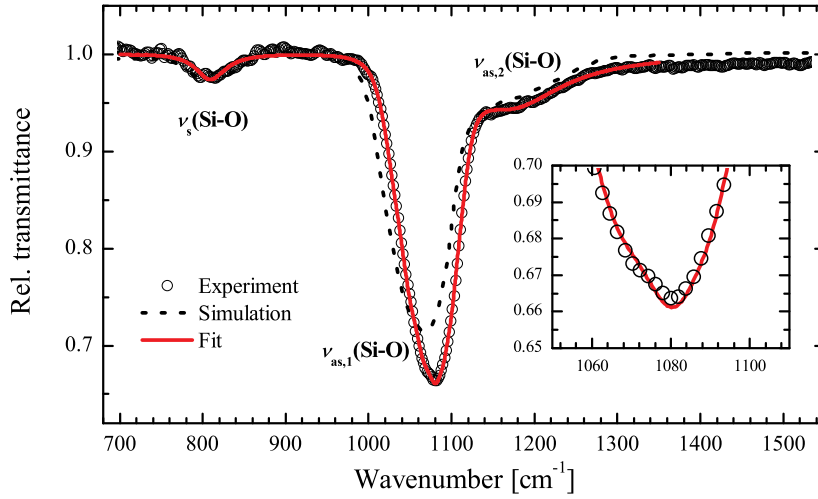


Figure 3.7.: Open circles: relative transmittance spectrum of a thermally oxidized silicon wafer ($d_{\text{SiO}_2} \approx 106\text{nm}$) versus a natural oxide covered one. The data was fitted with the SCOUT software resulting in the red solid curve (see Tab. B.1 for the fitting results). In addition, the dashed black curve shows a SCOUT simulation of the optical response of a 106nm SiO_2 layer on silicon using the SiO_2 dielectric function of GUNDE [103].

of them originate from two- and three-phonon processes with linear combinations of TO, LO, TA^5 and LA^6 phonons [131]. The strongest peak at 610cm^{-1} , for example, is caused by the combination of TO and TA [131]. The whole region below 1500cm^{-1} is therefore denoted as multiphonon absorption band.

3.3.1. Thermally Oxidized Silicon

To obtain the optical response of the 106nm thick SiO_2 layer, the IR measurement of the thermally oxidized silicon wafer (blue dotted curve in Fig. 3.6) is normalized to that of the natural oxide covered wafer (solid black curve), resulting in the open black circles of Fig. 3.7. Two major peaks are visible, which can be attributed to TO phonon bands in the silicon dioxide network [132]: The small peak at around 810cm^{-1} originates from the symmetric stretching vibration $\nu_s(\text{Si}-\text{O})$ of the oxygen atom relative to the silicon atoms, whereas the strong peak at around 1080cm^{-1} is due to the antisymmetric stretching vibration. Actually, two antisymmetric modes exist [133]: one in which two adjacent oxygen atoms move in phase, leading to the peak at 1080cm^{-1} [$\nu_{\text{as},1}(\text{Si}-\text{O})$], and one in which the movement is 180° out of phase, being responsible for the shoulder at around 1200cm^{-1} [$\nu_{\text{as},2}(\text{Si}-\text{O})$].

⁵Transverse acoustic

⁶Longitudinal acoustic

For comparison, the simulated relative transmittance of 106 nm SiO₂ / Si versus bare silicon is plotted in Fig 3.7 (dashed black curve). The discrepancies concerning the peak position and intensity of the $\nu_{\text{as},1}$ band are most likely due to the different structure of the SiO₂ films in the experiment (thermally oxidized SiO₂ film) and in the simulation (chemical vapor deposited SiO₂ film [103]). And in fact, the positions of the $\nu_{\text{as},1}$ peak of thermally grown SiO₂ reported in literature (1075 cm⁻¹ [134] and 1076 cm⁻¹ [132]) are in quite good agreement with the value of 1080 cm⁻¹ found in this work. Finally, to derive the dielectric function of the thermally oxidized SiO₂ film, the experimental data was fitted with four Brendel oscillators [135] using the SCOUT software (solid red curve).

3.4. Alkanethiol-Based Self-Assembled Monolayers

In this thesis, mercaptoundecanoic acid (MUA) was chosen as a probe molecule to monitor the electromagnetic near-field enhancement of nanoantennas. MUA belongs to the group of ω -functionalized alkanethiols, i.e. molecules of the type HS-(CH₂)_{*n*}-R with a thiol group (SH) at one end and another functional group (R) at the other end of the alkyl chain consisting of *n* methylene groups.

Alkanethiols allow an easy and well-defined preparation of self-assembled monolayers (SAMs) on gold [136–138]. Alkanethiol-based self-assembled monolayers (AT-SAMs) are formed by chemisorption of thiol molecules on metal surfaces since the sulfur-containing thiol group shows a very high affinity towards noble metal surfaces [139–141]. For this reason, selective adsorption of ATs on gold nanoantennas is possible. In contrast, no bonds between the molecule and the bare substrate are formed. Furthermore, the SAMs can be used to immobilize organic molecules, like biotin for example, as an initial step of a bio-sensor [142, 143].

The adsorption on gold surfaces is mainly described by the Langmuir kinetic process [147], which means that the adsorption rate is proportional to free and accessible adsorption sites. Immersing a gold surface in an alkanethiol solution for a sufficiently long time period (several hours) leads to the formation of an ordered AT-SAM on the gold surface (see Fig. 3.8). Here, the van-der-Waals interaction between the lipophilic alkyl chains of the individual adsorbates is the driving force for the well-ordered formation of the SAM [137]. Hence, the coverage and stability of a SAM is influenced by the alkyl chain length *n*: the longer the alkyl chain, the more stable the SAM. In this context, *n* = 10 was reported to be the shortest chain length for high quality SAM packing [148].

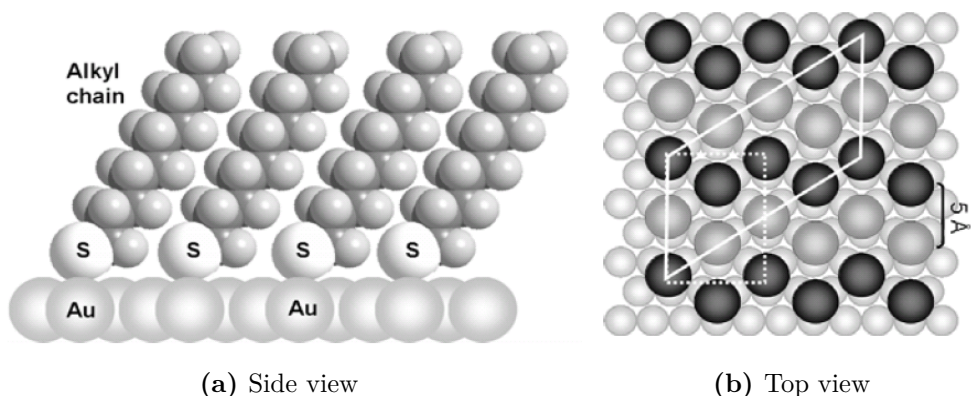


Figure 3.8.: Ordered structure of an AT-SAM on a Au(111) surface. (a) Side view of a decanethiol ($n = 9$, $R = CH_3$) SAM. The alkyl chains are tilted by 30° with respect to the surface normal [144] and adopt all-trans conformation [145]. (b) Top view on an AT lattice with $(\sqrt{3} \times \sqrt{3})R30^\circ$ structure. The small gray circles represent gold atoms, whereas the black and the dark gray circles illustrate the sulfur atoms of the thiol group chemisorbed on the gold atoms. Figures taken from [146].

Furthermore, the stability of AT-SAMs in aqueous solutions featuring different pH-values was found to be in the range of one week to several months [149]. However, oxidation of ATs when exposed to ambient conditions leads to increased disorder in the monolayer and gradual desorption of the molecules [150]. In this context, ozone (O_3) has been identified as the likely oxidant in air that reacts with the thiol group, forming oxidized sulfur (sulfonate) on the gold surface [151]. In addition, it is known that the oxidation process is accelerated by UV irradiation of the AT-SAM in air [152]. Again, long-chain AT-SAMs show a higher stability against oxidation compared to short-chain ones since the oxidant species is hindered to penetrate through the closely packed alkyl chain structure [153].

3.4.1. Mercaptoundecanoic Acid

Figure 3.9a shows a model of mercaptoundecanoic acid with a carboxyl functional group (Fig. 3.9b) at one end of its alkyl chain ($n = 10$). Depending on the pH-value of the solution, deprotonation of MUA is possible, resulting in a negatively charged carboxylate group [149, 154] (Fig. 3.9c). Furthermore, carboxyl terminated AT-SAMs form hydrogen bonds between the individual end groups, leading to additional stability of the SAM [155, 156].

3.4. Alkanethiol-Based Self-Assembled Monolayers

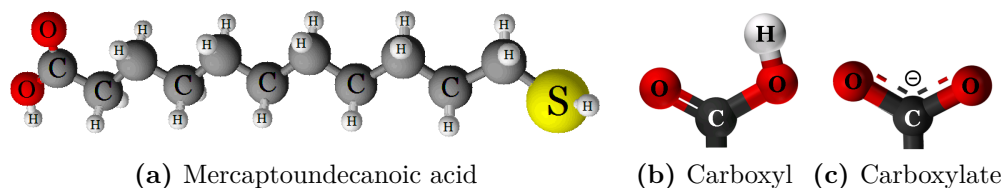


Figure 3.9.: (a) Structure of mercaptoundecanoic acid with a carboxyl group (COOH) at one end and a thiol group (SH) at the other end of the alkyl chain consisting of ten methylene (CH₂) groups. (b) Carboxyl group consisting of a carbonyl (C=O) and a hydroxyl (OH) group. (c) Negatively charged carboxylate group which originates from deprotonation of the carboxyl group shown in (a). The negative charge is delocalized and shared by both oxygen atoms.

Concerning the adsorption morphology, high-resolution STM⁷ studies confirmed the well-ordered structure of MUA SAMs on Au(111) substrates [158] similar to the one shown in Fig. 3.8a. For comparison, no uniform monolayer was observed for mercaptohexanoic acid ($n = 5$, R = COOH) [158], indicating the importance of relatively long alkyl chains. The distance between neighboring molecules (4 Å [158] and 4.1 Å [159], respectively) was estimated to be similar compared to that of alkanethiols (5 Å [137, 148, 159], see Fig. 3.8b). In addition, different methods were applied to measure the thickness of the MUA monolayer, which is in the range of 11 – 12 Å [159–161]. These results are in good agreement with calculated values taking into account the C – C distance of fully extended alkyl chains with a tilt angle of 30° like the ones shown in Fig. 3.8a.

MUA is commonly solved in ethanol and the gold substrate is immersed in this solution for at least 12 h, subsequently rinsed with ethanol and dried with nitrogen or argon. In addition, several publications report that a final rinsing with pure water is necessary to ensure a protonation of the carboxyl groups [162, 163]. However, elaborate studies of mercaptohexadecanoic acid ($n = 15$, R = COOH) showed that protonation can be achieved by using acidified ethanol for preparation as well as for rinsing [164, 165].

⁷Scanning tunneling microscopy [157]

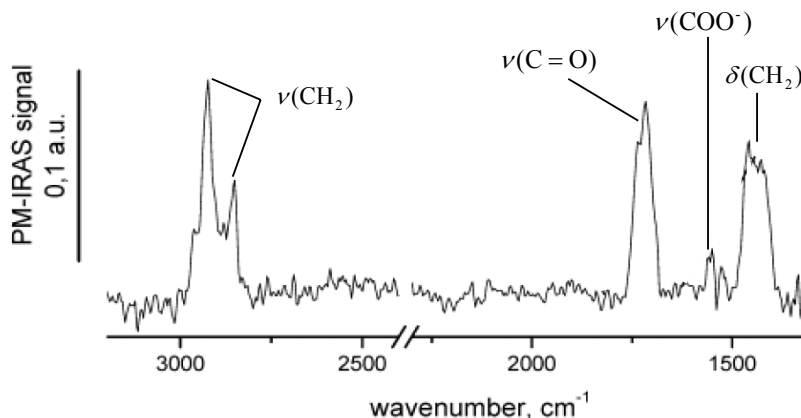


Figure 3.10.: PM-IRRAS spectrum of a MUA monolayer adsorbed on gold, measured *ex situ* (angle of incidence = 70°) [166]. Stretching and deformation vibrations are indicated by ν and δ , respectively. The exact frequencies of the IR active modes are summarized in Tab. 3.3.

Vibrational Bands

Figure 3.10 shows an *ex situ* PM-IRRAS⁸ measurement of a MUA monolayer adsorbed on a gold film [166]. Three strong IR active vibrational bands are observed. The first one, at around 2900cm^{-1} , consists of two strong peaks which are attributed to the symmetric and antisymmetric stretching vibration of the methylene groups. These modes, as well as the scissors deformation modes of the methylene group at around 1450cm^{-1} , are typical for every alkane-like species [1]. The third strong band at around 1700cm^{-1} is attributed to the C=O stretching vibration of the carboxyl group. In fact, the band consists of two peaks, the frequencies of which depend on the alignment of the COOH groups with respect to neighboring MUA molecules [168]. When hydrogen bonds between the carboxyl groups are formed, the frequency is slightly smaller (1716cm^{-1}) than in the non-hydrogen bonded case (1735cm^{-1}) [169]. Furthermore, a smaller peak in the range of $1570 - 1580\text{cm}^{-1}$ is found. It originates from the antisymmetric stretching of the carboxylate group, indicating the deprotonation of some carboxyl groups. *In situ* measurements in fact showed that deprotonation leads to a decrease of $\nu(\text{C}=\text{O})$ and an increase of the carboxylate vibration [166]. Finally, all vibrational modes and their frequencies are summarized in Tab. 3.3.

⁸Polarization modulation infrared reflection absorption spectroscopy enables *in situ* characterization of adsorbed monolayers [167]. An important advantage over the classical IRRAS technique (see Sec. on page 139) is that the signal is directly extracted from the reflectance of p- and s-polarized light, without the need of any reference spectrum.

Mode	$\tilde{\nu}$ [cm^{-1}]	Mode	$\tilde{\nu}$ [cm^{-1}]
$\nu_{\text{a}}(\text{CH}_2)$	2923	$\nu_{\text{a}}(\text{COO}^-)$	1570 – 1580
$\nu_{\text{s}}(\text{CH}_2)$	2850	$\delta(\text{CH}_2)$	1430 – 1460
$\nu(\text{C}=\text{O})$	1716 ^a	$\nu_{\text{s}}(\text{COO}^-)$	1430 – 1450
$\nu(\text{C}=\text{O})$	1735 ^b	$\nu(\text{C}-\text{O})$	1300

Table 3.3: Frequencies of the vibrational modes of a MUA monolayer adsorbed on gold (compare to Fig. 3.10). The frequency of the C=O stretching vibration depends on the configuration of the carboxyl groups, which can be hydrogen bonded (a) or non-hydrogen bonded (b). Data taken from [166].

3.5. Surface-Enhanced Infrared Spectroscopy Using Nanoantennas

The present section is based on [170] and intended to give a brief overview on the latest state of the art. As we saw in Sec. 2.7, the electromagnetic field enhancement of metal surfaces can be exploited to detect vibrational signals of adsorbed molecules. Since the spectral resonance position of metal nanoantennas can be easily tuned by changing their length (Sec. 2.4.1), nanoantenna samples with a match between plasmonic and molecular resonance can be reproducibly designed. Hence, surface-enhanced infrared spectroscopy using nanoantennas [171], referred to as nanoantenna-assisted IR spectroscopy in the remainder of the text, offers great potential for sensing and detection of molecules [33] or proteins [32]. Besides that, NAIRS is not restricted to enhance molecular vibrations and can also be applied to probe other excitations like phonon-polaritons [172], for example.

In Fig. 3.11, two examples of NAIRS are shown: the detection of the probe molecule octadecanethiol (ODT, see Fig. 3.11a), on the one hand, and the sensing of phonon-polaritons, on the other hand. These examples are discussed in the following two sections.

3.5.1. Octadecanethiol as Probe Molecule

First, the application of individual, electrochemically prepared [173, 174] gold nanoantennas will be considered. In Fig. 3.11a, relative transmittance spectra of cylindrical gold nanowires ($D = 100 \text{ nm}$) placed on CaF_2 are shown. Due to the different length of the nanorods, the plasmonic excitations are resonant at different frequencies (Sec. 2.4.1). Prior to the measurement, the nanowires were coated with a monolayer of ODT [$\text{HS} - (\text{CH}_2)_{17} - \text{CH}_3$], which chemically binds to gold but not to the sub-

3. Materials & Methods

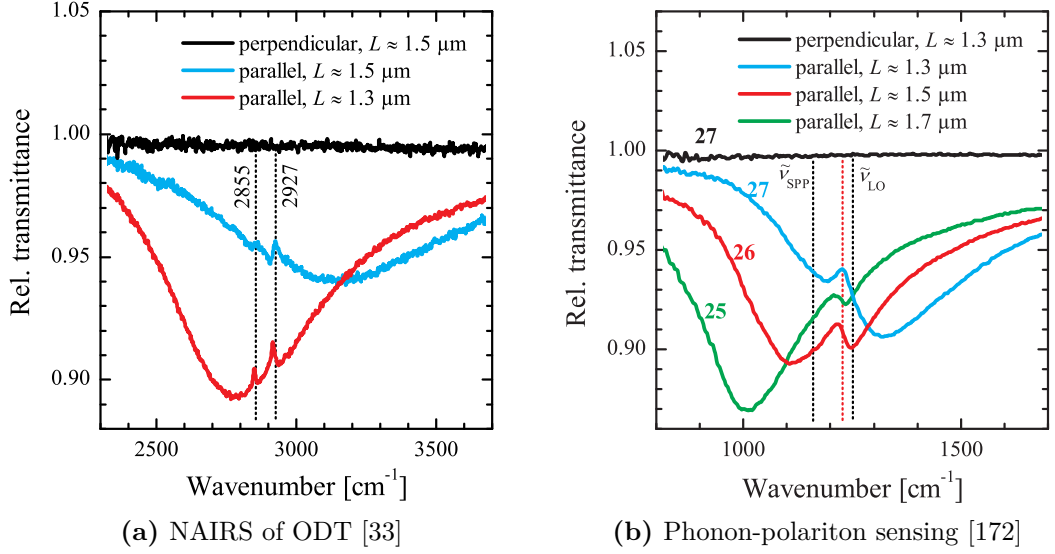


Figure 3.11.: (a) Relative transmittance spectra of individual, electrochemically prepared gold nanowires ($D = 100$ nm) coated with an ODT monolayer [33]. (b) Relative transmittance spectra of lithographic gold nanorod arrays ($w \approx 120$ nm, $h \approx 100$ nm, $d_x = d_y = 5$ μ m) on silicon [172]. The frequency of the thin-film SPP at 1230 cm^{-1} is marked by a vertical dashed red line. In addition, the frequency of the SPP at the air/SiO₂ interface ($\tilde{\nu}_{\text{SPP}} = 1161$ cm^{-1}) and the LO frequency of SiO₂ ($\tilde{\nu}_{\text{LO}} = 1251$ cm^{-1}) are indicated.

strate (Sec. 3.4). In case of parallel polarization, the spectral signature of ODT is visible at 2855 cm^{-1} and 2927 cm^{-1} (symmetric and antisymmetric CH₂ stretching vibrations [34, 175, 176]), whereas no signal is observed for perpendicularly polarized light. This is a clear proof that the enhanced near-fields of the nanoantennas cause the appearance of the ODT vibrational bands.

To quantify the observed signal enhancement, one has to compare the signal in the enhanced case to the non-enhanced case, which would be the measurement in perpendicular polarization. However, the signal of the adsorbate is below the noise level. For this reason, infrared reflection absorption spectroscopic (IRRAS) measurements of the adsorbate are used to provide the necessary reference [34] (see Sec. 7.1 for the method). Thus, the enhancement factor EF at a certain wavenumber $\tilde{\nu}_0$ is defined as [34]

$$EF(\tilde{\nu}_0) = \frac{I_{\text{NAIRS}}(\tilde{\nu}_0)}{I_{\text{IRRAS}}(\tilde{\nu}_0)} \cdot \frac{f_{\text{IRRAS}}}{f_{\text{NAIRS}}}, \quad (3.3)$$

3.5. Surface-Enhanced Infrared Spectroscopy Using Nanoantennas

where I_{NAIRS} , I_{IRRAS} are the signal intensities and f_{IRRAS} , f_{NAIRS} are the fractions of the illuminated spot that is effectively covered by the adsorbate in the respective NAIRS or IRRAS measurement.

While f_{IRRAS} can be set to one since the whole sample (smooth gold film) is covered by the adsorbate in case of IRRAS (Sec. 7.1), the molecules only cover a small fraction of the area in the case of NAIRS. Here, it is assumed that only those molecules located at the tip ends of the rods contribute to I_{NAIRS} [34], accounting for the distribution of the enhanced near-field (see Sec. 2.4.2).

Note that in the definition of Eq. (3.3), it is assumed that the molecules adsorb on the nanoantennas in the same manner compared to the smooth gold film. However, the effective area, which is occupied by one adsorbed alkanethiol, strongly depends on the crystalline structure of gold [177]. Whereas the unit cells on Au (111) and (110) are very similar (21.6 \AA^2 and 23.5 \AA^2 , respectively), the one on (100) is considerably larger (35.5 \AA^2) [177]. This has to be considered when single crystalline electrochemically and poly-crystalline lithographically prepared nanoantennas are compared. Former preferentially grow along the $\langle 110 \rangle$ -direction [34] whereas latter predominantly feature crystal grains with (111)-facets [122].

Furthermore, the signal intensity I_{NAIRS} is the change in the relative transmittance spectrum $(\Delta T/T)_{\text{NAIRS}}$ induced by the adsorbate (difference between maximum and minimum [34]). For the determination of I_{IRRAS} , one has to take into account that IRRAS measurements are performed in reflectance geometry at grazing incidence while NAIRS is carried out at normal transmittance. Hence, the measured signal intensity $(\Delta R/R)_{\text{IRRAS}}$ has to be transformed into a theoretical relative transmittance change $(\Delta T/T)_{\text{theo}}$ [34] via thin film approximations [178, 179]:

$$I_{\text{IRRAS}} = \left(\frac{\Delta T}{T} \right)_{\text{theo}} \approx \left(\frac{\Delta R}{R} \right)_{\text{IRRAS}} \cdot \frac{1}{2(n_{\text{sub}} + 1)} \cdot \frac{\cos \vartheta}{\sin^2 \vartheta}, \quad (3.4)$$

where ϑ is the angle of incidence in IRRAS and n_{sub} is the refractive index of the substrate in NAIRS.

In Fig. 3.12a, estimated enhancement factors of ODT are shown. The open red squares originate from measurements of individual, single crystalline, cylindrically shaped nanowires prepared by electrochemical methods whereas the open black circles result from lithographically prepared nanorod arrays (cuboid-like shape, see Sec. 3.1). On the abscissa, the ratio between the antenna resonance position $\tilde{\nu}_{\text{res}}$ and the frequency of the adsorbate $\tilde{\nu}_{\text{ODT}}$ is given. Accordingly, a ratio of $\tilde{\nu}_{\text{res}}/\tilde{\nu}_{\text{ODT}} \approx 1$ represents a perfect match between plasmonic and molecular excitation. Obviously,

3. Materials & Methods

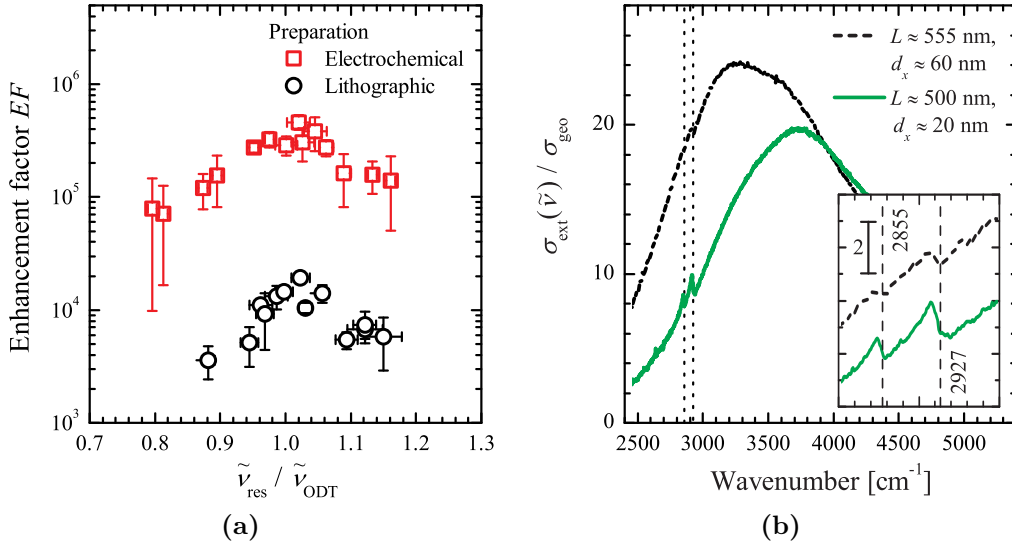


Figure 3.12.: (a) Experimentally estimated enhancement factors EF [Eq. (3.3)] for electrochemically prepared single nanowires and lithographic nanorod arrays [34]. (b) Extinction spectra [normalized to one antenna, see Eq. (4.4)] for lithographically prepared nanorod arrays ($w \approx h \approx 60 \text{ nm}$, $d_y = 5 \mu\text{m}$) coated with an ODT monolayer [171].

this condition yields the highest values of EF while the enhancement becomes smaller with increased detuning of antenna and adsorbate resonance. Note that a red-shift of the near-field spectrum with respect to the resonance curve in the far-field was theoretically found [30, 180] (see also Fig. 2.8), suggesting that maximal NAIRS intensity should be found at ratios $\tilde{\nu}_{\text{res}}/\tilde{\nu}_{\text{ODT}} > 1$. This behavior could not be resolved in the experiments of [34].

A big discrepancy exists between the EF -values of electrochemically and lithographically prepared nanoantennas. The lower values of the polycrystalline nanorods⁹ are attributed to residues on the nanorod's surface, hampering a complete covering of the nanorods by the adsorbate [34]. Moreover, the actual morphology of the tip ends heavily influences the near-field distribution and intensity [68]. Hence, it could be that less sharp tip ends of the cuboid-shaped lithographic nanorods (see e.g. Fig. 3.3) cause the observed differences. Nevertheless, the high experimental enhancement factors obtained with well-designed nanoantennas (up to 500 000) exceed those reached by common SEIRA techniques, e.g. rough films substrates [16, 25], by at least two orders of magnitude and those of homogeneous artificial gold particle films [181] by more than one order of magnitude.

⁹An influence of the nanorod's crystallinity on its far-field optical response was not detected [31, 34]

The line shape of the enhanced vibrational signal (see Fig. 3.11a) clearly differs from a typical Lorentzian absorption band (see e.g. Fig. 3.10) and in addition depends on the position of the resonance frequency with respect to the vibrational lines [33, 34, 182]. This effect can be explained with the appearance of Fano profiles and is discussed in Sec. 3.5.2 in more detail.

As a last point, the dependency of the NAIRS signal on the geometrical arrangement of the nanorods is briefly discussed. Figure 3.12b shows far-field extinction spectra of two lithographic gold nanorod arrays on ZnS, which have been covered by a monolayer of ODT [171]. In the array belonging to the black spectrum, the rods feature longitudinal separation distances (see Sec. 3.1) of $d_x \approx 60$ nm, whereas in other array, the distance d_y is only 20 nm ($d_x = 5 \mu\text{m}$ for both arrays). Although the resonance of the array with $d_x \approx 20$ nm is spectrally more separated from the CH₂ stretching vibrations of ODT (marked by vertical dashed lines), the signals of ODT are more pronounced compared to the measurement of the array with $d_x \approx 60$ nm. This clearly proves the stronger near-field enhancement of the smaller gap and is in accordance with simulation results showing increasing near-field intensity with decreasing gap size [30] (see also Fig. 2.8a).

Estimates of enhancement factors were performed according to Eq. (3.3) and values of $EF \approx 20000$ ($d_x \approx 20$ nm) and $EF \approx 7000$ ($d_x \approx 60$ nm) were obtained [171, 182]. These enhancement factors would become of about ten times larger for a better tuning [182]. However, related to residues of substances from the EBL preparation process, the NAIRS signals are still smaller than the ones from differently prepared individual nanocylinders (see Fig. 3.12a), even though the signal should be more enhanced due to interaction [182].

3.5.2. Antenna Sensing of Phonon-Polaritons

Figure 3.11b shows relative transmittance measurements of lithographically prepared nanorod arrays on natural oxide covered silicon. In case of the measurements with parallel polarized light, a vibrational feature at around 1230cm^{-1} is observed in contrast to the measurement with perpendicular polarization. This feature can be attributed to a polaritonic excitation in the thin silicon dioxide layer (thickness of about 3 nm) [172].

As reported in Sec. 2.6.1, different surface phonon-polariton modes exist in a three-layer-system (air/SiO₂/Si). With decreasing layer thickness of the oxide, the independent SPP modes at the interfaces air/SiO₂ and SiO₂/Si interact with each other resulting in the Fuchs-Kliwer modes. As can be seen from Fig. 2.10,

3. Materials & Methods

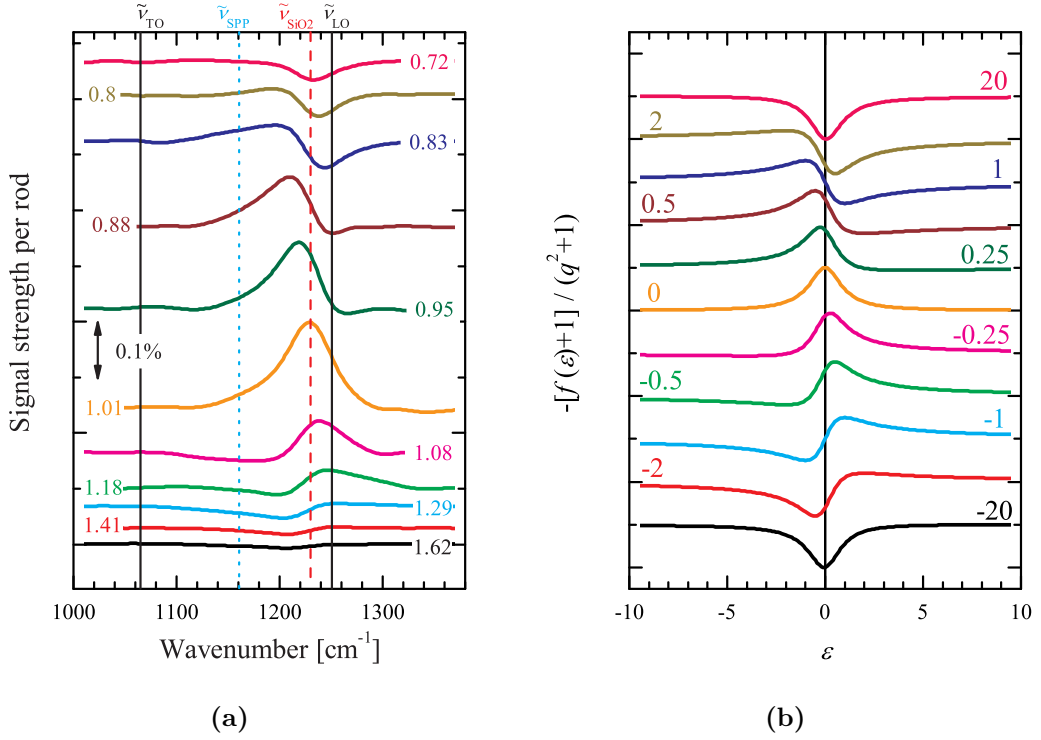


Figure 3.13.: (a) Baseline corrected thin-film SPP signals originating from relative transmittance spectra of nanorod arrays on natural oxide covered silicon (see Fig. 3.11b). The TO and LO frequencies of SiO₂ at $\tilde{\nu}_{\text{TO}} = 1065 \text{ cm}^{-1}$ and $\tilde{\nu}_{\text{LO}} = 1251 \text{ cm}^{-1}$ as well as the frequency of the SPP at the air/SiO₂ interface at $\tilde{\nu}_{\text{SPP}} = 1161 \text{ cm}^{-1}$ are indicated. The numbers at each curve represent the ratio between the antenna resonance frequency $\tilde{\nu}_{\text{res}}$ and the frequency of the thin-film SPP at $\tilde{\nu}_{\text{SiO}_2} = 1230 \text{ cm}^{-1}$. (b) Normalized and inverted Fano profiles calculated according to Eq. (3.5). For asymmetry parameters $q \neq 0$, asymmetric line shapes are obtained. Note that in case of $q = \pm 1$, the curves feature antisymmetry.

the higher energetic FK^+ mode is located between the surface phonon frequency $\tilde{\nu}_{\text{SiO}_2\text{-air}}^{\text{SPP}}$ and $\tilde{\nu}_{\text{LO}} = 1251 \text{ cm}^{-1}$ [103]. For an interface between a polar dielectric with dielectric function $\epsilon(\tilde{\nu})$ and air (dielectric half space), $\tilde{\nu}_{\text{SiO}_2\text{-air}}^{\text{SPP}}$ is the frequency for which $\Im\left(-\frac{1}{\epsilon(\tilde{\nu})+1}\right)$ becomes maximal [183]. Based on the SiO₂ dielectric function of GUNDE [103], it is $\tilde{\nu}_{\text{SiO}_2\text{-air}}^{\text{SPP}} = 1161 \text{ cm}^{-1}$. Since the observed feature in Fig. 3.11b ranges between these two border frequencies (marked by vertical dashed black lines), it can be attributed to the FK^+ mode at the air/SiO₂ interface. Note that the wave vector component parallel to the surface, which is necessary to excite phonon-polaritons [184], is provided by near-field scattering processes of nanoantennas [182], in agreement with scattering near-field infrared microscopic measurements [185, 186].

The line shape of the polaritonic signal obviously depends on the spectral position of the antenna resonance. To better illustrate the situation, Fig. 3.13a shows the

baseline corrected signal I_{SiO_2} (see Fig. 4.2) versus the wavenumber for nanorod arrays with different lengths. The strongest signal is found for a supposedly best match between polaritonic and plasmonic excitation (orange curve) and the position of the polariton feature can be determined to be $\tilde{\nu}_{\text{SiO}_2} \approx 1230 \text{ cm}^{-1}$. In analogy to Sec. 3.5.1, $\tilde{\nu}_{\text{res}}/\tilde{\nu}_{\text{SiO}_2}$ provides a measure for the detuning between plasmonic and vibrational excitation. The values of $\tilde{\nu}_{\text{res}}/\tilde{\nu}_{\text{SiO}_2}$ are given for each curve in Fig. 3.13a. As soon as the ratio $\tilde{\nu}_{\text{res}}/\tilde{\nu}_{\text{SiO}_2}$ becomes smaller or bigger than one, the line shape becomes asymmetric and I_{SiO_2} decreases. For larger mismatches, I_{SiO_2} further diminishes and its shape becomes more and more a Lorentzian.

The adsorbate signals originate from the interaction of the broader plasmonic excitation with the one of spectrally narrower vibrational dipoles [33, 182]. This effect can be understood in analogy to Fano profiles in wave and quantum mechanics, where the asymmetric line shape results from coupling between a discrete state and a continuum [187]. In our case, the broad plasmonic antenna resonance represents the continuum state whereas the molecular or phononic vibration can be interpreted as discrete state. Consequently, the phase difference between the two excitations determines the strength of the coupling and hence, the line shape.

To illustrate the theoretical shape of Fano profiles, Fig. 3.13b shows calculated line shapes for different asymmetry parameters q (indicated in the figure) according to the expression

$$f(\epsilon) = \frac{(\epsilon + q)^2}{\epsilon^2 + 1}, \quad (3.5)$$

given in the publication of FANO [187]. Note that the profiles are inverted and normalized to the maximum value $(q^2 + 1)$. Increasing or decreasing q leads to a change of the symmetric anti-resonance for $q = 0$ to asymmetric line shapes. For sufficiently high absolute values of q , symmetric resonances are obtained. Obviously, the experimentally observed line shapes of the thin-film SPP in Fig. 3.13a strongly resemble the ones shown in Fig. 3.13b.

3.6. Finite-Difference Time-Domain Simulations

The present section is partly adopted from [77]. Within this thesis, finite-difference time-domain simulations of antenna resonances are compared to experimental results. The FDTD method is a computational electrodynamics modeling technique and belongs to the general class of grid-based differential time-domain numerical modeling

3. *Materials & Methods*

methods. It is broadly established in computational electromagnetism to calculate the optical response of different nanostructures [188, 189]. The time-dependent Maxwell curl equations are discretized using central-difference approximations to the space and time partial derivatives. The temporal variations of electromagnetic waves within a finite space, which contains an object of arbitrary shape and properties, are solved iteratively (leapfrog method): the electric field vector components in a spatial volume are solved at a given instant in time. Afterwards, the magnetic field vector components in the same volume of space are solved at the next instant in time and the process is repeated over and over again until the desired electromagnetic field behavior is fully evolved. In practice, the space including the scatterer is discretized into a grid that contains the basic element of this discretization, the Yee cell [190, 191]. The precision of the results depend both on the number of the cells used in the simulation as well as on the appropriate selection of the simulation time.

Numerical simulations of the IR extinction of gold nanoantennas were performed by P. ALBELLA from the Center for Materials Physics in San Sebastian (Spain) using the FDTD software LUMERICAL.

Maxwell's equations were solved for a plane wave normally incident on an individual nanorod or a pair of nanorods, respectively, on a silicon wafer covered by a 3nm thin oxide layer. In addition, to obtain better agreement with the experimental results, some spectra were simulated by solving Maxwell's equations for an incident Gaussian beam (diameter of 40 μ m) illuminating gold nanoantenna arrays consisting of a large number of antenna units. The materials (gold, silicon, silicon dioxide) were described by the optical data of PALIK's reference book [58]. The results are fully converged, thus they can be considered an exact solution of Maxwell's equations.

4. Individual Nanoantennas Arranged in Arrays

Nanoantennas arranged in arrays with large separation distances d_x and d_y (see Sec. 3.1) can be considered as *non-interacting* and, hence, as an ensemble of individual nanoantennas. This argumentation is based on the fact that the optical properties of arrays do not significantly differ from those of single nanoantennas for d_x and d_y being at least $5\mu\text{m}$ [34].

Section 4.1 focuses on nanorods prepared on silicon covered with a natural oxide layer. Moreover, nanorod arrays on silicon featuring a thicker oxide layer (around 106nm) will be introduced in Sec. 4.2. Finally, Sec. 4.3 deals with the influence of the substrate on the nanorods' optical properties. To this end, the nanorod arrays on silicon are compared to lithographically fabricated nanorod arrays on quartz glass [109], zinc sulphide [34] and calcium fluoride [102]. In the end, important findings of this chapter are summarized in Sec. 4.4.

4.1. Nanorod Arrays on Natural Oxide Covered Silicon

As an introduction, characteristic resonance parameters are defined in Sec. 4.1.1 and their general behavior is illustrated with the help of nanorod arrays of sample Wef1 (see Tab. 3.1). In Sec. 4.1.2, the experimental results are compared with FDTD simulations. Afterwards, the reproducibility of the lithographic preparation process is analyzed in Sec. 4.1.3. Finally, Sec. 4.1.4 focuses on the influence of the titanium adhesion layer on the optical properties.

4.1.1. Resonance Parameters and General Properties

Figure 4.1 shows typical relative transmittance spectra of gold nanorod arrays on natural oxide covered silicon with different rod lengths L . The measurements were

4. Individual Nanoantennas Arranged in Arrays

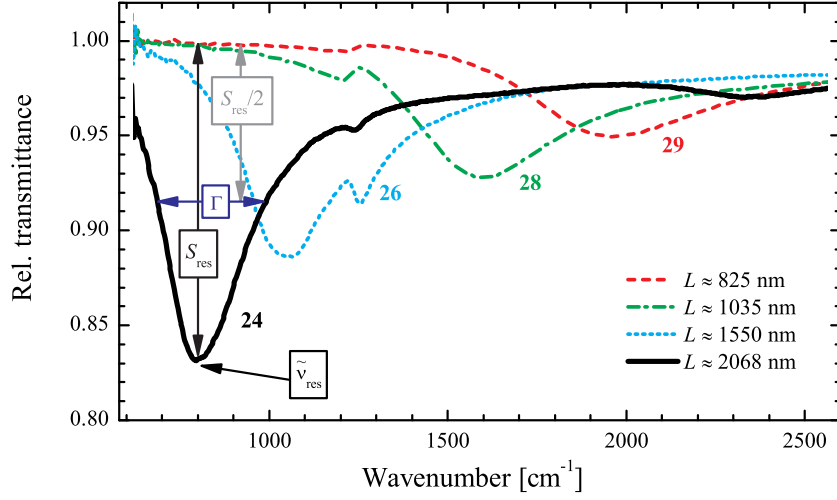


Figure 4.1.: Gold nanorod arrays on silicon ($d_x = d_y = 5 \mu\text{m}$, $w \approx 90 \text{ nm}$, $h \approx 100 \text{ nm}$) with different lengths L . The numbers indicate the approximate quantities of rods contributing to the signals. The definition of the characteristic resonance parameters is illustrated with the help of the solid black spectrum. The small feature at around 1230 cm^{-1} originates from the excitation of a thin-film SPP at the SiO_2/air interface (see Sec. 3.5.2).

performed with light polarized parallel to the long rod axis. If the orientation of the polarized light is not explicitly given in the remainder of the text, the reader may assume that the measurement or simulation was performed with parallel polarization.

The most important parameter, the resonance frequency $\tilde{\nu}_{\text{res}}$, is given by the minimum of the relative transmittance curve:

$$\tilde{\nu}_{\text{res}} = \min\{T_{\text{rel}}(\tilde{\nu})\}. \quad (4.1)$$

Furthermore, the maximum extinction S_{res} , which is defined as

$$S_{\text{res}} = S(\tilde{\nu}_{\text{res}}) = 1 - T_{\text{rel}}(\tilde{\nu}_{\text{res}}), \quad (4.2)$$

is used to characterize the intensity of the antenna resonance. The last parameter indicated in Fig. 4.1 is the full width at half maximum Γ , which is obtained by calculating the difference $\tilde{\nu}_1 - \tilde{\nu}_2$ with $T_{\text{rel}}(\tilde{\nu}_{1,2}) = 1 - S_{\text{res}}/2$. This parameter is used to calculate the quality factor Q [192]:

$$Q = \frac{\tilde{\nu}_{\text{res}}}{\Gamma}. \quad (4.3)$$

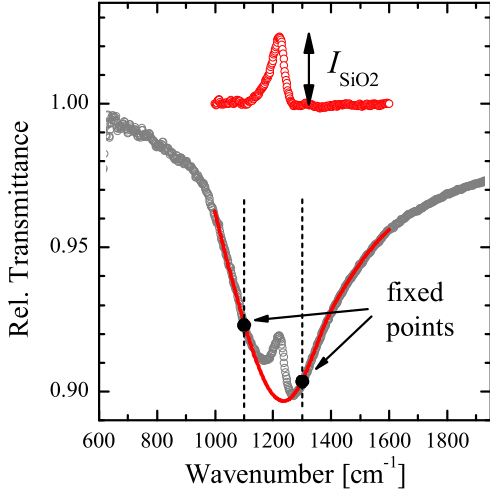


Figure 4.2: Determination of $\tilde{\nu}_{\text{res}}$, S_{res} and intensity I_{SiO_2} of the phonon-polariton band in the case of a nanorod array on silicon ($L \approx 1.4 \mu\text{m}$). The measured data (gray symbols) is baseline corrected with a polynomial (solid red) using the OPUS software. Fixed boundary values of 1100 and 1300cm^{-1} are used. By calculating the ratio between experimental spectrum and polynomial, I_{SiO_2} is determined.

For detailed information about the determination of characteristic parameters and its errors, the reader may be referred to former theses [34, 109, 110].

Besides the fundamental resonances, a small feature in the region around 1230cm^{-1} is present in all spectra. It originates from the excitation of a thin-film surface phonon-polariton at the SiO_2/air interface and its line shape depends on the spectral position of the antenna resonance (see 3.5.2). This Fano-like excitation complicates the determination of the characteristic resonance parameters, especially if it is excited resonantly. To overcome this problem, a baseline correction with the help of the OPUS software is performed (see Fig. 4.2). In this way, $\tilde{\nu}_{\text{res}}$ and S_{res} as well as the intensity I_{SiO_2} of the surface phonon-polariton band can be determined.

In the following, the behavior of the characteristic resonance parameters is discussed based on the antenna resonances of Fig. 4.1. Obviously, the spectral resonance position $\tilde{\nu}_{\text{res}}$ as well as the maximal extinction S_{res} are governed by the antenna length L . Concerning $\tilde{\nu}_{\text{res}}$, the resonance is located at smaller frequencies for longer antennas. In Fig. 4.3a, the values of the resonant wavelength $\lambda_{\text{res}} = 1/\tilde{\nu}_{\text{res}}$ are plotted versus the antenna length L , resulting in a linear relation between L and λ_{res} (compare to Sec. 2.4.1). Although this particular behavior is true for all investigated non-interacting arrays, Sec. 4.1.3 demonstrates that the exact progress of $\lambda_{\text{res}}(L)$ is influenced by the lithographic preparation process.

The values of Γ are plotted in Fig. 4.3b versus the resonance frequency $\tilde{\nu}_{\text{res}}$ (open black squares, left ordinate). The resonances of longer rods (featuring lower $\tilde{\nu}_{\text{res}}$) seem to be narrower compared to those of shorter rods. However, the conclusion that the plasmonic oscillation of longer rods exhibits less damping is delusive, since plotting the spectra over the wavelength would result in narrower resonances for

4. Individual Nanoantennas Arranged in Arrays

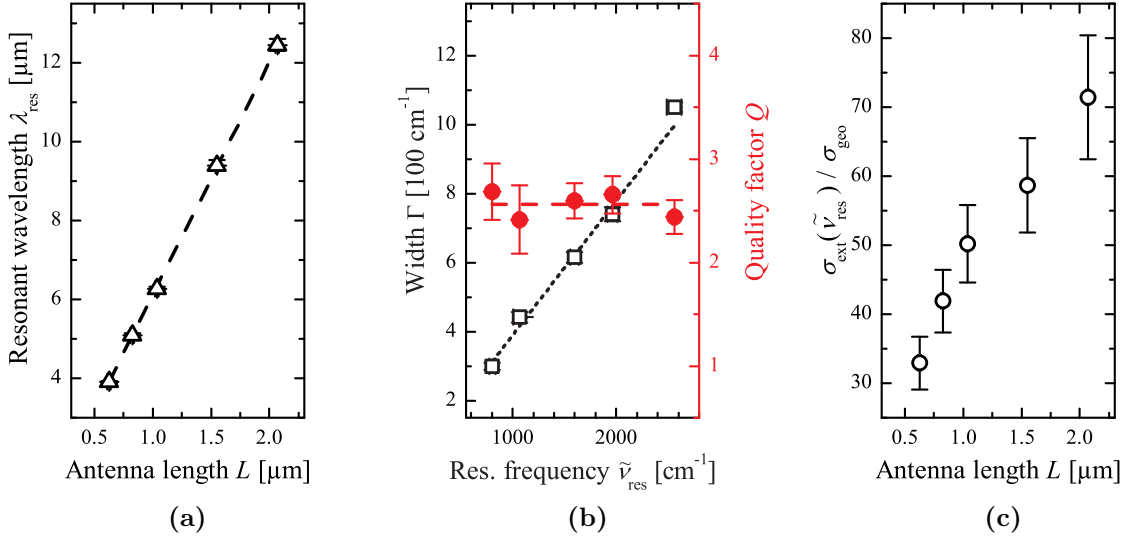


Figure 4.3.: (a) λ_{res} versus L for the nanorod arrays shown in Fig. 4.1. The dashed curve represents a linear fit. In (b), the corresponding values of Γ (left ordinate) and Q (right ordinate) are plotted versus $\tilde{\nu}_{\text{res}}$. The black dotted curve is a linear fit to the experimental data using $\Gamma(\tilde{\nu}_{\text{res}}) = \frac{1}{Q} \cdot \tilde{\nu}_{\text{res}}$. The result ($Q = 2.6 \pm 0.1$) is also represented by the red dashed line. (c) Normalized extinction cross-section at resonance $\sigma_{\text{ext}}(\tilde{\nu}_{\text{res}})/\sigma_{\text{geo}}$ versus L .

shorter rods. Hence, the quality factor $Q = \tilde{\nu}_{\text{res}}/\Gamma$ (full red squares, right ordinate) is a better measure to characterize the oscillation's damping. The values of Q feature a nearly constant value of about 2.6 (dashed horizontal line) and are relatively small compared to that of gold nanoantennas in the visible (e.g. $Q \approx 20$ reported in [193]). This is related to the much stronger radiative damping [192] in the IR where electronic damping gives a rather weak but non-negligible effect [31].

Furthermore, the extinction S_{res} of the nanorod arrays in Fig. 4.1 increases for longer antenna length L . For a quantitative analysis, one has to consider that different numbers N of rods contribute to the respective signals. In addition, longer rods also feature a bigger geometric cross-section $\sigma_{\text{geo}} = L \cdot w$ and hence a bigger geometric shadowing. To account for these two effects, the normalized extinction cross-section per nanorod [7, 194],

$$\frac{\sigma_{\text{ext}}}{\sigma_{\text{geo}}}(\tilde{\nu}) \approx \frac{A_0}{N} [1 - T_{\text{rel}}(\tilde{\nu})] \cdot \frac{n_{\text{sub}} + 1}{2Lw}, \quad (4.4)$$

is determined, where A_0 is the illuminated spot size. The influence of the substrate is taken into account via its refractive index n_{sub} in analogy to the normal transmittance change of a thin film [195] compared to a freestanding film [196].

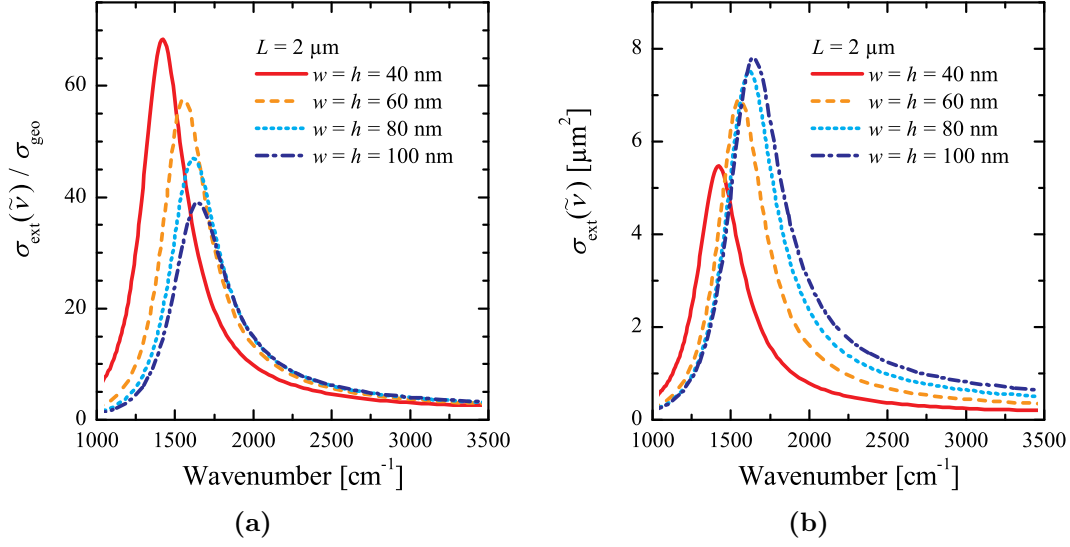


Figure 4.4.: FDTD simulations [93] of (a) normalized extinction cross-section $\sigma_{\text{ext}}(\tilde{\nu})/\sigma_{\text{geo}}$ and (b) extinction cross-section σ_{ext} of four individual nanorods with geometric dimensions indicated in the figures.

The Meaning of $\sigma_{\text{ext}}(\tilde{\nu})/\sigma_{\text{geo}}$

Any value of $\sigma_{\text{ext}}(\tilde{\nu})/\sigma_{\text{geo}}$ above one means an extinction of intensity above geometric shadowing. This is a clear indication of the nanorods' ability to confine light and therefore an indication for an enhanced local field in the vicinity of the nanorods [34, 194]. The maximum value $\sigma_{\text{ext}}(\tilde{\nu}_{\text{res}})/\sigma_{\text{geo}}$ is therefore a measure of a spatially averaged far-field enhancement.

Looking at Fig. 4.3c, a monotonic increase of $\sigma_{\text{ext}}(\tilde{\nu}_{\text{res}})/\sigma_{\text{geo}}$ with L is observed and, hence, one can conclude that longer rods provide higher electromagnetic field enhancement due to the increased lightning rod effect (see Sec. 2.4.2). Concerning nanorods of the same length L but different cross-sections ($w \cdot h$), $\sigma_{\text{ext}}(\tilde{\nu})/\sigma_{\text{geo}}$ also provides a measure of the field-enhancing properties of the nanorods. From near-field simulations it is known that thinner rods provide higher field enhancement [30]. And in fact, FDTD simulations (Fig. 4.4a) show that the values of $\sigma_{\text{ext}}(\tilde{\nu})/\sigma_{\text{geo}}$ increase with decreasing cross-section, in contrast to the values of σ_{ext} (Fig. 4.4b).

However, note that direct conclusions on the near-field behavior cannot be drawn when comparing $\sigma_{\text{ext}}(\tilde{\nu}_{\text{res}})/\sigma_{\text{geo}}$ of *interacting nanoantennas* (Chap. 5). Far- and near-field behavior significantly differ in these cases (see Sec. 2.5).

4. Individual Nanoantennas Arranged in Arrays

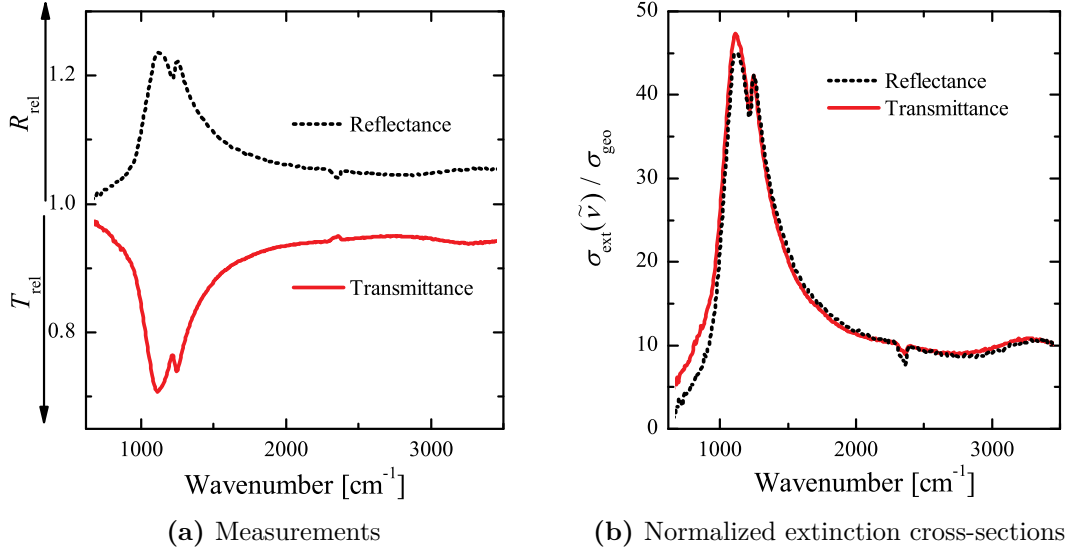


Figure 4.5.: (a) Relative reflectance and transmittance measurement, respectively, at normal incidence of a nanorod array on silicon ($L \approx 1.5 \mu\text{m}$, ≈ 26 rods in measurement spot). (b) Calculated normalized extinction cross-sections per nanorod of the measurements shown in (a) using Eqs. (4.4) and (4.5).

Transmittance vs. Reflectance

In Fig. 4.5a, relative transmittance and reflectance spectra of the same nanorod array are shown. In case of normal transmittance measurements, more light is scattered out of the normal direction when the nanorods are excited, leading to decreased transmittance at resonance. Conversely, more light is reflected by the nanorods in case of reflectance measurements, explaining the increased values of R_{rel} at resonance. To calculate $\sigma_{\text{ext}}(\tilde{\nu}) / \sigma_{\text{geo}}$ for the relative reflectance measurement, the influence of the substrate has to be taken into account in analogy to Eq. (4.4):

$$\frac{\sigma_{\text{ext}}}{\sigma_{\text{geo}}}(\tilde{\nu}) \approx \frac{A_0}{N} [R_{\text{rel}}(\tilde{\nu}) - 1] \cdot \frac{n_{\text{sub}}^2 - 1}{4Lw}, \quad (4.5)$$

where the factor $(n_{\text{sub}}^2 - 1)/4$ follows from thin film approximations at normal incidence [196, 197]. In Fig. 4.5b, calculated values of $\sigma_{\text{ext}}(\tilde{\nu}) / \sigma_{\text{geo}}$ for the measurements shown in Fig. 4.5a are plotted. Since the two curves are nearly identical, the use of the thin film approximations seems to be reasonable.

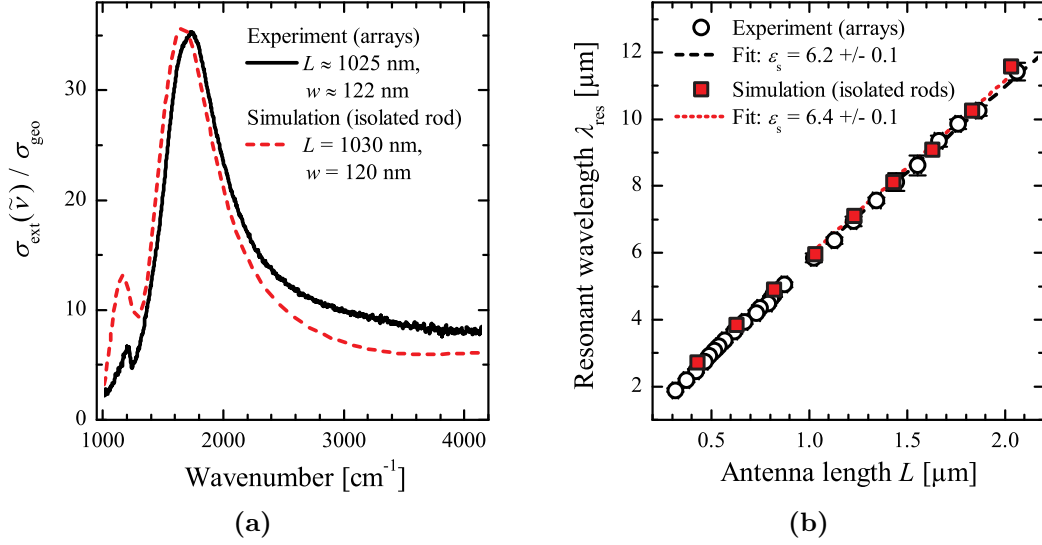


Figure 4.6.: Comparison between experiment and simulation. (a) $\sigma_{\text{ext}}(\tilde{\nu}_{\text{res}}) / \sigma_{\text{geo}}$ for a nanorod array ($d_x = d_y = 5 \mu\text{m}$) and an isolated nanorod with L and w given in the figure ($h = 100$ nm for both). (b) λ_{res} versus L for the nanorods arrays of sample Wb3 and FDTD simulations of isolated rods. Both sets of data were fitted with NOVOTNY’s model, resulting in the values of ϵ_s given in the figure.

4.1.2. Comparison with FDTD Simulations

In Fig. 4.6a, the experimental extinction spectrum per nanorod of an array is compared to a FDTD simulated (Sec. 3.6) spectrum of an isolated rod of similar length. Obviously, resonance position, full width at half maximum and extinction are in good agreement. The slight differences of $\tilde{\nu}_{\text{res}}$ might be due to the experimental uncertainties of L and thickness of the oxide layer. However, the phonon-polariton feature at around 1230cm^{-1} is much more pronounced in the simulation. Most likely, the SiO_2 IR optical textbook data and the ideal SiO_2/Si interface model used in the simulation do not exactly describe the real optical response of the thin natural oxide layer with non-ideal stoichiometry [77], leading to the observed spectral differences.

Despite these small discrepancies, the simulation of an isolated rod quite accurately reproduces the experimental spectrum of the nanorod array, corroborating that interaction within the array is negligibly small for $d_x = d_y = 5 \mu\text{m}$. This is further supported by Fig. 4.6b, where values of λ_{res} extracted from experiments and simulations are plotted versus L . Both data sets were fitted for $L \geq 1 \mu\text{m}^1$ with the

¹For smaller lengths and, thus, smaller aspect ratios, the assumption $L \gg R$ in NOVOTNY’s model does not hold any more and leads to deviations.

4. Individual Nanoantennas Arranged in Arrays

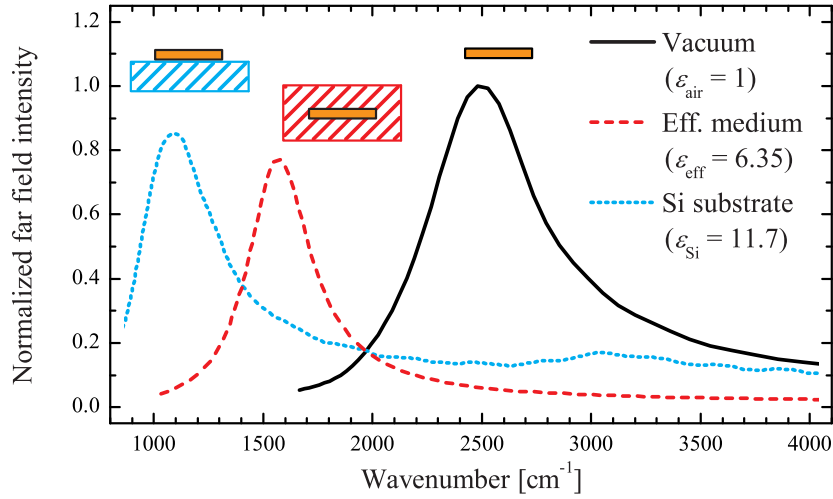


Figure 4.7.: Simulated far field intensity of an individual gold nanoantenna ($L = 1.5\ \mu\text{m}$, $w = h = 100\ \text{nm}$) for different surrounding media (see text). The spectra are normalized to the maximum intensity of the rod being surrounded by vacuum.

theoretical model of NOVOTNY (see Sec. 2.4.1) and similar results for the effective dielectric constant ϵ_s were obtained. Remember that the nanoantenna is surrounded by one homogeneous medium in NOVOTNY's model; hence, ϵ_s can be considered as an effective dielectric constant in case of nanorods on a substrate. Interestingly, the fitting result of $\epsilon_s \approx 6.3$ (average over experiment and simulation) suggests that ϵ_s can be predicted by simply averaging the dielectric constants of substrate ($\epsilon_{\text{Si}} \approx 11.7$) and air ($\epsilon_{\text{air}} \approx 1$). A similar result was found for gold nanorods on quartz glass substrates [109], whereas measurements on zinc sulphide [34] showed considerable deviations (see also Sec. 4.3.1).

Failure of the Effective Medium Model

Different FDTD simulations were performed to clarify if the arithmetic average of the dielectric constants of substrate and air is really a good approximation for the actual geometry (nanorod supported by substrate). Figure 4.7 shows simulated spectra of isolated nanorods with fixed length $L = 1.5\ \mu\text{m}$ but different surrounding media: a nanorod in vacuum, a nanorod surrounded by a homogeneous (effective) medium with $\epsilon_{\text{eff}} = \frac{1}{2}(\epsilon_{\text{Si}} + \epsilon_{\text{air}}) = 6.35$, and a nanorod supported by a substrate with dielectric constant of $\epsilon_{\text{Si}} = 11.7$. Although the effective medium model yields a red-shift of the resonance compared to the vacuum simulation, it does not reproduce the simulation of the nanorod on the substrate. This results implicates that simple averaging over

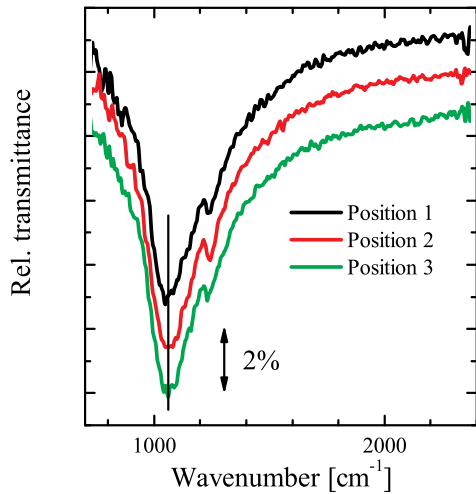


Figure 4.8: Relative transmittance measurements at three different positions within an array ($L \approx 1.6 \mu\text{m}$). The spectra are artificially shifted for better comparison. Same number of rods ($N \approx 26$) contribute to each spectrum.

dielectric constants is not able to predict the exact resonance position. Interface effects therefore cannot be neglected and are important to consider. Most important, the values of the dielectric constants ϵ_s obtained from NOVOTNY fits cannot be used to draw conclusions on the dielectric constant of the substrate.

4.1.3. Reproducibility of Lithographic Preparation

In each preparation series, several samples were usually fabricated (see Tab. 3.1). SEM measurements showed that the length distribution within the arrays is very narrow or, in other words, that the arrays feature a high homogeneity (usual size of $50 \times 50 \mu\text{m}^2$). This statement is supported by IR measurements as illustrated in Fig. 4.8. Here, three different positions within the array were measured and nearly no variation of $\tilde{\nu}_{\text{res}}$ is observed. Consequently, any observed spectral differences between different samples cannot be attributed to inhomogeneities within the arrays and must have other reasons, as will be discussed in the following.

The present section is divided into two parts. First, the optical properties of samples within the *same preparation series* are considered. Afterwards, *different preparation series* are compared with each other.

Same Preparation Series

Figure 4.9 shows the relations $\lambda_{\text{res}}(L)$ of the two samples Wc1 and Wc2 of preparation series C. NOVOTNY fits (see Sec. 2.4.1) to the experimental data were performed for both samples. Since the fitting results of ϵ_s , which can be used as a quantitative measure to compare the two samples, are nearly the same, a good reproducibility

4. Individual Nanoantennas Arranged in Arrays

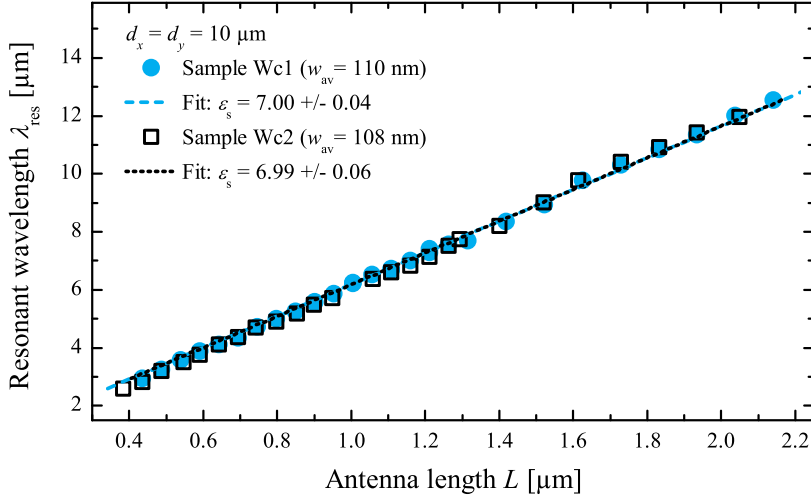


Figure 4.9.: Resonant wavelength λ_{res} versus antenna length L for two samples of the same preparation series. The error bars have been omitted since their size is smaller than the symbols in most cases. The straight lines are NOVOTNY fits to the experimental data.

Series	d_x, d_y [μm]	ϵ_s , sample 1	ϵ_s , sample 2	$\Delta\epsilon_s$
B	5	6.06 ± 0.13	6.04 ± 0.09	0.02
C	10	7.00 ± 0.04	6.99 ± 0.06	0.01
E	5	7.23 ± 0.16	7.19 ± 0.20	0.04

Table 4.1.: Results of ϵ_s obtained from NOVOTNY fits.

within this preparation series is given. Moreover, the data of different samples of preparation series B and E were fitted using NOVOTNY’s model and the results of ϵ_s are summarized in Tab. 4.1. As the last column indicates, very good agreement between samples of the *same preparation* series is obtained.

Different Preparation Series

In Fig. 4.10, normalized extinction cross-sections $\sigma_{\text{ext}}(\tilde{\nu})/\sigma_{\text{geo}}$ of nanorod arrays from different preparation series are shown. Since the rod width w is smaller in series E, the higher extinction of the array of series E (E-array in the following) compared to the array with similar length of series B (B-array) can be explained by an increased lighting rod effect (see Sec. 4.1.1). Moreover, the resonance position of the E-array is red-shifted compared to the B-array with similar length. This behavior, which is observed for all investigated arrays of these two series (see Fig. 4.11a), cannot

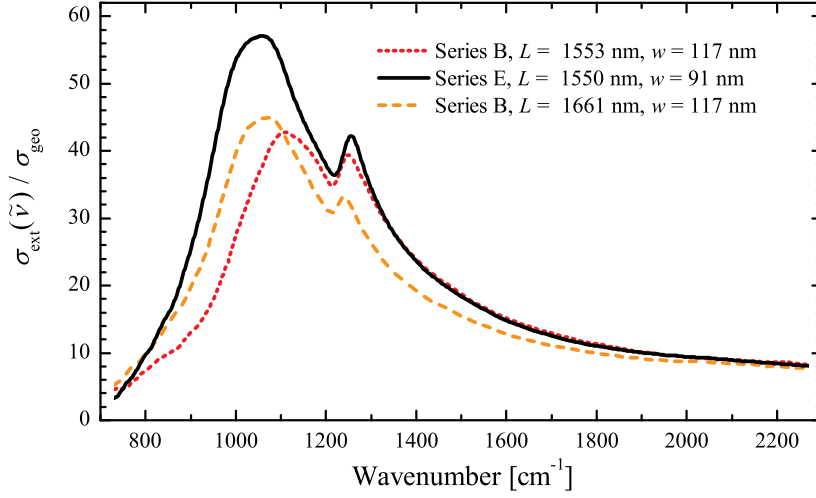


Figure 4.10.: Comparison of the normalized extinction cross-section $\sigma_{\text{ext}}(\tilde{\nu})/\sigma_{\text{geo}}$ between different preparation series (see text).

be attributed to interaction since both nanorod arrays feature identical separation distances ($d_x = d_y = 5\ \mu\text{m}$).

The assumption, that the measured lengths L of the E-arrays exhibit systematic larger values, can be ruled out as a comparison between the resonances of the E-array with $L \approx 1.5\ \mu\text{m}$ and the B-array with $L \approx 1.6\ \mu\text{m}$ shows: the values of $\tilde{\nu}_{\text{res}}$ are similar, but the length difference is about 100 nm. This value is clearly above the accuracy of the SEM measurement ($\pm 30\ \text{nm}$, see Sec. 3.1.2).

It is known from simulations that a smaller rod diameter leads to a red-shift of the resonance (see Sec. 2.4.1 and also Fig. 4.4), although only a weak influence of the rod radius R was reported for $R > 40\ \text{nm}$ in the near-infrared [29]. Thus, the smaller width w of the E-array rods could explain the observed red-shift. However, as Fig. 4.11a shows, the samples of series C and E feature similar relations $\lambda_{\text{res}}(L)$ even though the rod width w differs. Moreover, the influence of w is taken into account in the fitting result of ϵ_s via the effective radius R (see Sec. 2.4.1). Obviously, big discrepancies between the values of ϵ_s of samples from different preparation series exist (see Tab. 4.1). The deviating values of ϵ_s suggest that the substrate polarizability varies for the individual preparation series. This may be caused by the different stoichiometry or thickness of the SiO_2 layer beneath the nanorods. This assumption is supported by the fact that the thin-film SPP at around $1230\ \text{cm}^{-1}$ is clearly more pronounced in case of the E-array compared to the B-array with same $\tilde{\nu}_{\text{res}}$ (dashed orange curve in Fig. 4.10).

4. Individual Nanoantennas Arranged in Arrays

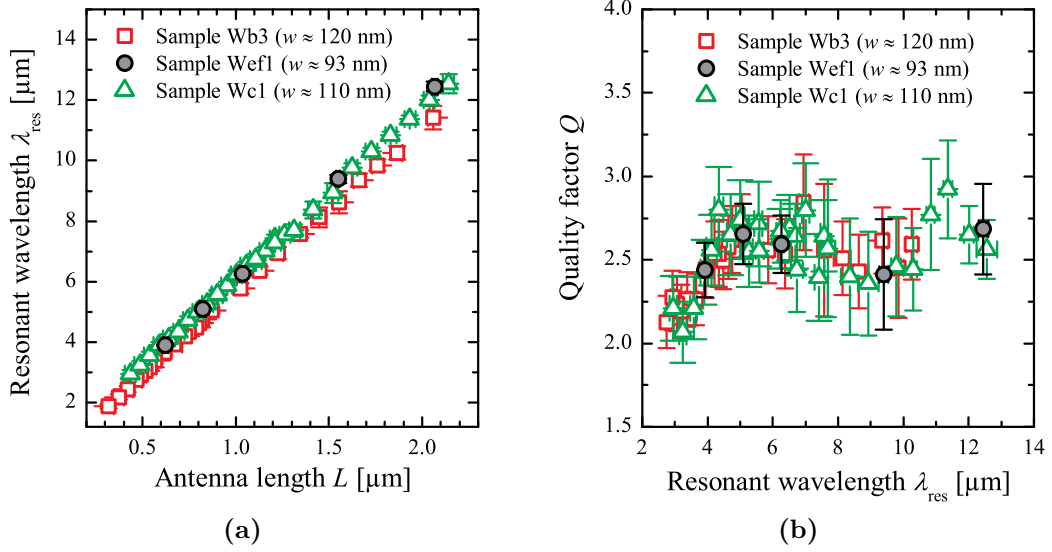


Figure 4.11.: (a) Resonant wavelength λ_{res} versus antenna length L and (b) quality factor Q versus λ_{res} of three samples from different preparation series. The characteristic separation distances are $d_x = d_y = 5 \mu\text{m}$ for the samples Wb3 and Wef1 and $10 \mu\text{m}$ for sample Wc1, respectively. The dip in (b) around $9 \mu\text{m}$ may originate from the phonon-polariton band in this range which hampers the exact determination of Γ .

In summary, the relation $\lambda_{\text{res}}(L)$ does not provide a good reference value to compare different preparation series. Although the same silicon wafers were used for the fabrication of series B, C, and E, it seems that details of the preparation process influence the exact resonance position. This is corroborated by the fact that the relation $\lambda_{\text{res}}(L)$ within one preparation series is well reproduced.

However, Fig. 4.11b shows that the relations $Q(\lambda_{\text{res}})$ of three different preparation series are in very good accordance. Note that the values of Q and λ_{res} are exclusively determined out of the optical IR measurements. Hence, measurement errors of L , w or the number of rods [contributing to $\sigma_{\text{ext}}(\tilde{\nu}_{\text{res}})/\sigma_{\text{geo}}$] do not affect the value of $Q(\lambda_{\text{res}})$. Accordingly, Q can be used as a reference parameter to identify spectral discrepancies between different preparation series.

Conclusion

The relation $\lambda_{\text{res}}(L)$ may depend on the preparation process which hampers the interpretation of spectral shifts between different samples, especially in the case of interaction effects (Chap. 5). However, the relation $Q(\lambda_{\text{res}})$ seems to be less preparation-dependent and can therefore be used to compare various sample series.

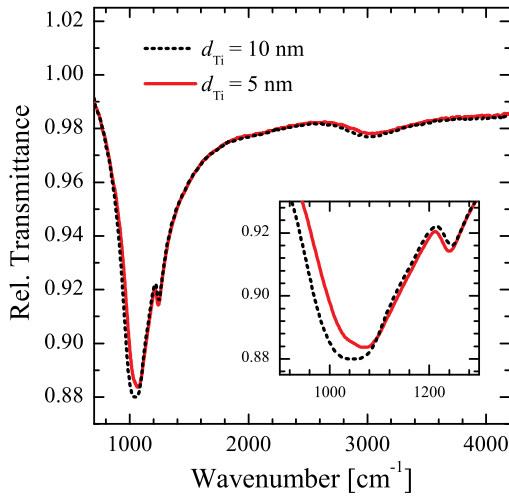


Figure 4.12: Relative transmittance spectra of two nanorod arrays (both from series B) with similar geometric dimensions ($L \approx 1.6 \mu\text{m}$, $w \approx 120 \text{ nm}$, $h \approx 100 \text{ nm}$) but different titanium adhesion layers. Same number of rods ($N \approx 26$) contribute to each spectrum.

4.1.4. Influence of the Adhesion Layer

In preparation series B, two samples with different titanium adhesion layers (5 nm and 10 nm) were prepared. Figure 4.12 shows relative transmittance spectra of two nanorod arrays with similar geometric dimensions. A small shift of the resonance frequency is observed, which could be explained by slightly different geometric dimensions of the rods (below 30 nm) or the thickness of the SiO_2 layer. However, no influence on the spectral width or the extinction could be detected (deviations within the error limit). Moreover, a reduction of the titanium layer to about 5 nm did not result in a lower adhesion of the nanorods to the substrate (proved by SEM).

4.2. Nanorod Arrays on Thermally Oxidized Silicon

For the nanogap preparation by FIB (see Sec. 6.3.4), gold nanorod arrays were prepared on thermally oxidized silicon ($d_{\text{SiO}_2} \approx 106 \text{ nm}$ [123], see Sec. 3.1.3). Concerning the relative transmittance spectra of three shortest nanorod arrays in Fig. 4.13, a peak at around 1000 cm^{-1} is growing in intensity as the respective antenna resonance (located at $\tilde{\nu}_{\text{res}} > 1500 \text{ cm}^{-1}$) approaches it. This feature, referred to as “oxide feature” in the remainder of the text, is certainly related to the excitation of a surface phonon-polariton in the SiO_2 film below the nanoantennas. However, it is much more pronounced than in the case of a thin natural oxide layer (compare to Sec. 4.1). To prove that its excitation is due to the antenna resonance, a measurement with perpendicular polarization (\perp) was performed. Here, only a very weak peak around

4. Individual Nanoantennas Arranged in Arrays

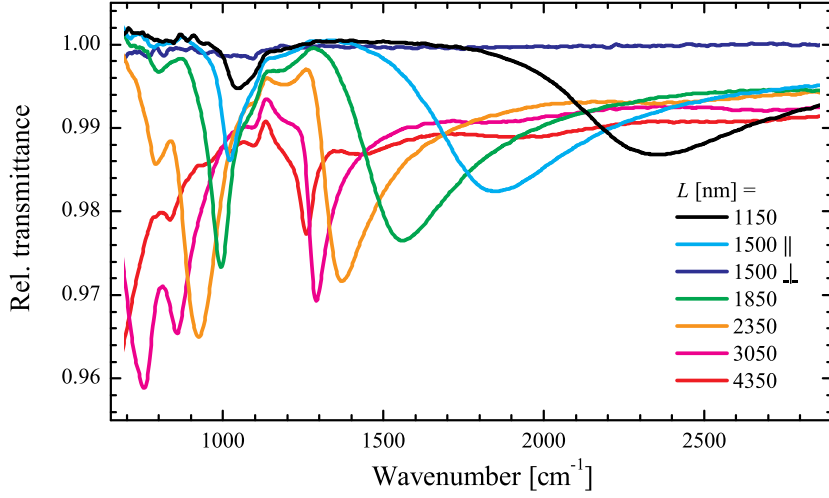


Figure 4.13.: Relative transmittance spectra of gold nanorod arrays ($w \approx h \approx 60$ nm, $d_x = d_y = 10$ μ m) on a silicon substrate covered by a 106 nm thick oxide layer. Exactly nine rods contribute to each spectrum. For the array with $L \approx 1.5$ μ m, spectra with parallel (\parallel) and perpendicular (\perp) light polarization were recorded.

1080 cm^{-1} is observed, which can be explained by inhomogeneities (different oxide thickness) of the substrate (see Fig. B.1 in the appendix).

With increasing rod length, the strong oxide feature in the range between 1000 cm^{-1} and 1200 cm^{-1} completely interferes with the antenna resonance, hampering the determination of λ_{res} , Γ , and $S(\tilde{\nu}_{\text{res}})$ for the nanorods with $L > 2$ μ m. This is illustrated in Fig. 4.14, where simulated relative transmittance spectra of 2350 nm long gold nanorods are shown. In the dashed red spectrum, the dielectric function of the substrate is adjusted to that of SiO_2 by implementing a harmonic oscillator with resonance at 1060 cm^{-1} [198]. And in fact, the obtained spectrum is very similar to the experimental data of a 2350 nm long nanoantenna on 106 nm SiO_2/Si (orange spectrum in Fig. 4.13), featuring two peaks at around 900 cm^{-1} and 1400 cm^{-1} . For comparison, the same geometric situation is simulated, but the silicon dioxide is modeled by a constant dielectric function, resulting in the solid black curve. In this case, no coupling between plasmonic and phononic excitation is present, leading to an antenna resonance at $\tilde{\nu}_{\text{res}} \approx 1250$ cm^{-1} . Now it becomes clear that neither of the two peaks in the dashed red spectrum corresponds to the antenna resonance or the oxide feature. The plasmonic excitation rather couples to the phonon-like excitation in the silicon dioxide producing a Fano-like line shape. However, a reproducible baseline correction like the one shown in Fig. 4.2 is almost impossible as the example of Fig. 4.14 shows.

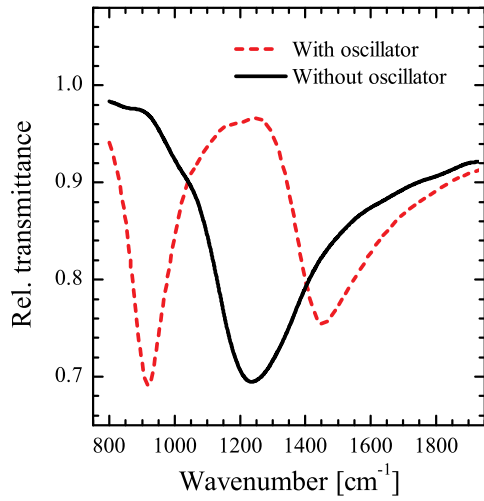


Figure 4.14: FDTD simulations of 2350nm long gold nanoantennas ($w = 60 = 60\text{nm}$) on a 100nm thick silicon dioxide layer on silicon (see text). The data have been taken from [198].

Resonance Position

In order to get an impression how the thick oxide layer on silicon influences the antenna resonance position, FDTD simulations using the software package MEEP were performed [102], which are depicted in Fig. 4.15a. Here, the relative transmittance of a 900nm-long gold nanorod is shown for three different cases: pure silicon, 100nm SiO₂ on silicon, and pure SiO₂. For the simulations, the substrates were modeled with constant dielectric functions ($\epsilon_{\text{Si}} = 11.7$, $\epsilon_{\text{SiO}_2} = 2.1$). Interestingly, the spectrum of the nanorod on 100nm SiO₂ / Si resembles the one on SiO₂ with respect to the resonance frequency. This result suggests that the SiO₂ layer exerts the main influence on the resonance position. This could be explained by the decay length of the electric field, i.e. the distance at which the electric field strength has decreased to $1/e$, which is in the range of 10 – 40 nm for nanoantennas resonant in the IR [34]. Hence, it seems quite reasonable to assume that the nanoantenna on the thick oxide layer behaves like a nanoantenna on quartz glass. However, the solid green spectrum in Fig. 4.15a is still slightly red-shifted and lowered in intensity, indicating that the silicon substrate at least slightly contributes to the optical response.

Calculating the Normalized Extinction Cross-Section

In order to calculate the value of $\sigma_{\text{ext}}(\tilde{\nu}_{\text{res}})/\sigma_{\text{geo}}$, the influence of the substrate has to be considered. In Eq. (4.4), the factor $(n_{\text{sub}} + 1)/2$ originates from thin film approximations at normal incidence for a three-layer-system (air / thin film / substrate). To correctly account for the situation with the thick oxide layer, one would have to calculate the transmittivity of a four-layer-system (air / thin film / 106nm SiO₂ / Si

4. Individual Nanoantennas Arranged in Arrays

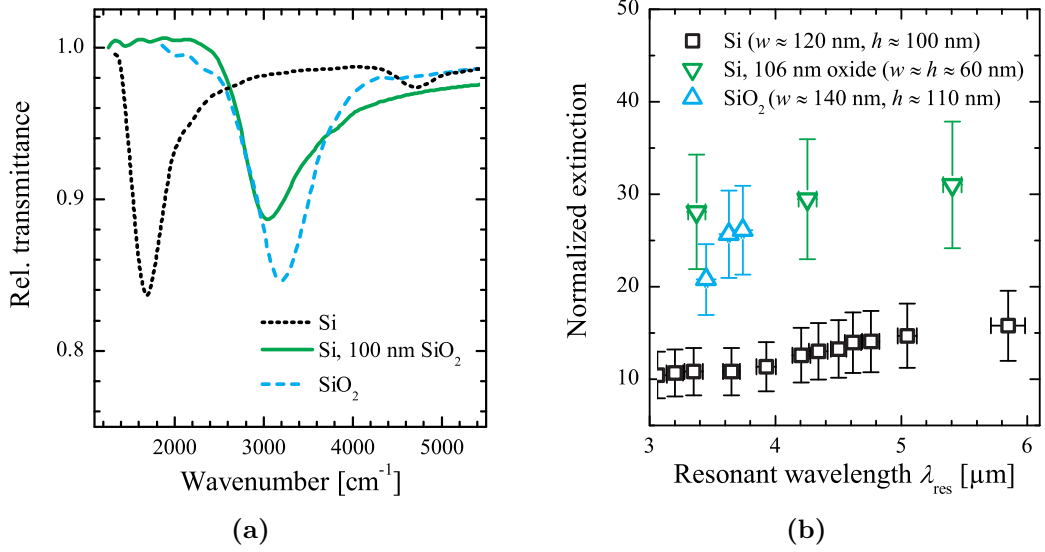


Figure 4.15.: (a) FDTD simulations [102] of single gold nanorods ($L = 900\text{ nm}$, $w = h = 60\text{ nm}$) and (b) normalized extinction S_{norm} [Eq. (4.6)] versus λ_{res} for lithographically prepared nanorod arrays on different substrates.

substrate), which is a rather complicated derivation. As a first approximation, the normalized extinction,

$$S_{\text{norm}}(\tilde{\nu}_{\text{res}}) = \frac{A_0}{N} [1 - T_{\text{rel}}(\tilde{\nu}_{\text{res}})] \cdot \frac{1}{Lw}, \quad (4.6)$$

is shown in Fig. 4.15b versus λ_{res} for lithographic nanorod arrays on Si, 106 nm SiO₂/Si, and quartz glass (SiO₂). Equation (4.6) is essentially the same as Eq. (4.4) but without the substrate factor $(n_{\text{sub}} + 1)/2$. Obviously, the values of the arrays on the thermally oxidized silicon are in the same range as those of arrays on quartz glass. Note that the rod cross-sections ($w \cdot h$) differ for the arrays on 106 nm SiO₂/Si and quartz glass. Consequently, the increased lightning rod effect (Sec. 4.1.1) might explain the higher values of the rods on 106 nm SiO₂/Si. Nevertheless, the extinction of the rods on 106 nm SiO₂/Si is apparently more governed by the refractive index of glass than that of silicon. As stated above, this might be due to the smaller decay length of the electric field compared to the oxide thickness. As a simple approximation, $n_{\text{sub}} = n_{\text{SiO}_2} = 1.45$ will be used in the following for the arrays on 106 nm SiO₂/Si to calculate values of $\sigma_{\text{ext}}(\tilde{\nu}_{\text{res}})/\sigma_{\text{geo}}$.

4.2. Nanorod Arrays on Thermally Oxidized Silicon

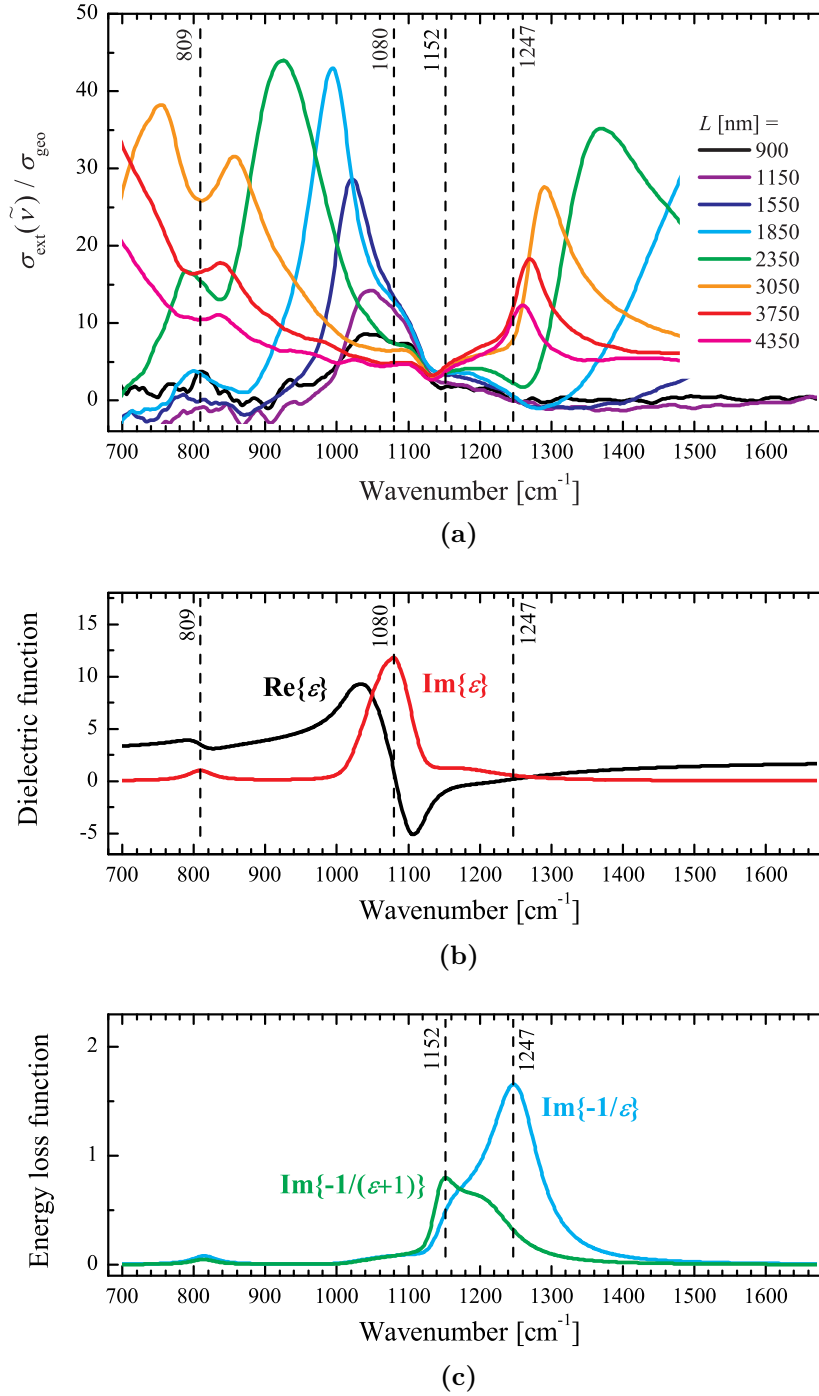


Figure 4.16.: (a) Calculated values of $\sigma_{\text{ext}}(\tilde{\nu}_{\text{res}}) / \sigma_{\text{geo}}$ ($n_s = 1.45$) for different nanorod arrays ($w = h = 60 \text{ nm}$, $d_x = d_y = 10 \mu\text{m}$) on 106 nm SiO_2/Si . (b) Real ($\text{Re}\{\epsilon\}$) and imaginary part ($\text{Im}\{\epsilon\}$) and (c) energy loss functions $\text{Im}\{-\frac{1}{\epsilon}\}$ and $\text{Im}\{-\frac{1}{\epsilon+1}\}$ of the dielectric function of the 106 nm thick SiO_2 film, which is derived from relative transmittance measurements (Fig. 3.7) using the software package SCOUT [46].

Cloaking the Antenna Resonance

In Fig. 4.16a calculated values of $\sigma_{\text{ext}}(\tilde{\nu}_{\text{res}})/\sigma_{\text{geo}}$ for all investigated rod lengths in the range of the oxide feature are plotted. Interestingly, the extinction drastically drops down in the range between 1100cm^{-1} and 1200cm^{-1} . A look at the dielectric function ϵ of the thermally grown oxide in Fig. 4.16b reveals that the real part of ϵ is negative between $\tilde{\nu}_{\text{TO}} = 1080\text{cm}^{-1}$ and $\tilde{\nu}_{\text{LO}} = 1247\text{cm}^{-1}$, leading to high reflectivity in this *reststrahlen* band (see Sec. 2.6). Nevertheless, the relative transmittance measurements of Fig. 3.7 show that approximately 65% of the IR light passes through the 106 nm thick oxide layer. Hence, the negative real part of ϵ alone cannot account for the low extinction in this frequency band. More likely, the excitation of the SPP in the thick oxide layer, similar to the one observed for the natural oxide covered silicon, leads to the nearly vanishing extinction. The possible frequency range of the Fuchs-Kliwer phonon-polariton at the air / SiO_2 interface is between $\tilde{\nu}_{\text{SiO}_2\text{-air}}^{\text{SPP}}$ and $\tilde{\nu}_{\text{LO}}$ (Sec. 2.6.1). While $\tilde{\nu}_{\text{SiO}_2\text{-air}}^{\text{SPP}}$ is the frequency where $\text{Im}\left\{-\frac{1}{\epsilon+1}\right\}$ becomes maximal, $\tilde{\nu}_{\text{LO}}$ is given by the maximum of $\text{Im}\left\{-\frac{1}{\epsilon}\right\}$ [172]. These values can be derived from Fig. 4.16c and are also indicated in Fig. 4.16a. And in fact, it seems that the extinction is minimal in this frequency range. Obviously, the excitation of the SPP somehow hides the antenna resonance in a certain frequency band, an interesting effect which might be exploited for cloaking applications. However, the detailed analysis and understanding of this effect goes beyond the scope of this thesis. As a last point it should be mentioned that another Fano-shaped feature appears in the relative transmittance spectrum (Fig. 4.16a) at 809cm^{-1} , which is the position of the symmetric Si-O stretching vibration (see Figs. 4.16b and 3.7).

4.3. Influence of the Supporting Substrate

In this section, the optical properties of non-interacting nanorod arrays on different substrates are shown. Besides the spectral resonance position (Sec. 4.3.1), the quality factor (Sec. 4.3.2), and normalized extinction cross-section (Sec. 4.3.3), the effect of the substrate on the appearance of dark modes is discussed in Sec. 4.3.4.

4.3.1. Spectral Resonance Position

In Fig. 4.17, the resonant wavelength λ_{res} is plotted versus the antenna length L for nanorod arrays on different substrates. Concerning the nanorod arrays on 106 nm SiO_2 / Si, only antenna resonances which are spectrally separated from the strong

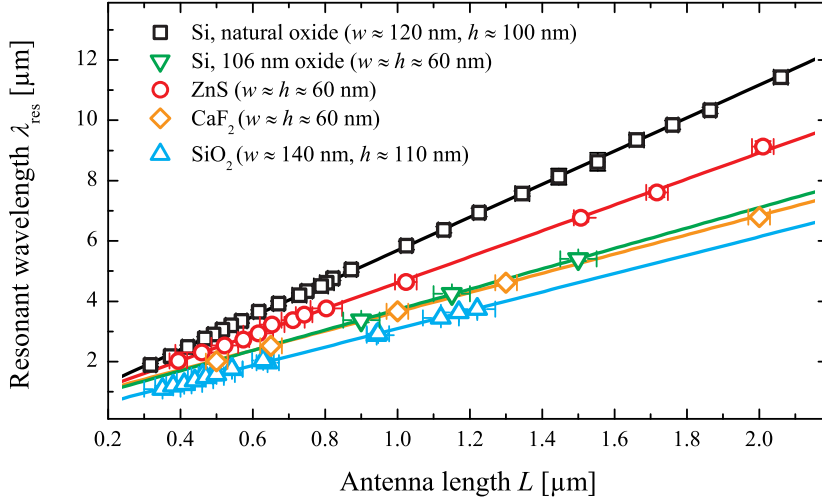


Figure 4.17.: Relation $\lambda_{\text{res}}(L)$ for different non-interacting nanorod arrays. It is $d_x = d_y = 5\mu\text{m}$ for the arrays on Si, ZnS, and SiO₂; $d_x = d_y = 10\mu\text{m}$ for the ones on 106 nm SiO₂ / Si and $d_x = 5\mu\text{m}$, $d_y = 8\mu\text{m}$ for the ones on CaF₂. The solid straight lines are linear fits to the experimental data according to $\lambda_{\text{res}}(L) = a + b \cdot L$, see Tab. 4.2a.

oxide feature have been evaluated. In addition to the measurements, linear fits to the experimental data using the relation $\lambda_{\text{res}}(L) = a + b \cdot L$ are shown. The fitting results of the coefficients a and b as well as the values of the squared correlation coefficient² R^2 are summarized in Tab. 4.2a. The values of R^2 are close to 1.0, indicating nearly perfect linear behavior between λ_{res} and L in the spectral range between $\lambda = 1.4\mu\text{m}$ and $\lambda = 12\mu\text{m}$.

Obviously, the slope b varies, featuring higher values for substrates with higher refractive index (see Tab. 4.2a). This red-shift of the resonance is because induced screening charges in the substrate reduce the intra-rod restoring force (see Sec. 2.4.1). However, the data of the rods on CaF₂ does not fit into this scheme: the rods exhibit longer λ_{res} compared to the rods on SiO₂ even though the refractive index of CaF₂ is slightly smaller (see Tab. 4.2a). This can be explained by the different cross-sections ($w \cdot h$) of the rods on CaF₂, leading to an increased lightning rod effect which red-shifts the resonance (see 2.4.1).

The rods on thermally oxidized silicon feature nearly the same λ_{res} compared to the ones on CaF₂ and the cross-sections ($w \cdot h$) are similar for both arrays ($60 \times 60\text{nm}^2$), indicating that the supporting substrate influences the resonance in the same way.

²The quantity R^2 provides information about the goodness of a fit [199]. In regression, it is a statistical measure of how well the regression line describes the experimental data. A value of $R^2 = 1.0$ indicates that the fit perfectly reproduces the data.

4. Individual Nanoantennas Arranged in Arrays

Substrate	refr. index	a [μm]	b	corr. R^2
Si, natural oxide	3.42	0.20 ± 0.02	5.49 ± 0.02	0.99954
ZnS	2.2	0.35 ± 0.04	4.24 ± 0.05	0.99799
Si, 106 nm oxide	-	0.34 ± 0.08	3.38 ± 0.07	0.99924
SiO ₂	1.45	0.04 ± 0.02	3.05 ± 0.03	0.99886
CaF ₂	1.41	0.46 ± 0.04	3.19 ± 0.03	0.99961

(a)

Substrate	R_{eff} [nm]	ϵ_s	ϵ_{sub}	portion p of ϵ_{sub}
Si, natural oxide	62	6.0 ± 0.1	11.69	47%
Si, 106 nm oxide	34	2.38 ± 0.02	?	-
ZnS	34	4.1 ± 0.1 [34]	4.84	80%
CaF ₂	34	2.23 ± 0.03	1.99	> 100 %
SiO ₂	70	1.57 ± 0.08 [109]	2.1	52%

(b)

Table 4.2.: Results of (a) linear fits $\lambda_{\text{res}}(L) = a + b \cdot L$ and (b) NOVOTNY fits to the data of Fig. 4.17. The effective radius R_{eff} in (b) was calculated according to $R_{\text{eff}} = \sqrt{w \cdot h / \pi}$ and set as fix input. The contribution p of ϵ_{sub} to ϵ_s is calculated according to $\epsilon_s = (1 - p) \cdot \epsilon_{\text{air}} + p \cdot \epsilon_{\text{sub}}$.

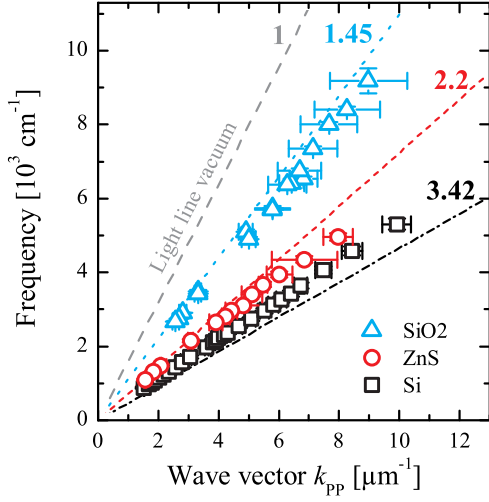


Figure 4.18: Resonance frequency $\tilde{\nu}_{\text{res}}$ versus wave vector $k_{\text{PP}} = \pi/L$ of the standing wave of the fundamental antenna resonance for nanorod arrays on SiO₂, ZnS, and Si. The straight lines represent the light lines in the corresponding media with refractive index as indicated.

This result supports the findings from Sec. 4.2, i.e. that the nanorods on the thick oxide layer almost behave like nanorods on a substrate with refractive index near 1.4 and, thus, like pure glass. Note that the variations between the nanorods on SiO₂ and the ones on 106 nm SiO₂ / Si can be again explained by the different cross-sections ($w \cdot h$).

In addition, the experimental data of Fig. 4.17 have been fitted according to NOVOTNY'S model and the results of the effective dielectric constant ϵ_s are summarized in Tab. 4.2b. Comparing those values with the literature values ϵ_{sub} of the substrates demonstrates that a direct relation [e.g. $\epsilon_s = \frac{1}{2}(\epsilon_{\text{air}} + \epsilon_{\text{sub}})$] between ϵ_s and ϵ_{sub} does not exist. A prediction of $\lambda_{\text{res}}(L)$ with the help of NOVOTNY'S approximation based on the dielectric constant of the substrate is therefore not possible (compare to Sec. 4.1.2). Besides the substrate polarizability, also other factors like crystallinity and surface roughness of the rods or details of the interface layers between gold and substrate might influence the exact resonance position.

At this point, it should be mentioned that instead of the relation between λ_{res} and L , one can consider the dispersion relation $\tilde{\nu}_{\text{res}}(k_{\text{PP}})$ between the measured resonance frequency $\tilde{\nu}_{\text{res}}$ and wave vector of the plasmon-polariton wave $k_{\text{PP}} = \frac{\pi}{L}$ for the standing wave of the fundamental antenna resonance. Figure 4.18 shows this relation for the nanorod arrays on SiO₂, ZnS, and Si. In addition, the light lines [$\tilde{\nu}(k) = k / (2\pi \cdot n_{\text{sub}})$] in vacuum and in the corresponding substrates with refractive index n_{sub} according to Tab. 3.2 are plotted. The data of the nanorod arrays on SiO₂ and ZnS nicely follows the respective light lines for small wave vectors. However, stronger deviations emerge as the wave vector increases. This discrepancy, which becomes even more pronounced for larger wave vectors ($k > 15 \mu\text{m}^{-1}$, see [73]),

4. Individual Nanoantennas Arranged in Arrays

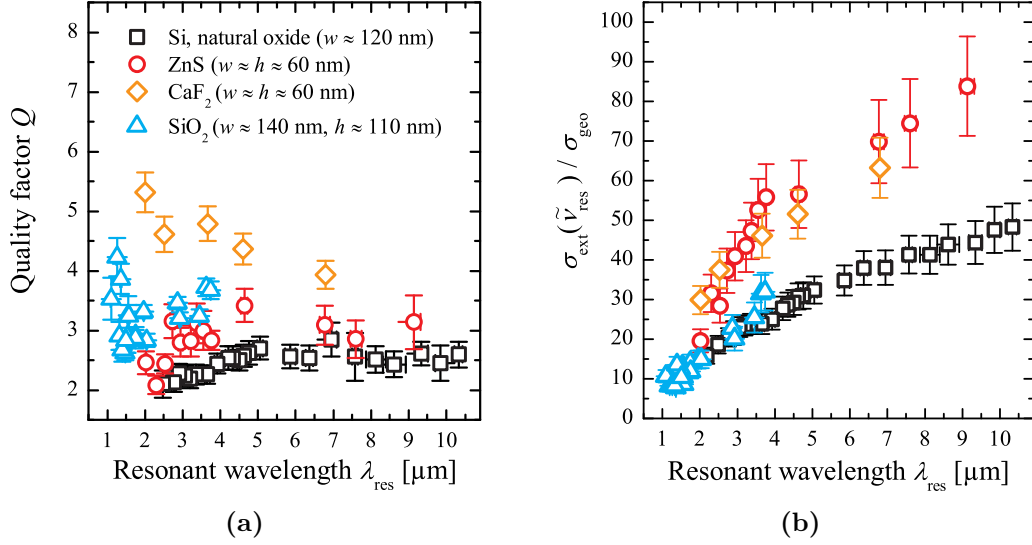


Figure 4.19.: (a) Quality factor Q and (b) normalized extinction cross-section $\sigma_{\text{ext}}(\tilde{\nu}_{\text{res}}) / \sigma_{\text{geo}}$ versus resonant wavelength λ_{res} of non-interacting nanorod arrays on different substrates. The legend in (a) also applies for the symbols in (b).

represents the plasmonic character of the antenna resonances (compare to Sec. 2.3). Concerning the nanorods on natural oxide covered silicon, the higher values of $\tilde{\nu}_{\text{res}}$ compared to those of the light line in (pure) silicon indicate that the thin natural oxide layer slightly influences the resonance position. Nevertheless, it can be concluded from Fig. 4.18 that higher n_{sub} leads to a lower plasmon-polariton group velocity, which is equivalent to the red-shift of the resonance depicted in Fig. 4.17.

4.3.2. Quality Factor

Figure 4.19a shows the values of Q for different nanorod arrays plotted versus the spectral resonance position. It is obvious, that the substrates with high refractive index, silicon and zinc sulphide, feature lower quality factors compared to the low refractive index substrates glass and calcium fluoride. This behavior can be explained by induced screening charges in the substrate, leading to a more damped electron oscillation in the nanorod.

4.3.3. Extinction Cross-Section

In Fig. 4.19b, values of $\sigma_{\text{ext}}(\tilde{\nu}_{\text{res}}) / \sigma_{\text{geo}}$ are plotted in dependence of λ_{res} . For all nanorod arrays, a monotonic increase of $\sigma_{\text{ext}}(\tilde{\nu}_{\text{res}}) / \sigma_{\text{geo}}$ with antenna length is

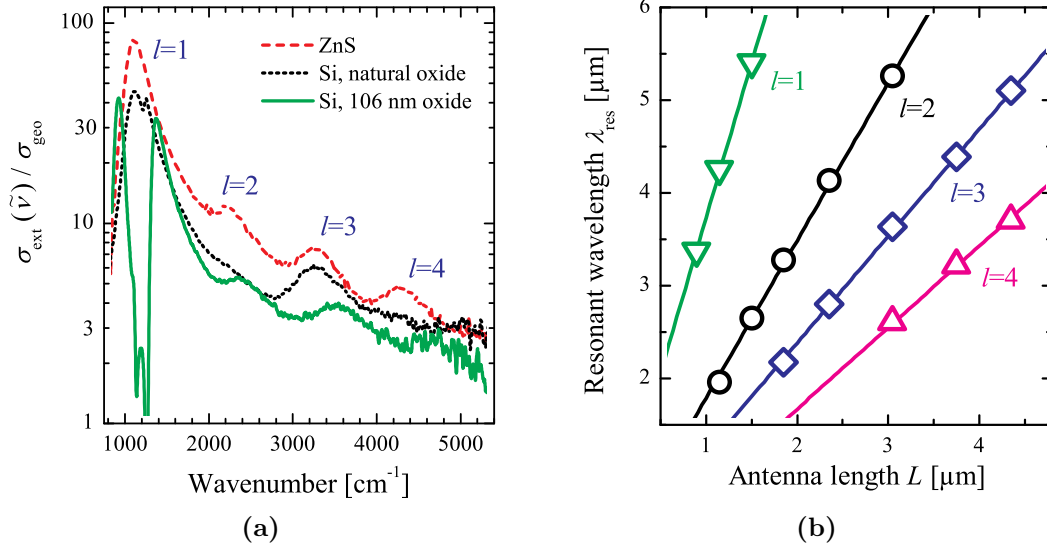


Figure 4.20.: (a) Normalized extinction cross-section per nanorod for non-interacting nanorod arrays on different substrates. (b) λ_{res} versus L for different resonance orders of nanorod arrays on thermally oxidized silicon. The solid straight lines represent linear fits to the experimental data using the relation $\lambda_{\text{res},l}(L) = a_l + b_l \cdot L$.

observed due to increasing lightning rod effect. The influence of the substrate on the signal strength cannot be directly observed in Fig. 4.19b due to the factor $(n_{\text{sub}} + 1)/2$ in Eq. (4.4). For this reason, the nanorods on silicon and glass feature similar values of $\sigma_{\text{ext}}(\tilde{\nu}_{\text{res}})/\sigma_{\text{geo}}$, even though the signal strength on silicon is much smaller due to increased damping caused by screening charges. Consequently, the measured signal will always be higher for nanorods on a substrate with low refractive index. The difference between the rods on CaF_2 and ZnS, which both feature significantly higher values of $\sigma_{\text{ext}}(\tilde{\nu}_{\text{res}})/\sigma_{\text{geo}}$, on the one hand, and the ones on SiO_2 and Si, on the other hand, can be explained by the increased lightning rod effect due to the smaller cross-sectional areas (see Sec. 4.1.2).

4.3.4. Higher Order Modes

The solid green spectrum in Fig. 4.20a shows an antenna resonance of a nanorod array on thermally oxidized silicon. Besides the fundamental resonance ($l = 1$), which is overlaid by a huge phononic excitation at around 1200 cm^{-1} (see Sec. 4.2), additional higher order modes ($l > 1$) appear (see Fig. 2.7a). Figure 4.20b shows the dispersion relations of these modes; comparison of the slopes of the linear fits (see Tab. 4.3) reveals that the assignment of the modes is correct, as previously found in [70].

4. Individual Nanoantennas Arranged in Arrays

	b_2/b_1	b_3/b_1	b_4/b_1
Linear fit	0.51 ± 0.01	0.34 ± 0.01	0.26 ± 0.01
$1/l$	$1/2$	$1/3$	$1/4$

Table 4.3.: The experimental data in Fig. 4.20b was fitted for the different modes l using the relations $\lambda_{\text{res},l}(L) = a_l + b_l \cdot L$. The table shows the ratio between the slopes of the higher order modes and the fundamental mode (as performed in [70]).

The excitation of even order modes at normal incidence is forbidden for symmetry reasons. In contrast, if the symmetry is broken (defects or oblique incidence), these dark modes can be excited (see Sec. 2.4.3). Now it is striking that the even order modes are usually very weak or even not observable for the nanorods on silicon (see dotted black curve in Fig. 4.20a). One could argue that the lithographic preparation on silicon features less defects of the rods, leading to decreased intensity of the even order modes. In addition, it is true that ZnS substrates feature a very high surface roughness, leading to preparation imperfections [70] and explaining the appearance of the even order modes for the dashed red spectrum in Fig. 4.20a. However, the lithographic preparation of the nanorods on silicon and thermally oxidized silicon was identical (same initial substrates were used). In addition, the surface roughness is not expected to change during the oxidation process [122]. Hence, it is surprising that the even order modes appear for the nanorods on the thick oxide layer, while they are absent for the ones on the natural oxide covered silicon.

One possible explanation could be, that the refractive index of the substrate plays an important role. The IR light is focused onto the substrate by the Schwarzschild objective in a geometry that is best described with a “thick cone-shaped shell”. The maximum and minimum angles of incidence are 10.3° and 30° , respectively (see Fig. A.6). Figure 4.21 shows side views on two different substrates and the corresponding light rays being incident 30° from the surface normal. Due to the high refractive index of silicon, these rays are refracted towards the surface normal (Fig. 4.21a), while the rays in silicon dioxide are only weakly deflected (Fig. 4.21b). If the substrate is perfectly aligned perpendicular to the axis of the incident light cone, all components of the electric field vector which are not parallel to the surface cancel out, effectively leading to normal light incidence. However, a slight tilt of the sample results in oblique incidence, activating dark modes. And due to the different light refraction in substrates with low and high refractive index, this effect will be more pronounced for substrates featuring low refractive indices, like CaF_2 or

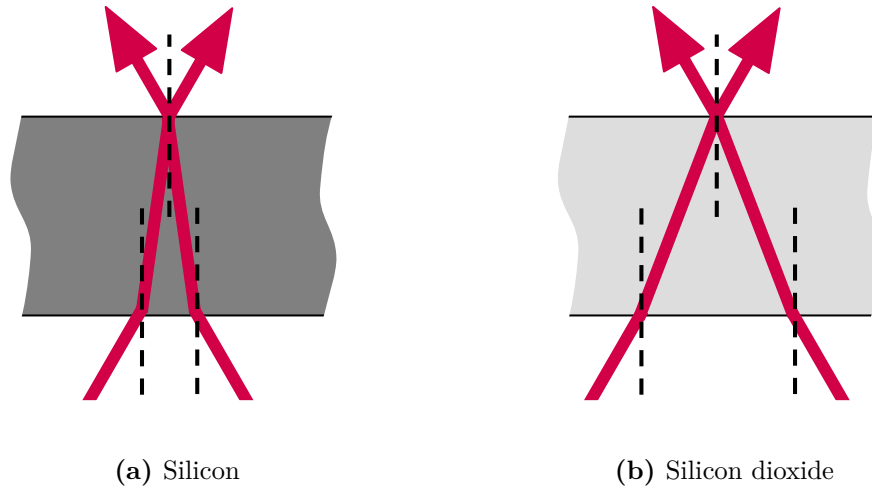


Figure 4.21.: Light refraction at the interfaces of the substrate. The IR light is coming from beside the substrate under an maximum angle of incidence of 30° (compare to Fig. A.6). The angles in the substrate are (a) 8° for silicon and (b) 21° for silicon dioxide.

glass. Supportingly, strong signals of the $l = 2$ modes were measured by scattering near-field optical microscopy for nanorods on CaF_2 for a substrate tilt of only 2° from the horizontal [200].

4.3.5. Summary

The substrate polarizability differently influences the optical properties of nanorod arrays. A high refractive index leads to a red-shift and broadening of the resonance which comes along with a decreased signal intensity. All these effects can be explained by induced screening charges in the substrate. In addition, it was found that thinner rods feature higher values of the normalized extinction cross-section $\sigma_{\text{ext}}(\tilde{\nu}_{\text{res}})/\sigma_{\text{geo}}$ in accordance with FDTD simulations (see Fig. 4.4a); this effect is attributed to the increased lightning rod effect of thinner rods. Concerning multipolar antenna resonances, it was concluded that a higher refractive index leads to the suppression of dark modes. Finally, it was found that nanorods on a relatively thick oxide layer (106nm) show similar behavior concerning $\lambda_{\text{res}}(L)$ compared to nanorods on pure glass.

4.4. Important Findings

- The value of $\sigma_{\text{ext}}(\tilde{\nu})/\sigma_{\text{geo}}$ indicates the ability of the nanorod to confine light and to enhance electromagnetic fields. However, it can be exclusively used to compare non-interacting nanoantennas.
- The effective medium model fails to predict the resonance position of a nanoantenna placed on a substrate. Hence, the fitting result of the effective dielectric constant ϵ_s obtained from NOVOTNY's model cannot be related to the actual substrate polarizability.
- The relation between λ_{res} and L depends on the preparation process and cannot be used to compare nanorod arrays of different samples.
- Nanorods on thermally oxidized silicon ($d_{\text{SiO}_2} \approx 100\text{ nm}$) behave similar to nanorods on pure quartz glass as long as the plasmonic resonance is spectrally separated from the surface phonon-polariton feature.
- For nanorods placed on a thick SiO₂ layer on silicon ($\approx 100\text{ nm}$), it was found that almost the same amount of light can pass by the antenna (on the substrate) compared to the bare substrate in the small frequency range of the surface phonon-polariton. This means that the antenna resonance is cloaked by the excitation of the surface phonon-polariton.
- Dark modes are more pronounced for substrates with lower refractive index which is probably due to slightly oblique incidence.

5. Interaction Effects in Nanoantenna Arrays

In this chapter, the IR optical properties of nanorod arrays on silicon (natural oxide) with *varying* separation distances d_x and d_y in longitudinal (x -) and transverse (y -)direction, respectively (see Fig. 5.1), are discussed. Note that major parts of the analysis are adopted from WEBER *et al.* [77]. The notations longitudinal and transverse are chosen with respect to the direction parallel to the long rod axis. Hence, Sec. 5.1 (“Transverse Interaction”) deals with nanorod arrays in which d_y is reduced from $d_y = 5\mu\text{m}$ to $d_y = 0.1\mu\text{m}$. Accordingly, Sec. 5.2 (“Longitudinal Interaction”) analyzes the effects of different distances d_x . In both cases, the respective other separation distance is constantly kept to $5\mu\text{m}$ to investigate possible interaction effects in both directions independently. Moreover, nanorod arrays with $d_x = d_y = 5\mu\text{m}$ (on the same sample) are used as reference since the rods can be considered as non-interacting (Chap. 4). Besides that, arrays with reduced separation distances in both directions are investigated in Sec. 5.3, which is therefore denoted as “Mixed Interaction”. After the conclusion (Sec. 5.4), the important findings are summarized in Sec. 5.5.

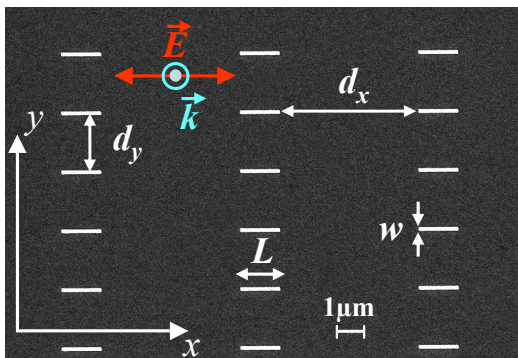


Figure 5.1: SEM image of a part of a typical gold nanoantenna array on silicon [77]. Besides the separation distances d_x and d_y , the rod length L and width w , also the orientation of the electric field vector \vec{E} (parallel to long rod axis) and the incoming wave vector \vec{k} (perpendicular to substrate plane) are shown.

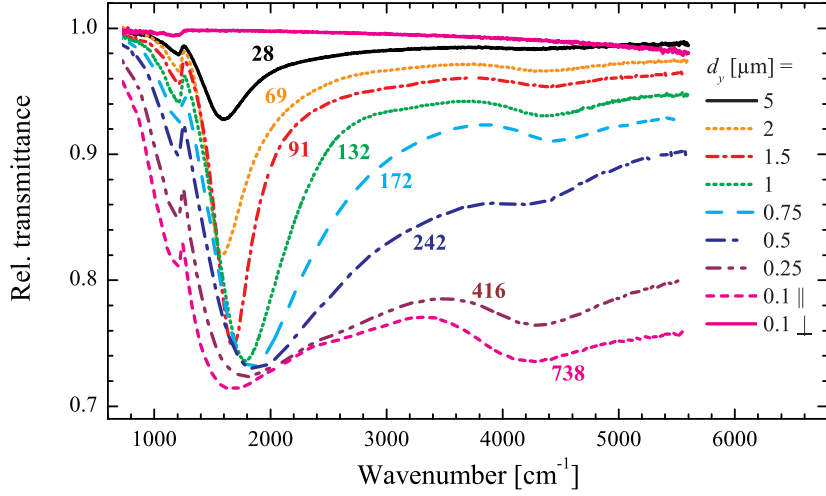


Figure 5.2.: Relative transmittance spectra of nanorod arrays featuring different d_y ($L \approx 1030\text{ nm}$, $w \approx 90\text{ nm}$, $h \approx 100\text{ nm}$, $d_x = 5\text{ }\mu\text{m}$). In all spectra, the polarization of the electric field is parallel to the long rod axis except for the solid pink curve, showing a spectrum in perpendicular (\perp) polarization. The numbers give the approximate quantity of rods contributing to the signals. The small feature at around 1230 cm^{-1} is due to the SPP in the natural SiO_2 layer covering the Si substrate (see Sec. 3.5.2).

5.1. Transverse Interaction

Figure 5.2 shows relative transmittance spectra of nanorod arrays with rods of the same length but different transverse separation distances d_y . Obviously, a decrease of d_y results in a blue-shift of the fundamental mode accompanied by extremely broadening. Consequently, the broad resonances of various orders overlap and therefore couple by dipolar interaction. This coupling, in principle, should lead to new kinds of mixed excitations with new positions for extinction maxima, possibly explaining the red-shift of the fundamental and third order resonance for $d_y = 0.1\text{ }\mu\text{m}$ compared to $d_y = 0.5\text{ }\mu\text{m}$. Moreover, a spectrum with perpendicular polarization is shown for the shortest separation of $d_y = 0.1\text{ }\mu\text{m}$. A slight decrease of the transmittance towards higher frequencies is visible, which can be interpreted as the tail of the transverse resonance, being located in the visible range.

Since different numbers of rods contribute to each spectrum, σ_{ext} per nanorod (Fig. 5.3a) is better suited to analyze the evolution of the far-field intensity¹. Interestingly, the extinction spectrum of the array with $d_y = 1.5\text{ }\mu\text{m}$ is narrower and features higher maximum extinction than the reference array ($d_y = 5\text{ }\mu\text{m}$). Since dominant

¹ σ_{ext} is plotted to allow a better comparison with the simulations of Figs. 5.3b and 5.3c since the rod width is different in experiment ($w \approx 90\text{ nm}$) and simulation ($w = 120\text{ nm}$).

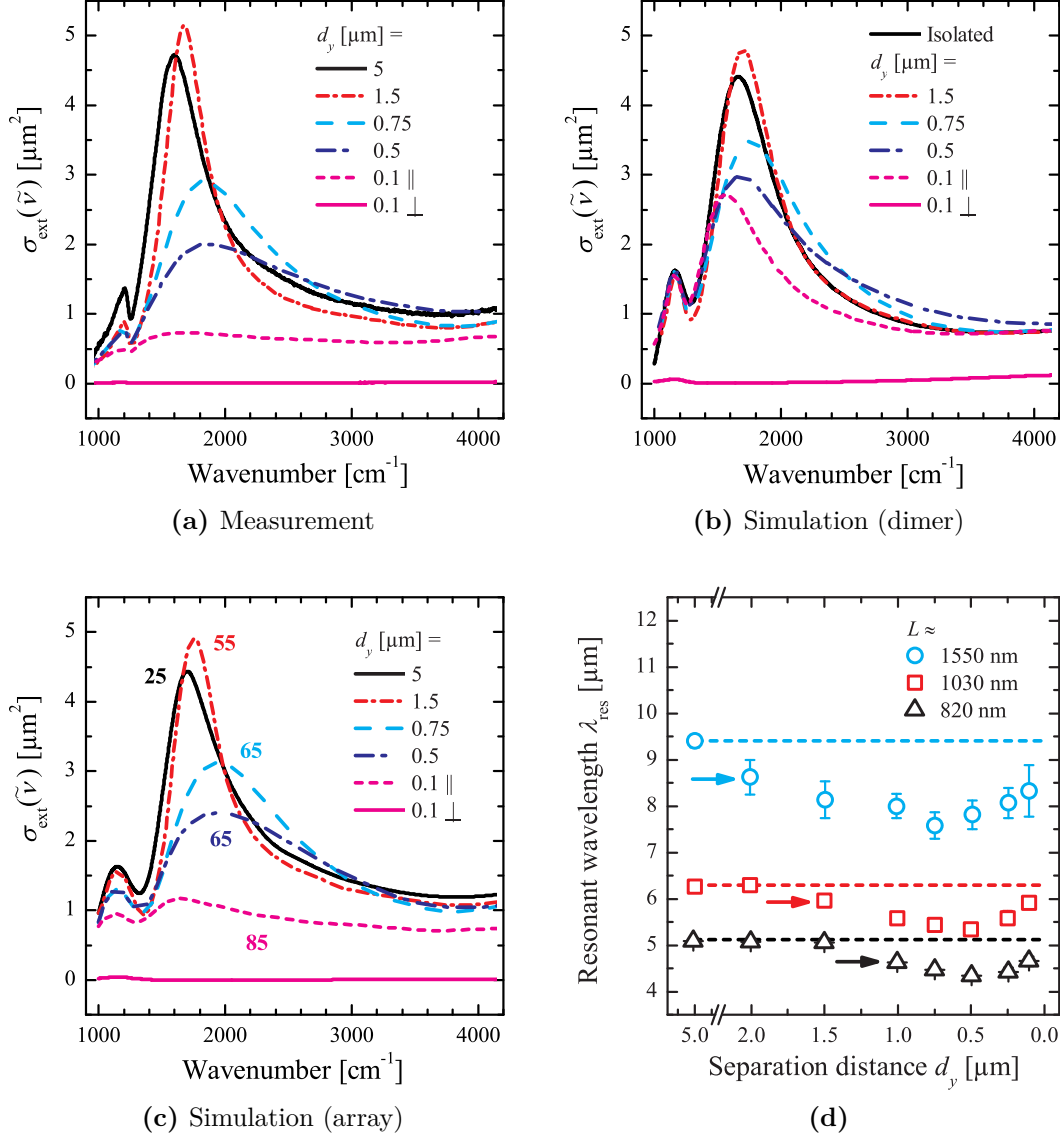


Figure 5.3.: (a) Extinction cross-section σ_{ext} per nanorod of selected nanorod arrays of Fig. 5.2. Simulated far-field extinction per nanorod of (b) an isolated nanorod and nanorod dimers with indicated separation distances d_y and (c) of nanorod arrays consisting of a certain quantity of rods as given by the numbers. The rod dimensions in the simulations of (b) and (c) are $L = 1030$ nm, $w = 120$ nm, and $h = 100$ nm. (d) Resonant wavelength λ_{res} versus separation distance d_y for three different nanorod arrays ($d_x = 5 \mu\text{m}$). The arrows mark the onset of the blue-shift of λ_{res} compared to the non-interacting reference array with $d_y = 5 \mu\text{m}$.

5. Interaction Effects in Nanoantenna Arrays

near-field dipolar coupling can be excluded at a distance of $1.5\mu\text{m}$, this effect is attributed to radiative dipolar coupling (see Sec. 2.5). Furthermore, the spectra broaden very much as d_y decreases and σ_{ext} becomes almost a flat “background” in case of $d_y = 0.1\mu\text{m}$. This decrease of σ_{ext} , which is still clearly above the geometric cross-section $\sigma_{\text{geo}} = L \cdot w \approx 0.1\mu\text{m}^2$, might be related to near-field coupling across the gap.

5.1.1. Comparison with FDTD Simulations

In addition to the IR spectroscopic measurements, far-field simulations (see Sec. 3.6) were performed, which are shown in Fig. 5.3b for an isolated nanorod (solid black curve) and nanorod dimers with different d_y . For large d_y , the simple dimer model is in good agreement with the experimental data of Fig. 5.3a. However, for small separations below $0.5\mu\text{m}$, the decrease of σ_{ext} is not as dramatic as for the nanorod arrays. Even for $d_y = 0.1\mu\text{m}$, the antenna resonance is clearly visible at around 1600cm^{-1} , whereas only a broad background at $\sigma_{\text{ext}} \approx 0.5\mu\text{m}^2$ is observed in the experiment. These differences demonstrate the effect of missing neighbors in the simulation, where mainly the near-field in the gap between the two rods is modified by interaction, while in the array, modified near-fields on both sides of the rods exist. To account for that, simulations with an increasing number of interacting rods were carried out (Fig. 5.3c) and nearly perfect agreement with the experimental results is obtained. Nevertheless, deviations between measurement and calculation occur concerning the shape of the surface phonon-polariton signal, which can be attributed to the ideal SiO_2 layer in the simulation (compare to Sec. 4.1.2).

5.1.2. Spectral Resonance Position

Figure 5.3d shows the resonant wavelength λ_{res} versus the separation distance d_y for three different rod lengths L . In all three cases, a blue-shift of the resonance is observed with decreasing d_y ; however, the onset of this spectral change occurs at different d_y as indicated by the arrows. Consequently, d_y is not the sole parameter which determines the strength of the dipolar coupling. Moreover, because of the substrate polarizability, the wavelength in the substrate ($\lambda_{\text{res}}/n_{\text{Si}}$) and its

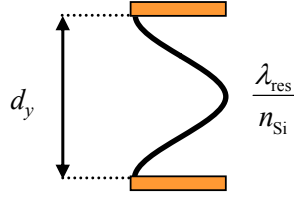


Figure 5.4: Constructive interference condition in transverse direction. At $\lambda_{\text{res}}/n_{\text{Si}} = d_y$, the emitted electromagnetic field of the lower rod at the position of the upper rod is *in phase* with the electron oscillation of the upper rod (and vice versa).

relation to d_y is the crucial quantity when interaction between plasmonic particles is considered [32, 86, 92]. For this reason, the *relative shift* of the resonance position,

$$\frac{\Delta\lambda_{\text{res}}}{\lambda_{\text{res}}} = \frac{\lambda_{\text{res}}(L, d_y)}{\lambda_{\text{res}}(L, d_y = 5\ \mu\text{m})} - 1, \quad (5.1)$$

is plotted versus the ratio $\lambda_{\text{res}}/(n_{\text{Si}}d_y)$ in Fig. 5.5a. The definition of Eq. (5.1) means that λ_{res} of a certain array with rods of length L and separation distance d_y is normalized to the corresponding reference array with $d_y = 5\ \mu\text{m}$. Hence, any positive values of $\Delta\lambda_{\text{res}}/\lambda_{\text{res}}$ indicate a red-shift of the resonance while negative values accordingly represent a blue-shift. Moreover, Fig. 5.4 illustrates the relation $\lambda_{\text{res}}/(n_{\text{Si}}d_y) = 1$, which can be considered as constructive interference condition in transverse direction. Here, the emitted electromagnetic fields of adjacent rods are in phase with the electronic oscillation inside the respective other rods.

First, it is remarkable that all data points more or less lie on one curve even though the data originates from two samples with different rod width and deviating relations $\lambda_{\text{res}}(L)$ of the reference arrays (see to Sec. 4.1.3). For this reason, reference arrays have to be prepared *on the same substrate* to be sure that any optical changes are really due to interaction. Nevertheless, one can conclude that the *relative changes* do not depend on the preparation process or rod width.

Furthermore, the arrays with $\lambda_{\text{res}}/(n_{\text{Si}}d_y) < 1$ show no significant difference of λ_{res} compared to the reference arrays, indicating no measurable far-field interaction for these separation distances. In contrast, beginning from $\lambda_{\text{res}}/(n_{\text{Si}}d_y) \approx 1$, a blue-shift of the resonance emerges, which is attributed to radiative dipolar coupling. Finally, as discussed in Sec. 5.1.1, the simulation of arrays nearly perfectly reproduces the experimental data, while the dimer simulations show considerable deviations for small separations.

5. Interaction Effects in Nanoantenna Arrays

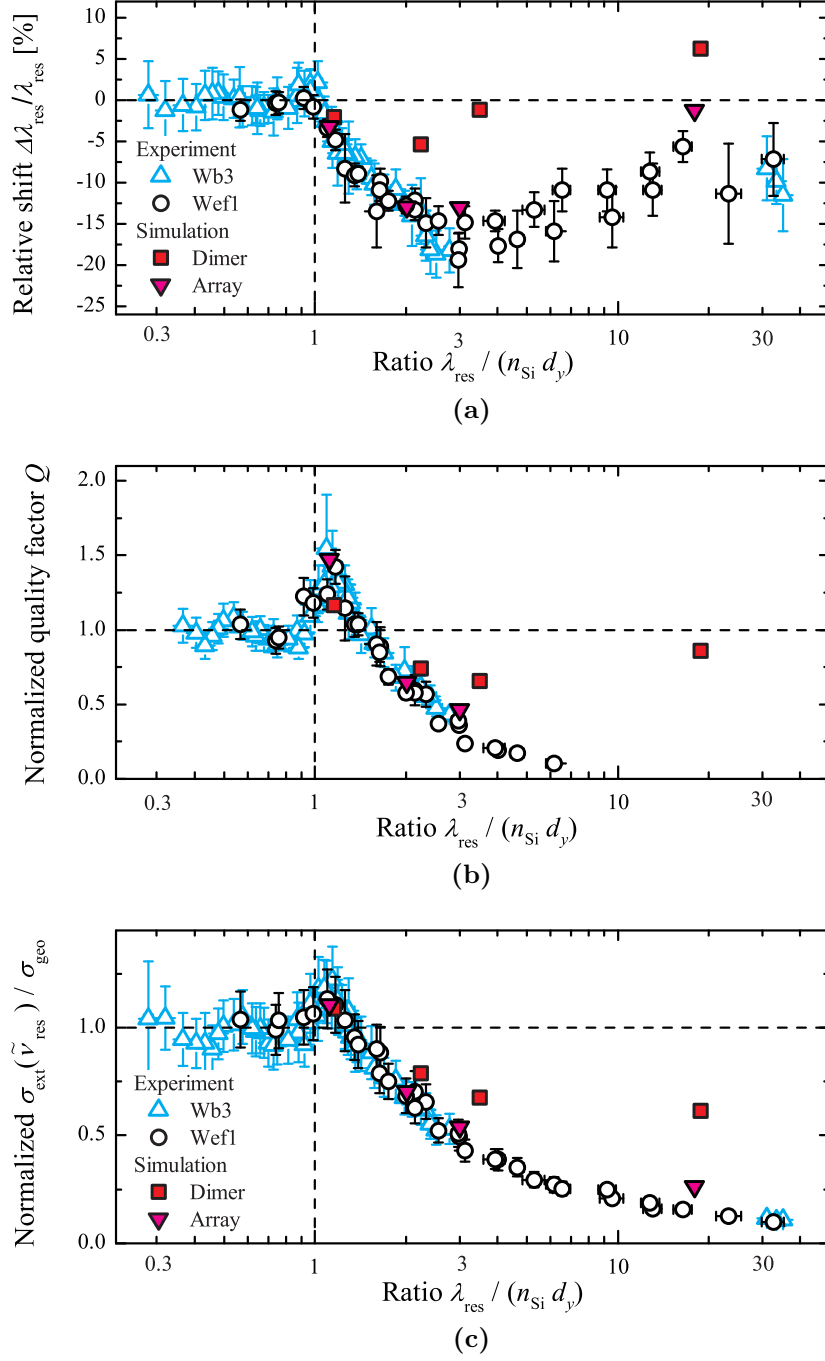


Figure 5.5.: (a) Shift of λ_{res} with respect to the arrays with $d_y = 5 \mu\text{m}$ [see Eq. (5.1)] for the samples Wb3 ($w \approx 120 \text{ nm}$) and Wef1 ($w \approx 90 \text{ nm}$). Solid red squares and pink triangles represent the simulation results of Figs. 5.3b and 5.3c. In addition, the relative changes of (b) Q and (c) $\sigma_{\text{ext}}(\tilde{\nu}_{\text{res}}) / \sigma_{\text{geo}}$ are shown.

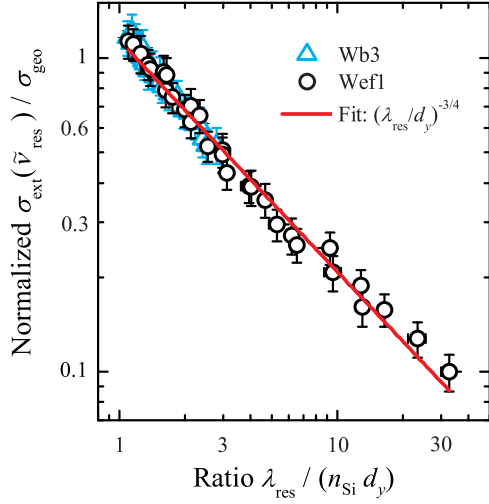


Figure 5.6: Normalized values of $\sigma_{\text{ext}}(\tilde{\nu}_{\text{res}})/\sigma_{\text{geo}}$ versus $\lambda_{\text{res}}/(n_{\text{Si}}d_y)$ with both axis in logarithmic scale. The solid red straight line represents the fit function $y(x) = a \cdot x^b$ with the fitting results $a = 1.14 \pm 0.03$ and $b = -0.74 \pm 0.02$.

5.1.3. Quality Factor and Extinction

Similar plots like the one of Fig. 5.5a were generated for the normalized values of Q and $\sigma_{\text{ext}}(\tilde{\nu}_{\text{res}})/\sigma_{\text{geo}}$ in Figs. 5.5b and 5.5c. For ratios of $\lambda_{\text{res}}/(n_{\text{Si}}d_y) < 1$, the normalized values of Q and $\sigma_{\text{ext}}(\tilde{\nu}_{\text{res}})/\sigma_{\text{geo}}$ are more or less equal to one, indicating the absence of significant far-field interaction. However, weak oscillatory behavior is present, leading to slightly bigger values around $\lambda_{\text{res}}/(n_{\text{Si}}d_y) = 0.5$ (constructive interference condition for $2 \cdot \frac{\lambda_{\text{res}}}{n_{\text{Si}}} = d_y$). Furthermore, a qualitative change in dipolar interaction occurs at $\lambda_{\text{res}}/(n_{\text{Si}}d_y) \approx 1$: After reaching a maximum for $\lambda_{\text{res}}/(n_{\text{Si}}d_y)$ slightly bigger than one (in accordance with [32, 86, 88]), the normalized values of Q and $\sigma_{\text{ext}}(\tilde{\nu}_{\text{res}})/\sigma_{\text{geo}}$ strongly decrease towards larger $\lambda_{\text{res}}/(n_{\text{Si}}d_y)$ ratios.

Finally, the data of Fig. 5.5c is plotted for $\lambda_{\text{res}}/(n_{\text{Si}}d_y) > 1$ in double-logarithmic scale in Fig. 5.6. Since the data shows linear behavior in this representation, a fit using the function $y(x) = a \cdot x^b$ with the two fitting parameters a and b was performed, resulting in the solid red straight line in Fig. 5.6. Based on the fitting result of $b \approx -\frac{3}{4}$, the decrease of $\sigma_{\text{ext}}(\tilde{\nu}_{\text{res}})/\sigma_{\text{geo}}$ seems to be proportional to $(d_y/\lambda_{\text{res}})^{3/4}$.

5.1.4. Investigation of the Near-Field

Now the question arises how the near-field behaves for small separation distances. Note that a lowered far-field intensity does not necessarily implicate a decreased near-field distribution (see Sec. 2.5). Hence, to provide direct experimental evidence of the near-field behavior with transverse coupling, near-field mappings of selected antenna arrays were performed by infrared scattering-type near-field optical microscopy (SNOM [201]).

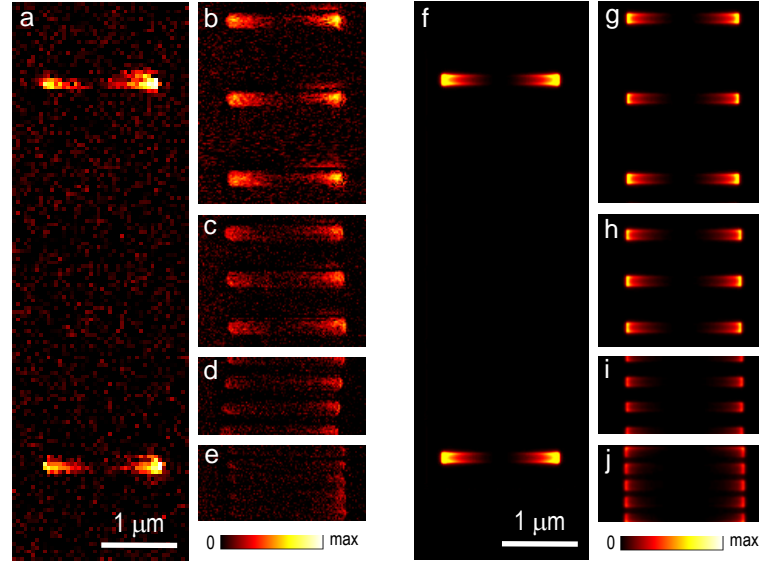


Figure 5.7.: (a-e) Near-field amplitude images [77] obtained by s-SNOM of $1.5\ \mu\text{m}$ long gold nanorods with varying transverse distances d_y : (a) $5\ \mu\text{m}$, (b) $1\ \mu\text{m}$, (c) $0.5\ \mu\text{m}$, (d) $0.25\ \mu\text{m}$, and (e) $0.1\ \mu\text{m}$. All images were recorded at a wavelength of $\lambda = 11.1\ \mu\text{m}$. For comparison, (f) to (j) show simulations of the near-field for the same structures as (a) to (e) [77].

The measurements were performed by P. ALONSO-GONZALEZ and R. HILLENBRAND at the CIC nanoGUNE Consolider in San Sebastian, Spain, using a commercial s-SNOM (Neaspec NeaSNOM [202]). It is based on an AFM where dielectric silicon tips are employed as scattering near-field probes [203, 204]. Both silicon tip and gold nanorod are illuminated by s-polarized IR light (parallel to the long rod axis) under an angle of 60° from the surface normal. For all measurements, a CO_2 laser of fixed wavelength ($\lambda = 11.1\ \mu\text{m}$) was used as illumination source. After being scattered by the tip, the IR light is detected with a pseudo-heterodyne interferometer [205]. By selecting the p-polarized tip-scattered light with a polarizer, the amplitude of the vertical near-field component E_z was recorded [204].

Figures 5.7a to 5.7e show the amplitude of the vertical near-field component E_z for a set of parallel $1.5\ \mu\text{m}$ -long gold nanorods with varying transverse spacing d_y from $5\ \mu\text{m}$ to $0.1\ \mu\text{m}$. To compare the near-field amplitude signals of the different transverse separations, all images were taken with the same tip, the same mapping parameters, and the same laser alignment. In Fig. 5.7a ($d_y = 5\ \mu\text{m}$), a typical dipole pattern is observed: two bright spots at the rod extremities [203], proving enhanced near-field amplitudes. With decreasing d_y , the amplitude signals decrease, nearly vanishing for $d_y = 0.1\ \mu\text{m}$ (Fig. 5.7e).

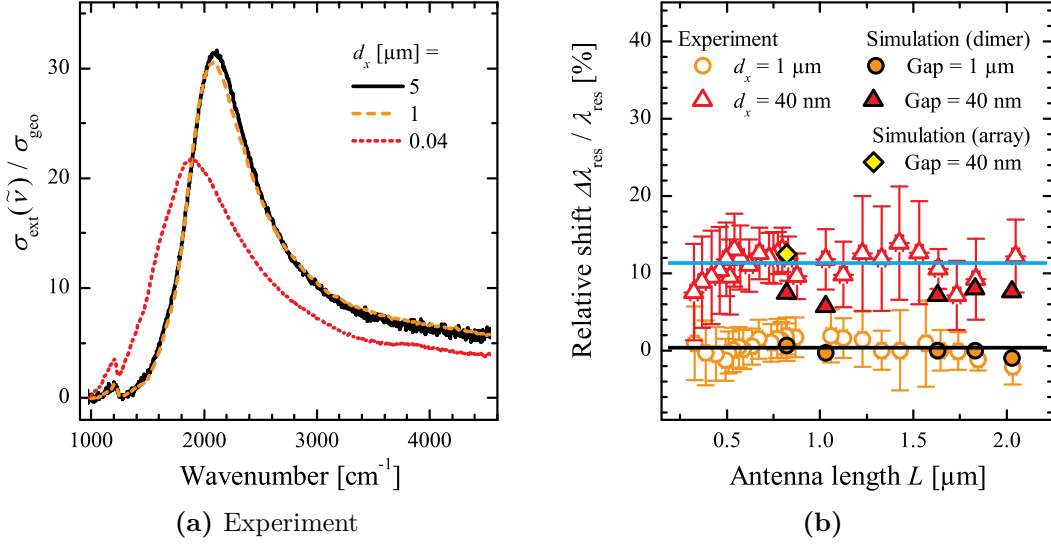


Figure 5.8.: (a) Far-field extinction spectra for nanorod arrays with similar rod dimensions but different longitudinal separation distances d_x ($L \approx 820 \text{ nm}$, $w \approx 120 \text{ nm}$, $h \approx 100 \text{ nm}$, $d_y = 5 \mu\text{m}$). (b) Relative shift $\Delta\lambda_{\text{res}}/\lambda_{\text{res}}$ of nanorod arrays with $d_x = 1 \mu\text{m}$ and $d_x \approx 40 \text{ nm}$ with respect to the reference arrays with $d_x = 5 \mu\text{m}$. The solid blue and black horizontal lines represent constant fits to the experimental data, resulting in $(10.9 \pm 0.3)\%$ for $d_x \approx 40 \text{ nm}$ and $(0.2 \pm 0.2)\%$ for $d_x = 1 \mu\text{m}$. Results from FDTD simulations of a nanorod array as well as nanorod dimers ($w = 120 \text{ nm}$, $h = 100 \text{ nm}$) are added.

In addition to the experimental results, FDTD simulations were carried out for the near-fields around the nanorods (Figs. 5.7f to j). In fact, qualitative good agreement between experiment and simulation is obtained. The two image series lead to the conclusion that the reduced values of $\sigma_{\text{ext}}(\tilde{\nu}_{\text{res}})/\sigma_{\text{geo}}$ observed in far-field spectroscopy (Fig. 5.5c) indicate a near-field decrease due to transverse near-field coupling. This near-field decay is also experimentally visible in Fig. 5.3a, where a weaker signal of the SiO_2 phonon-polariton is observed for $d_y = 0.1 \mu\text{m}$. From these findings and from the strong broadening and weakening of the antenna resonance spectrum, one can conclude that transverse separation distances d_y below $\lambda_{\text{res}}/n_{\text{Si}}$ are not beneficial for any application that exploits enhanced near-fields (e.g. NAIRS).

5.2. Longitudinal Interaction

The present study is not as systematic as the one of Sec. 5.1 concerning the variation of the separation distance. Only two different separation distances d_x ($1 \mu\text{m}$ and 40 nm) were prepared on sample Wb3 besides the reference distance of $d_x = 5 \mu\text{m}$.

5. Interaction Effects in Nanoantenna Arrays

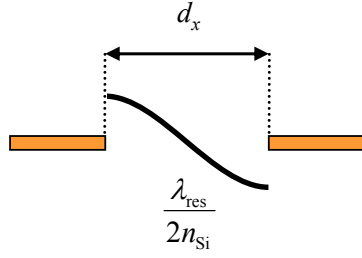


Figure 5.9: Constructive interference condition in longitudinal direction. At $\lambda_{\text{res}}/2n_{\text{Si}} = d_x$, the emitted electromagnetic fields are *in phase* with the intra-rod electron oscillations.

Figure 5.8a shows selected extinction spectra of arrays with similar rod lengths ($L \approx 820\text{nm}$) and the three different longitudinal separations d_x ($d_y = 5\mu\text{m}$ is kept constant). Obviously, a reduction of d_x to about 40nm leads to a red-shift and broadening of the resonance accompanied by a decrease in extinction, which will be analyzed in the following in more detail.

5.2.1. Spectral Resonance Position

In analogy to Sec. 5.1, the relative shift $\Delta\lambda_{\text{res}}/\lambda_{\text{res}}$ [see Eq. (5.1)] of the array sets with $d_x \approx 40\text{nm}$ and $d_x = 1\mu\text{m}$ is plotted versus L in Fig. 5.8b. For the arrays with the small gap of $d_x \approx 40\text{nm}$, an approximately constant relative shift of $\Delta\lambda_{\text{res}}/\lambda_{\text{res}} = (10.9 \pm 0.3)\%$ (solid blue horizontal fit) is found, indicating near-field interaction across the gap (see Sec. 2.5). The red-shift can be understood by a coupled dipole model including retardation, where the intra-rod restoring force is diminished by the charges of opposite sign from the adjacent rod [30]. FDTD simulations of dimers (full red triangles) also predict a nearly constant relative shift, however, they do not reproduce the experiment. The discrepancy can be explained by the fact that in an array, each rod features two direct neighbors, leading to a weaker intra-rod restoring force and smaller resonance frequency compared to the dimer case, where only one direct neighbor exists. And in fact, the simulation of an array with $L = 820\text{nm}$ (full yellow diamond) nicely fits to the experiment. In contrast, nearly no shift is observed for the relatively large separation of $d_x = 1\mu\text{m}$, leading to the conclusion that neither near-field nor significant radiative dipolar coupling exists for $d_x = 1\mu\text{m}$. Supportingly, good agreement with the simulations of dimers is achieved.

5.2.2. Quality Factor and Extinction

Similar to Sec. 5.1, radiative dipolar coupling in longitudinal direction requires that the emitted fields are in phase with the electronic oscillation of adjacent rods. This

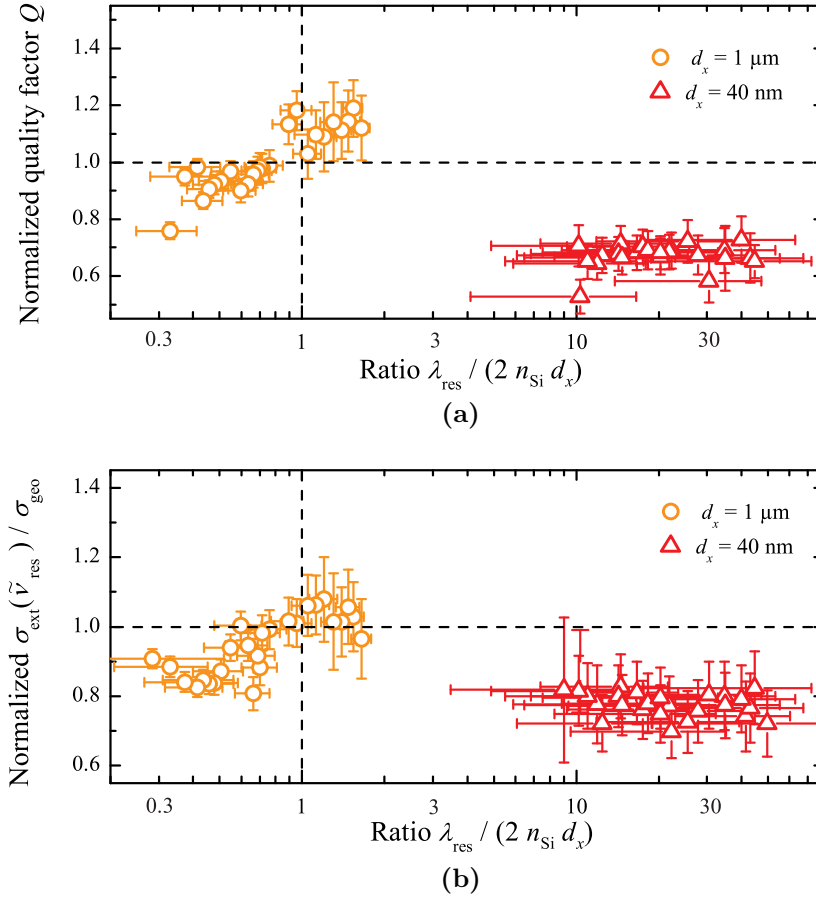


Figure 5.10.: Normalized values of (a) Q and (b) $\sigma_{\text{ext}}(\tilde{\nu}_{\text{res}})/\sigma_{\text{geo}}$ of the arrays with $d_x = 1 \mu\text{m}$ and $d_x \approx 40 \text{ nm}$ with respect to the reference arrays with $d_x = 5 \mu\text{m}$.

leads to the constructive interference condition $\frac{1}{2} \cdot \frac{\lambda_{\text{res}}}{n_{\text{Si}}} = d_x$ illustrated in Fig. 5.9. For this reason, the normalized values of Q and $\sigma_{\text{ext}}(\tilde{\nu}_{\text{res}})/\sigma_{\text{geo}}$ are plotted in Fig. 5.10 versus the ratio $\lambda_{\text{res}}/(2n_{\text{Si}}d_x)$. And in fact, slight increase of Q and $\sigma_{\text{ext}}(\tilde{\nu}_{\text{res}})/\sigma_{\text{geo}}$ is observed for values of $\lambda_{\text{res}}/(2n_{\text{Si}}d_x)$ slightly bigger than one, implicating that at least weak far-field interaction in longitudinal direction occurs for $d_x = 1 \mu\text{m}$.

The arrays with the small gap of $d_x \approx 40 \text{ nm}$ feature systematically lower values of Q and $\sigma_{\text{ext}}(\tilde{\nu}_{\text{res}})/\sigma_{\text{geo}}$ (see Fig. B.2 for absolute values), resulting in relatively constant normalized values (see Fig. 5.10). The reduced values are evidences of near-field dipolar coupling [30], becoming the dominating interaction at small distances. Note that the observed *lower far-field* extinction values indicate a lower amount of scattering out of the incident photon wave vector direction and do not necessarily mean *lower near-field* intensity. In fact, near-field coupling over small gaps in longitudinal direction leads to drastic increase of the near-field amplitude [30] (see also

5. Interaction Effects in Nanoantenna Arrays

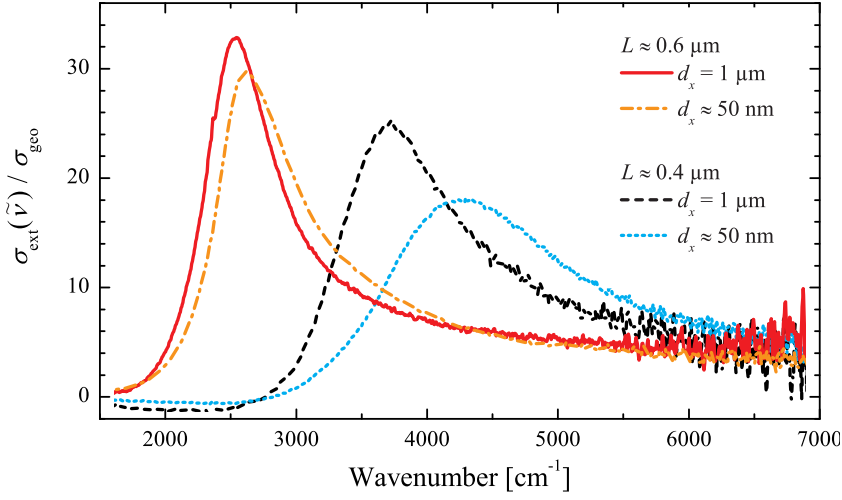


Figure 5.11.: Extinction cross-sections for nanorod arrays ($w \approx 40 \text{ nm}$, $h \approx 60 \text{ nm}$) with transverse separation distance $d_y = 1 \mu\text{m}$.

Fig. 2.8a). Supportingly, SEIRS measurements [171] (Fig. 3.12b) suggest increased electromagnetic field enhancement for coupled nanorods in tip-to-tip configuration.

5.3. Mixed Interaction

This section deals with the samples of series A, where nanorod arrays with separation distances below $5 \mu\text{m}$ in both directions ($d_y = 1 \mu\text{m}$, $d_x = 1 \mu\text{m}$ and 50 nm , see Tab. 3.1) were prepared. Based on the findings of Sec. 5.1, the values of $d_y = 1 \mu\text{m}$ should lead to transverse interaction for $\lambda_{\text{res}} > n_{\text{Si}} d_y = 3.42 \mu\text{m}$ ($\tilde{\nu}_{\text{res}} \lesssim 2920 \text{ cm}^{-1}$). In addition, the nanorods most likely interact over the small gap of $d_x \approx 50 \text{ nm}$, leading to “mixed” interaction. Unfortunately, reference arrays ($d_x = d_y = 5 \mu\text{m}$) were not fabricated within this series. In addition, a comparison between the data of series A and the references of series B or E, for example, might be misleading due to the different rod cross-sections ($w \approx 40 \text{ nm}$, $h \approx 60 \text{ nm}$ for A opposed to $w \approx 120 \text{ nm}$ for B and $w \approx 90 \text{ nm}$ for E, respectively, with $h \approx 100 \text{ nm}$ for both). Consequently, any observed shift of λ_{res} cannot be clearly attributed to interaction (compare to Sec. 4.1.3). As a result, a systematic analysis of the mixed interaction is not possible, however, the qualitative results are important for the understanding of the first photo-induced metal deposition experiment in Sec. 6.2.2.2, where a sample of series A was used.

Figure 5.11 shows $\sigma_{\text{ext}}(\tilde{\nu}) / \sigma_{\text{geo}}$ for selected nanorod arrays of sample Wa4, extracted from relative reflectance measurements (see Fig. B.3a) using Eq. (4.5). The

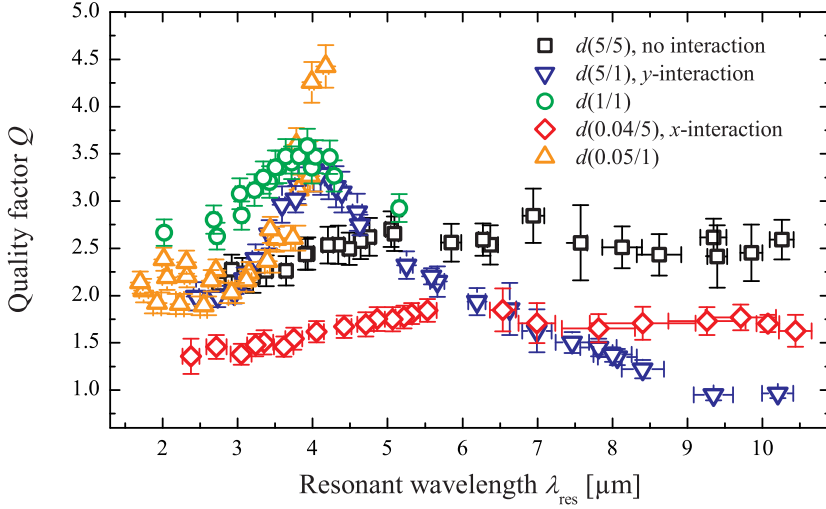


Figure 5.12.: Quality factor Q versus resonant wavelength λ_{res} for different arrays of sample Wa4 [$d(1/1)$ and $d(0.05/1)$] and Wb3 (all others). The abbreviation $d(x/y)$ denotes arrays with separation distances of $d_x = x \mu\text{m}$ and $d_y = y \mu\text{m}$.

reduced values of $\sigma_{\text{ext}}(\tilde{\nu}_{\text{res}})/\sigma_{\text{geo}}$ for decreasing d_x argues for increased near-field interaction in the case of $d_x \approx 50 \text{ nm}$ (compare to Sec. 5.2.2). However, a *blue-shift* of the resonance is detected for decreasing d_x , which seems to be contrary to observed *red-shift* for decreasing d_x found in Sec. 5.2. Thus, the reduced transverse separation of $d_y = 1 \mu\text{m}$ seems to strongly influence the optical behavior, even for $\tilde{\nu}_{\text{res}} > 2920 \text{ cm}^{-1}$. Besides the directly neighboring rods in transverse direction, it could be that also the diagonally opposite ones interact with each other in the case of $d_x \approx 50 \text{ nm}$. Consequently, the system becomes very complicated and a more systematic study would be necessary to understand the origin of the observed blue-shift.

As shown in Sec. 4.1.3, the quality factor Q can be used to compare different preparation series. In Fig. 5.12, Q -values of the arrays of sample Wa4 (green circles and orange triangles) are compared with arrays of sample Wb3 (all others).

The Q -values of the arrays $d(1/1)$ (see figure caption for definition) first increase with λ_{res} and feature a maximum at around $\lambda_{\text{res}} \approx 4 \mu\text{m}$, which is slightly bigger than the wavelength $\lambda_{\text{res}} = n_{\text{Si}} \cdot d_y = 3.42 \mu\text{m}$ of the constructive interference condition in transverse direction, see Sec. 5.1). After reaching the maximum, the Q -values seem to decrease for longer wavelengths. This behavior is similar to the transversely interacting arrays $d(5/1)$, indicating that strong transverse interaction also broadens the resonances for $d_x = 1 \mu\text{m}$ in case of sufficiently long λ_{res} . However, the Q -values of $d(1/1)$ are slightly bigger for $\lambda_{\text{res}} < 4 \mu\text{m}$ compared to the reference arrays $d(5/5)$, possibly due to weak longitudinal interaction in this range.

5. Interaction Effects in Nanoantenna Arrays

The arrays $d(0.05/1)$ feature broader resonances for $\lambda_{\text{res}} < 4\mu\text{m}$ compared to the arrays $d(1/1)$. This is explained by longitudinal near-field coupling, also being responsible for the systematic lower values of $d(0.04/5)$ compared to $d(5/5)$. Furthermore, the Q -values of $d(0.05/1)$ rise as λ_{res} is approaching the value of $4\mu\text{m}$ and even exceed the Q -values of $d(1/1)$. This behavior suggests that direct transverse interaction becomes important at $\lambda_{\text{res}} \approx 4\mu\text{m}$. However, the blue-shift of the arrays $d(0.05/1)$ compared to the $d(1/1)$ arrays indicates that “mixed” interaction is already present for $\lambda_{\text{res}} < 4\mu\text{m}$, which could explain the relatively high Q -values in this range.

5.4. Conclusion

Considering the results above, it is possible to identify the optimum geometry for maximum Q (in far-field extinction) and plasmonic resonances only marginally shifted from those of non-interacting antennas: $0.5 \leq \lambda_{\text{res}}/(2n_{\text{Si}}d_x) \leq 2$ and $\lambda_{\text{res}}/(n_{\text{Si}}d_y)$ slightly bigger than one, see Figs. 5.10a and 5.5b. This is in reasonable agreement with the work of ADATO *et al.* [32] and accounts for the constructive interference conditions of the two coupling directions (see Figs. 5.9 and 5.4). In longitudinal direction, resonances are only slightly sharper in a range around $\lambda_{\text{res}}/(2n_{\text{Si}}d_x) \approx 1$, whereas in transverse direction, a significant constructive first order interference appears at $\lambda_{\text{res}}/(n_{\text{Si}}d_y) \approx 1$. The anisotropy of the far-field interaction in the array is influenced by the anisotropic emission pattern of an oscillating dipole. Here, most of the electromagnetic power is radiated perpendicular to the oscillation axis [206] and, thus, changes in d_y cause stronger interference effects. Strong anisotropy is also measured for the near-field coupling range of gap sizes (compare Figs. 5.5 and 5.10 for values on the abscissa bigger than one). Significant blue-shift, decrease of normalized $\sigma_{\text{ext}}(\tilde{\nu}_{\text{res}})/\sigma_{\text{geo}}$ and extraordinary broadening are only observed for transverse gap size decrease below $\lambda_{\text{res}}/n_{\text{Si}}$. Coupling of the antennas over a small d_y (of about 100nm) disturbs the confinement of resonant near-field at the nanorod ends very differently compared to the increased confinement at small d_x .

In NAIRS, near-field enhancement of plasmonic resonances has to be maximized, suggesting that very small longitudinal gaps with transverse separation distances according to the first constructive interference condition are optimal. Concerning the array design, it has to be considered that the longitudinal near-field coupling strongly changes the resonance position. Hence the antenna length needs to be adjusted to the vibrational frequencies of interest. Note that a simultaneous optimization of Q and near-field intensity is not possible.

5.5. Important findings

- The relative shift $\Delta\lambda_{\text{res}}/\lambda_{\text{res}}$ as well as the normalized values of Q and $\sigma_{\text{ext}}(\tilde{\nu}_{\text{res}})/\sigma_{\text{geo}}$ do not depend on the preparation process or rod cross-section.
- Concerning transverse interaction, maximum values of Q and $\sigma_{\text{ext}}(\tilde{\nu}_{\text{res}})/\sigma_{\text{geo}}$ are found near the constructive interference condition $\lambda_{\text{res}}/n_{\text{Si}} = d_y$. Furthermore, a qualitative change of the optical properties (blue-shift, broadening, decrease of extinction) occurs for $\lambda_{\text{res}}/n_{\text{Si}} > d_y$.
- For small transverse separations, near-field coupling leads to a decrease of near-field enhancement, as shown by SNOM measurements.
- Small longitudinal gaps lead to a red-shift of the resonance accompanied by broadening and decrease of extinction. The increased near-field enhancement for the tip-to-tip configuration is known from literature [30].
- A resonance blue-shift was found for a reduction of d_x from $1\mu\text{m}$ to about 50nm at fixed $d_y = 1\mu\text{m}$. This behavior might be due to increased interaction of diagonally opposite rods.

6. Characterization and Preparation of Nanogaps

In this thesis, two different approaches to nanogap formation were investigated. The first one, the chemically induced metal deposition, is based on growth of lithographic nanoantennas. In this way, already existing intra-rod gaps become narrower, as illustrated in Fig. 6.1a. The nanorod growth was performed by using two methods, the wet-chemical and the photo-induced metal deposition, which are introduced and discussed in Sec. 6.1 and Sec. 6.2. In contrast to these “bottom-up” techniques, the second approach (Sec. 6.3) can be considered as “top-down” process: lithographic nanorods are cut in the middle by a focused ion beam to prepare dimers with small gaps (see Fig. 6.1b).

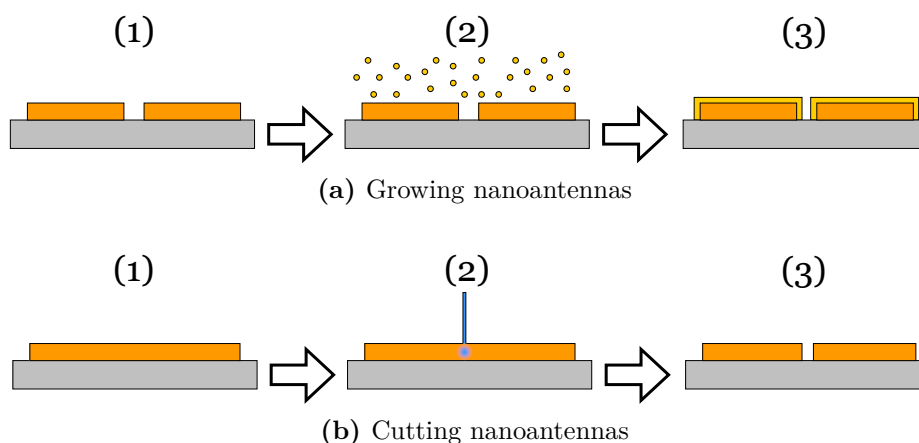


Figure 6.1.: (a) Nanorods with relatively small gaps (20 – 50 nm) are lithographically prepared (1); by reduction of gold ions (2), deposition of gold on the nanoantennas narrows the gap (3). (b) Long nanorods are fabricated (1) and cut in the middle by a focused ion beam (2) to prepare dimers (3).

6.1. Wet-Chemical Metal Deposition

After a short introduction to the principle of the method (Sec. 6.1.1), the measurement process is shortly explained in Sec. 6.1.2. Finally, the results are discussed in Sec. 6.1.3.

6.1.1. Principle

The wet-chemical metal deposition or hydroxylamine seeding method is a well-known technique in nanotechnology to enlarge existing gold nanoparticles solved in solutions or immobilized on surfaces [37, 207–210]. It is based on the thermodynamical reduction of Au^{3+} ions to metallic gold by hydroxylamine (NH_2OH). The gold ions are usually provided by a gold salt, hydrogen tetrachloroaurate (HAuCl_4) for example. The reduction process is dramatically accelerated in presence of gold surfaces [211], leading to gold deposition on existent gold particles while new particle nucleation does not occur [207, 209].

6.1.2. Measurement Process

HAuCl_4 (99.999 %) and hydroxylamine hydrochloride¹ $\text{NH}_2\text{OH} \cdot \text{HCl}$ (99 + %) were obtained from SIGMA ALDRICH and FISHER SCIENTIFIC, respectively, and used without further purification. Aqueous solutions of both components were prepared with concentrations of 0.3mM (HAuCl_4) and 0.4mM ($\text{NH}_2\text{OH} \cdot \text{HCl}$), respectively, according to [208].

First, a defined volume (20 – 40ml) of $\text{NH}_2\text{OH} \cdot \text{HCl}$ solution was given in one beaker. After adding the same amount of HAuCl_4 solution, the sample was immersed in this growth solution and swayed² for two minutes. Finally, gold deposition was terminated by rinsing the sample with pure water and drying it with compressed air.

6.1.3. Results

IR Optical Characterization

The experiment was performed with sample Wa4 of series A (see Tab. 3.1), featuring two sets of arrays, A1 and A2, with different separation distances d_x ($d_y = 1\mu\text{m}$ for both). In Fig. 6.2, typical relative reflectance spectra³ before and after the

¹The hydrochloride form of NH_2OH is more convenient compared to simple NH_2OH [176].

²Swaying provides a more homogeneous growth than simple immersing [212].

³Sample Wa4 features a rough backside which is not well suited for transmittance measurements.

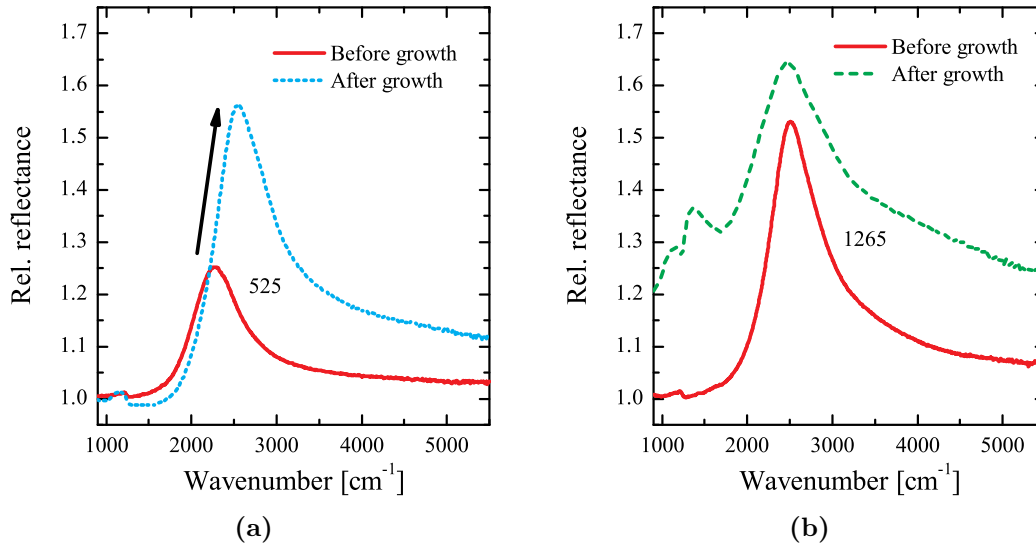


Figure 6.2.: Relative reflectance spectra before and after wet-chemical metal deposition for (a) an array of set A1 ($d_x = 1 \mu\text{m}$, $L \approx 0.65 \mu\text{m}$) and (b) one of set A2 ($d_x \approx 50 \text{nm}$, $L \approx 0.6 \mu\text{m}$). The numbers indicate the approximate quantity of rods contributing to the signals.

metal deposition are displayed. The arrays of set A1 ($d_x = 1 \mu\text{m}$, Fig. 6.2a) show an increase of extinction accompanied by a shift of the resonance to higher frequencies. Furthermore, the antenna resonance does not broaden significantly, indicating a rather homogeneous rod growth. In contrast, nearly no shift of the fundamental mode is detected for the A2-arrays ($d_x \approx 40 - 50 \text{nm}$, Fig. 6.2b). Moreover, a second resonance has emerged at around 1250cm^{-1} , interfering with the excitation of the thin-film SPP (Sec. 3.5.2). All other arrays of A2 showed similar behavior with a more or less pronounced peak at half frequency of the fundamental mode.

SEM Measurements

Whereas the shape of lithographically prepared nanorods seems to be quite regular and cuboid-like (see e.g. Fig. 3.3), the surface morphology drastically changes after the wet-chemical metal deposition, as illustrated by Fig. 6.3. The roughness of the rods heavily increased and the rods look very irregular and grainy. In addition, small gold nanospheres have formed on the whole substrate. In the case of the arrays of A1, small gaps below 10nm were found (see arrow in Fig. 6.3b), however, also the coalescence of individual was observed (not shown).

Histograms of the maximum particle dimension were generated for selected nanorod arrays. In the representative example of Fig. 6.4, an average increase of the rod length

6. Characterization and Preparation of Nanogaps

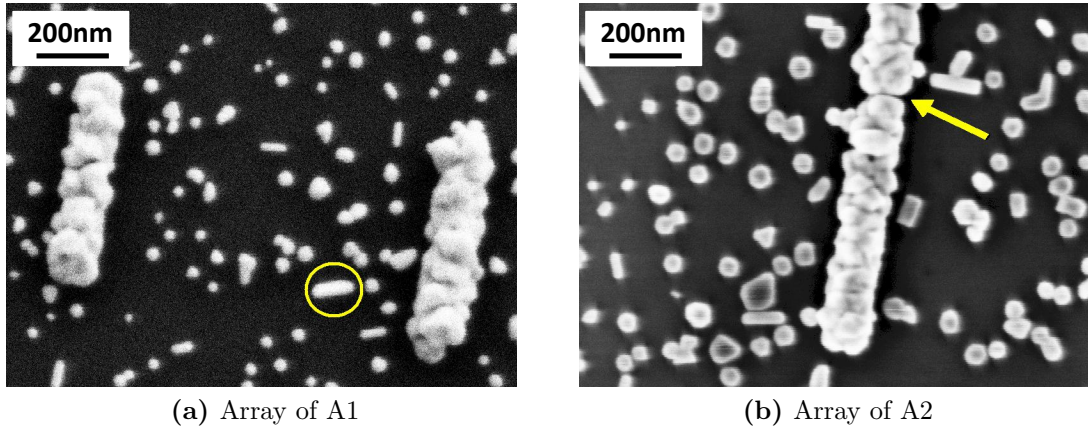


Figure 6.3.: SEM images of nanorods after wet-chemical metal deposition.

of about 100 nm was monitored. Note that a very homogeneous length distribution⁴ was present before the experiment (red bars). Moreover, most of the small gold nanoparticles are spherical, featuring diameters of about 40 – 60 nm. In addition, cylindrically shaped particles (see encircled one in Fig. 6.3a) have formed with maximal dimensions up to 200 nm. Concerning the length growth of the A2-arrays, an average increase of only 50 nm was detected (not shown). This value is reasonable taking into account that the rods were initially separated by 40 – 50 nm and that coalescence of several rods have occurred. Finally, the rod width w was found to have increased from 40 nm to about 120 nm for the rods of both sets.

Discussion

An increase of the rod length L leads to a resonance red-shift whereas the growth of the rod diameter results in a blue-shift (Sec. 2.4.1). Since both geometric dimensions grow simultaneously, the blue-shift of the resonances of the A1-arrays (see Fig. 6.2a) is explained by the dominating influence of the increased rod diameter. This can be derived from the simulations depicted in Fig. 2.5, where a 100 nm increase of L accompanied by an augmentation of R from 20 nm to 60 nm results in a shift of the resonance to shorter wavelengths.

Concerning the A2-arrays, the increased interaction over the narrower gap, which is expected to red-shift the resonance (Sec. 5.2), might cancel the effect of the bigger rod diameter, leading to no significant shift of the resonance. Moreover, the second

⁴The histograms were generated with the help of SEM images at lower magnification to obtain a better statistical averaging. The observed length difference of $L_2 - L_1 = 26$ nm corresponds to one pixel in the images and hence to the error of the measurement.

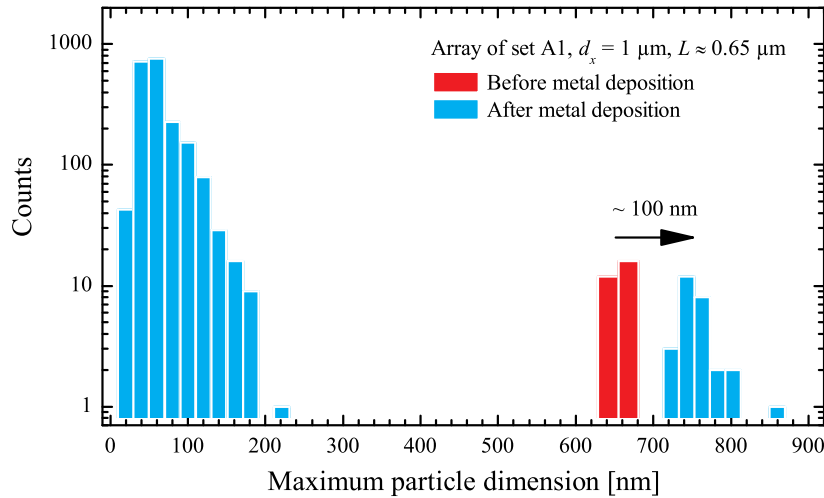


Figure 6.4.: Maximum particle dimension before and after metal deposition for an array of set A1.

resonance at half frequency of the fundamental mode is attributed to merged rods of doubled length. This conclusion is based on the linear relation between L and λ_{res} in the IR (Secs. 2.4.1 and 4.3.1).

Conclusion

The experiments showed that the wet-chemical method can be applied to enlarge gold nanorods, offering the possibility to prepare nanogaps suited for NAIRS. However, one critical point is still the formation of gold nanoparticles on the substrate. One possible reason for their appearance could be the argon-sputtering of the sample prior to the experiment (see Sec. A.4), possibly creating nucleation seeds on the substrate. This is supported by the absence of gold nanoparticles on the back side of the sample, which was monitored by SEM (not shown). Moreover, the concentration of the gold salt, adopted from BROWN *et al.* [37] (seeding of colloidal particles), could be too large for the manipulation of nanorods. In addition, the reduction process might proceed too fast, explaining the irregular shape of the rods.

One major disadvantage of the method is the simultaneous modification of all prepared nanorod arrays on the sample. Consequently, the whole sample is corrupt if an experiment fails. For this reason, the method was given up in favor of the photo-chemical technique, which promises *selective* modification of the sample.

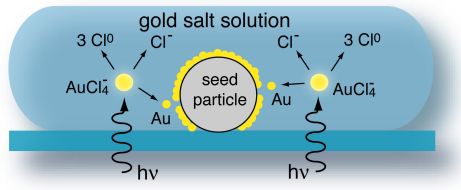


Figure 6.5: Schematic drawing of the photo-induced metal deposition [36]. Illumination with light triggers the reduction of the gold salt complexes. Metallic gold is preferably deposited on present gold surfaces.

6.2. Photo-Induced Metal Deposition

First, the principle of the method is reviewed in Sec. 6.2.1. Afterwards, Sec. 6.2.2 presents the experimental findings from gold nanorod arrays on silicon illuminated by the halogen lamp of the IR microscope. Besides that, illumination experiments with individual nanorod dimers on CaF₂ were performed with the help of an inverted microscope and a laser light source (Sec. 6.2.3).

6.2.1. Principle

The basic idea of the photo-induced metal deposition [213–215] is the reduction of HAuCl₄ to bulk gold in the presence of gold surfaces [216]. However, in contrast to the wet-chemical reduction, the reaction is triggered by light illumination [217]. The gold surface of present gold particles serves as catalyst for the reduction reaction, thereby leading to particle growth rather than agglomeration of the reduced gold atoms [216], as illustrated in Fig. 6.5. Moreover, only photons with sufficiently high energy ($E > 2.25\text{eV}$ or $\lambda < 550\text{nm}$) are able to initiate the reduction reaction [36]. Note that the substrate surface does not provide the required catalytic activity and, hence, the deposition occurs with high spatial selectivity. Details of the chemical process can be found in [214, 218].

6.2.2. Nanorod Arrays on Silicon Substrates

The first experiments were performed with sample Wa2 of series A (see Tab. 3.1). Besides that, arrays with small d_x of about 40nm on sample Wb3 were used to narrow the gap. Two examples of each sample will be presented and discussed after the introduction of the measurement process.

6.2.2.1. Measurement Process

Initially, a drop (volume of 20 μl) of immersion oil (CARGILLE #1160), containing a defined concentration of HAuCl₄ (1 – 5 mM), was given on the sample. Immersion

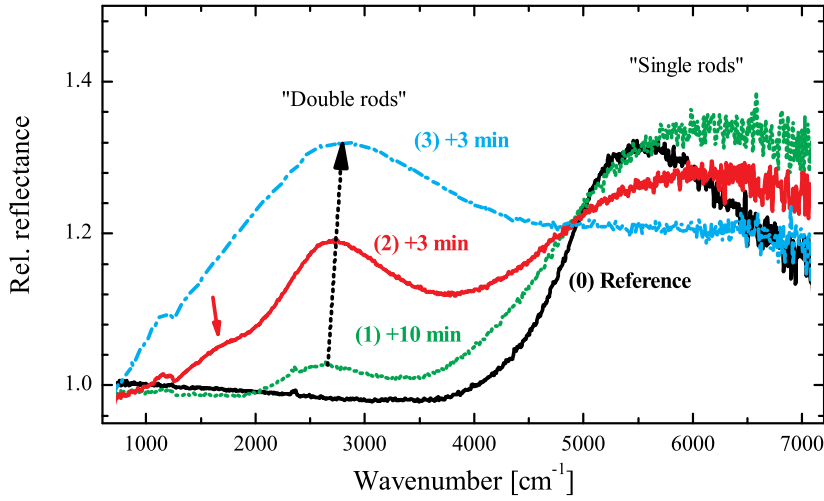


Figure 6.6.: Photo-induced growth of an array of sample Wa2 ($L \approx 320$ nm, $w \approx 40$ nm, $d_x \approx 60$ nm, $d_y = 1$ μ m before metal deposition).

oil was used instead of water due to its low surface tension and slow evaporation at ambient conditions. To avoid any triggering of the deposition process during localization of the sample position, a red-filter was inserted in front of the white light source (NIKON halogen lamp, 12 V, 100 W) to filter out the short-wave portion of the halogen spectrum. After selection of a certain nanorod array, the red-filter was removed and the whole array was illuminated for a defined time. As a result of top illumination, which is necessary due to the opaque silicon substrate, gold ions are photo-chemically formed *at the surface* of the gold salt solution. Consequently, they have to *diffuse* towards the gold nanorods where they finally precipitate. After each deposition step, the sample was flushed with pure ethanol and dried with compressed air to allow IR spectroscopic measurements.

6.2.2.2. Results of Sample Wa2

First, a reference spectrum [spectrum (0) in Fig. 6.6] was recorded before metal deposition, featuring an antenna resonance at around 5500 cm^{-1} . After 10 minutes of illumination [$c(\text{HAuCl}_4) = 5 \text{ mM}$], the fundamental resonance shifted to *higher* wavenumbers [$\tilde{\nu}_{\text{res}} \approx 6300 \text{ cm}^{-1}$, spectrum (1)]. This is contrary to the expected resonance red-shift with decreasing gap size (Secs. 2.5 and 5.2). However, one has to take into account that the transverse separation distance of $d_y = 1 \mu\text{m}$ leads to “mixed interaction”, for which a blue-shift of the resonance with decreasing d_x was observed (Sec. 5.3). In addition to the shift of the fundamental resonance, originating from

6. Characterization and Preparation of Nanogaps

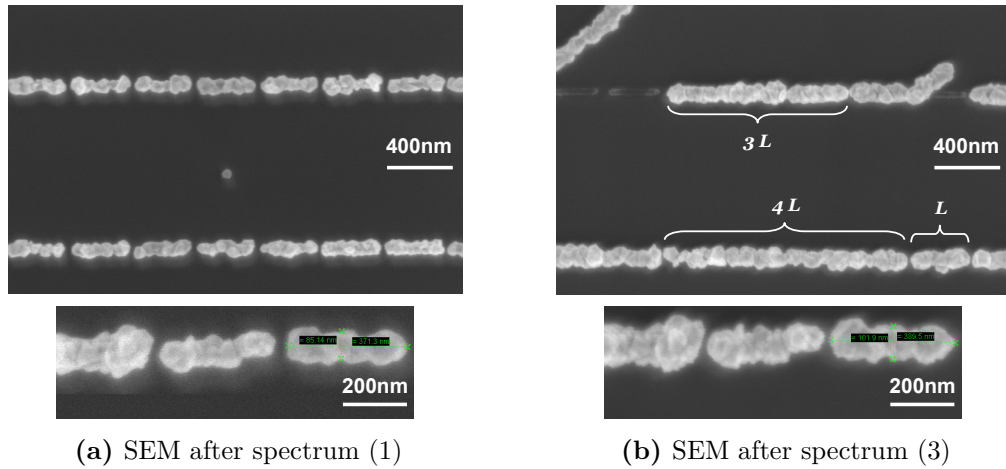


Figure 6.7.: SEM images taken after the acquisition of (a) spectrum (1) and (b) spectrum (3) of Fig. 6.6. L and w of the rightmost rods in the zoom images are (a) $L \approx 371$ nm, $w \approx 80$ nm and (b) $L \approx 390$ nm, $w \approx 102$ nm. In (b), rods of multiple L have formed. Note that only very small parts of the array (overall size of $50 \times 50 \mu\text{m}^2$) are shown.

“single rods”, a second peak at lower frequency ($\approx 2700 \text{ cm}^{-1}$, marked by “double rods”) emerges, indicating the coalescence of rods, now featuring approximately the double length (compare to Sec. 6.1.1).

The SEM image of Fig. 6.7a, recorded after the 10 min-deposition step, shows very rough and grainy rods which resemble the ones of the wet-chemical approach. However, no particle nucleation on the substrate occurred, which is a clear improvement compared to the wet-chemical preparation. Concerning the growth of the rods, length and width increased of about 40 nm compared to the initial state (not shown) and gaps of down to 20 nm were found.

Subsequently, two additional 3 min-deposition steps were carried out [spectra (2) and (3)]. While the single rod resonance slightly blue-shifts and loses in intensity, the double rod becomes more pronounced. This can be explained by cumulative coalescence of individual rods. Moreover, a small shoulder (indicated by a red arrow) emerges in spectrum (2) at about one third of the fundamental resonance, possibly originating from three connected rods, as illustrated in Fig. 6.7b. On average, the rod length and width gained about 20 nm with respect to the situation after 10 min illumination, leading to the formation of gaps below 10 nm (see zoom image of 6.7b). However, a systematic correlation between IR spectra and structural information could not be established due to the inhomogeneous growth.

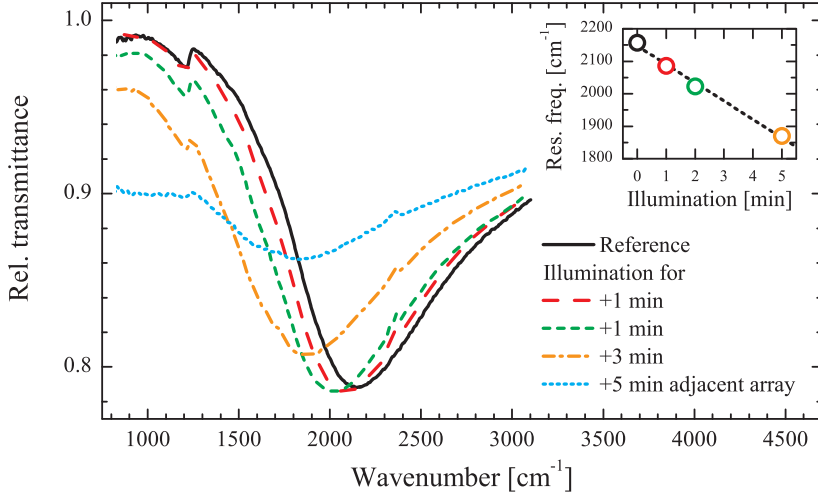


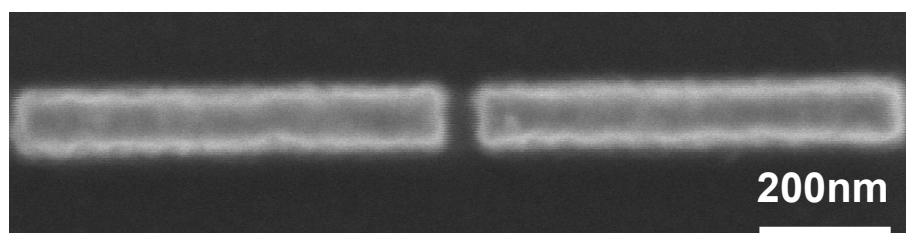
Figure 6.8.: Photo-induced metal deposition of an array of sample Wb3 ($L \approx 670$ nm, $w \approx 95$ nm, $d_x \approx 50$ nm, $d_y = 5 \mu\text{m}$ before metal deposition).

6.2.2.3. Results of Sample Wb3

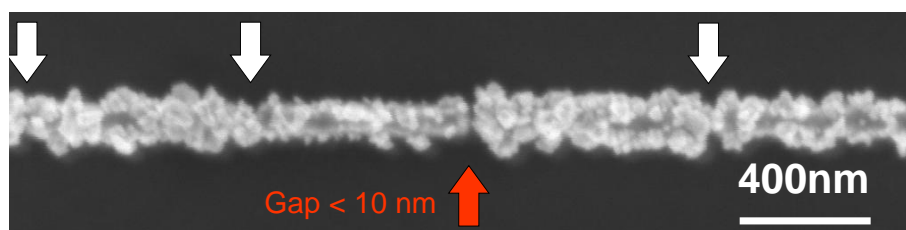
The second series of experiments was performed with a lower concentration of HAuCl_4 in immersion oil (1 mM). Figure 6.8 shows a series of relative transmittance spectra of an array of sample Wb3 (initial gap size of about 50 nm, see Fig. 6.9a). Three consecutive deposition steps were performed with illumination times given in Fig. 6.8. Starting from the reference measurement, the position of the antenna resonance shows the expected red-shift with increasing illumination time and, hence, supposedly decreasing gap size (Sec. 5.2). Note that this result is not contrary to the findings of Sec. 6.2.2.2 (blue-shift with increasing illumination time), since the transverse separation of $d_y = 5 \mu\text{m}$ excludes “mixed interaction” (Sec. 5.3).

Concerning the shift of the resonance, a linear dependency between $\tilde{\nu}_{\text{res}}$ and illumination time is monitored (see inset in Fig. 6.8). Furthermore, the extinction slightly increases during the first deposition steps, most likely due to increased particle volume, while it decreases after the third deposition step. The decrease suggests that some rods merged (see white arrows in Fig. 6.9b), leading to resonances at lower frequencies (note the increased extinction at around 1000 cm^{-1}). Moreover, very small gaps in the sub 10 nm-range have formed (see e.g. gap marked in Fig. 6.9b). Nevertheless, an irregular deposition can be concluded from the shape of the rods in Fig. 6.9b. In addition, some rods have been modified more than others (see Fig. 6.9c), resulting in a very inhomogeneous growth within the array. Consequently, a direct correlation between IR optical response and geometrical structure cannot be drawn.

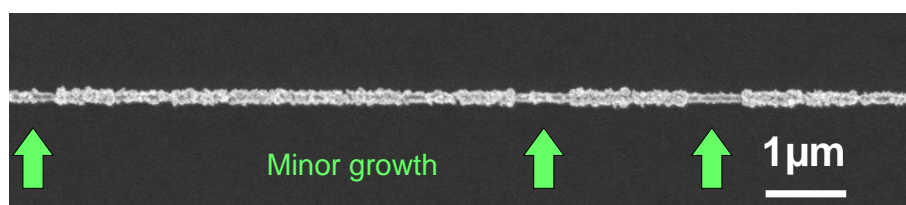
6. Characterization and Preparation of Nanogaps



(a) SEM before metal deposition



(b) SEM after metal deposition



(c) SEM after metal deposition

Figure 6.9.: SEM images (a) before and (b,c) after metal deposition. Image (a) belongs to the solid black spectrum of Fig. 6.8, whereas (b) and (c) were taken after the final deposition step. The width and length of the rods increased due to gold deposition, leading to the coalescence of rods (white arrows) besides the formation of small gaps (red arrow). Inhomogeneous rod growth can be observed in (c), where the green arrows label rods of minor growth.

Finally, the selectivity of the method (i.e. only illuminated rods should grow) was tested. Thus, another nanorod array, located approximately $150\mu\text{m}$ away from the previous one, was illuminated for $t = 5$ min and the behavior of the non-illuminated array was investigated. As the dotted blue curve Fig. 6.9a shows, a red-shift of the resonance accompanied by decreasing extinction is observed, excluding absolute selectivity. This leads to the conclusion that additional gold was deposited and more conductive connections between several rods formed. Most likely, this undesirable growth can be attributed to diffusion of gold ions from illuminated spots to other sites. The illumination geometry from the top of the sample is supposed to cause this phenomenon [219]. This might be related to the relatively long diffusion length from the place of ion formation (surface of the growth solution) to the target (gold nanorods on the substrate's surface). For this reason, new nanorods on CaF_2 were prepared, allowing illumination from the bottom (see Sec. 6.2.3).

6.2.2.4. Conclusion

The experiments demonstrated the proof-of-concept, i.e. the preparation of gaps in the nm-range is possible. However, nanorod arrays turned out to be not suited for a systematic investigation due to the very inhomogeneous deposition within the array. In addition, gold growth of non-illuminated nanorods was found and attributed to gold ion diffusion.

6.2.3. Nanorod Dimers on Calcium Fluoride Substrates

The second series of experiments was performed at the Fraunhofer Institute for Non-Destructive Testing, Dresden, with gold nanorod dimers on CaF_2 (samples Antenna#18 and #19, see Tab. 3.1). Due to the high transparency of CaF_2 in the visible spectral range, illumination from the bottom was carried out by an inverted microscope. After the explanation of the measurement process (Sec. 6.2.3.1) and the special sample layout (Sec. 6.2.3.2), IR optical investigations before metal deposition are presented in Sec. 6.2.3.3. Subsequently, the results of samples Antenna#18 (Sec. 6.2.3.4) and Antenna#19 (Sec. 6.2.3.5) are analyzed separately, since Antenna#18 served as a testing sample for determination of useful experiment parameters (concentration of gold salt solution, illumination time, laser power). Following metal deposition, it was covered with carbon to allow SEM measurements, which were used to derive new parameters for the treatment of Antenna#19. In the end, Sec. 6.2.3.6 discusses the appearance of additional modes in the IR spectra.

6. Characterization and Preparation of Nanogaps

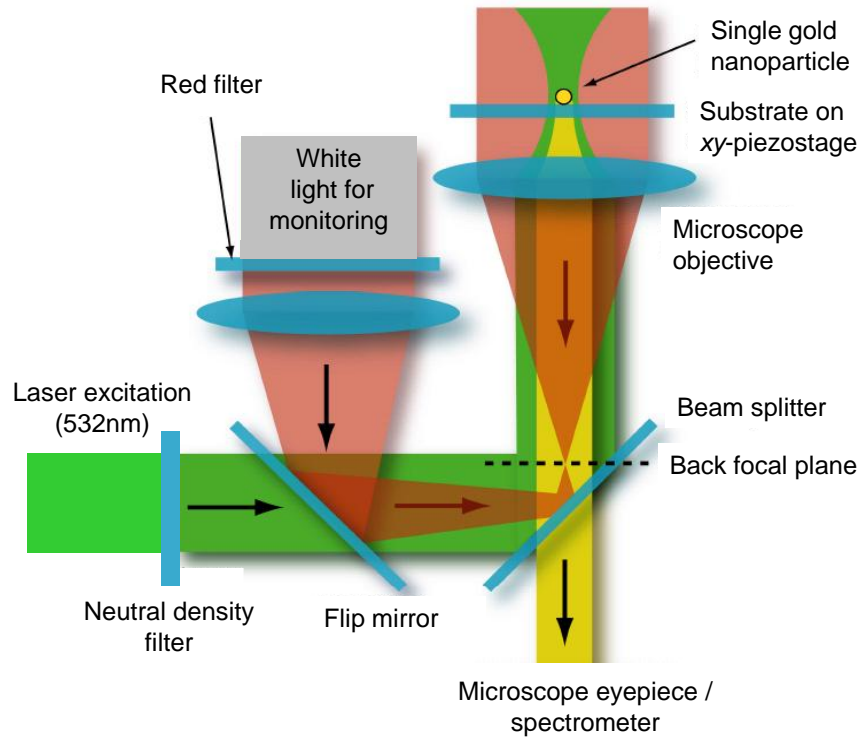


Figure 6.10.: Scheme of the set-up used for photo-induced metal deposition (see text).

6.2.3.1. Measurement Process

Figure 6.10 schematically shows the experimental set-up: the samples were located on a movable *xy*-piezostage of an inverted microscope (ZEISS AXIO OBSERVER Z1) and covered by an approximately 20 μl droplet of a 5 μM solution of HAuCl_4 (ABCR, 99.9%) in glycol. Using the white light beam of a mercury arc lamp (XCITETM 120XL PC, $P = 120\text{ W}$), certain nanorod dimers or single rods, respectively, were selected and brought into the focus. In analogy to Sec. 6.2.2.1, a red-filter was used to avoid any triggering of the reduction process.

After localization, the white light beam was blocked and green light of a frequency-doubled Nd:YAG-laser ($\lambda = 532\text{ nm}$, $P = 100\text{ mW}$) was directed into the microscope by means of a flip mirror. Consequently, illumination of the nanostructure was performed for a defined period of time (0.5 – 10 min) at a certain laser power⁵ (90 μW – 200 μW) with the help of a microscope objective (100-fold magnification, $NA = 0.75$), producing a light spot on the substrate of about 5 μm in diameter⁶.

⁵The laser power varied by inserting different neutral density filters into the beam path.

⁶This diameter is bigger than the one of the smallest possible, diffraction-limited spot size. The spot size on the substrate was expanded by moving the sample for a defined distance towards

After illumination of the selected structure, the laser beam was blocked and another single nanorod or pair of nanorods was addressed and exposed to the laser radiation. In the end, the sample was cleaned with isopropanol and dried by air purging.

In addition, the set-up offers the possibility to record scattering spectra of the illuminated nanoparticles in the visible range [36]. To this end, the back scattered white light of the mercury arc lamp (without red-filter) is guided via a glass fiber to a grating based spectrometer (ZEISS AXIO OBSERVER Z1).

In contrast to the illumination of whole arrays (Sec. 6.2.2), single nanorod dimers or individual nanorods, respectively, were illuminated with this set-up. Note that the low concentration of the gold salt leads to a weak absorption of 532nm laser energy in the solution [36]. However, the energy absorbed by the solution in the vicinity of the addressed particle is certainly higher than far away from it, as the excited particle plasmon-polariton leads to an electric field enhancement even in the non-resonant case [36]. Due to this process and due to the tight focusing of the laser spot, reduced gold ions are predominantly formed near the gold nanorods [219] where they precipitate. Thus, adjacent unexposed particles should not grow in size.

6.2.3.2. Sample Layout

Six identical sets, each with 12 patterns, were prepared on both samples. Figure 6.11 depicts the arrangement and notation of the sets as well as the patterns with their respective dimensions. In addition, one of the patterns intended for photo-chemical metal deposition is shown in the bottom right of Fig. 6.11. It consists of six nanorod dimers and three individual nanorods, all of them featuring rectangular cross-sections ($w \approx h \approx 60\text{nm}$) and the same initial length $L \approx 1460\text{nm}$.

The gap g_x between the nanorod dimers was set to 20nm, the smallest possible gap size that could be reproducibly prepared by EBL [102]. Besides nine patterns with $g_x \approx 20\text{nm}$ (T0 - T8), two reference arrays with bigger gap sizes (R100 with $g_x \approx 100\text{nm}$ and R50 with $g_x \approx 50\text{nm}$) as well as one pattern with nine single rods (R) exist in each set.

the microscope objective to ensure illumination of the whole nanorod dimer (total length of about $3\mu\text{m}$).

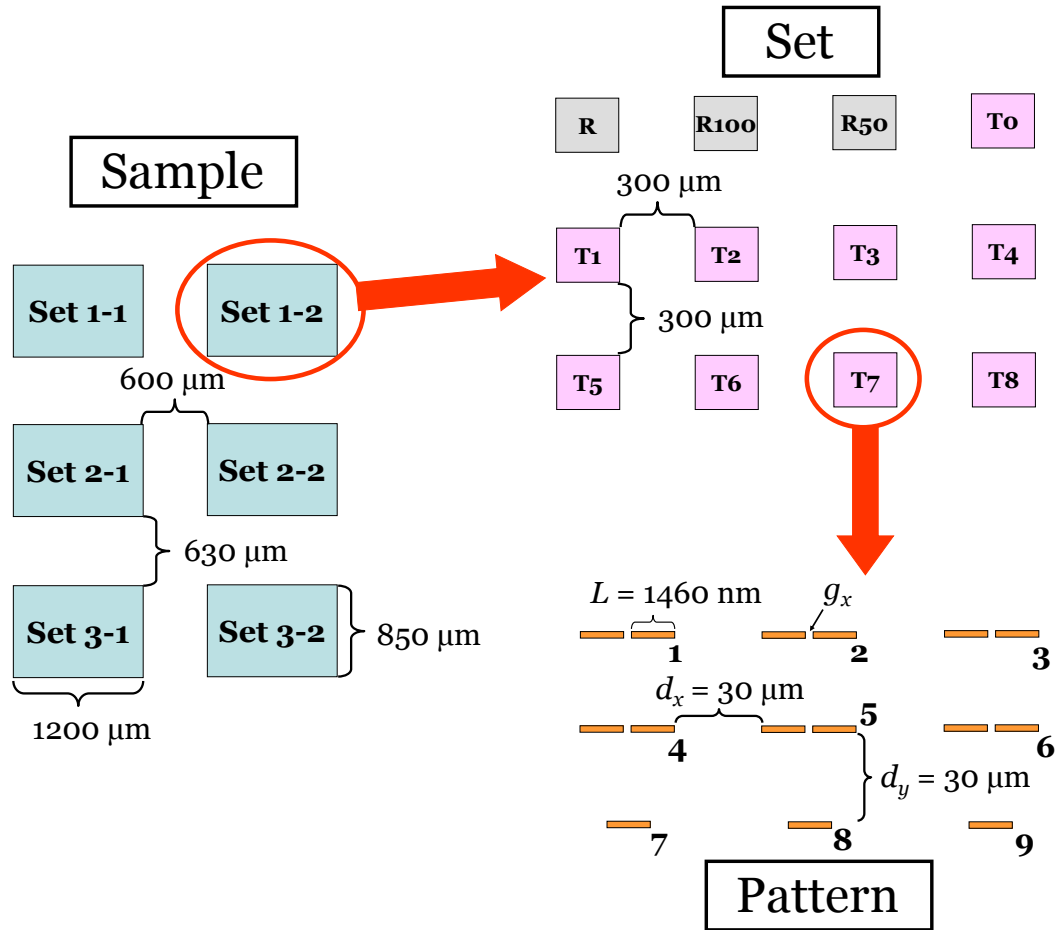


Figure 6.11.: The six sets of each sample consist of 12 patterns. The reference patterns R, R100 and R50 feature nine single rods and nine dimers with gaps of 100 nm and 50 nm, respectively. All other patterns (T0 - T8) consist of six dimers with a gap of 20 nm and three single rods. The dimensions of all rods are: $L \approx 1460 \text{ nm}$, $w \approx h \approx 60 \text{ nm}$.

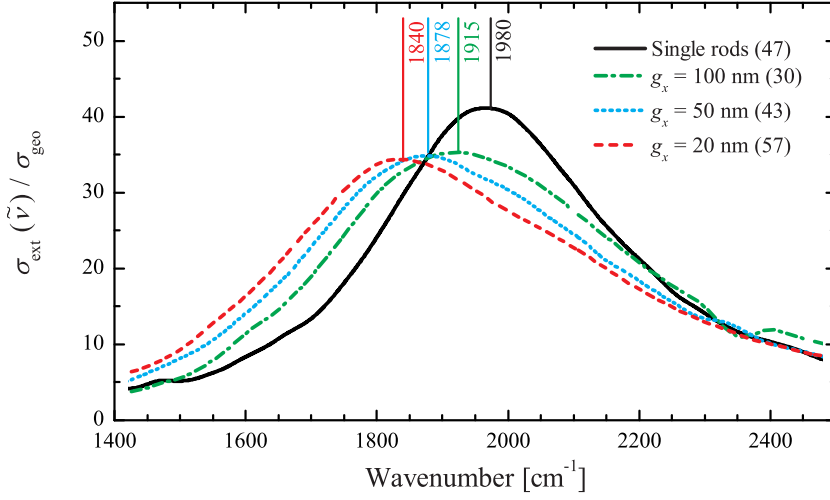


Figure 6.12.: Averaged extinction spectra of single nanorods and nanorod dimers with decreasing gap size of sample Antenna#19 (resolution 32 cm^{-1} , 500 scans). The numbers in brackets give the quantity of measurements used for the average spectrum.

6.2.3.3. IR Optical Characterization before Metal Deposition

In Fig. 6.12, extinction spectra of single nanorods as well as nanorod dimers with varying gap size are shown. These spectra are averages over several measurements of single rods or dimers (total amount indicated in the figure), respectively. Due to the preparation process, variations of $\tilde{\nu}_{\text{res}}$ are found, as illustrated by Fig. 6.13a for the case of $g_x \approx 20 \text{ nm}$. However, the distribution of $\tilde{\nu}_{\text{res}}$ is very narrow, nearly all values of $\tilde{\nu}_{\text{res}}$ are close to the average value of 1840 cm^{-1} .

As Fig. 6.12 shows, the fundamental resonance shifts to smaller frequencies and looses in intensity with decreasing gap size g_x due to increased interaction, in accordance with the findings of Sec. 5.2. In analogy to Eq. (5.1), the change of the resonance position of a dimer with gap g_x compared to a single rod of *same geometric dimensions* can be quantified by calculating the relative shift

$$\frac{\Delta\lambda_{\text{res}}}{\lambda_{\text{res}}} = \frac{\lambda_{\text{res}}^{\text{dimer}}(g_x)}{\lambda_{\text{res}}^{\text{single}}} - 1. \quad (6.1)$$

The open red circles in Fig. 6.13b show the gap-dependency of $\Delta\lambda_{\text{res}}/\lambda_{\text{res}}$ for the nanorod dimers of Antenna#19. For comparison, experimental data [102] of sample Antenna#15 as well as simulations of dimers on silicon and CaF_2 are added. A linear relation between $\Delta\lambda_{\text{res}}/\lambda_{\text{res}}$ and g_x seems to be present in the double logarithmic plot, suggesting that $\Delta\lambda_{\text{res}}/\lambda_{\text{res}}(g_x)$ can be described by a power function $y = a \cdot x^{-b}$

6. Characterization and Preparation of Nanogaps

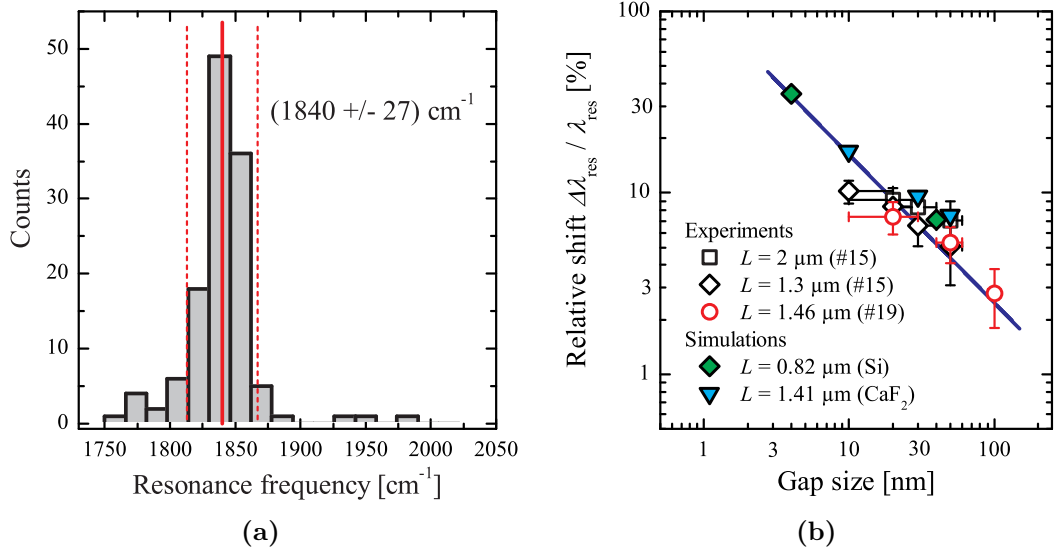


Figure 6.13.: (a) Histogram of $\tilde{\nu}_{\text{res}}$ of nanorod dimers with $g_x \approx 20$ nm (125 dimers in total, bin width is half of the spectral resolution). The solid and dotted red vertical represent the average value of $\tilde{\nu}_{\text{res}}$ as well as the standard deviation of the mean. (b) Relative shift $\Delta\lambda_{\text{res}}/\lambda_{\text{res}}$ versus gap size. The open red circles result from the spectra of Fig. 6.12. The data of sample Antenna#15 originates from *arrays of dimers* [102] with $w \approx h \approx 60$ nm. Moreover, FDTD simulations [93] of dimers on natural oxide covered silicon ($w = 120$ nm, $h = 100$ nm) and CaF_2 ($w = h = 40$ nm) are shown. The solid blue line represents a fit to the data according to $y = a \cdot x^{-b}$ ($a = 106 \pm 13$, $b = 0.82 \pm 0.06$).

(solid blue line). Due to the linear relation between λ_{res} and L in the IR (Sec. 2.4.1), $\Delta\lambda_{\text{res}}/\lambda_{\text{res}}$ in the border case of $g_x = 0$ is supposed to be 100% ($2 \times L \Rightarrow 2 \times \lambda_{\text{res}}$). Hence, the solid blue line can only serve as a guide to the eye and cannot be extrapolated to smaller gap sizes. Nevertheless, the plot will be used in Sec. 6.2.3.5 to roughly estimate gap sizes based on the observed spectral shift.

6.2.3.4. Results of Antenna#18

Several nanorod dimers and single rods on Antenna#18 were illuminated for different times at fixed laser power ($P = 200 \mu\text{W}$) and gold salt solution [$c(\text{HAuCl}_4) = 5 \mu\text{M}$]. This section includes a qualitative analysis of the observed spectral changes, providing better understanding of the results of Antenna#19 in Sec. 6.2.3.5. Quantitative statements cannot be derived due to the coverage of the sample with carbon, as demonstrated in the following.

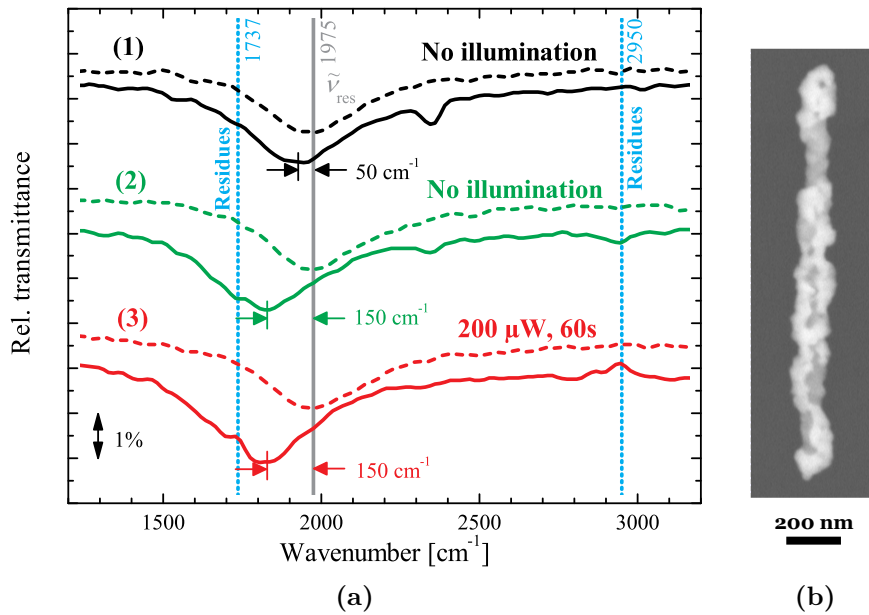


Figure 6.14.: (a) Relative transmittance spectra of three rods before (dashed) and after (solid) carbon evaporation. The solid gray line indicates the initial resonance position whereas the blue dotted lines represent vibrational positions of organic molecules. The peaks at around 2350 cm⁻¹ are due to CO₂. (b) SEM image of rod (3) taken with the BSE detector. Agglomerations of photo-chemically reduced gold show up in brighter color.

Influence of Carbon Layer To investigate the influence of the carbon layer, Fig. 6.14a compares IR spectra of individual rods before and after carbon evaporation. Note that the spectra were recorded at a resolution of 32 cm⁻¹ to allow short measurement times at sufficient signal-to-noise ratio. Nevertheless, the low-resolution spectra can be used for analysis, as the comparison to spectra of higher resolution suggests (see Fig. B.4). The resonance of the non-illuminated rod (1) shifts about 50 cm⁻¹ to smaller frequencies, possibly caused by the higher refractive index of the surrounding carbon layer (see Sec. 2.4.1). However, the spectral shift of the other non-illuminated rod (2) is clearly bigger than that of rod (1) and nearly identical to the illuminated rod (3). This discrepancy could be explained by a nonuniform thickness of the carbon layer. The more likely variant, however, is that residues of the solvent cause the shifts of rod (2) and (3), as the weak features at around 1737 cm⁻¹ (C=O stretching) and 2950 cm⁻¹ (CH₂ stretching), being typical for organic molecules, suggest. Moreover, rod (3) has photo-chemically grown (see Fig. 6.14b), which certainly contributes to spectral changes. Consequently, observed shifts cannot be clearly attributed to either changes of rod geometry or surrounding polarizability, respectively. For this reason, a quantitative analysis of $\Delta\lambda_{\text{res}}/\lambda_{\text{res}}$ cannot be performed for Antenna#18.

6. Characterization and Preparation of Nanogaps

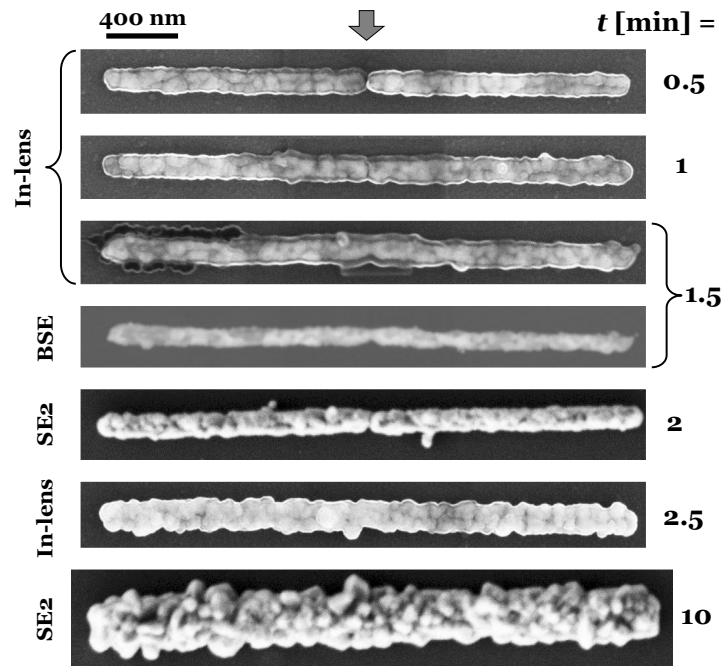


Figure 6.15.: Series of SEM images of nanorod dimers with initial gap width of $g_x \approx 20$ nm. The illumination times ($P = 200 \mu\text{W}$) are indicated on the right side whereas the electron detector is given on the left side.

SEM Images Figure 6.15 shows a selection of SEM images of nanorod dimers that were illuminated between 0.5 and 10 min. It is hard to decide whether the dimers illuminated for $t = 0.5$ min and $t = 1$ min are already merged or not (potential gap position indicated by an arrow). In addition, the rods are covered with a carbon layer which be identified as a shell surrounding the rod in the In-lens detector. In contrast, the dimer appears narrower in the material-specific BSE detector⁷ image and also the dirt agglomeration on the left side of the In-lens image is invisible. Moreover, darker and brighter facets can be identified in the BSE image (see also Fig. 6.14a). Most likely, the brighter parts originate from photo-chemically deposited gold. Nevertheless, the SEM images suggest a coalescence of the dimer illuminated for $t = 1.5$ min, resulting in a single rod of double length. Concerning the dimers irradiated for $t = 2.5$ min and $t = 10$ min, the coalescence is obvious, whereas no conclusion can be drawn for the dimer with $t = 2$ min.

⁷The images were recorded at the Dresden University of Technology and the SEM was equipped with a BSE detector besides the standard SE2 and In-lens detectors (see Sec. 3.1.2 for different detector types).

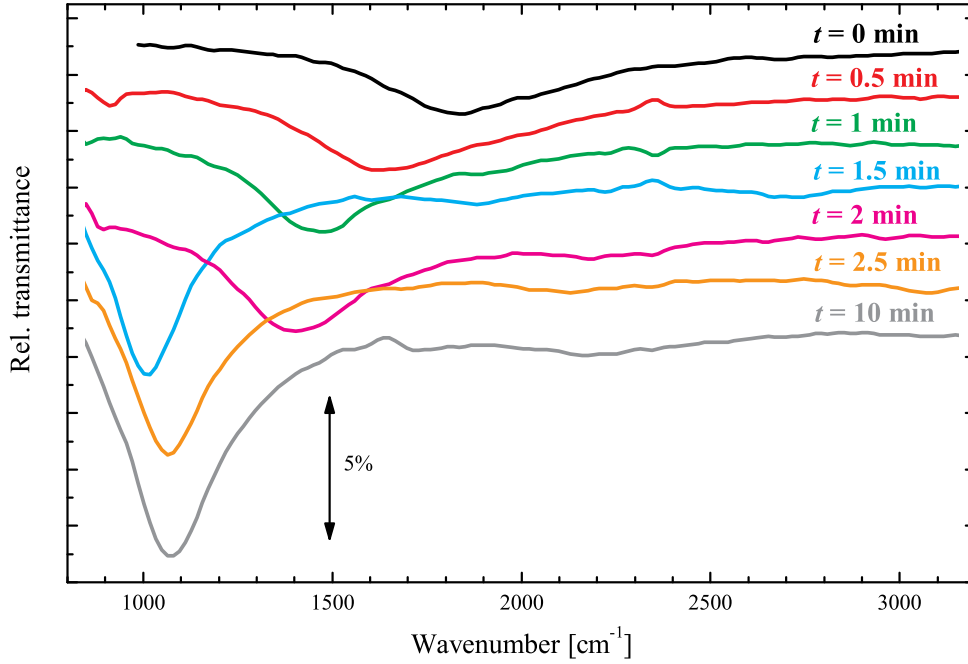


Figure 6.16.: Relative transmittance spectra corresponding to the dimers shown in Fig. 6.15. The spectra are artificially shifted.

IR Optical Characterization The question whether the first three dimers of Fig. 6.15 are connected or not can be figured out by analyzing their IR optical spectra shown in Fig. 6.16 (red, green and blue spectra). The resonances of the $t = 0.5$ min and $t = 1$ min dimer are shifted to lower frequencies compared to the resonance of a dimer with $g_x \approx 20$ nm *before* the metal deposition (black spectrum), indicating a decrease of the gap size (Sec. 2.5). In contrast, a strong resonance at around 1000 cm^{-1} is found for the dimer illuminated for $t = 1.5$ min. The resonance frequency is roughly one half of the resonance frequency of a single nanorod ($\tilde{\nu}_{\text{res}} \approx 1980 \text{ cm}^{-1}$, see Sec. 6.2.3.3), suggesting that the two individual rods of the dimer merged into a single rod of doubled length ($L \rightarrow 2L \Rightarrow \tilde{\nu}_{\text{res}} \rightarrow \frac{1}{2}\tilde{\nu}_{\text{res}}$, see Sec. 2.4.1). Similar behavior is observed for the dimers illuminated for 2.5 min and 10 min. These findings support the conclusions made from the SEM images of Fig. 6.15, namely that the dimers illuminated for 1.5, 2, and 10 min have merged. Concerning the dimer illuminated for $t = 2$ min, the IR spectrum suggests that the gap between the rods still exists. This result is surprising since this dimer was illuminated for a longer time compared to the already merged dimer with $t = 1.5$ min. To explain the observed discrepancy, the spatial arrangement of the illuminated rods within one pattern has to be considered.

6. Characterization and Preparation of Nanogaps

In the case of the dimer with $t = 2$ min, being located at position 6 within the pattern (see Fig. 6.11), only position 4 was additionally irradiated. Conversely, all other positions within the pattern of the dimer with $t = 2$ min (position 6) have been illuminated, leading to the conclusion that gold ions have diffused from irradiated to non-irradiated places. This result will be supported by the findings of sample Antenna#19.

Preparation Defects and Appearance of Additional Mode The lithographic preparation of dimers failed in some cases, which is for example illustrated in Fig. 6.17a, where dimer (1) consists of a longer ($L_1 \approx 1460$ nm) and a shorter rod ($L_2 \approx 950$ nm). The corresponding IR spectra before and after photo-induced metal deposition are shown in red in Fig. 6.17b. Since the dimer was located far away from any illumination spot (more than 1 mm), no gold deposition should have occurred. Most likely, the slight red-shift of the resonance is due to the carbon layer covering the dimer. Nevertheless, two resonances are visible: a stronger at around 1980 cm^{-1} , corresponding to the one of a single rod (see Fig. 6.12), and a weaker at around 2850 cm^{-1} . Based on the relation $\lambda_{\text{res}}(L)$ of non-interacting nanorod arrays on CaF_2 (Sec. 4.3.1),

$$\lambda_{\text{res}}(L) = 0.46\ \mu\text{m} + 3.19 \cdot L,$$

one calculates $\tilde{\nu}_{\text{res}}(L_2 \approx 950\text{ nm}) \approx 2870\text{ cm}^{-1}$. Hence, the observed resonances can be attributed to those of individual nanorods of different length.

In the spectrum of dimer (2), which was illuminated for $t = 2$ min at $200\ \mu\text{W}$, an additional mode at around 2200 cm^{-1} (marked by arrow) appears after gold deposition. The origin of this mode cannot be explained by different rod lengths, as shown by the SEM image of dimer (2). Moreover, the slight asymmetry of the left rod of dimer (2) cannot account for the additional mode, otherwise, this mode should be clearly more pronounced for dimer (3).

Admittedly, a slight dent at around 2000 cm^{-1} is visible for dimer (3) after carbon evaporation, however, this dent is also present in the spectrum of dimer (4) featuring no obvious defect in shape besides the irregular and rough surface structure. As we will see in the analysis of sample Antenna#19, this additional mode preferentially appears for dimers which have been photo-chemically grown. Hence, its appearance is probably related to the narrowing of the gap.

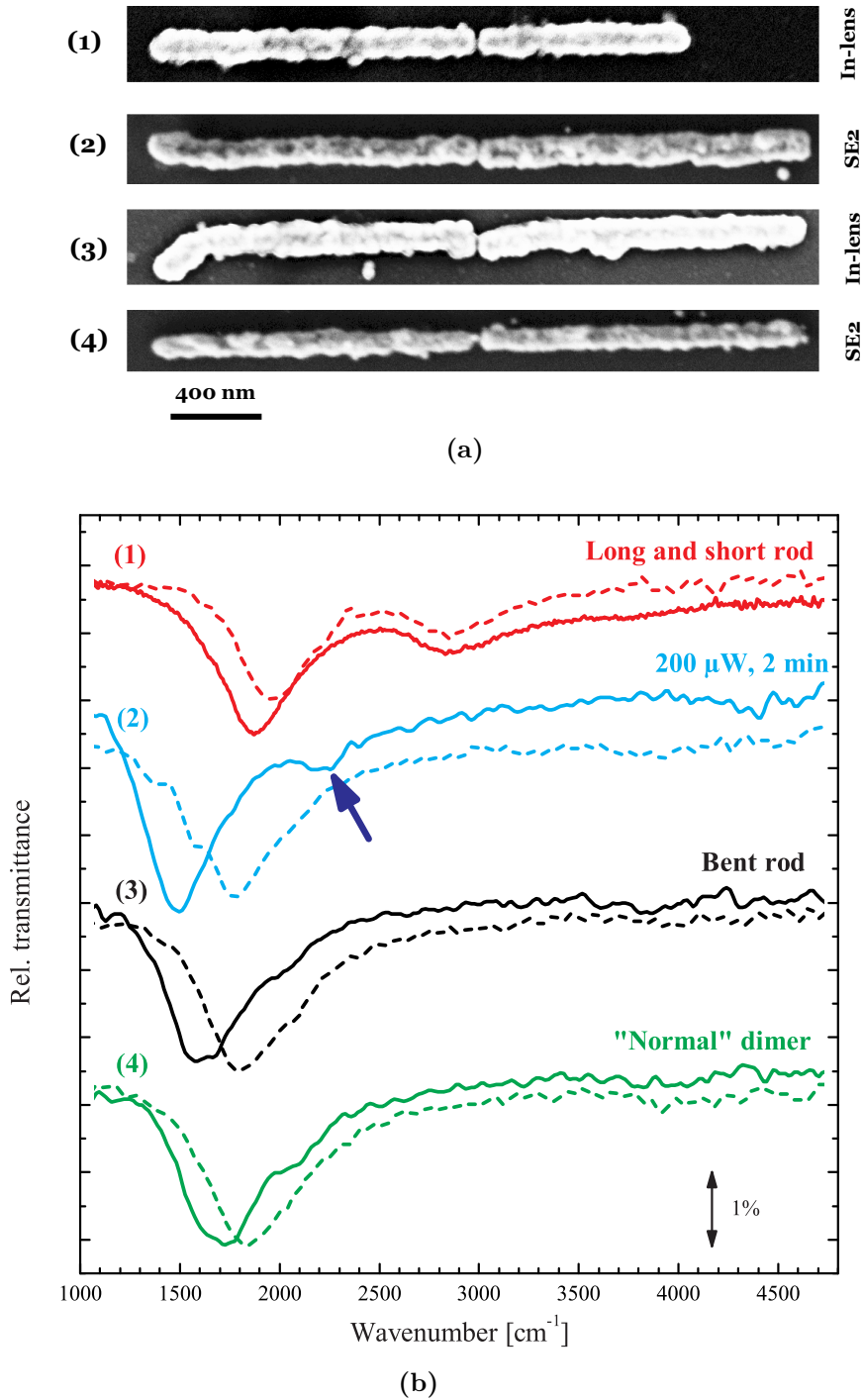


Figure 6.17.: (a) SEM images of four dimers with initial gap size of $g_x \approx 20$ nm. (b) Relative transmittance spectra before (dashed) and after (solid) metal deposition for the dimers shown in (a). Dimers (1), (3), and (4) were not directly illuminated whereas dimer (2) was irradiated for 2 min at a power of $P = 200 \mu\text{W}$. All spectra were recorded at a resolution of 32 cm^{-1} (500 scans) except the spectrum of dimer (1) after deposition (4 cm^{-1} , 10000 scans).

6. Characterization and Preparation of Nanogaps

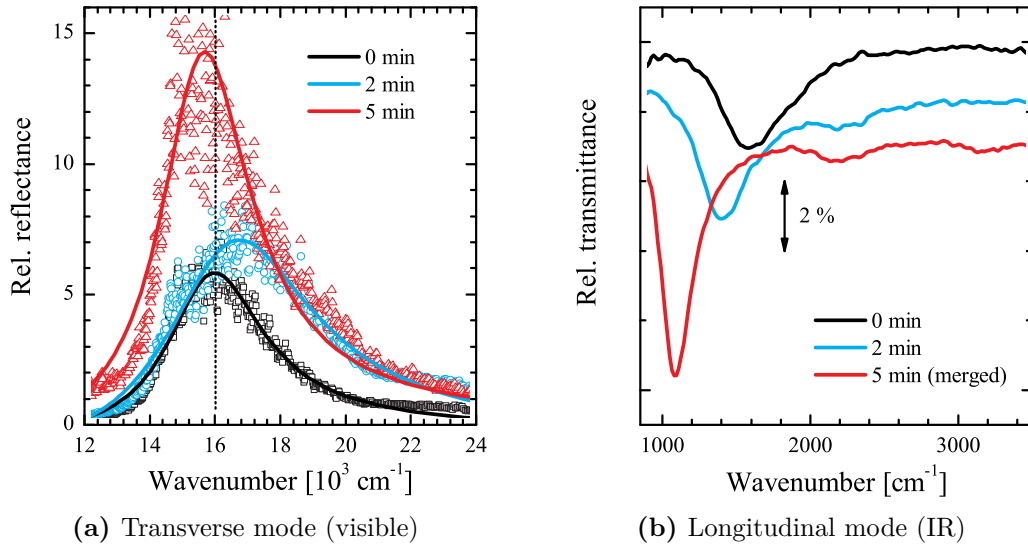


Figure 6.18.: (a) Transverse and (b) longitudinal antenna resonances for nanorod dimers illuminated for different time periods at a constant laser power of $P = 200 \mu\text{W}$. The sample was covered with glycol to record the spectra of (a), where the measured data (open symbols) were fitted with Lorentz profiles (solid lines). The spectra of (b) were acquired after the sample was covered with carbon.

Transverse Antenna Mode Figure 6.18a shows relative reflectance spectra in the visible range of three nanorod dimers (initial gap size $g_x \approx 20 \text{ nm}$) which were illuminated for the indicated time periods at $P = 200 \mu\text{W}$. Due to the perpendicular polarization of the incident light relative to the long rod axis, the observed peaks are attributed to transverse antenna resonances of dimers. The intensity of the resonances grows with illumination time, indicating the larger volume of the dimers. However, the blue-shift of the resonance from $t = 0 \text{ min}$ to $t = 2 \text{ min}$ might be surprising since a red-shift of the transverse mode is expected with increasing rod diameter (in analogy to the longitudinal mode with increasing L).

In addition, Fig. 6.18b shows the longitudinal antenna resonances of the same dimers, suggesting that the dimer illuminated for 5 min has already merged while the dimer irradiated for 2 min seems to still feature a gap. Consequently, the blue-shift of the *transverse* mode can be explained in analogy to the blue-shift of the *longitudinal* mode with decreasing d_y (Sec. 5.1), as illustrated by Fig. 6.19. Here, a reduction of the distance d_y perpendicular to the long rod axis considering the longitudinal mode corresponds to a decrease of the gap g_x in case of the transverse modes. Furthermore, the slight red-shift of the transverse mode after 5 min (red spectrum in Fig. 6.18a) compared to the initial state (black spectrum) can be explained by the increased

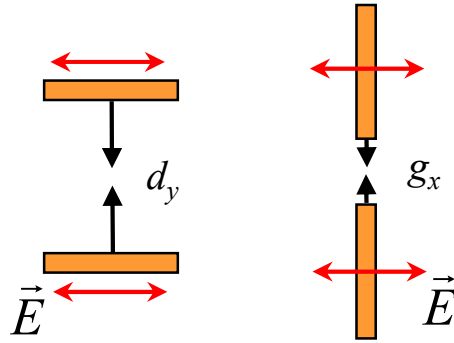


Figure 6.19.: The reduction of the gap size g_x when considering coupling of the transverse resonances (right) is similar to the decrease of the transverse distance d_y in case of longitudinal resonance coupling (left). The red arrows indicate the orientation of the incident electric field.

diameter of the merged dimer. Hence, the transverse mode seems to be suited to identify the coalescence of the two dimer parts.

Summary (Antenna#18) First of all, nanorod dimers covered by a carbon layer feature the expected IR optical response of dimers, indicating that carbon coverage does not result in a “short-cut” between the two individual rods of the dimer. Furthermore, the precipitation of gold on the rods occurs quite irregularly. Moreover, conclusions from observed spectral shifts cannot be drawn due to the carbon coverage and due to residues of the solvent. However, IR spectroscopy could be used to determine coalescence of the rods. In addition, the transverse antenna mode, located in the visible spectral range, seems to be a useful indicator for the merging process.

6.2.3.5. Results of Antenna#19

On sample Antenna#19, the sets 1-1 and 1-2 (see Fig. 6.11) were illuminated for different times, each at a constant laser power of $P = 90\mu\text{W}$ and $P = 180\mu\text{W}$, respectively. First of all, single rods that have not been illuminated by the laser beam will be analyzed to check the selectivity of the method.

Non-Illuminated Single Rods In Fig. 6.20a, the *normalized resonance frequency* (ratio between $\tilde{\nu}_{\text{res}}$ after and before metal deposition) is plotted for several single nanorods. The values of the rods of set 3-2, which is spatially far away from any illumination spot (more than 2mm), are all very close to 1.0, indicating no change of the rod’s geometry. In contrast, the values of the sets 1-1 and 1-2 strongly deviate

6. Characterization and Preparation of Nanogaps

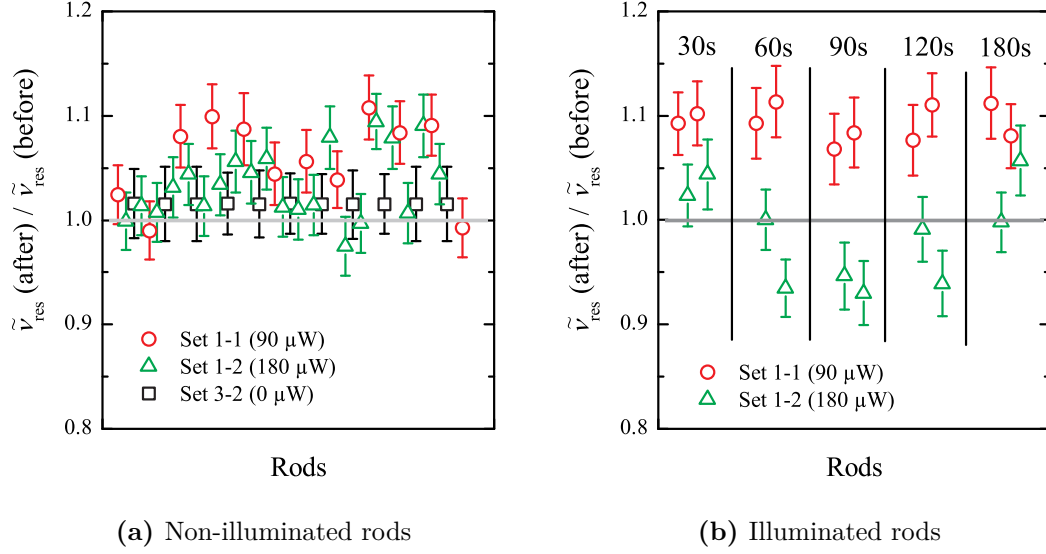


Figure 6.20.: Normalized resonance frequency for (a) non-illuminated and (b) illuminated single nanorods.

from the ideal 1.0-horizont. Most of the normalized resonance frequencies feature values bigger than one, corresponding to a resonance blue-shift probably due to increased rod diameter (see 2.4.1). Consequently, the photo-chemical method is not absolutely selective. Most likely, gold ions from illuminated spots diffuse to other sites. Hence, the separation distance of $30\mu\text{m}$ between the dimers seems to be insufficient to avoid metal deposition on non-illuminated sites (for the given gold salt concentration and laser power).

Illuminated Single Rods The relative spectral shift $\Delta\lambda_{\text{res}}/\lambda_{\text{res}}$ is defined as the change of λ_{res} of dimers, consisting of rods with length L , width w , and height h , compared to λ_{res} of single rods featuring *the same geometric dimensions* [see Eq. (6.1)]. However, growth of dimers results in variations of g_x as well as all geometric dimensions of the rods. Hence, to account for these morphological modifications, λ_{res} of grown dimers should be compared to λ_{res} of single rods that have been treated in the same way. Figure 6.20b shows the normalized resonance frequency of all illuminated single rods of the two sets 1-1 and 1-2. Concerning the data of set 1-1, all resonances shift to higher frequencies most likely due to increased rod diameter. In contrast, the data of set 1-2, which was irradiated with higher laser power, shows changes of $\tilde{\nu}_{\text{res}}$ to smaller *and* higher values. Since gold ion diffusion is expected to be stronger for higher laser intensity, set 1-2 is not discussed in the remainder of the analysis.

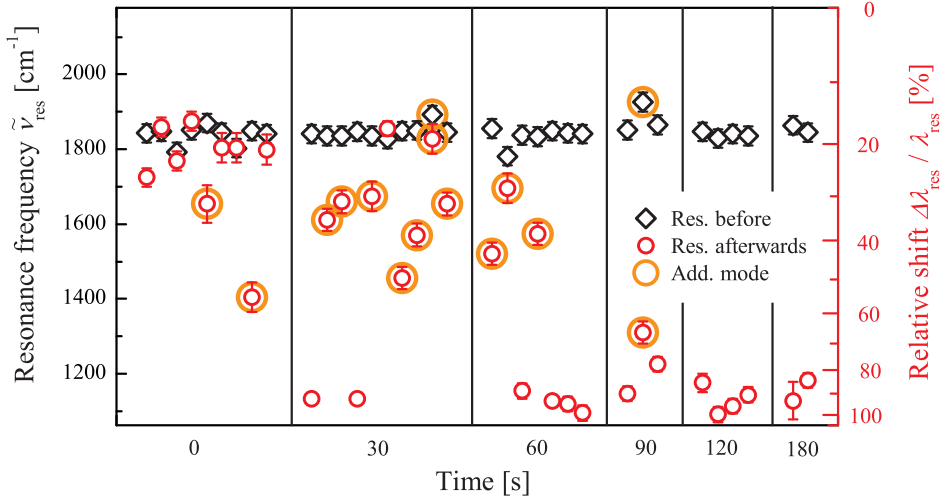


Figure 6.21.: Resonance frequency $\tilde{\nu}_{\text{res}}$ before and after the photo-induced metal deposition experiment ($P = 90\mu\text{W}$) of nanorod dimers with initial gap $g_x \approx 20\text{nm}$. The dimers are ordered on the abscissa corresponding to the illumination time. The order within one block of constant time is arbitrary. The resonances featuring an additional, higher energy mode are marked with orange circles. On the right ordinate, the relative shift $\Delta\lambda_{\text{res}}/\lambda_{\text{res}}$ for the grown dimers is given (see text).

Analysis of Dimers Figure 6.21 shows the absolute values of $\tilde{\nu}_{\text{res}}$ (left ordinate) for several dimers before and after metal deposition ($P = 90\mu\text{W}$). The orange encircled data points represent dimers with an additional mode similar to the labeled one in Fig. 6.17b. The origin of this mode will be discussed in Sec. 6.2.3.6. The upper border of Fig. 6.21 at $\tilde{\nu}_{\text{res}} = 2180\text{cm}^{-1}$ represents the resonance position of a single, photo-chemically grown nanorod, which is approximately 10% higher than the resonance of a non-grown one (see Fig. 6.20b). On the right ordinate, the relative shift $\Delta\lambda_{\text{res}}/\lambda_{\text{res}}$ is given, which only applies for grown nanorods since the reference value of $\tilde{\nu}_{\text{res}} = 2180\text{cm}^{-1}$ was used to calculate $\Delta\lambda_{\text{res}}/\lambda_{\text{res}}$ ⁸.

The observed changes of $\tilde{\nu}_{\text{res}}$ of some non-illuminated dimers confirm the possibility of gold ion diffusion from illuminated to non-illuminated dimers. Furthermore, the deposition process seems to be quite inhomogeneous for $t = 30\text{s}$ and $t = 60\text{s}$ since the values of $\tilde{\nu}_{\text{res}}$ after deposition are strongly dispersed. While two dimers do not show any significant change of $\tilde{\nu}_{\text{res}}$, others exhibit strong shifts and some of them even merged, as indicated by their relative shifts of $\Delta\lambda_{\text{res}}/\lambda_{\text{res}} \approx 100\%$. Moreover,

⁸It is $\Delta\lambda_{\text{res}}/\lambda_{\text{res}} \approx 8\%$ for the non-illuminated dimers before metal deposition (see Fig. 6.13b).

6. Characterization and Preparation of Nanogaps

after 90s and more, all dimers have merged⁹. The broad distribution of $\tilde{\nu}_{\text{res}}$ for $t = 30\text{s}$ and $t = 60\text{s}$ is related to experimental difficulties concerning the focusing of the laser spot onto the sample. As soon as the laser for illumination is switched on, the sample has to be brought into the focus by maximizing the observed scattering signal. Since this manual focusing process is not easy to reproduce, the errors of the effective illumination time are more pronounced for shorter time periods.

Based on the reference value of $\tilde{\nu}_{\text{res}} = 2180\text{cm}^{-1}$, values of $\Delta\lambda_{\text{res}}/\lambda_{\text{res}}$ in the range between 25% and 50% are obtained for the supposedly separated dimers. A comparison with Fig. 6.13b suggests that gap sizes below 10nm have been prepared by the photo-chemical method. However, the calculated values of $\Delta\lambda_{\text{res}}/\lambda_{\text{res}}$ have to be treated with caution, since identical geometric dimensions of dimers and single rods are necessary for a quantitative comparison with the data of Fig. 6.13b. Hence, the values of $\Delta\lambda_{\text{res}}/\lambda_{\text{res}}$ may show a trend but they are not suited to exactly determine the gap size.

Summary (Antenna#19) It was shown that the photo-chemical approach can be used to modify gold nanorod dimers. From the observed spectral shifts of the fundamental resonance, gap sizes g_x in the range below 10nm seem to be prepared. However, the direct determination of g_x (e.g. by SEM) was not carried out yet, since the sample is intended for further (NAIRS) experiments. In addition, SEM measurements of g_x are very difficult (compare to the SEM data of Antenna#18). Other experimental methods, like transmission electron microscopy (see Sec. 6.3.2), might be better suited for measuring very small gaps. Moreover, an elaborate comparison with simulations could help to understand the spectral shifts of rods which are simultaneously growing in three dimensions. Finally, the reproducibility as well as the selectivity of the method still have to be improved. First approaches could be the reduction of the laser power or gold salt concentration and the increase of illumination time in order to minimize errors of the effective irradiation time. Moreover, the distance between individual dimers should be increased in future experiments.

⁹At $t = 90\text{s}$, one dimer with a shift of only $\Delta\lambda_{\text{res}}/\lambda_{\text{res}} \approx 70\%$ is present. Since an additional mode was observed before the metal deposition, it is most likely that the dimer features a structural defect similar to the one of rod (1) in Fig. 6.17b.

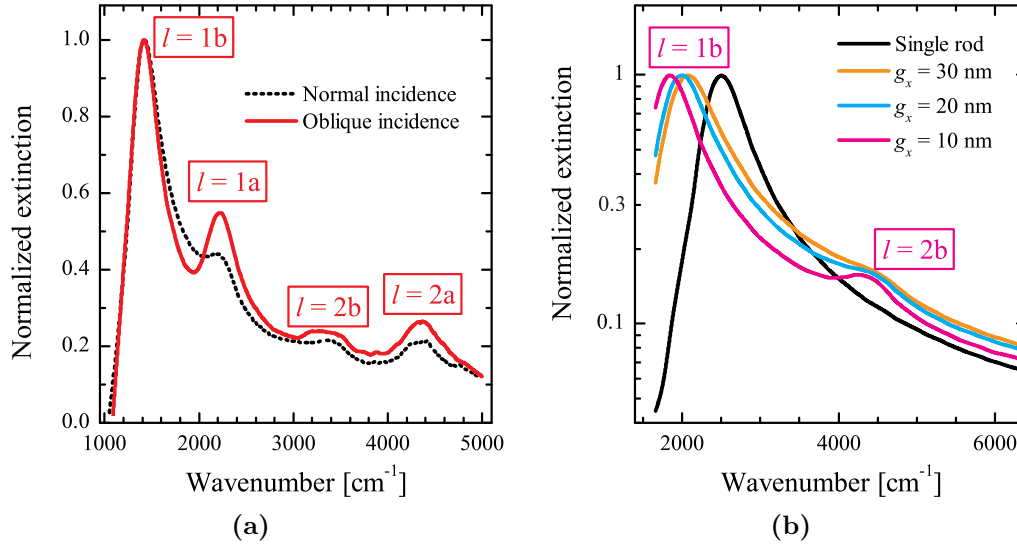


Figure 6.22.: (a) Normalized extinction spectrum of a photo-chemically grown nanorod dimer at normal and at oblique incidence (angle of incidence $\approx 30^\circ$, measurement geometry given in [110]). (b) Simulated, normalized extinction spectra [220] at normal incidence of a single nanorod and nanorod dimers featuring the same length L and cross-section $w \cdot h$ using the software CST microwave studio.

6.2.3.6. Mode Assignment

This section deals with the additional mode (see e.g. Fig. 6.17b) that preferentially appears for grown dimers with strong spectral shifts (see Fig. 6.21). The two dimers in Fig. 6.21, for which the mode was observed *before* metal deposition, are excluded from discussion since they most likely feature structural defects (compare to Sec. 6.2.3.4).

In Fig. 6.22a, the dotted black curve shows a normalized extinction spectrum of a dimer with a relatively large shift ($\Delta\lambda_{\text{res}}/\lambda_{\text{res}} \approx 50\%$). Besides the fundamental resonance at around 1400 cm^{-1} , three other modes can be identified. First, the mode at around 2220 cm^{-1} is considered, which was referred to as “additional mode” in the previous analysis. For oblique incidence of light ($\approx 30^\circ$, solid red curve), this mode gains in intensity relative to the fundamental mode, indicating dipole inactivity of the mode [70, 110]. The coupling of the fundamental ($l = 1$) modes of individual rods to bonding ($l = 1b$) and antibonding ($l = 1a$) dimer modes (see Fig. 6.23) could provide a possible explanation. In case of the $l = 1a$ mode, charge carriers of equal sign are repelling each other near the gap, leading to a higher energy of the mode compared to the $l = 1$ mode. In contrast, the $l = 1b$ mode features lower energy since opposite charges attract each other [82]. Since an overall dipole moment does not exist for the

6. Characterization and Preparation of Nanogaps

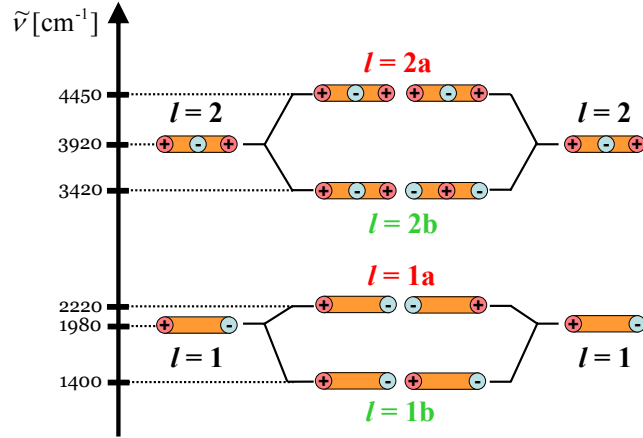


Figure 6.23.: Schematic representation of possible mode couplings in a nanorod dimer. The frequency values of the coupled dimer modes are extracted from Fig. 6.22a, whereas the ones of the single rods are taken from measurements before metal deposition (Sec. 6.2.3.3).

$l = 1a$ mode, this dark mode is attributed to the “additional mode”. It is known that the $l = 1a$ mode can be excited when either the symmetry of the structure [221–224] or the symmetry of the excitation [225–228] is disturbed. In our case, a slight tilt of the sample (see Sec. 2.4.3) and the non-perfect structure of the grown dimers (see SEM images in Fig. 6.15) are possible reasons for symmetry breaking. In addition, only very small gap sizes below 20 nm lead to a sufficiently high energy splitting of the two modes [229]. Hence, the appearance of $l = 1a$ suggests that the preparation of very small gaps was successful with the presented method.

The origin of the other two modes in Fig. 6.22a can be explained in a similar way. The $l = 2$ modes of single rods can couple to dimer modes, one at higher energy ($l = 2a$) and another at lower energy ($l = 2b$, see Fig. 6.23). Note that the dark $l = 1a$ and $l = 2a$ modes should not appear at normal incidence for perfectly symmetric dimers. This is confirmed by the simulations shown in Fig. 6.22b, where the weak mode at around 4300 cm^{-1} in case of $g_x = 10 \text{ nm}$ is attributed to the $l = 2b$ mode¹⁰.

Figure 6.24 shows the resonance positions of the identified dimer modes in dependence of the fundamental resonance position as a measure for the separation distance g_x . Starting from the single rod at $\tilde{\nu}_{\text{res}} = 1980 \text{ cm}^{-1}$, only two distinct modes exist ($l = 1$ and $l = 2$). As soon as the frequency of the fundamental resonance (and accordingly the gap size) decreases, the second order mode (now $l = 2a$) shifts two higher values. For sufficiently small gaps, the $l = 2b$ and $l = 1a$ modes appear. After

¹⁰The assignment is based on the fact that the ratios between the resonance frequencies of the $l = 2b$ and the $l = 1b$ are 2.4 for both experiment (Fig. 6.22a) and simulation (Fig. 6.22b).

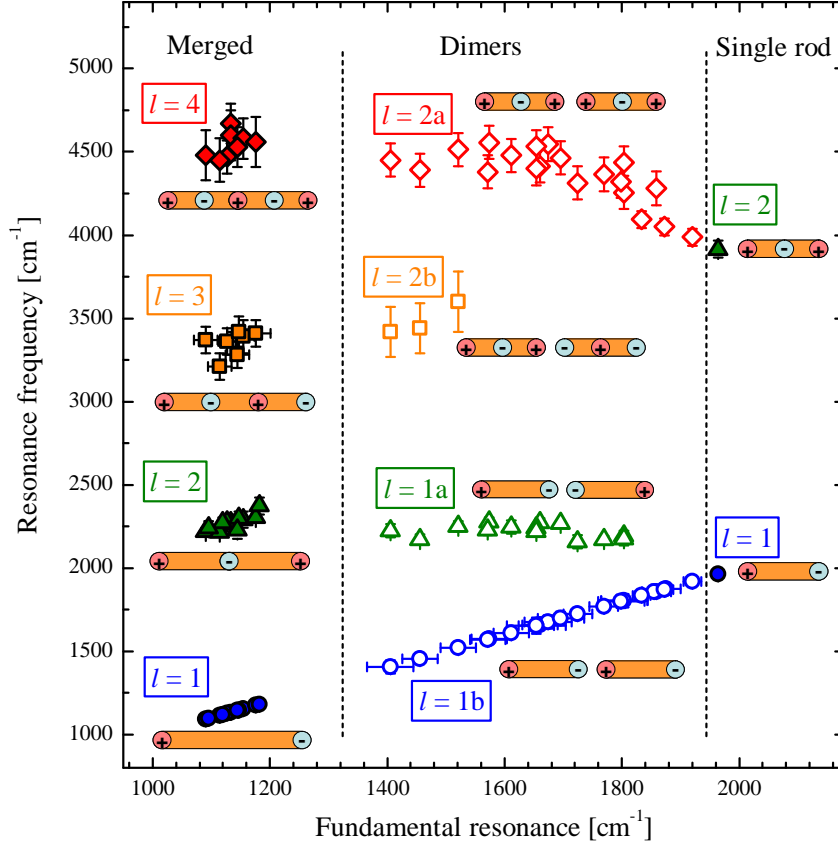


Figure 6.24.: Behavior of all assigned modes of nanorod dimers with respect to the fundamental resonance position as a measure for separation (see text). The idealized charge carrier distributions of the respective modes are indicated.

merging of the rods, four distinct modes are observed which are attributed to $l = 1$ to $l = 4$. These modes can be considered as the border cases of the coupled dimer modes for $g_x = 0$ (in case of the bonding modes, the opposite charges at the gap cancel out). In Fig. B.5, selected relative transmittance spectra of the data shown in Fig. 6.24 are depicted.

Finally, it should be mentioned that the $l = 1b$ and $l = 2a$ modes are always visible in spectra of nanorod dimers on CaF_2 . Concerning these two modes, the oscillations of the electrons inside the respective single rods occur *in-phase* (see Fig. 6.24). In contrast, the $l = 1a$ and $l = 2b$ modes feature *anti-phase* oscillations which can only be excited for very small gaps below 20 nm. Hence, the *phase correlation* between the oscillations in the rods is the decisive factor determining mode activation at rather large gaps (> 20 nm), while the selection rule (dipole activity) does not hold due to symmetry breaking.

6. Characterization and Preparation of Nanogaps

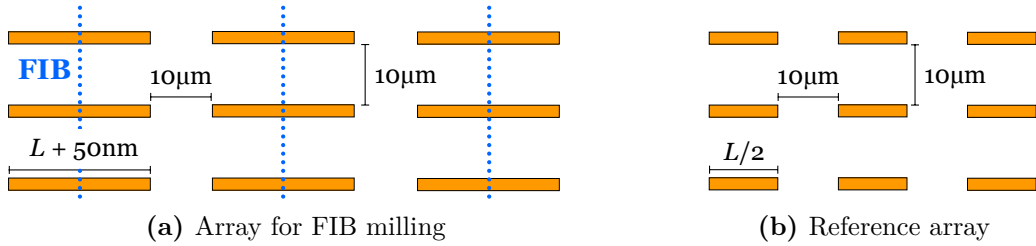


Figure 6.25.: (a) Schematic drawing of a nanoantenna array intended for nanogap formation. Nine rods of length $L + 50\text{nm}$ were cut in the middle by FIB to prepare dimers with a length of about $L/2$, taking into account the approximate material loss caused by FIB milling. (b) Corresponding reference array with nine nanorods of length $L/2$.

6.3. Focused Ion Beam milling

Some parts of the present section are adopted from [108]. The focused ion beam (FIB) technology is an established technique for the preparation of nanoelectrodes [230–232]. Especially FIB milling can be used to prepare gaps between metallic electrodes [38, 233]. The small spot size and low lateral exposure of the ion beam (in the order of 10nm [234]) allow a direct fabrication of well-defined nanostructures in the sub-20nm range. In addition, *in situ* monitoring provides the possibility of precise control over the fabrication process. Moreover, the speed of the nanogap cutting and reproducibility of the method are further advantages [38]. Besides the possibility of removing material (“milling”), a FIB machine can record images in analogy to a scanning electron microscope (“imaging”). The basic principles of FIB milling and imaging are nicely reviewed in [235].

The sample preparation by FIB as well as the sample layout are introduced in Sec. 6.3.1. Afterwards, Sec. 6.3.2 briefly explains the transmission electron microscopic (TEM) technique, which was used to investigate the success of the nanogap formation. The experimental results are divided into two parts: First, the results of silicon samples covered with a natural oxide layer (preparation series C, see Tab. 3.1) are shown in Sec. 6.3.3. After that, findings from thermally oxidized silicon samples (preparation series H) are analyzed in Sec. 6.3.4. In both cases, IR spectroscopic measurements are compared to SEM and TEM images.

6.3.1. FIB Sample Preparation and Layout

Nanogaps were milled in EBL-fabricated gold nanorods using Ga^+ ions in a HITACHI FB-2000 single-beam FIB machine (acceleration voltage $U_{\text{acc}} = 40\text{kV}$) at the NIMS

Series	Dose no.	N	I_{beam} pA	t_{dwell} μs	A_{spot} nm^2	$D \cdot A_{\text{spot}}$ $10^{-15} \text{ C / spot}$	D C / cm^2
C	I	140	20	3	12×12	8.4	5.8
C	II	280	20	3	12×12	16.8	11.7
H	III	2	10	140	6×6	2.8	7.7
H	IV	2	10	170	6×6	3.4	9.4
H	V	2	10	200	6×6	4	11.1

Table 6.1.: Overview on the different FIB parameters (scan repetition N , beam current I_{beam} , dwell time t_{dwell} , and exposed spot size A_{spot}). The calculated doses D [Eq. (6.2)] are given in charge per scanning spot as well as charge per exposed area, since A_{spot} differs for the two preparation series C and H.

in Tsukuba, Japan. The focused Ga^+ beam with a spot size of A_{spot} is scanned over the substrate and the rods, as indicated by the blue dotted lines in Fig. 6.25a. Each spot was exposed to the FIB for a certain (dwell) time t_{dwell} at a constant beam current I_{beam} , and this process was repeated for N times. To quantify the amount of Ga^+ ions impinging on the sample, the dose D is defined as:

$$D = N \cdot \frac{I_{\text{beam}} \cdot t_{\text{dwell}}}{A_{\text{spot}}}. \quad (6.2)$$

All arrays consist of exactly nine rods which are separated by $10 \mu\text{m}$ in each direction. For each FIB-milled array (Fig. 6.25a), a reference array was prepared with nanorods featuring approximately one half of the length (Fig. 6.25b). Hence, a complete separation of the two parts should lead to an optical response similar to the one of the reference array. Finally, Tab. 6.1 summarizes the different Ga^+ ion doses, labeled dose I to V, used for nanogap fabrication.

6.3.2. Transmission Electron Microscopic Analysis

Transmission electron microscopy is a technique similar to optical microscopy. However, electrons and electromagnetic lenses are used instead of light and refractive lenses to create the image. Since high energetic electrons feature a very small wavelength compared to visible light, atomic resolution is possible. The image is formed from the interaction of the electrons transmitted through the specimen which therefore has to be very thin [236].

6. Characterization and Preparation of Nanogaps

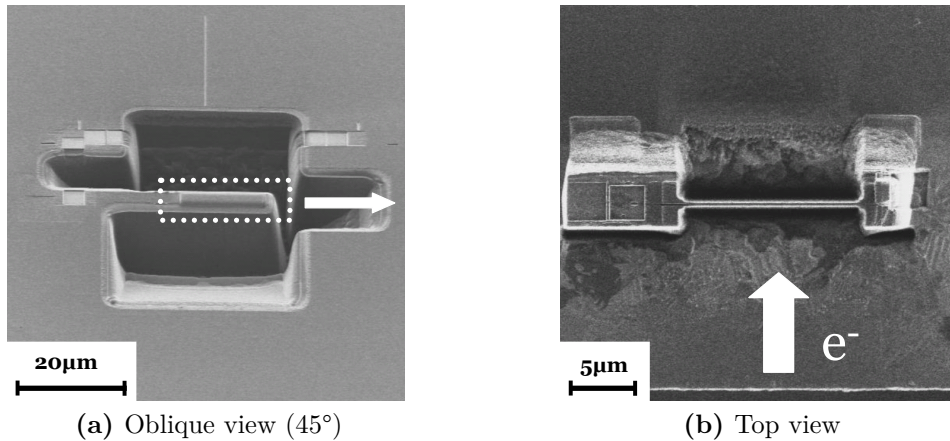


Figure 6.26.: Preparation of TEM samples. (a) The substrate around the dimer is milled out by the FIB. Subsequently, a part of the sample (labeled with white dots) is further thinned out and transferred on a Cu mesh for observation. (b) Top view on the TEM specimen. The electrons pass the sample in the plane of projection, indicated by the white arrow.

First, the substrate was covered with an organic protection layer and a 30 nm electron-beam deposited platinum layer. Afterwards, a cross-sectional slice (thickness less than 100 nm) was prepared with the Ga^+ ion beam (see Fig. 6.26). TEM measurements on this specimen were carried out using a *JEOL JEM-3100F* high resolution scanning transmission electron microscope coupled to an *NORAN EDX* attachment allowing energy-dispersive x-ray (EDX) spectroscopic measurements¹¹.

TEM Example

Figure 6.27a shows a TEM image of a FIB-milled nanogap (dose comparable to dose II, see Tab. 6.1) with a complete cut through a gold nanorod. The layered structure of the lithographically prepared test sample can be identified. Above the silicon substrate, there is a very thin native SiO_2 layer (≈ 3 nm), a 25 nm thick titanium adhesion layer and a part of a 100 nm thick gold rod. The rod is completely cut by the FIB and the gap size is about 80 nm to ensure a complete separation of the milled parts for this particular sample. The recess at the Au/Ti interface (marked by an arrow in Fig. 6.27a) can be explained by the higher sputtering rate of gold compared to titanium [38]. The dark, particulate-like materials at the bottom of the gap are Ga residues (confirmed by EDX [122]) implanted into the Si substrate. In

¹¹EDX is an analytical technique to analyze the chemical composition of a sample and can be coupled to SEM or TEM, respectively. The atoms of the sample are excited by the electron beam and emit element-specific x-rays [237].

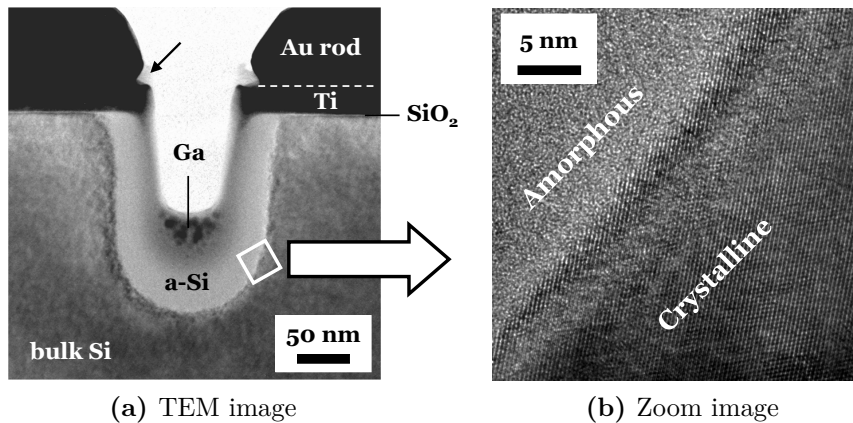


Figure 6.27.: (a) TEM image of a cross-sectional FIB-milled nanogap specimen. (b) High-resolution TEM image of the region marked by a square in (a). The lattice-resolved image shows the interface between crystalline silicon substrate and ion beam-induced amorphous silicon.

addition, Fig. 6.27b shows a high-resolution image of the square in Fig. 6.27a. While the ion beam changes the silicon structure to be amorphous, the rest of the bulk silicon remains crystalline, showing the lattice fringes from (111) atomic planes [238].

6.3.3. Results - Natural Oxide Covered Silicon

6.3.3.1. Effect of FIB Imaging

During nanogap preparation, the area around the nanorods is scanned with the Ga⁺ beam (FIB imaging) to localize the nanorods as well as to properly focus the ion beam [123]. In addition, FIB images recorded after the fabrication process are used to control the quality of the preparation. However, it turned out that FIB imaging induced changes of the substrate's optical properties, as shown in the visible microscopic image of Fig. 6.28a. The FIB imaging area appears brighter, which can be explained by the increasing reflectivity towards higher frequencies monitored in the relative reflectance spectrum of Fig. 6.28b. Due to this enhanced reflectance, less light is transmitted through the sample, explaining the decline of the baseline in the relative transmittance spectrum¹² of Fig. 6.28b.

Since FIB imaging always comes along with an implantation of Ga⁺ ions into the substrate [235, 239], the Ga⁺ ions might modify the optical properties of the substrate.

¹²Note that higher surface roughness of the substrate due to Ga⁺ bombardment would lead to a decrease of both transmittance and reflectance towards higher wavenumbers compared to a smooth surface.

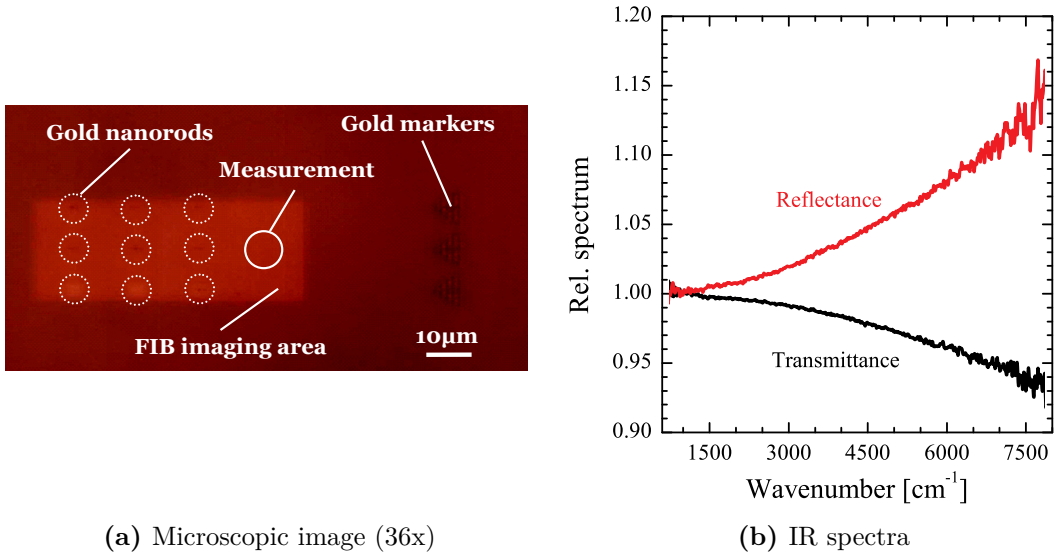


Figure 6.28.: (a) Image recorded by the CCD camera of the IR microscope (36-fold magnification). The triangular-shaped gold markers help to localize the nanorods, which are indicated by dotted circles. On the bright FIB scanned area, IR transmittance and reflectance spectra [see (b)] were taken at the position marked with an solid circle (“Measurement”, reference bare silicon, no polarizer).

In this context, a similar decrease of the transmittance was found for diamond in which gallium ions have been implanted by FIB [239]. In addition, it was reported that gallium preferentially accumulates at the SiO₂/Si interface, featuring the highest concentration on the silicon side of the interface [240] (gallium is a faster diffuser in silica [241]). Hence, amorphous gallium nanoparticles could form at this interface. Since amorphous gallium is a good metal [242], these nanoparticles could exhibit plasmon resonances. Taking the plasma frequency of gallium¹³, $\tilde{\nu}_p \approx 111\,500\text{ cm}^{-1}$ [242–244], into account, a resonance frequency of the Ga nanoparticles in silicon of $\tilde{\nu}_{\text{res}} \approx 22\,500\text{ cm}^{-1}$ follows from Eq. (2.15) with $\epsilon_d = \epsilon_{\text{Si}} = 11.7$. For this reason, it is possible that the observed decline of the baseline represents a tail of a plasmonic resonance located in the visible or UV spectral range.

6.3.3.2. FIB and SEM Characterization

Two FIB milling conditions (D_{I} and D_{II} with $D_{\text{II}} = 2 \cdot D_{\text{I}}$, see Tab. 6.1) were used to fabricate gaps between nanoantennas as described in Sec. 6.3.1. After

¹³SHKLYAREVSKII *et al.* showed that the plasma frequency of Ga grains is in the same range as the plasma frequency of gallium films [243].

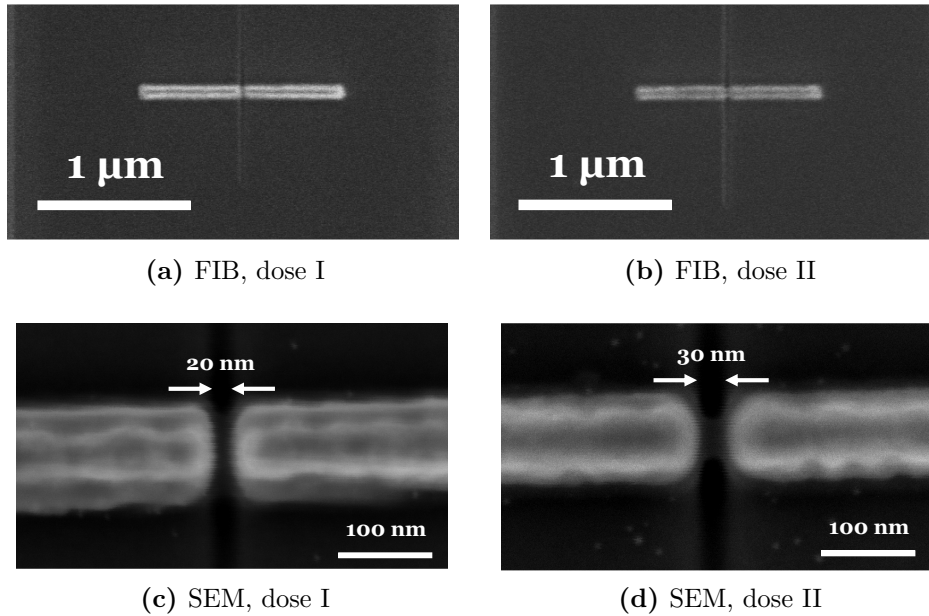


Figure 6.29.: (a,b) FIB images of FIB-milled (different doses indicated) nanorods recorded immediately after nanogap fabrication. The initial lengths were (a) $L \approx 1.35 \mu\text{m}$ and (b) $L \approx 1.25 \mu\text{m}$. (c,d) SEM images (In-lens detector) of the same FIB-milled nanogaps recorded after the IR optical characterization.

gap preparation, FIB images of the milled nanorods were recorded to control the fabrication process. Figures 6.29a and 6.29b show examples of two milled nanorods which seem to be completely cut in the middle. In addition, SEM images of the same milled nanorods (Figs. 6.29c and 6.29d), taken after IR spectroscopic investigation, apparently corroborate the successful milling process. Here, the gap produced by D_{II} seems to be slightly broader than that prepared by D_{I} , a result which was obtained for all investigated arrays (at least seven samples per dose condition).

6.3.3.3. IR Optical Characterization

Figure 6.30a shows relative transmittance measurements of two nanorod arrays, each of them measured with parallel and perpendicular polarization (relative to long rod axis). While FIB imaging and milling was performed on one of the arrays (labeled as “FIB”), the other array was not in contact with Ga^+ ions (“No FIB”). Consequently, the baseline decline is only observed for the FIB-scanned and -milled array, which shows an antenna resonance at around 1500cm^{-1} in case of parallel polarization.

6. Characterization and Preparation of Nanogaps

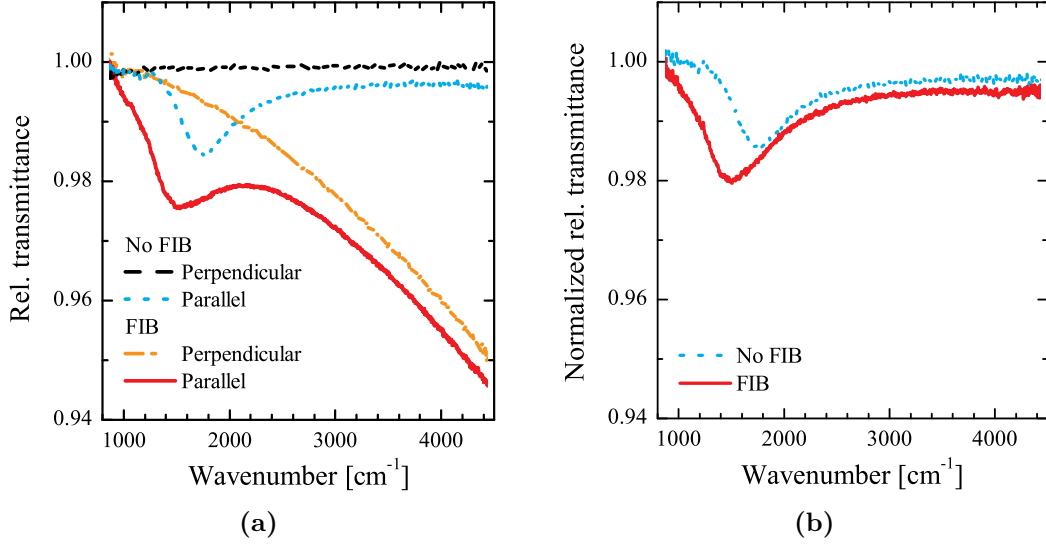


Figure 6.30.: (a) Relative transmittance spectra of two nanorod arrays ($w \approx 110\text{nm}$, $h \approx 100\text{nm}$) in parallel and perpendicular polarization. (b) Normalized relative transmittance spectra T_{norm} [Eq. (6.3)] of the same nanorod arrays.

Since the influence of the Ga^+ ions on the spectrum is polarization-independent, it can be eliminated by calculating the *normalized relative transmittance*

$$T_{\text{norm}} = \frac{T_{\text{rel},\parallel}}{T_{\text{rel},\perp}}, \quad (6.3)$$

which is the ratio between the relative transmittance in parallel ($T_{\text{rel},\parallel}$) and perpendicular ($T_{\text{rel},\perp}$) polarization. The solid red curve in Fig. 6.30b represents the T_{norm} -spectrum of the FIB-milled array of Fig. 6.30a. For comparison, the T_{norm} -spectrum of the reference array (“No FIB”) is added. Note that calculating T_{norm} is not absolutely necessary for non-milled arrays, since T_{norm} does not significantly differ from $T_{\text{rel},\parallel}$ (Fig. 6.30a).

Figure 6.31a shows normalized relative transmittance spectra of four nanorod arrays. The solid red and green spectra originate from two nanorod arrays of similar length which were milled with the different doses D_{I} and D_{II} . Obviously, the positions and line shapes of the resonances significantly differ for these two curves. While a nice antenna resonance with $\tilde{\nu}_{\text{res}} \approx 1900\text{cm}^{-1}$ is observed for the array milled with D_{II} , the array milled with D_{I} features a very broad resonance somewhere between 1100cm^{-1} and 1300cm^{-1} . Note that the double peak structure at around 1200cm^{-1} results from the excitation of the thin-film SPP in the SiO_2 layer (see Sec. 3.5.2).

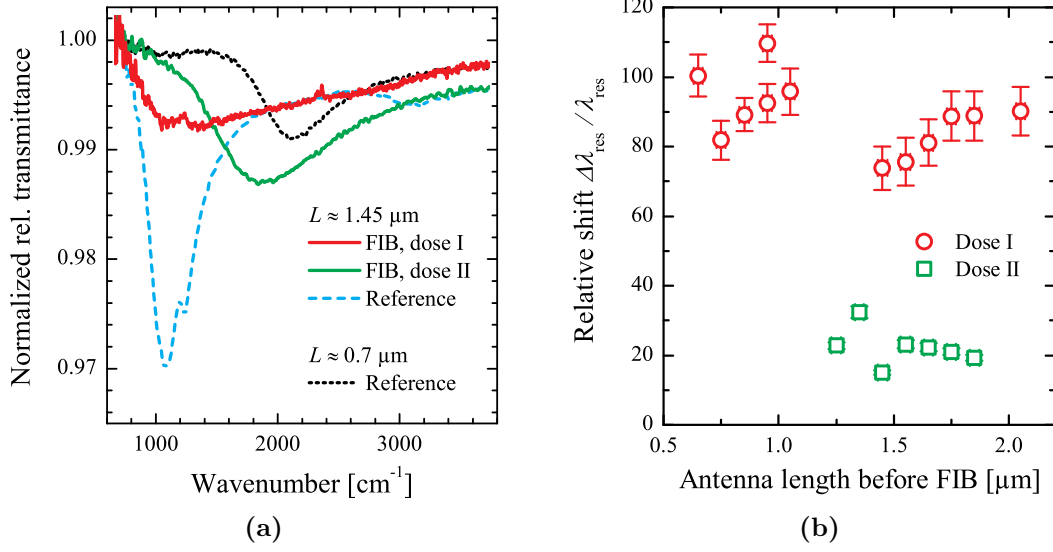


Figure 6.31.: (a) Normalized relative transmittance spectra of four nanorod arrays ($w \approx 110\text{nm}$, $h \approx 100\text{nm}$) with lengths *before* FIB milling as indicated in the figure. (b) Relative shift $\Delta\lambda_{\text{res}}/\lambda_{\text{res}}$ for nanorod arrays milled by different FIB dose conditions.

Complete Cut (D_{II}) To decide whether a complete separation of the nanorods was achieved, it is useful to compare the obtained spectra with those of non-milled reference arrays. The dashed blue spectrum in Fig. 6.31a is that of a nanorod array with approximately the same length L as the milled nanorods before FIB cutting. In addition, a spectrum of a reference array with rods featuring approximately half of the length ($L/2$, dotted black curve) is shown. In case of a complete cut of the rods, the resonances of the fabricated dimers should be similar to the one of the reference array with $L/2$. However, this is only true for the array milled with D_{II} . The shift to smaller wavenumbers and the increased resonance width Γ can be explained by interaction between the two separated parts (Sec. 5.2) and further support this conclusion. In addition, $\sigma_{\text{ext}}(\tilde{\nu}_{\text{res}})/\sigma_{\text{geo}}$ of the milled rods is smaller compared to $\sigma_{\text{ext}}(\tilde{\nu}_{\text{res}})/\sigma_{\text{geo}}$ of the reference array if one assumes that 18 rods contribute in case of a complete cut. All these results nicely fit to the findings from the FIB/SEM measurements (Sec. 6.3.3.2), which suggested a complete cut of the rods for D_{II} .

Incomplete Cut (D_{I}) In contrast, the resonance of the D_{I} -milled array is near the one of the reference array with the same length L before FIB milling. If the nanorods were separated, this very strong shift compared to the array with $L/2$ ($\Delta\lambda_{\text{res}}/\lambda_{\text{res}} \approx 90\%$) would indicate a very small gap and huge interaction. Moreover,

6. Characterization and Preparation of Nanogaps

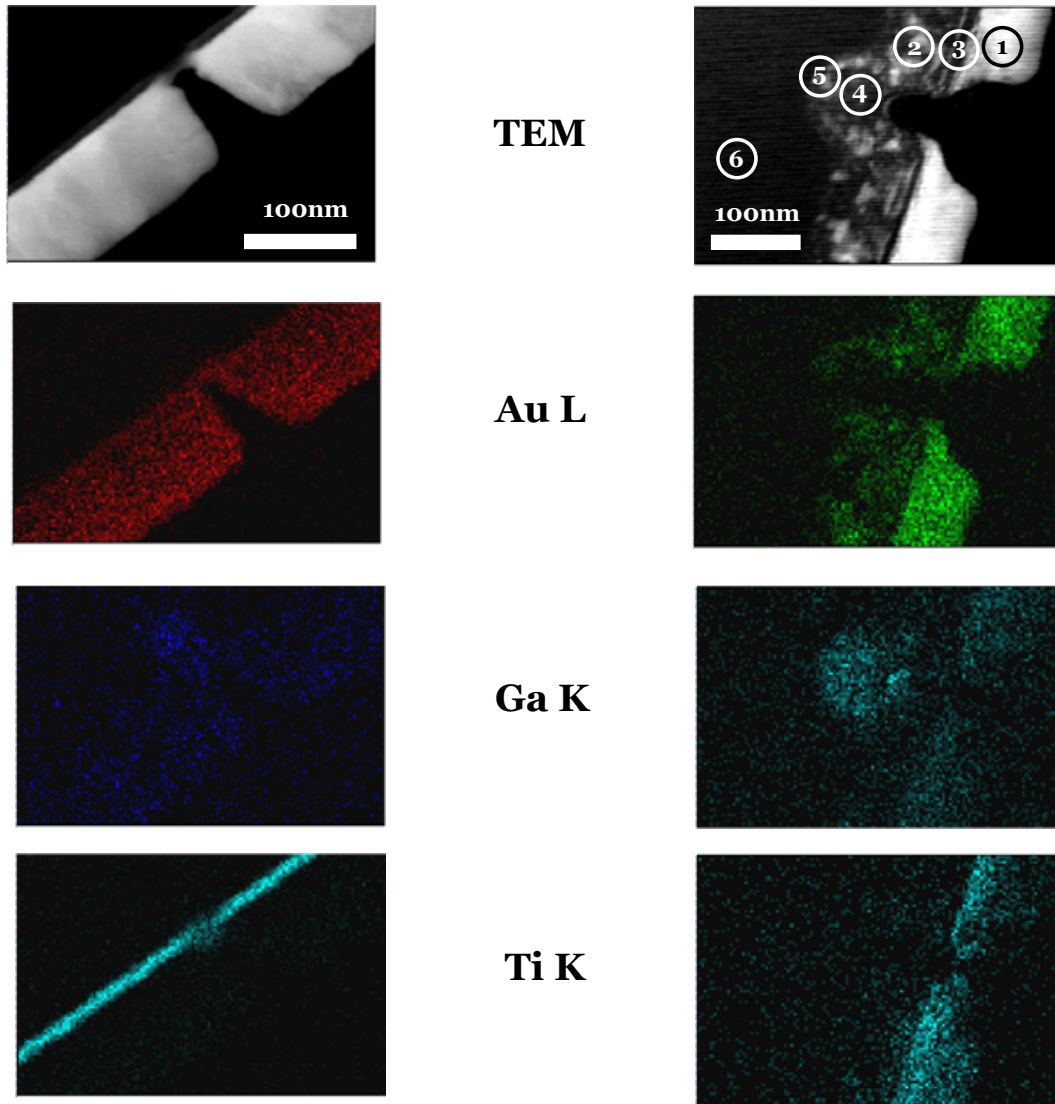
simulations of a dimer with a gap of only 4nm result in a shift of “only” 35% (see Fig. 6.13b). Hence, it is most likely that the two parts of the D_I -milled rods still feature conductive connections, leading to a plasmonic resonance position similar to the one of the reference array with length L . The decreased intensity and strong broadening may be related to the random structure of that connection, which distributes plasmonic intensity over various multipolar resonances [108]. Similar results were found for all other D_I -milled nanorods, resulting in values of $\Delta\lambda_{\text{res}}/\lambda_{\text{res}}$ near 100% (see Fig. 6.31b). In contrast, the relative shifts $\Delta\lambda_{\text{res}}/\lambda_{\text{res}}$ of the D_{II} -milled arrays are distributed between 10 and 30%, indicating complete gaps. Note that the exact values of $\Delta\lambda_{\text{res}}/\lambda_{\text{res}}$ may not be overinterpreted since the geometric dimensions of the reference rods might differ from those of the milled rods. The relative shifts can merely serve as an indicator for the completeness of the FIB cut and cannot be used to determine the gap size according to Fig. 6.13b.

6.3.3.4. TEM and EDX Characterization

The following analysis is mainly adopted from [108]. However, note that the notation “dose I” and “dose II” in [108] is vice versa and that the absolute values given in [108] are a factor of 10^3 too small.

FIB and SEM images of FIB-milled rods, as exemplary shown in Fig. 6.29, suggest that both dose conditions lead to perfectly separated rods. However, based on IR spectroscopic measurements, it was found that only the arrays milled with the higher dose D_{II} give rise to the expected optical response of dimers (Fig. 6.31b). In order to structurally characterize the gap region of these nanorod dimers in more detail, TEM measurements (see Sec. 6.3.2) of several samples were performed and correlated with the optical spectra.

Figure 6.32 shows two sets of TEM and EDX mappings for FIB-milled nanogaps prepared with doses D_I and D_{II} . In the upper two graphs, dark field TEM images of differently cut samples are shown, whereas the other graphs correspond to the element-specific EDX mappings of the respective samples. Under the lower dose condition D_I , the gold layer seems to be nearly milled while the titanium adhesion layer remains almost connected. In contrast, increasing the Ga^+ ion dose (D_{II}) results in a complete cut, reaching down to the Si substrate and considerably broadening the gap. Furthermore, gallium accumulated in the silicon substrate and titanium and gold clusters were dispersed in the same region due to the sputtering by FIB bombardment.



(a) FIB dose I

(b) FIB dose II

Figure 6.32.: TEM dark field images and EDX mapping of a cross-sectional view of gold nanorods milled with FIB dose condition (a) D_I and (b) D_{II} , respectively. The EDX mappings show the distribution of gold, gallium, and titanium (K and L denote to the characteristic x-ray line). The narrowest and widest dimensions of the gap milled by D_{II} are roughly 40 nm and 120 nm, respectively.

6. Characterization and Preparation of Nanogaps

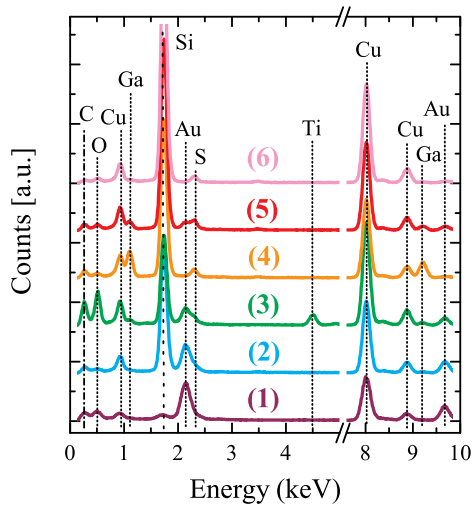


Figure 6.33: EDX spectra of designated positions on the sample milled by D_{II} shown in 6.32b. Each spectrum is shifted by 4000 counts for comparison.

Figure 6.33 shows position-dependent EDX spectra (sites indicated by numbers in Fig. 6.32b) for the nanogap prepared by D_{II} . The copper peak originates from the copper mesh used to support the specimen. Additionally, carbon, oxygen and sulfur are assigned to the elements of the organic protection layers, which are necessary to cap the gold rods and gaps during TEM specimen fabrication [123].

Spectrum (1) shows mostly the signal from gold, whereas in (2), a large signal of silicon is present since the measurement spot is located at the silicon substrate. The third spot is located at the interface between nanorod and substrate and, thus, titanium (adhesion layer) appears besides gold and silicon. Note that oxygen, carbon, and sulfur are also detected as they are gettered in the titanium region most probably during the TEM sample preparation [123]. The fourth and the fifth spectra were measured near the bottom of the milled gap region. Here, gallium peaks are observed, which are attributed to the Ga^+ implantation during gap formation by FIB. Finally, spot six shows mainly the silicon signals from the substrate.

6.3.3.5. Conclusion

The obtained spatially-resolved structural and chemical information is useful for assessment of the electronic connectivity of gold nanorod dimers. Especially for the virtually cut nanorod by condition D_I , the two milled parts seem to be separated physically in the SEM image, but are found to be significantly connected in their plasmonic resonance. The most probable scenario might be the existence of a weak electrical connection through the rest of the titanium interlayer, mixed with FIB-sputtered gold and sustaining electrical connectivity. Further contributions

could be related to impurities from the milling process, resulting in shallow acceptor levels in the Ga doped silicon (57 meV [245] and 72 meV [246] above the Si valence band). Consequently, holes could be efficiently pumped up to the conductive state by low-energy IR excitation. These contaminations might be also relevant for gaps prepared with higher gallium doses, except the material in the gap is removed as much as possible. Besides that, sputtered gold and titanium in amorphous silicon can also form impurity states with activation energies similar to the energy range of IR light [122], thereby modifying the gold nanorods' resonance spectrum. The last explanation would be the formation of randomly-shaped Ga particles, the broad plasmonic resonance of which may hybridize with that of the gold nanorod and thus blur the spectral feature. In fact, the IR transmission spectra of the Ga-implanted silicon substrates (without nanorods, see Fig. 6.28b) exhibits substantial broadband absorption in the mid-infrared region. However, the spectral behavior corresponds to resonance frequencies far away from the nanorod resonances, thereby excluding any plasmonic coupling between the two systems.

It can be concluded that already small conducting residues inside a FIB-milled nanogap lead to an optical response very different from that of a dimer. The plasmonic resonance behavior of dimer rods (with length $L/2$) is only realized for FIB cuts being deep enough to sufficiently separate the dimer gap from any metal-silicon mixture formed by FIB milling. Furthermore, it was shown that IR spectroscopy provides a powerful tool to non-destructively investigate the completeness of a FIB-milled nanogap. In addition, FIB imaging was found to change the optical properties of the substrate.

6.3.4. Results - Thermally Oxidized Silicon

The second series of experiments was performed with gold nanorods on thermally oxidized silicon (thickness of about 106 nm) to push the Ga accumulation zone at the SiO_2 / Si interface (compare to Sec. 6.3.3.1) further away from the gap region. Furthermore, the insulator SiO_2 should prevent the formation of conductive channels between the milled rod parts, in contrast to the semiconductor silicon which can be doped easily. FIB milling was performed for three dose conditions ($D_{\text{III}} - D_{\text{V}}$, see Tab. 6.1 for absolute values), which are characterized by their respective dwell times t_{dwell} in the remainder of the text.

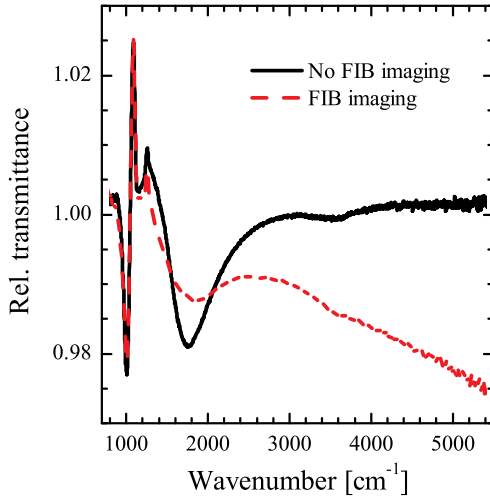


Figure 6.34: Relative transmittance spectra (parallel polarization) of two FIB-milled nanorod arrays (length before milling was $L \approx 3.05 \mu\text{m}$). On one array, FIB imaging was performed, whereas on the other array, FIB imaging was omitted.

6.3.4.1. Effect of FIB Imaging and Milling

Due to the FIB imaging-induced modification the substrate's optical properties (Sec. 6.3.3), it was tried to avoid FIB imaging for the thermally oxidized silicon sample. Nevertheless, FIB imaging of at least some arrays was necessary to localize the optimal milling position and to properly focus the ion beam [123]. As the dashed red spectrum in Fig. 6.34 shows, FIB scanning also causes a decline of the baseline in case of thermally oxidized silicon. Moreover, this decrease of transmittance is clearly related to FIB *imaging*, since it was not observed for FIB-milled arrays *without* FIB imaging (see e.g. solid black curve in Fig. 6.34). Nevertheless, polarization-independent spectral features appear in both spectra of Fig. 6.34 due to FIB milling. To impede the excitation of the antenna resonance, measurements with perpendicularly polarized light were performed to monitor these features (see Fig. 6.35).

Concerning the low wavenumber region of the spectra in Fig. 6.35a, a strong peak pointing upwards at 1085cm^{-1} is visible besides a peak at around 1005cm^{-1} pointing downwards, suggesting that the frequency of the antisymmetric Si-O vibration at 1080cm^{-1} (see Sec. 3.3.1) has shifted to lower frequencies due to FIB milling. In this context, it was reported that gallium atoms are incorporated into the silicon dioxide network by replacing the silicon atoms (GaO_4 tetrahedrons are formed) [247]. Since gallium atoms feature a higher mass than silicon atoms, this could explain the red-shift of the Si-O vibration.

Besides the quite complex and strong optical changes in the range between 800 and 1300cm^{-1} , a very small and asymmetric peak appears at around 3600cm^{-1} (Fig. 6.35b). One possibility would be that Ga atoms form impurity levels in SiO_2 , thereby giving

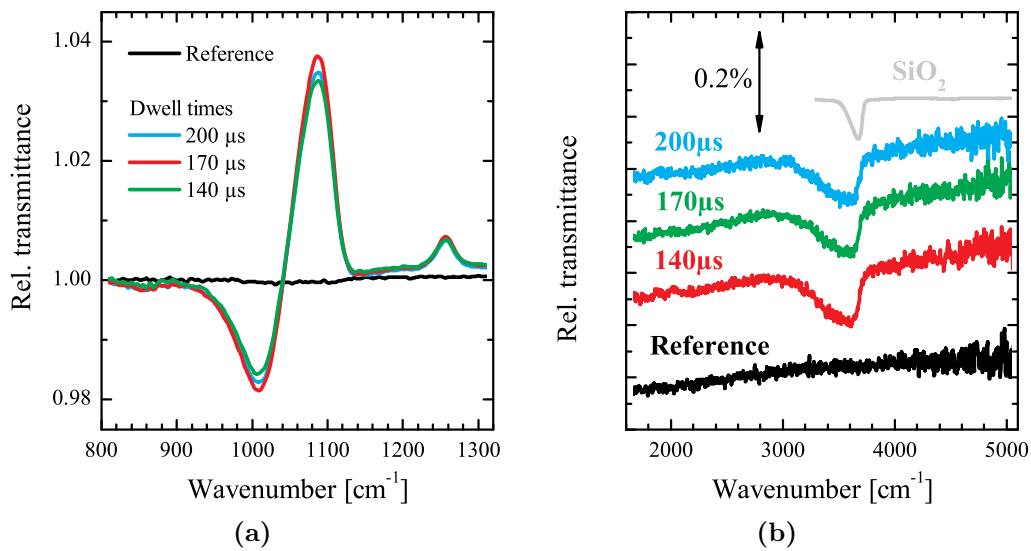


Figure 6.35.: Relative transmittance measurements of FIB-milled nanorod arrays (blue, red, and green spectra) with polarization perpendicular to the long rod axis in the range of (a) $800 - 1300\text{cm}^{-1}$ and (b) $2000 - 5000\text{cm}^{-1}$. In addition, the black curves show spectra of non-milled reference rods (perpendicular polarization). The spectra are averages over various measurements of rods of different lengths but same t_{dwell} to increase signal-to-noise ratio. In (b), the spectra are artificially shifted and the gray curve is a scaled transmittance measurement of a quartz glass substrate [109].

6. Characterization and Preparation of Nanogaps

rise to interband transitions. However, the impurity level of Ga in SiO₂ was calculated to be 0.88 eV above the minimum of the valence band [247], which would correspond to an interband transition frequency of $\tilde{\nu} \approx 7100 \text{ cm}^{-1}$. Another candidate could be the O-H stretching vibration in SiO₂ (see gray curve in Fig. 6.35b) which originates from hydrogen contaminations [130]. However, hydrogen implantation during the FIB milling process can be nearly excluded [122].

6.3.4.2. IR Optical Characterization

In Fig. 6.36a, normalized extinction spectra¹⁴ are shown for three nanorod arrays of same initial length milled by different FIB conditions. Since the plasmonic resonances of the FIB-milled arrays are slightly red-shifted compared to the one of the reference array of approximately half length (solid black curve), a complete cutting of the nanorods was achieved for all three dwell times (compare to Sec. 6.3.3). The SEM images of Fig. 6.36b apparently corroborate this assumption. Note that these images have to be treated with caution since SEM was found to be not suited to assess the completeness of a FIB cut (see Sec. 6.3.3).

Although the SEM images are quite blurred due to the bad conductivity of the SiO₂ substrate¹⁵, the gap prepared by the shortest dwell time of 140 μs seems to be the narrowest one. This smaller gap size would lead to increasing interaction between the milled parts, explaining the smallest extinction and the biggest full width at half maximum of the red spectrum in Fig. 6.36a (compare to Sec. 5.2). Furthermore, the milling condition with $t_{\text{dwell}} = 140 \mu\text{s}$ always resulted in the lowest values of Q and $\sigma_{\text{ext}}(\tilde{\nu}_{\text{res}})$, as illustrated in Figs. 6.36c and 6.36d.

6.3.4.3. TEM and EDX Characterization

As demonstrated in Sec. 6.3.3, TEM provides a tool to investigate FIB-milled nanogaps with high precision. However, this technique destroys the sample, making it useless for further experiments. Therefore, TEM measurements were performed on dummy samples that have not been investigated by IR spectroscopy. These samples were prepared at the same time and, hence, under the same conditions as the actually spectroscopied samples. Figure 6.37a shows a TEM image of a very long

¹⁴The spectra were determined from normalized relative transmittance measurements according to Eq. (6.3).

¹⁵Charging effects in the substrate corrupt the image quality. This problem can be overcome by covering the sample with a thin conductive layer. Consequently, the sample cannot be used for further experiments such as NAIRS. A coating of the sample was therefore omitted.

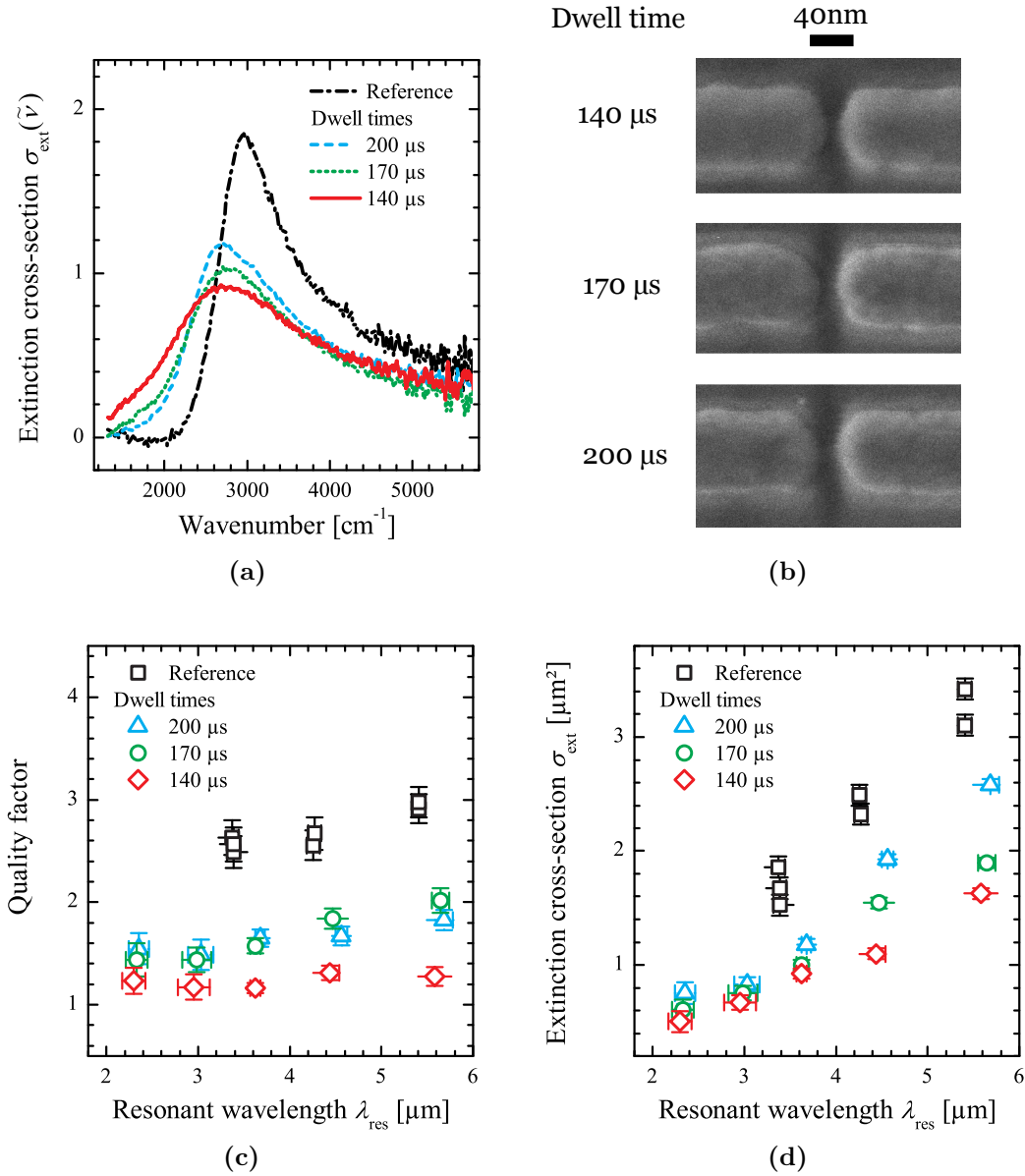
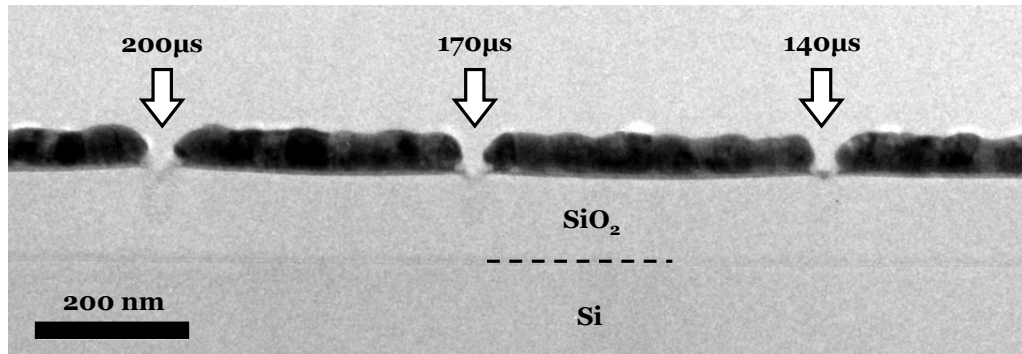
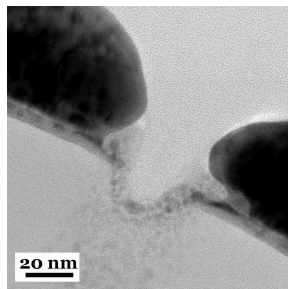


Figure 6.36.: (a) Normalized extinction spectra of differently milled nanorod arrays ($L \approx 1.85 \mu\text{m}$). For comparison, a spectrum of a reference array ($L \approx 0.9 \mu\text{m}$) is shown. All spectra were calculated from normalized relative transmittance measurements [Eq. (6.3)]. (b) SEM images of the gap region of gold nanorods milled with different dwell times as indicated. The images originate from the same nanorods that have been measured in (a). The gap width for $t_{\text{dwell}} = 140 \mu\text{s}$ appears slightly smaller than the gaps of the other two milling conditions (15 nm compared to 17 nm and 18 nm, respectively). (c) Q -values and (d) $\sigma_{\text{ext}}(\tilde{\nu}_{\text{res}})$ versus λ_{res} for the three dwell times as well as for the reference arrays. For the shortest two rod lengths, no reference arrays were prepared.

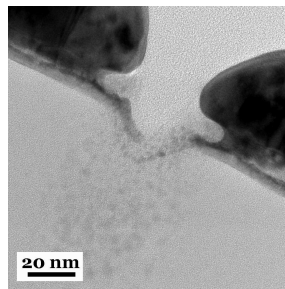
6. Characterization and Preparation of Nanogaps



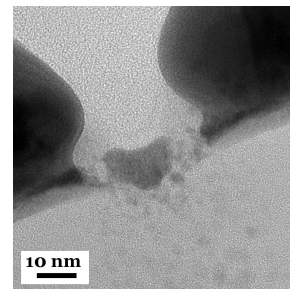
(a) Overview



(b) $t_{\text{dwell}} = 200 \mu\text{s}$



(c) $t_{\text{dwell}} = 170 \mu\text{s}$



(d) $t_{\text{dwell}} = 140 \mu\text{s}$

Figure 6.37.: (a) Overview TEM image (side view) of a long gold nanorod (dummy sample, $w = h = 60 \text{ nm}$) on thermally oxidized silicon with a thickness of about 106 nm . The arrows indicate the positions where FIB milling was performed with the indicated dwell times. (b-d) High resolution TEM images of the gap regions shown in (a). The dwell times are indicated below each image. The gap sizes g_x become narrower with decreasing dwell time: (a) $g_x \approx 33 \text{ nm}$, (b) $g_x \approx 29 \text{ nm}$, and (c) $g_x \approx 22 \text{ nm}$. In addition, the depth of the depression is reduced from (a) 17 nm , (b) 10 nm to (c) 6 nm .

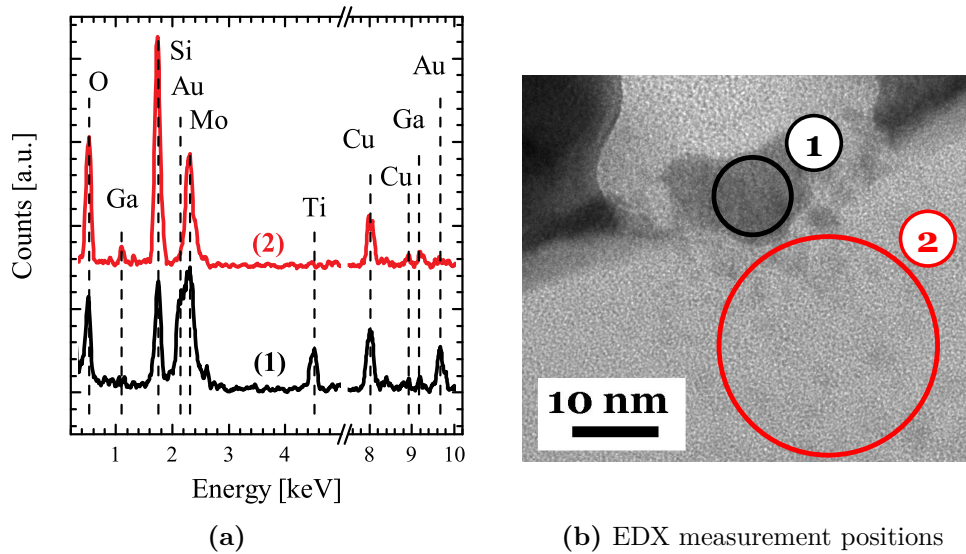


Figure 6.38.: (a) EDX spectra taken at the positions indicated in the TEM image of (b). Au and Ti signals can be identified in spectrum (1). The signals of Mo and Cu originate from the mesh and sample holder, respectively, used for TEM observation.

gold nanorod ($w = h = 60\text{ nm}$) that has been milled with the three dose conditions. The interface between the SiO_2 layer and the supporting Si substrate is indicated by a dashed line. In Figs. 6.37b to 6.37d, zooms on the respective gap regions are depicted and a complete separation of the milled parts was achieved in all cases. Consequentially, the shortest dwell time yields to the narrowest gap and the best result. Moreover, longer dwell times lead to a depression in the substrate and to undesired broadening of the gap.

In addition, EDX spectra were taken for the sample with the shortest dwell time of $140\ \mu\text{s}$ and are plotted in Fig. 6.38a. Below the gap [position (2) in Fig. 6.38b], a weak signal of Ga at 1.1 keV is present due to the Ga ion bombardment. Furthermore, it is obvious from spectrum (1) that the dark material inside the gap consists of residues of gold and titanium (see peaks at 9.7 keV and 4.5 keV , respectively). Although the gap region is quite contaminated, the plasmonic resonances do not seem to be distorted as the experimental findings from IR spectroscopy suggest (Fig. 6.36a). This is in contrast to the findings from natural oxide covered silicon samples in Sec. 6.3.3. Hence, SiO_2 might help to sustain electrical insulation between the two parts of the milled nanorod.

6.3.4.4. Conclusion

A complete, non-conductive separation between the two parts of FIB-milled nanorods was achieved with all three dwell times. IR spectroscopic measurements as well as TEM investigations figured out that the shortest dwell time of 140 μ s led to the smallest gap size which is in the range of 20nm. Moreover, silicon dioxide seems to be the better substrate compared to silicon since no conductive connections between the gold nanorod parts emerge.

6.4. Important Findings

- Infrared spectroscopy offers a non-destructive method to assess the conductivity or insulation, respectively, of nanogaps in nanorod dimers. The same findings can be obtained with transmission electron microscopy, however, this method is very elaborate and expensive and, in addition, destroys the sample, which becomes useless for further experiments.
- Scanning electron microscopy is not suited for investigating nanosized gaps.
- The smallest gaps (supposedly in the range of 10nm or even less) were prepared by the photo-induced metal deposition technique which therefore possesses great potential for nanogap fabrication.
- The activation of additional dimer modes was observed for very small gap sizes below 20nm. They could be attributed to the coupled $l = 1$ and $l = 2$ modes of individual nanorods.
- The scanning of silicon samples with a focused gallium ion beam leads to a decrease of the relative transmittance towards higher frequencies, which is most likely due to the formation of Ga nanoparticles at the SiO₂/Si interface.
- Thermally oxidized silicon promises to be the better substrate for the FIB fabrication of nanogaps compared to natural oxide covered silicon, since SiO₂ seems to sustain electrical insulation between the two parts of the milled nanorod.

7. Sensing of Mercaptoundecanoic Acid

The present chapter deals with the IR optical properties of mercaptoundecanoic acid (see Sec. 3.4.1). First, the characterization of MUA by infrared reflection absorption spectroscopy is presented in Sec. 7.1. These IRRAS measurements serve as reference for the nanoantenna-assisted infrared spectroscopy of MUA in Sec. 7.2. Finally, Sec. 7.3 summarizes the important findings of this chapter.

7.1. Infrared Reflection Absorption Spectroscopy

IRRAS is a well-established and important method in surface science [248, 249] due to its ability to determine the orientation of molecules on metal substrates [250, 251]. The principle is based on the surface selection rule, stating that molecular vibrations can be only excited if their induced transition dipole moment features a component perpendicular to the metal surface [252]. This is illustrated in Fig. 7.1: Every charge distribution above a metal surface induces image charges of opposite sign inside the metal. Hence, transition dipole moments of molecular vibrations perpendicular to the surface are enhanced by image charges, while dipole moments parallel to the surface are canceled.

After the description of the sample preparation (Sec. 7.1.1), the measurement principle is shortly explained in Sec. 7.1.2. In the end, the experimental findings are presented in Sec. 7.1.3. For more details about the IRRAS technique, the reader is referred to former thesis [176, 253–256].



Figure 7.1: Surface selection rule: Image dipoles are induced in the metal, either enhancing (left) or canceling (right) the molecular transition dipole moment.

7.1.1. Sample Preparation

The substrates are quadratic mica wafers (area of $2.5 \times 2.5 \text{ cm}^2$, thickness of $250 \mu\text{m}$) covered with an approximately 300 nm thick gold layer prepared by physical vapor deposition¹ by G. ALBERT [258]. In analogy to relative transmittance measurements in the IR microscope (see Sec. 3.2.2), the (sample) measurement of the probe molecule MUA (see Sec. 3.4.1) requires a reference measurement. The first approach would be a “clean” gold mirror without any adsorbate. However, since the gold mirrors always feature some residual carbon hydride contaminations², the reference has to be coated with another molecule. Deuterated octadecanethiol (d-ODT) provides an adequate reference since the vibrational bands of d-ODT (see e.g. [176]) do not interfere with those of MUA.

Self-assembled monolayers (Sec. 3.4) of the adsorbates on the gold films were prepared by immersing the purchased substrates for at least 15 h in the following solutions:

- 20 μM MUA in ethanol + 5 % acetic acid,
- 10 μM d-ODT in ethanol.

Acetic acid was added to the ethanol to ensure full protonation of the carboxyl groups [165]. After immersion, the MUA-sample was rinsed with 0.5 % AA in ethanol to retain the protonated configuration [165] and to remove any physisorbed molecules. Pure ethanol was used to rinse the d-ODT-sample. Finally, both substrates were dried by purged air.

7.1.2. Measurement Principle

The measurements were performed in the sample compartment of a FT-IR spectrometer (BRUKER IFS66 v/S) using the reflection unit constructed by D. ENDERS [176]. After passing an entrance slit, the IR beam is reflected by a gold mirror (see Fig. 7.2) onto a sample area of defined size which has to be completely covered by the sample. Thus, always the same sample area is illuminated by the IR beam and no adjustment of the sample is necessary [176].

¹The physical vapor deposition method allows epitaxial layer growth, leading to very low surface roughness [257].

²Since no adhesion promoter is used, sonication of the substrate should be omitted to avoid displacement of the gold layer [258]. Moreover, former studies showed that residues of acetone on the substrate can hamper the absorption of the actual adsorbate [109].

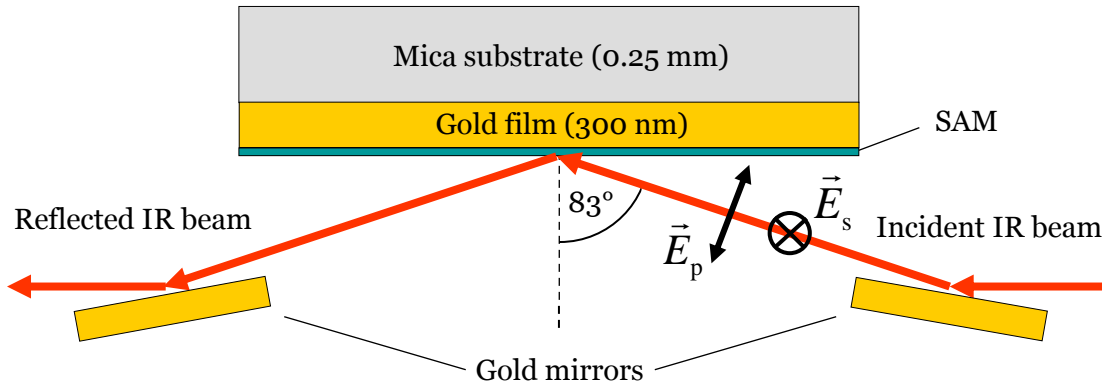


Figure 7.2.: Schematic IRRAS set-up: The SAM is adsorbed on a smooth gold film and illuminated under a fixed angle of incidence (83°). The two different light polarization states perpendicular (\vec{E}_s) and parallel (\vec{E}_p) to the plane of incidence are indicated.

After being reflected by the sample, the IR light is guided to the liquid nitrogen cooled MCT detector by means of another gold mirror. The positions of the two gold mirrors are not displaceable with respect to the sample position, leading to a fixed angle of incidence of 83° . Furthermore, the reflection unit is constructed in a way that only the light reflected by the sample reaches the detector [176].

After placing the sample on the reflection unit, the spectrometer is pumped to a base pressure of $p = 4$ mbar. Each sample was measured with light being p- and s-polarized (see Fig 7.2). According to the surface selection rule, measurements with s-polarization do not yield any signal from the adsorbed molecules and can therefore be used to determine the baseline, which is very sensitive to any displacement of the sample relative to the reflection unit [109]. For this reason, the IRRAS spectra of the present thesis always show the *normalized* relative reflectance,

$$R_{\text{norm}} = \frac{R_p(\text{MUA})/R_p(\text{d-ODT})}{R_s(\text{MUA})/R_s(\text{d-ODT})}, \quad (7.1)$$

where R_p and R_s denote the p- and s-polarized reflectance of MUA or d-ODT, respectively. Note that the ratio between $R_p(\text{MUA})$ and $R_s(\text{MUA})$ does not result in the spectrum of MUA due to the different reflection conditions of the two polarization states [176] and the anisotropy of the IR polarizer. Hence, the reference measurement of d-ODT is mandatory with this set-up. Details about the stability of the apparatus as well as raw IRRAS spectra of MUA and d-ODT can be found in Sec. A.5.

7.1.3. Results

The focus of Chap. 7 is on the IR optical behavior of the carboxyl group of MUA under different immersion conditions. To this end, three subsequent measurements with one MUA-coated gold mirror sample were performed:

- (a) Freshly prepared MUA sample, immersed over night in a solution of 20 μM MUA in ethanol (EtOH) acidified with 5% acetic acid (AA), rinsed with ethanol containing 0.5% AA prior to measurement;
- (b) MUA sample immersed in pure ethanol for 3h after measurement of spectrum (a), rinsed with pure ethanol prior to measurement;
- (c) MUA sample immersed in EtOH / 0.5% AA for 30 min after recording spectrum (b), rinsed with EtOH / 0.5% AA prior to measurement.

Figure 7.3 shows the normalized relative reflectance spectra of (a) to (c), which were baseline corrected with the help of the software OPUS. Starting from spectrum (a), a relatively strong band near 1700cm^{-1} is observed, originating from protonated carboxyl groups (COOH). In fact, two peaks, one at 1710cm^{-1} and another at 1738cm^{-1} , can be identified within the broad band. This band splitting is due to the partial formation of hydrogen bonds between the carboxyl groups (Sec. 3.4.1).

After immersion of the sample in pure ethanol [spectrum (b)], the band vanishes and another prominent peak at 1465cm^{-1} arises which is caused by the symmetric stretching of deprotonated carboxyl groups (COO^-). Moreover, the antisymmetric COO^- stretching vibration at 1549cm^{-1} gains in intensity. Note that these peaks are already observed in spectrum (a), implying that not all carboxyl groups were able to retain their hydrogen atom. However, the more basic environment³ [preparation (b)] clearly leads to a complete deprotonation of the carboxyl group in accordance with IRRAS measurements of mercaptohexadecanoic acid (MHDA) [165].

Reprotonation of MUA is possible by immersing the sample in acidic solution, as spectrum (c) shows. Here, the band at 1465cm^{-1} is slightly more pronounced than in spectrum (a), indicating an incomplete reprotonation process. Immersion of the sample for a longer period of time or in a more concentrated acidic solution might lead to results similar to those of spectrum (a).

³IRRAS experiments with a basic ethanolic solution containing NaOH showed similar results as those with “pure” ethanolic solution in case of MHDA [165]. This is explained by the fact that “pure” ethanol always contains minor contaminations of NaOH which are responsible for deprotonation.

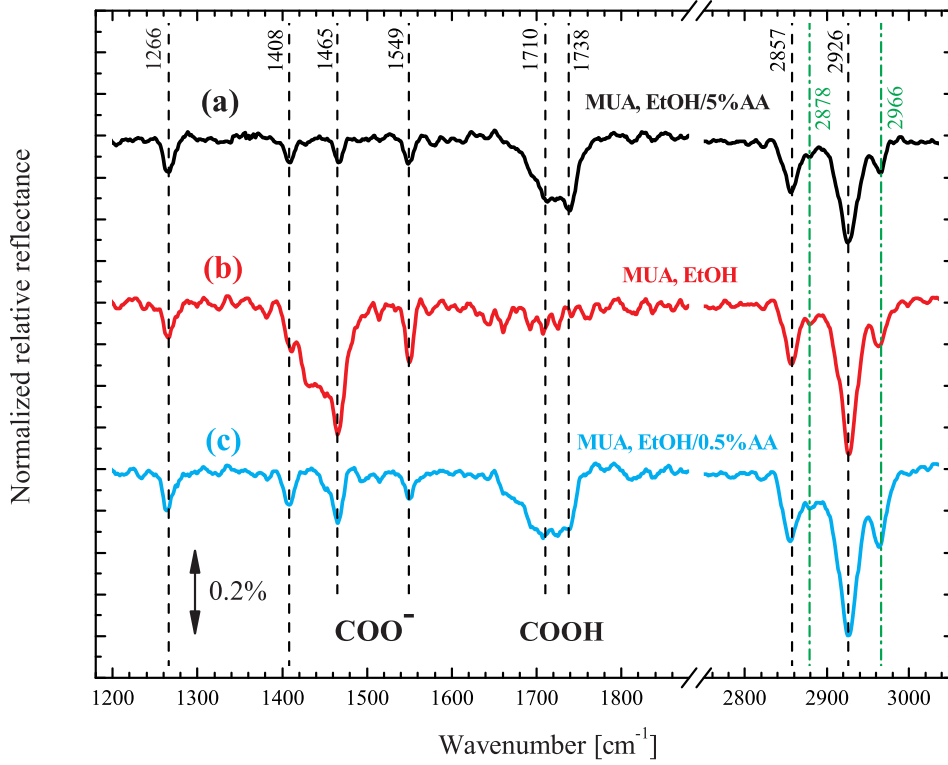


Figure 7.3.: Baseline corrected normalized relative reflectance spectra [Eq. (7.1)] of three differently prepared MUA monolayers (reference d-ODT). See text for the preparation details. All spectra were acquired with 3000 scans at a resolution of 2 cm^{-1} .

Measurement $\tilde{\nu}[\text{cm}^{-1}]$	Intensity [%]			Mode	MUA [166]	MHDA [165]
	(a)	(b)	(c)		$\tilde{\nu}[\text{cm}^{-1}]$	$\tilde{\nu}[\text{cm}^{-1}]$
1266	0.9	0.9	0.9	$\nu(\text{C-O})$	1300	1220
1408	0.7	1.2	0.8	$\delta(\text{CH}_2)$	1430-1460	
1465	0.6	3.2	1.3	$\nu_s(\text{COO}^-)$	1430-1450	1466
1549	0.7	1.4	0.7	$\nu_a(\text{COO}^-)$	1570-1580	1568
1710	1.5	-	1.6	$\nu(\text{C=O})^a$	1716	1711-1718
1738	1.8	-	1.5	$\nu(\text{C=O})^b$	1735	1740-1745
2857	1.4	1.5	1.8	$\nu_s(\text{CH}_2)$	2850	2851
2926	2.5	3.6	3.9	$\nu_a(\text{CH}_2)$	2923	2920

Table 7.1.: Peak positions and corresponding peak signal strengths of MUA extracted from spectra (a) to (b) of Fig. 7.3. In addition, the mode assignments based on literature values of MUA [166] and MHDA [165] are given. The superscripts *a* and *b* refer to the hydrogen- and non-hydrogen bonded configuration of the carboxyl groups (see Sec. 3.4.1).

7. Sensing of Mercaptoundecanoic Acid

Besides the symmetric and antisymmetric CH_2 stretching vibrations at 2857cm^{-1} and 2927cm^{-1} , two weak absorption peaks at 2878cm^{-1} and at 2966cm^{-1} (dashed-dotted green lines) appear, which most likely originate from symmetric and antisymmetric stretching vibrations of CH_3 groups [175]. Since MUA does not possess any CH_3 groups, the bands might arise from residual dirt on the MUA-coated sample or from alkanethiol contaminations in the purchased MUA powder, featuring a purity of “only” 99 %. The frequencies, intensities and assignments of the vibrational peaks of MUA are summarized in Tab. 7.1.

In summary, it was shown that MUA adsorbs on gold surfaces and that a “switching” of the absorption frequency of the functionalized end group can be achieved by different immersion conditions. To obtain a mostly protonated configuration of MUA, it is essential to use acidified ethanolic solutions for immersing as well as for rinsing the sample. In contrast, applying pure ethanol leads to the deprotonated phase due to residual OH^- ions in the ethanol.

7.2. Nanoantenna-Assisted Infrared Spectroscopy

Lithographically prepared gold nanorod arrays on calcium fluoride were used (Sample Antenna#2, $L \approx 2\mu\text{m}$, $w \approx h \approx 60\text{nm}$, $d_x = d_y = 5\mu\text{m}$) to perform nanoantenna-assisted IR spectroscopy of the probe molecule MUA. Prior to the actual NAIRS measurement (Secs. 7.2.2 and 7.2.3), the sample was cleaned by an oxygen plasma (Sec. 7.2.1) at the Institute of Applied Physical Chemistry. Based on the IRRAS measurements of Sec. 7.1.3, an enhancement factor for MUA is estimated in Sec. 7.2.5.

7.2.1. Oxygen Plasma Cleaning

Figure 7.4a shows antenna resonances before and after plasma cleaning [$t = 2\text{min}$, $p(\text{O}_2) = 0.4\text{mbar}$, $P = 150\text{W}$]. Some organic residues seemed to be present before the cleaning process, leading to a very small dent around 1740cm^{-1} (see zoom in Fig. 7.4b), which might originate from $\text{C}=\text{O}$ stretching vibrations [175]. Although this dent vanishes after the cleaning procedure, additional spectral features appear at around 1080cm^{-1} and 1450cm^{-1} . A comparison with the IR active modes of calcium carbonate [259] leads to the suspicion that the CaF_2 substrate was modified by the cleaning process. However, these plasma-induced changes have to occur at certain sites on the substrate since a modification of the whole substrate would not lead to spectral features in the relative transmittance spectrum. And in fact, no absorption

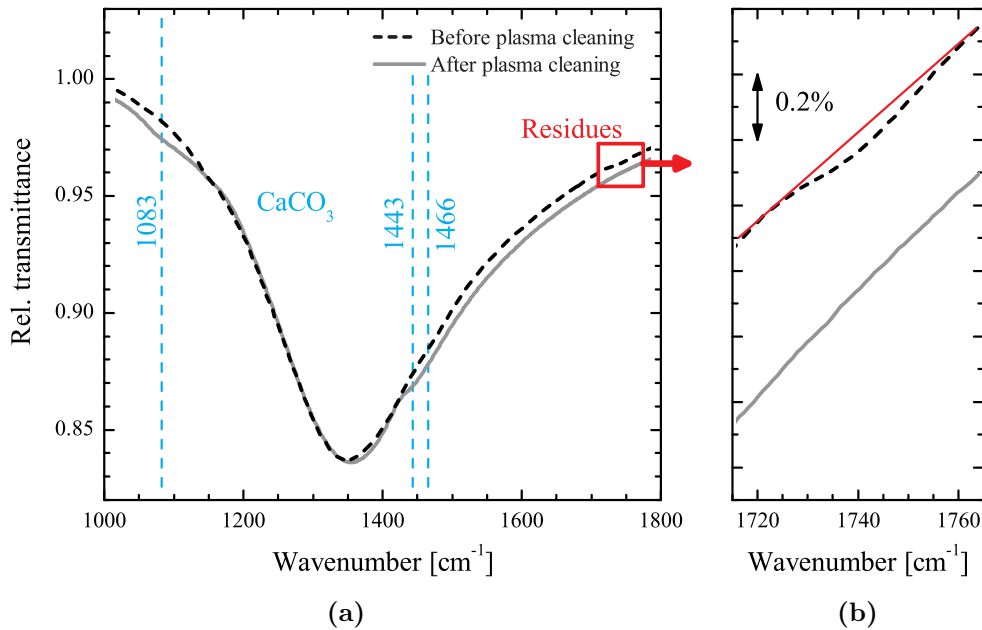


Figure 7.4.: (a) Relative transmittance spectra (≈ 154 rods, see Sec. 7.2.5) before and after oxygen plasma cleaning. The IR active modes of CaCO_3 are marked by vertical lines. (b) Zoom on the spectral range between 1720cm^{-1} and 1760cm^{-1} of (a). The straight red line is a guide to the eye to recognize the bending of the dashed black curve.

bands at 1083cm^{-1} , 1443cm^{-1} , or 1466cm^{-1} were found for plasma-cleaned CaF_2 substrates without gold nanostructures [260]. Hence, the gold nanorods might act as catalyst for substrate degradation.

7.2.2. Identifying the Spectral Signature of MUA

For the NAIRS experiment, the sample was immersed over night in a solution of $20\mu\text{M}$ MUA in EtOH / 5% AA, rinsed with EtOH / 0.5% AA and dried with purged air in analogy to the IRRAS measurements (Sec. 7.1.3). The dotted blue spectrum in Fig. 7.5a shows the relative transmittance measurement in comparison to the spectrum after plasma cleaning. Interestingly, the dent around 1450cm^{-1} , which was attributed to the modified substrate, disappeared after the immersion in the MUA solution. Since CaCO_3 dissolves in acetic acid solutions [261], the resulting calcium acetate might be removed by the immersion and rinsing process.

Concerning the enhancement of the MUA absorption bands, only very weak dents can be identified at the expected positions (dashed lines in Figs. 7.5a and 7.5b), indicating that adsorption of MUA molecules took place. Since the vibrational bands

7. Sensing of Mercaptoundecanoic Acid

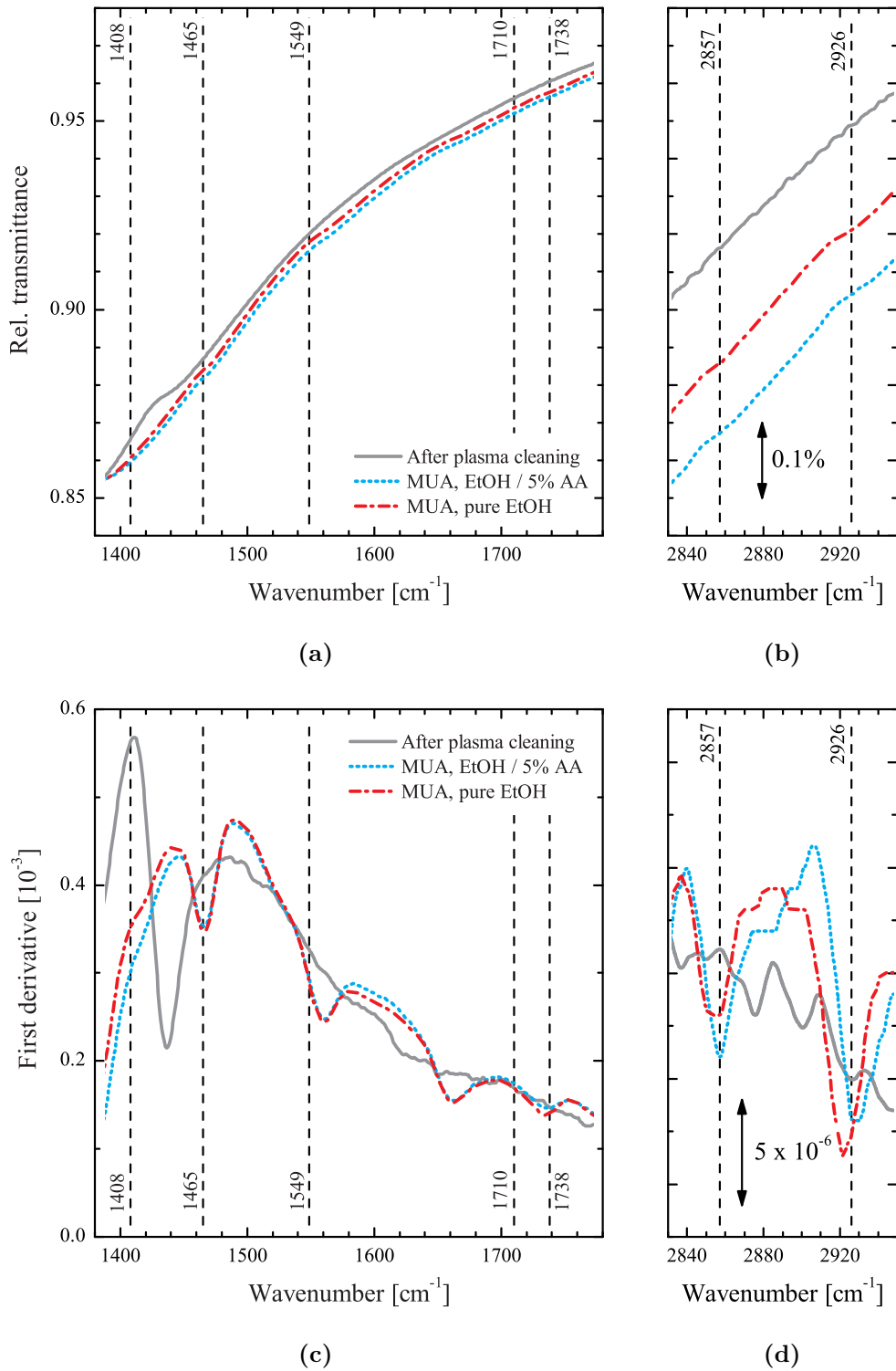


Figure 7.5.: NAIRS of MUA adsorbed on a nanorod array ($L \approx 2\mu\text{m}$, $w \approx h \approx 60\text{nm}$, $d_x \approx d_y \approx 5\mu\text{m}$) on CaF_2 . Approximately 154 rods contribute to the signal. (a,b) show the relative transmittance spectra (raw data) whereas (c,d) show the first derivatives (13 smoothing points) of the respective spectra of (a) and (b). In (d), the spectrum after plasma cleaning was additionally smoothed (30 smoothing points).

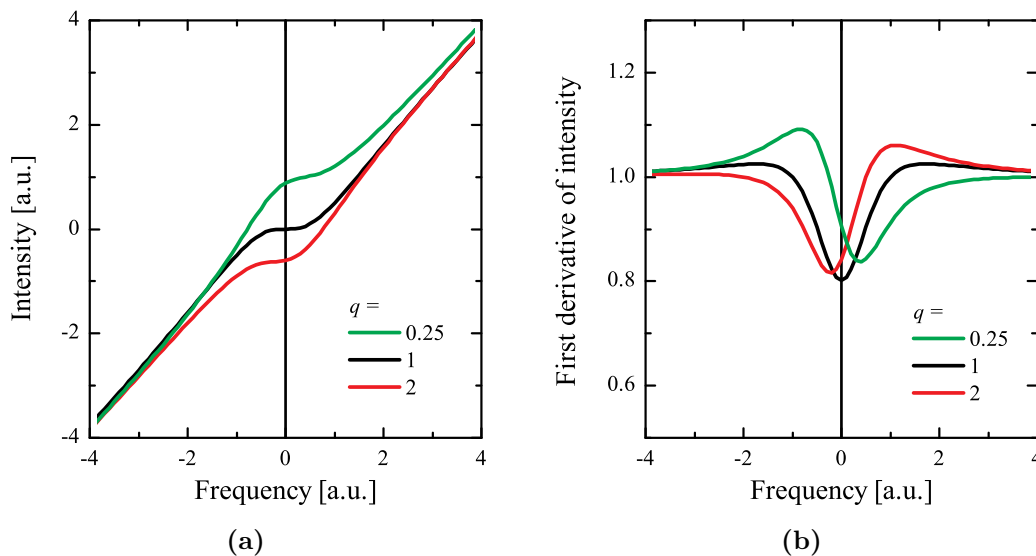


Figure 7.6.: (a) Calculated Fano curves $I_q(x)$ using the function $I_q(x) = x + \left(1 - \frac{(x+q)^2}{x^2+1}\right) / (q^2 + 1)$ with the asymmetry parameter q as indicated in the figure. (b) First derivative spectra of the intensity spectra shown in (a). At the resonance position $x = 0$, a minimum in the first derivative is present for $q = 1$.

of MUA are mainly located on the flank of the antenna resonance, asymmetric Fano-like line shapes should appear (Sec. 3.5). The ratios between molecular resonance $\tilde{\nu}_{\text{vib}}$ and plasmonic resonance $\tilde{\nu}_{\text{res}} \approx 1370 \text{ cm}^{-1}$ range between 0.97 and 0.79 for the signals of MUA in Fig. 7.5a. A comparison between the measured line shapes of the SiO_2 SPP in Fig. 3.13a and the calculated Fano profiles in Fig. 3.13b suggests that the asymmetry parameter q [Eq.(3.5)] features values between 0.25 and 2.

In Fig. 7.6a, calculated Fano profiles for different q are superimposed on a linear function. As can be seen from Fig. 7.6b, the first derivative of these curves leads to peaks pointing downwards near the resonance $x = 0$. Note that the peak minimum and $x = 0$ only coincide for the antisymmetric profile ($q = 1$). Nevertheless, the first derivative of the NAIRS spectra can be used to reveal the signature of MUA⁴.

Looking at Fig. 7.5c, relatively strong peaks in the first derivative spectrum near 1465 cm^{-1} and 1549 cm^{-1} are detected and attributed to the stretching vibrations of the deprotonated carboxyl groups. Furthermore, a small feature at around 1740 cm^{-1} appears, which is most likely caused by protonated carboxyl groups. In addition, a peak at around 1660 cm^{-1} is present which cannot be assigned to any MUA vibration.

⁴Note that the derivative method only works since the spectra were recorded with a large number of scans (66 000), featuring nearly no noise.

7. Sensing of Mercaptoundecanoic Acid

One possibility could be that the hydrophilic carboxyl groups attract liquid water from the atmosphere, which features a strong absorption band at 1644cm^{-1} [262].

Moreover, the CH_2 stretching vibrations located at 2857cm^{-1} and 2926cm^{-1} are identified in Fig. 7.5d, even though they are spectrally very far away from the main antenna resonance ($\tilde{\nu}_{\text{res}} \approx 1370\text{cm}^{-1}$). However, the second order plasmonic resonance at around 2730cm^{-1} (not shown) probably contributes to the enhancement of these bands.

7.2.3. Changing the Carboxyl Configuration

At a first glance, it might be surprising that the bands of the COO^- group (1465cm^{-1} and 1549cm^{-1}) are more pronounced than the bands of the COOH group at around 1740cm^{-1} , since the preparation with the acidified ethanol should provide protonated MUA adsorbates. However, one has to take into account that the enhancement depends on the spectral position of the adsorbate with respect to the plasmonic resonance (Sec. 3.5.1).

To check whether the configuration of the carboxyl group can be changed by the solvent, the sample was immersed in pure ethanol for about 3h prior to a repeated measurement (dashed-dotted red curves in Figs. 7.5a and 7.5b). In the derivative spectrum of Fig. 7.5c, no significant changes of the carboxyl bands can be observed. Hence, it seems that the immersion solution had no effect on the carboxyl configuration, in contrast to the findings from IRRAS.

One possible reason for this discrepancy could be the long exposure of the sample to air during the whole NAIRS measurement, which lasted around 18h in total to provide the necessarily high signal-to-noise ratio. In IRRAS, the sample is taken out from solution, flushed with the respective solvent and immediately placed in the sample compartment which is pumped to $p = 5\text{mbar}$ (measurement time of only 30 – 60 min). Hence, ambient conditions might result in the formation of an equilibrium configuration of the carboxyl groups, featuring protonated and deprotonated fractions and being independent of the immersion solution.

7.2.4. Destroying the Adsorbate by Plasma Cleaning

After the NAIRS measurement, the sample was again plasma cleaned [$t = 5\text{min}$, $p(\text{O}_2) = 0.4\text{mbar}$, $P = 150\text{W}$] and IR transmittance measurements were recorded. The dashed green spectrum in Fig. 7.7 shows the first derivative spectrum after the cleaning process. In comparison to the NAIRS derivative spectrum of MUA

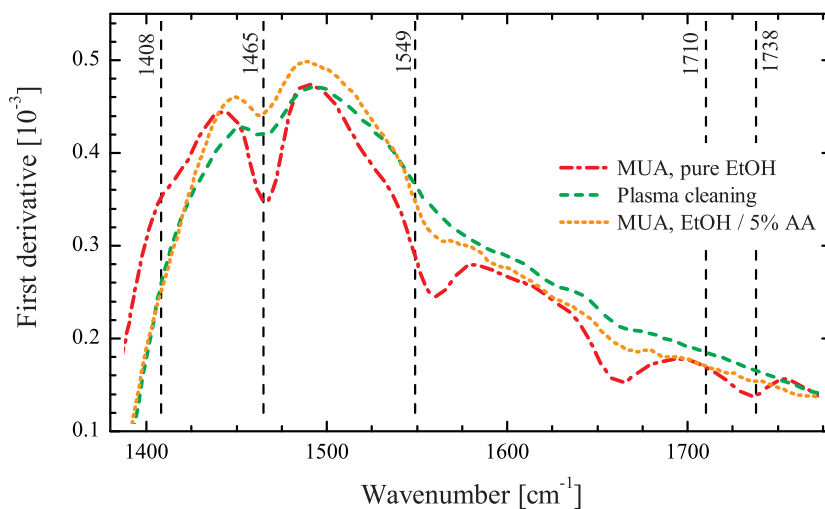


Figure 7.7.: Effect of plasma cleaning on adsorbed MUA (see text).

(dashed-dotted red curve), all MUA-specific bands nearly vanished after oxygen plasma cleaning, suggesting that almost all adsorbates have been removed from the gold nanoantennas. However, the small peak at 1465cm^{-1} indicates that at least a small fraction of the adsorbates has remained. Note that this time, no peak at 1450cm^{-1} has emerged after plasma cleaning, excluding the plasma-induced formation of CaCO_3 . This might be due to the pretreatment with oxygen plasma or simply due to the different cleaning times that have been applied.

To investigate, if the plasma cleaned sample can be used for new NAIRS experiments, it was again immersed in the acidified MUA solution over night (identical solution and similar immersion time compared to Sec. 7.2.2). In Fig. 7.7, the dotted orange curve represents the first derivative of this repeated NAIRS measurement. Obviously, there is no significant difference compared to the spectrum after plasma cleaning. The MUA bands might have marginally increased in intensity, but the dashed-dotted red spectrum is not reproduced.

The absence of MUA bands after plasma cleaning can be interpreted as follows: during the cleaning process, the adsorbate molecules are destroyed but not completely removed. The alkyl chains could have been removed from the thiol groups which are still bound to the gold surface, blocking adsorption sites. Consequently, plasma cleaning does not seem to be an appropriate method to completely remove a chemisorbed adsorbate.

7.2.5. Estimation of an Enhancement Factor

To obtain quantitative statements on the electromagnetic field enhancement, enhancement factors EF based on the definition of Eq. (3.3) are estimated in this section. First of all, the relative fractions, f_{IRRAS} and f_{NAIRS} , of the illuminated spots effectively covered by MUA molecules have to be determined. While $f_{\text{IRRAS}} = 1$ can be assumed (whole gold film is covered by MUA), only a small part of the illumination spot $A_0 = \pi(D/2)^2$, with aperture diameter D , is covered by MUA molecules due to the selective adsorption on the gold nanorods (see Sec. 3.4). The number N of rods contributing to the spectrum in Fig. 7.5a is calculated by considering the length L and width w of the rods as well as the separation distances d_x and d_y [109]:

$$N \approx \frac{A_0}{(L + d_x) \cdot (w + d_y)} = \frac{\pi(83.3/2)^2}{(2 + 5) \cdot (0.06 + 5)} \approx 154. \quad (7.2)$$

Furthermore, it is assumed that only MUA molecules adsorbed on the tip ends contribute to I_{NAIRS} due to the near-field distribution of resonant nanoantennas (see e.g. Fig. 2.6). The tips of the nanorods are approximated by hemispheres featuring an effective radius of $R_{\text{eff}} = \sqrt{w \cdot h/\pi}$. Thus, the fraction of the area contributing to I_{NAIRS} is estimated to

$$f_{\text{NAIRS}} \approx \frac{N \cdot 4\pi R_{\text{eff}}^2}{\pi\left(\frac{D}{2}\right)^2} = \frac{154 \cdot 4 \cdot 60 \cdot 60 \text{ nm}^2}{\pi\left(\frac{83.3 \mu\text{m}}{2}\right)^2} \approx 4 \cdot 10^{-4}. \quad (7.3)$$

First, the supposedly strongest band at 1465 cm^{-1} in the dashed-dotted red spectrum of Fig. 7.7 is considered. Concerning the NAIRS spectrum after immersion in ethanol (dashed-dotted red curve in Figure 7.5a), a baseline correction is necessary to estimate $I_{\text{NAIRS}}(1465 \text{ cm}^{-1})$. A simple approximation is a straight line with fixed points on the measured spectrum. Since the signal intensity of the carboxylate vibration nearly drops down to zero at 1420 cm^{-1} and 1520 cm^{-1} (see Fig. 7.8a), these frequencies are used as fixed points, resulting in the dashed black straight line in Fig. 7.8b.

Dividing these two curves leads to the solid red curve in Fig. 7.8c, featuring a Fano-like signal of the adsorbate. For comparison, a similar line shape is obtained for the ratio between the spectrum of MUA after immersion in ethanol and the one after the final plasma cleaning step (dashed green line). In analogy to [34], the intensity I_{NAIRS} is defined as the difference between the signal's maximum and minimum, resulting in a value of $I_{\text{NAIRS}} \approx 0.16\%$.

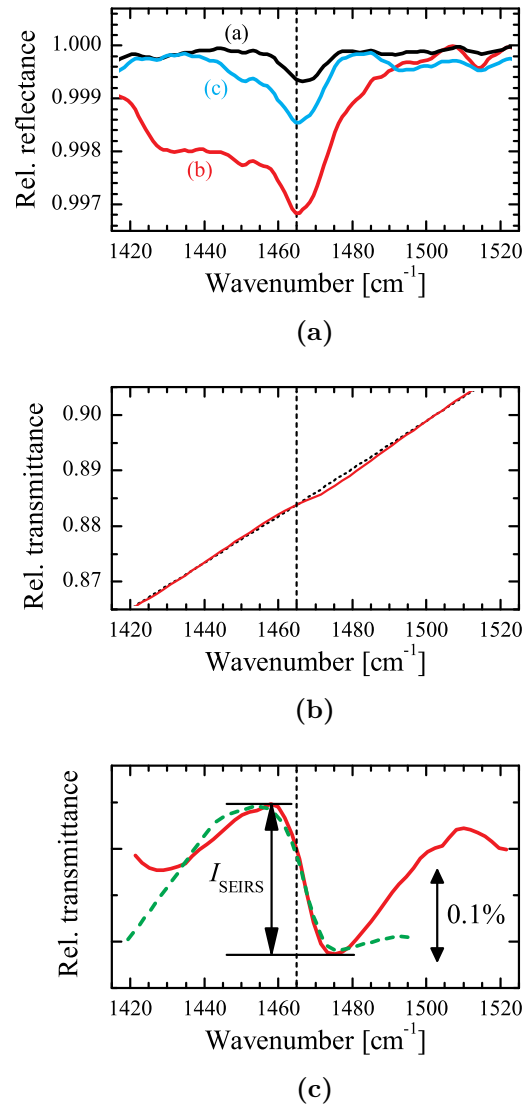


Figure 7.8.: (a) IRRAS measurements of MUA (data of Fig. 7.3) in the range of the symmetric carboxylate vibration (1465 cm⁻¹, indicated by vertical dashed line). (b) NAIRS spectrum of MUA (solid red) on gold nanoantennas after immersion in ethanol (data of dashed-dotted red curve in Fig. 7.5a). The dotted black line is the assumed baseline without the signal of MUA (see text). (c) Red curve: baseline corrected, Fano-like signal of the MUA adsorbate [ratio between the solid red and dotted black curves in (b)]. For comparison, the dashed green curve shows the ratio between the measured relative transmittance spectrum after immersion in ethanol [solid red curve in (b)] and the measurement after plasma cleaning (not shown).

7. Sensing of Mercaptoundecanoic Acid

To determine the signal strength I_{IRRAS} , a theoretical relative transmittance change $(\Delta T/T)_{\text{theo}}$ has to be calculated [see Eq. (3.4) in Sec. 3.5.1]:

$$\left(\frac{\Delta T}{T}\right)_{\text{theo}} \approx \left(\frac{\Delta R}{R}\right)_{\text{IRRAS}} \cdot \frac{1}{2(n_{\text{CaF}_2} + 1)} \cdot \frac{\cos \vartheta}{\sin^2 \vartheta} \approx 0.026 \cdot \left(\frac{\Delta R}{R}\right)_{\text{IRRAS}}. \quad (7.4)$$

The measured value of $(\Delta R/R)_{\text{IRRAS}}$ ranges between 0.06% and 0.32%, depending on the carboxyl configuration (see Tab. 7.1). In regard to the NAIRS measurements, it is hard to identify the carboxyl configuration since no variation of I_{NAIRS} in dependence of the immersion medium was observed (Sec. 7.2.3). However, most of the carboxyl groups seem to be deprotonated as no change of I_{NAIRS} was monitored after immersion in ethanol. Consequently, assuming complete deprotonation [$(\Delta R/R)_{\text{IRRAS}} \approx 0.32\%$] yields⁵

$$EF(1465 \text{ cm}^{-1}) = \frac{I_{\text{NAIRS}}}{I_{\text{IRRAS}}} \cdot \frac{f_{\text{IRRAS}}}{f_{\text{NAIRS}}} \approx \frac{1.6 \cdot 10^{-3}}{0.026 \cdot 3.2 \cdot 10^{-3}} \cdot \frac{1}{4 \cdot 10^{-4}} \approx 48000. \quad (7.5)$$

The same procedure was performed for the band at 1549 cm^{-1} . The baseline corrected signal of $I_{\text{NAIRS}}(1549 \text{ cm}^{-1}) \approx 0.05\%$ leads to

$$EF(1549 \text{ cm}^{-1}) \approx 34000. \quad (7.6)$$

The evaluation of the 1738 cm^{-1} band was omitted since it was very hard to determine the weak signal I_{NAIRS} by a baseline correction. In addition, the signal of the IRRAS measurement in case of complete deprotonation is below the noise level [see spectrum (b) in Fig. 7.3].

Comparison with ODT Measurements

In Fig. 7.9, the estimated EF -values of Eqs. (7.5) and (7.6) are plotted versus the ratio between $\tilde{\nu}_{\text{res}}$ and molecular resonance frequency $\tilde{\nu}_{\text{vib}}$ together with EF -values of ODT [34]. Note that the data of ODT on lithographic nanorods has been corrected compared to the data shown in Fig. 3.12a in the following way: in [34], the signal strength I_{NAIRS} was determined by the difference between maximum and minimum of the signal, underestimating the real signal intensity. To allow a better comparison

⁵It is assumed that the surfaces of the lithographic gold nanorods and the smooth gold film on mica mainly feature (111)-orientation, see Secs. 3.5.1 and 7.1.1, respectively.

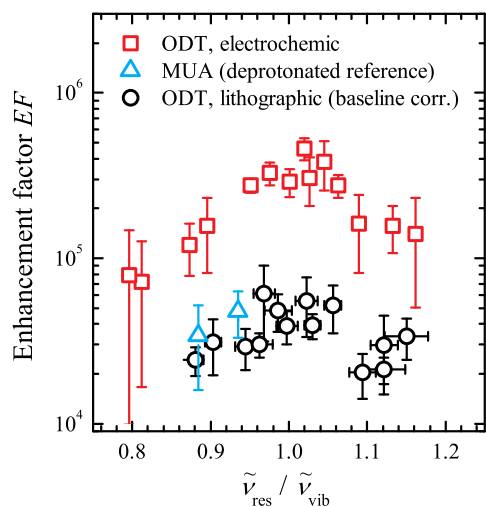


Figure 7.9: Estimated enhancement factors EF for ODT and MUA versus ratio between plasmonic resonance $\tilde{\nu}_{\text{res}}$ and molecular resonance $\tilde{\nu}_{\text{vib}}$.

with the MUA data, baseline corrections like the one illustrated in Fig. 7.8b were performed for the ODT data, leading to the higher values shown in Fig. 7.9.

The EF -values of MUA are comparable to the values of ODT on lithographically prepared nanorods, although the ODT measurements were performed with nanorod arrays featuring gap sizes d_x between 50 and 100nm. This should lead to higher field enhancement compared to the non-interacting nanorod array used for the MUA experiment. The discrepancy might be explained by residues of the EBL preparation process, preventing complete covering of the nanorods with ODT [34].

Nevertheless, the EF -values of MUA are still lower than those found for ODT on electrochemically prepared nanowires. If one assumes a sufficiently clean rod surface, allowing full adsorption in both cases, there must be other reasons for the lower MUA values. First of all, the enhancement factors were estimated by using the completely deprotonated IRRAS reference [spectrum (b) in Fig. 7.3]. This certainly underestimates the actual enhancement since at least some carboxyl groups are still protonated (Sec. 7.2.3). Furthermore, due to the very broad vibrational bands of MUA, only broad dents without extrema were present in the NAIRS spectra (see Fig. 7.5a). Hence, taking only the signal intensity maybe also underestimates the actual enhancement. Instead, comparing the peak areas would be a better option. However, the determination of a peak area is very difficult and error afflicted in case of the Fano-like MUA signal shown in Fig. 7.8c. Last but not least, the tip end morphology could also cause the seemingly higher enhancement of the electrochemically prepared nanorods (see Sec. 2.4.2).

7.3. Important Findings

- The configuration of the carboxyl group of MUA can be changed by the immersion solvent in case of IRRAS measurements. In contrast, no change was observed for nanoantenna-assisted IR spectroscopic measurements.
- The first derivative of a NAIRS spectrum can be used to identify the spectral signature of adsorbates, provided that the signal-to-noise ratio is high enough.
- The enhancement factors of the symmetric and antisymmetric COO^- stretching vibrations of MUA were estimated to be 48000 and 34000, respectively. These values are comparable to former experiments of ODT on lithographic gold nanorods, but still smaller than the values obtained for electrochemically prepared, single crystalline nanowires.
- Oxygen plasma cleaning does not completely remove alkanethiol adsorbates. Residues remain bound to the gold nanoantenna, preventing new adsorption of molecules.

8. Summary

The main focus of the present thesis was on the characterization and preparation of nanosized gaps between the tip ends of nanoantennas in order to increase near-field coupling and, hence, increase the sensitivity for the potential sensing application “nanoantenna-assisted IR spectroscopy”. Furthermore, the dependence of the infrared far-field optical properties of lithographically prepared nanorods on the substrate polarizability as well as on the arrangement of the rods within an array was investigated. Finally, the probe molecule mercaptoundecanoic acid was optically characterized by IRRAS as well as by NAIRS using a gold nanorod array.

Lithographically prepared nanorods with lengths in the μm -range show antenna-like plasmon resonances in the infrared [29, 31, 34]. In this work, the far-field optical properties of non-interacting nanoantenna arrays (distances between nearest neighbors being large enough to exclude interaction) were analyzed. It was shown that a higher substrate refractive index leads to resonances at longer wavelengths, which can be explained by induced image charges in the substrate. Moreover, the linear relation between rod length and resonant wavelength can be described by the analytical model of L. NOVOTNY [65]. However, NOVOTNY’s model, considering a nanoantenna surrounded by a homogeneous, effective medium, fails to account for the experimental geometry where the nanorod is placed on a substrate. Consequently, a direct correlation between the effective dielectric constant obtained from the NOVOTNY fit and the dielectric constant of the substrate does not exist.

In addition to natural oxide covered silicon, thermally oxidized silicon with an oxide thickness of about 100nm was used as substrate for gold nanorod arrays. It turned out that the optical properties of the nanorods resemble those of nanorods on quartz glass as long as the antenna resonance is located at higher frequencies compared to the *reststrahlen* band of the oxide ($1080 - 1247\text{cm}^{-1}$). For resonances near or inside the *reststrahlen* band, the excitation of a surface phonon-polariton at the air/oxide interface cloaks the antenna resonance, i.e. the same amount of light compared to the bare substrate can pass by the metal nanorods.

8. Summary

Rectangular nanorod arrays on natural oxide covered silicon featuring different separation distances parallel (longitudinal) and perpendicular (transverse) to the long rod axis were investigated. The aim was to figure out an optimal array design for nanoantenna-assisted IR spectroscopy of adsorbates. For future applications, the rod density within an array should be high to ensure a sufficient signal-to-noise ratio at short measurement times. Thus, small separations between individual rods would be desirable. While very small (longitudinal) gaps between the tip ends of the rods promise dramatic increase of near-field coupling and enhancement [30, 35], it was demonstrated in this thesis that a transverse separation below the first constructive interference condition (resonant wavelength in the substrate equals separation distance) is counterproductive for NAIRS. Besides a shift of the resonance position to smaller wavelengths accompanied by extraordinary broadening and decrease of extinction in the far-field, the near-field amplitude decreases as shown by scattering-type near-field optical microscopic mappings. Hence, the optimal rod density on the substrate depends on the substrate polarizability via the constructive interference condition.

Since the lithographic preparation of gaps between the tip ends of the nanorods is limited to about 10 – 20 nm [124], two different approaches were applied to fabricate nanosized gaps. First wet-chemical metal deposition experiments showed that nanogaps can be principally fabricated. However, since the whole sample is modified within one deposition step, the photo-induced metal deposition technique was chosen, promising spatial selectivity of the deposition process on the sample.

In experiments with nanorod arrays on silicon substrates, it turned out that the deposition within the array occurs quite inhomogeneous, leading to small gaps on the one hand, and merged rods on the other hand. Thus, additional experiments with individual nanorod dimers on calcium fluoride substrates (initial gap size of 20 nm) were carried out by using an inverted microscope and a laser light source ($\lambda = 532$ nm). Based on SEM images of a carbon covered test sample, the growth of the dimers could be observed and qualitatively related to the IR optical response. However, it was not possible to precisely determine the gap size.

Another sample of nanorod dimers on calcium fluoride was photo-chemically modified and spectroscopied. Gap sizes below 10 nm have been most likely prepared as indicated by the comparison with FDTD simulations. Furthermore, the appearance of additional modes in the IR spectra with increasing interaction was monitored and attributed to bonding and antibonding combinations of the $l = 1$ and $l = 2$ modes of individual rods.

Besides growing of nanorods, focused ion beam milling was applied to prepare nanogaps by cutting long rods in the middle. The far-field IR spectroscopic investigations were compared with SEM as well as transmission electron microscopic images. The data indicated that SEM was not able to identify a complete separation of the two milled parts, in contrast to TEM, which precisely determined gap sizes down to 20nm. Most importantly, it was found that IR spectroscopy offers a non-destructive method to assess the completeness of a FIB-milled nanogap. Concerning the substrate, thermally oxidized silicon promises to be the better choice compared to natural oxide covered silicon since SiO₂ seems to sustain electrical insulation between the two parts of the milled nanorod.

Moreover, mercaptoundecanoic acid was used as a probe molecule to demonstrate the NAIRS approach. Enhancement factors of the COO⁻ stretching vibration in the range of 34000 – 48000 could be estimated which are in the same order of magnitude compared to findings from ODT adsorbed on lithographic gold nanorods [34, 102]. However, the enhancement factors of electrochemically prepared, single crystalline gold nanowires could not be reached. Possible reasons for the observed discrepancy could be a reduced molecule adsorption on the gold nanorods due to residues of the EBL fabrication or intrinsic differences between nanowires and nanorods (crystallinity, tip end morphology). Finally, the change of the carboxyl configuration of MUA depending on the immersion solution could not be monitored in NAIRS experiments which is in contrast to findings of IRRAS. The different measurement conditions (air in NAIRS, vacuum in IRRAS) might explain why the adsorbate behaves differently in NAIRS.

9. Outlook

So far, possible interaction effects in nanorod arrays in longitudinal and transverse direction were investigated separately. However, IR measurements of nanorod arrays with reduced separations in both directions showed an unexpected blue-shift of the resonance with decreasing longitudinal spacing. Besides IR spectroscopic measurements of new samples in which both separation distances are varied, comparisons with FDTD simulations of arrays might help to more systematically analyze this behavior.

The photo-induced metal deposition turned out to be the most promising approach to nanogap formation. In order to obtain a quantitative statement on the near-field enhancing properties of the prepared nanorod dimers, NAIRS measurements of MUA could be performed, since the resonance frequencies of the photo-chemically manipulated dimers are in the range of the characteristic bands of MUA ($1400 - 1700 \text{ cm}^{-1}$). However, the NAIRS measurements of MUA shown in this thesis suggest that the MUA monolayer is not very stable at ambient conditions. For this reason, it is recommended to use to a synchrotron light source for future NAIRS experiments to reduce the measurement time and, thus, the exposure to air.

After the SEIRS experiment, the sample could be investigated by TEM to precisely determine the gap sizes. In addition, simulations of dimers with different gap sizes, lengths and diameters should be performed to gain insight on the complex optical behavior. Moreover, the simulations may be used to estimate the gap sizes since TEM measurements are very elaborate and expensive.

In regard to future photo-induced metal deposition experiments, some improvements have to be made concerning the control the deposition process. The dimers should be separated for a larger distance on the substrate to avoid non-selective particle growth. Furthermore, the concentration of the gold salt as well as the laser power should be reduced to ensure more homogeneous metal deposition. In addition, annealing of the sample after deposition could probably lead to a smoother rod surface.

9. Outlook

In addition, the focused ion beam milling of nanorods needs to be further improved to reduce the fabricated gap sizes. A first approach would be to decrease the dwell times to avoid opening of the gaps. Furthermore, the lithographic fabrication could be modified in the following way: instead of preparing a long nanorod, one should try to prepare “touching dimers” which are then milled by the FIB. In this way, the total amount of gold, which has to be milled to achieve complete separation, and, hence, also the amount of implanted gallium ions could be decreased. Due to the gallium ion induced change of the optical properties of the substrate, only thermally oxidized silicon wafers should be used for further fabrication series.

Finally, the thickness of the oxide layer could be varied to investigate the cloaking effect of the antenna resonances.

Bibliography

- [1] H. Günzler and H.U. Gremlich. *IR spectroscopy - An introduction*. Wiley-VCH, 2002.
- [2] D.F. Swinehart. The Beer-Lambert law. *Journal of Chemical Education*, 39(7):333, 1962. doi:10.1021/ed039p333.
- [3] D.Z. Robinson. Quantitative analysis with infrared spectrophotometers. *Analytical Chemistry*, 23(2):273–277, 1951. doi:10.1021/ac60050a013.
- [4] J.T. Pelton and L.R. McLean. Spectroscopic methods for analysis of protein secondary structure. *Analytical Biochemistry*, 277(2):167–176, 2000. doi:10.1006/abio.1999.4320.
- [5] J. Kong and S. Yu. Fourier transform infrared spectroscopic analysis of protein secondary structures. *Acta Biochimica et Biophysica Sinica*, 39(8):549–559, 2007. doi:10.1111/j.1745-7270.2007.00320.x.
- [6] J.R. Ferraro and K. Nakamoto. *Introductory Raman Spectroscopy*. Academic Press, Inc., San Diego, 2nd edition, 2003.
- [7] A. Pucci, F. Neubrech, J. Aizpurua, T.W. Cornelius, and M. Lamy de la Chapelle. *One-Dimensional Nanostructures*, chapter "Electromagnetic nanowire resonances for field-enhanced spectroscopies", pages 175–213. Springer, 2008.
- [8] M. Fleischmann, P.J. Hendra, and A.J. McQuillan. Raman spectra of pyridine adsorbed at a silver electrode. *Chemical Physics Letters*, 80(2):163–166, 1974.
- [9] M. Moskovits. Surface-enhanced spectroscopy. *Reviews of Modern Physics*, 57(3):783–826, 1985. doi:10.1103/RevModPhys.57.783.
- [10] A. Hartstein, J.R. Kirtley, and J.C. Tsang. Enhancement of the infrared absorption from molecular monolayers with thin metal overlayers. *Physical Review Letters*, 45(210), 1980.

- [11] M. Osawa. *Near-field optics and surface plasmon polaritons*, chapter Surface-Enhanced Infrared Absorption, pages 163–187. Springer, Berlin, Heidelberg, 2001.
- [12] M.G. Albrecht and J.A. Creighton. Anomalous intense raman spectra of pyridine at a silver electrode. *Journal of the American Chemical Society*, 99:5215, 1977.
- [13] A. Otto. Surface enhanced Raman scattering of adsorbates. *Journal of Raman Spectroscopy*, 22:743–752, 1991.
- [14] A. Otto. Surface-enhanced Raman scattering. *Journal of Physics: Condensed Matter*, 4:1143–1212, 1992.
- [15] A. Otto. The "chemical" (electronic) contribution to surface-enhanced Raman scattering. *Journal of Raman Spectroscopy*, 36(6-7):497–509, 2005. doi:10.1002/jrs.1355.
- [16] R. Aroca. *Surface-enhanced Vibrational Spectroscopy*. John Wiley and Sons, England, 2006.
- [17] E.C. Le Ru and P.G. Etchegoin. *Principles of Surface-Enhanced Raman Spectroscopy and related plasmonic effects*. Elsevier, Amsterdam, 2009.
- [18] M. Pelton, J. Aizpurua, and G. Bryant. Metal-nanoparticle plasmonics. *Laser & Photonics Reviews*, 2(3):136–159, 2008. doi:10.1002/lpor.200810003.
- [19] S.A. Maier and H.A. Atwater. Plasmonics: Localization and guiding of electromagnetic energy in metal/dielectric structures. *Journal of Applied Physics*, 98(1):011101, 2005. doi:doi:10.1063/1.1951057.
- [20] S.A. Maier. *Plasmonics: Fundamentals and Applications*. Springer, New York, USA, 2007.
- [21] J. A. Schuller, E. S. Barnard, W. Cai, Y.C. Jun, J.S. White, and M.L. Brongersma. Plasmonics for extreme light concentration and manipulation. *Nature Materials*, 9:193–204, 2010. doi:10.1038/nmat2630.
- [22] E. Ozbay. Plasmonics: Merging photonics and electronics at nanoscale dimensions. *Science*, 311(5758):189–193, 2006. doi:10.1126/science.1114849.

- [23] M. Sinther. *UHV-Studien zur oberflächenverstärkten Infrarotabsorption auf rauhen Kupferfilmen*. PhD thesis, Heidelberg University, Kirchhoff Institut for Physics, 2002.
- [24] A. Priebe, M. Sinther, G. Fahsold, and A. Pucci. The correlation between film thickness and adsorbate line shape in surface enhanced infrared absorption. *Journal of Chemical Physics*, 119(9):4887, 2003. doi:10.1063/1.1597232.
- [25] D. Enders and A. Pucci. Surface enhanced infrared absorption of octadecanethiol on wet-chemically prepared Au nanoparticle films. *Applied Physics Letters*, 88(18):184104, 2006. doi:10.1063/1.2201880.
- [26] D. Enders, T. Nagao, T. Nakayama, and M. Aono. Precisely controlled fabrication of a highly sensitive au sensor film for surface enhanced spectroscopy. *Japanese Journal of Applied Physics*, 46(49):L1222–L1224, 2007. doi:10.1143/JJAP.46.L1222.
- [27] D. Enders, T. Nagao, A. Pucci, T. Nakayama, and M. Aono. Surface-enhanced ATR-IR spectroscopy with interface-grown plasmonic gold-island films near the percolation threshold. *Physical Chemistry Chemical Physics*, 13:4935–4941, 2011. doi:10.1039/C0CP01450H.
- [28] F. Le, D.W. Brandl, Y.A. Urzhumov, H. Wang, J. Kundu, N.J. Halas, J. Aizpurua, and P. Nordlander. Metallic nanoparticle arrays: A common substrate for both surface-enhanced Raman scattering and surface-enhanced infrared absorption. *ACS Nano*, 2(4):707–718, 2008. doi:10.1021/nn800047e.
- [29] G. Bryant, F.J. García de Abajo, and J. Aizpurua. Mapping the plasmon resonances of metallic nanoantennas. *Nano Letters*, 8(2):631–636, 2008. doi:10.1021/nl073042v.
- [30] J. Aizpurua, G.W. Bryant, L.J. Richter, F. J. García de Abajo, B.K. Kelley, and T. Mallouk. Optical properties of coupled metallic nanorods for field-enhanced spectroscopy. *Physical Review B*, 71(23):235420, Jun 2005. doi:10.1103/PhysRevB.71.235420.
- [31] F. Neubrech, D. Weber, R. Lovrincic, A. Pucci, M. Lopes, T. Toury, and M. Lamy de La Chapelle. Resonances of individual lithographic gold nanowires in the infrared. *Applied Physics Letters*, 93(16):163105, 2008. doi:10.1063/1.3003870.

- [32] R. Adato, A.A. Yanik, J.J. Amsden, D.L. Kaplan, F. G. Omenetto, M.K. Hong, S. Erramilli, and H. Altug. Ultra-sensitive vibrational spectroscopy of protein monolayers with plasmonic nanoantenna arrays. *Proceedings of the National Academy of Sciences*, 106(46):19227–19232, 2009. doi:10.1073/pnas.0907459106.
- [33] F. Neubrech, A. Pucci, T.W. Cornelius, S. Karim, A. García-Etxarri, and J. Aizpurua. Resonant plasmonic and vibrational coupling in a tailored nanoantenna for infrared detection. *Physical Review Letters*, 101(15):157403, 2008. doi:10.1103/PhysRevLett.101.157403.
- [34] F. Neubrech. *Surface enhanced infrared spectroscopy using gold nanoantennas*. PhD thesis, Heidelberg University, Kirchhoff Institute for Physics, 2008.
- [35] N. Yu, E. Cubukcu, L. Diehl, M.A. Belkin, K.B. Crozier, F. Capasso, D. Bour, S. Corzine, and G. Höfler. Plasmonic quantum cascade laser antenna. *Applied Physics Letters*, 91(17):173113, 2007. doi:10.1063/1.2801551.
- [36] T. Härtling. *Photochemical tuning of surface plasmon resonances in metal nanoparticles*. PhD thesis, Dresden University of Technology, 2009.
- [37] K.R. Brown, D.G. Walter, and M.J. Natan. Seeding of colloidal Au nanoparticle solutions. 2. Improved control of particle size and shape. *Chemistry of Materials*, 12:306–313, 2000. doi:10.1021/cm980065p.
- [38] T. Blom, K. Welch, M. Stromme, E. Coronel, and K. Leifer. Fabrication and characterization of highly reproducible, high resistance nanogaps made by focused ion beam milling. *Nanotechnology*, 18(28):285301, 2007. doi:10.1088/0957-4484/18/28/285301.
- [39] M. Klevenz. *Infrared spectroscopy and vapour pressure measurements of silicon monoxide, silicon dioxide and forsterite*. PhD thesis, Heidelberg University, Kirchhoff Institut for Physics, 2009.
- [40] J.D. Jackson. *Klassische Elektrodynamik*. Gruyter, 4. Auflage, 2006.
- [41] C. Kittel. *Einführung in die Festkörperphysik*. Oldenbourg Verlag, 2002.
- [42] S. Hunklinger. *Festkörperphysik*. Oldenbourg Verlag, 2007.
- [43] M. Dressel and G. Grüner. *Optical Properties of Electrons in Matter*. Cambridge University Press, 2002.

- [44] M.A. Ordal, L.L. Long, R.J. Bell, R.R. Bell, R.W. Alexander, and C.A. Ward. Optical properties of the metals Al, Co, Cu, Au, Fe, Pb, Ni, Pd, Pt, Ag, Ti and W in the infrared and far infrared. *Applied Optics*, 22(7):1099–1119, 1983. doi:10.1364/AO.22.001099.
- [45] P.B. Johnson and R.W. Christy. Optical constants of the noble metals. *Physical Review B*, 6(12):4370–4379, 1972. doi:10.1103/PhysRevB.6.4370.
- [46] SCOUT. software package for optical spectroscopy, including dielectric function database. *supplied by M. Theis Hard- and Software, Aachen, Germany.*
- [47] U. Kreibig and M. Vollmer. *Optical properties of Metal Clusters*. Springer, Berlin, 1995.
- [48] P. Drude. Zur Elektronentheorie der Metalle. *Annalen der Physik*, 306:566–613, 1900.
- [49] H. Ibach and H. Lüth. *Festkörperphysik*. Springer Verlag, 1999.
- [50] F. Neubrech. Untersuchung plasmonischer und thermischer eigenschaften von goldnanodrähten mittels infrarot-spektroskopie. Diplomarbeit, Universität Heidelberg, Kirchhoff-Institut für Physik, 2006.
- [51] K. Singer. Infrared-optical and dc-measurements of the conductivity of ultrathin Cu-films on Si(111)-7x7:. Diploma thesis, Heidelberg University, Kirchhoff-Institut für Physik, 2000.
- [52] N.W. Ashcroft and N.D. Mermin. *Solid State Physics*. New York, 1976.
- [53] N.E. Christensen. Relativistic band calculation and the optical properties of gold. *Physical Review B*, 4(10):3321–3344, 1971. doi:10.1103/PhysRevB.4.3321.
- [54] K.A. Willets and R.P. Van Duyne. Localized surface plasmon resonance spectroscopy and sensing. *Annual Review of Physical Chemistry*, 58:267–297, 2007. doi:10.1146/annurev.physchem.58.032806.104607.
- [55] J.M. Pitarke, V.M. Silkin, E.V. Chulkov, and P.M. Echenique. Theory of surface plasmons and surface-plasmon polaritons. *Reports on Progress in Physics*, 70(1):1–87, 2007. doi:10.1088/0034-4885/70/1/R01.

- [56] H. Raether. *Surface plasmons on smooth and rough surfaces and on gratings*. Springer Verlag, Berlin, 1988.
- [57] G. Mie. Beiträge zur Optik trüber Medien, speziell kolloidaler Metallösungen. *Annalen der Physik*, 25(3):377–445, 1908. doi:10.1002/andp.19083300302.
- [58] E.D. Palik. *Handbook of Optical Constants of Solids*. Academic, New York, 1985.
- [59] P.K. Jain, S. Eustis, and M.A. El-Sayed. Plasmon coupling in nanorod assemblies: Optical absorption, discrete dipole approximation simulation, and exciton-coupling model. *Journal of Physical Chemistry B*, 110(37):18243–18253, 2006. doi:10.1021/jp063879z.
- [60] A.A. Oraevsky and A.N. Oraevsky. On a plasmon resonance in ellipsoidal nanoparticles. *Quantum Electronics*, 32(1):79–82, 2002. doi:10.1070/QE2002v032n01ABEH002131.
- [61] C.F. Bohren and D.R. Huffmann. *Absorption and Scattering of Light by Small Particles*. John Wiley and Sons, New York, 1983.
- [62] T.G. Ruck. *Radar Cross Section Handbook*. Plenum press, New York, 1970.
- [63] C.A. Brebbia, J.C. Telles, and L.C. Wrobel. *Boundary Element Techniques*. Springer, Berlin, 1984.
- [64] F.J. García de Abajo and J. Aizpurua. Numerical simulation of electron energy loss near inhomogeneous dielectrics. *Physical Review B*, 56(24):15873–15884, 1997. doi:10.1103/PhysRevB.56.15873.
- [65] L. Novotny. Effective wavelength scaling for optical antennas. *Physical Review Letters*, 98(26):266802, 2007. doi:10.1103/PhysRevLett.98.266802.
- [66] J. Aizpurua. Private communication.
- [67] P.F. Liao and A. Wokaun. Lightning rod effect in surface enhanced raman scattering. *Journal of Chemical Physics*, 76:751–752, 1982.
- [68] M.I. Stockman, editor. *Simulating electromagnetic response in coupled metallic nanoparticles for nanoscale optical microscopy and spectroscopy: nanorod-end effects*, volume 6323 of *Proceedings of SPIE*, 2006. doi:10.1117/12.680701.

- [69] E. Hao and G.C. Schatz. Electromagnetic fields around silver nanoparticles and dimers. *Journal of Chemical Physics*, 357120(1):357, 2004. doi:10.1063/1.1629280.
- [70] F. Neubrech, A. Garcia-Etxarri, D. Weber, J. Bochterle, H. Shen, M. Lamy de la Chapelle, G.W. Bryant, J. Aizpurua, and A. Pucci. Defect-induced activation of symmetry forbidden infrared resonances in individual metallic nanorods. *Applied Physics Letters*, 96(21):213111, 2010. doi:10.1063/1.3437093.
- [71] D. Weber and A. Pucci. *Nanoantenna (tentative title)*, chapter "Antenna Interaction in the Infrared". Pan Stanford Publishing, Singapore, 2011.
- [72] J.R. Krenn, G. Schider, W. Rechberger, B. Lamprecht, A. Leitner, F.R. Aussenegg, and J.C. Weeber. Design of multipolar plasmon excitations in silver nanoparticles. *Applied Physics Letters*, 77(21):3379, 2000. doi:10.1063/1.1327615.
- [73] G. Schider, J.R. Krenn, A. Hohenau, H. Ditlbacher, A. Leitner, F.R. Aussenegg, W.L. Schaich, I. Puscasu, B. Monacelli, and G. Boreman. Plasmon dispersion relation of au and ag nanowires. *Physical Review B*, 68(15):155427, 2003. doi:10.1103/PhysRevB.68.155427.
- [74] P. Nordlander, C. Oubre, E. Prodan, K. Li, and M.I. Stockman. Plasmon hybridization in nanoparticle dimers. *Nano Letters*, 4(5):899–903, 2004. doi:10.1021/nl049681c.
- [75] G. Laurent, N. Felidj, J. Aubard, G. Levi, J.R. Krenn, A. Hohenau, G. Schider, A. Leitner, and F.R. Aussenegg. Evidence of multipolar excitations in surface enhanced raman scattering. *Physical Review B*, 71(4):045430, 2005. doi:10.1103/PhysRevB.71.045430.
- [76] J. Dorfmueller, R. Vogelgesang, R.T. Weitz, C. Rockstuhl, C. Etrich, T. Pertsch, F. Lederer, and K. Kern. Fabry-pérot resonances in one-dimensional plasmonic nanostructures. *Nano Letters*, 9(6):2372–2377, 2009. doi:10.1021/nl900900r.
- [77] D. Weber, P. Albella, P. Alonso-González, F. Neubrech, G. Han, T. Nagao, R. Hillenbrand, J. Aizpurua, and A. Pucci. Longitudinal and transverse coupling in infrared gold nanoantenna arrays: long range versus short range interaction regimes. *Optics Express*, 19(16):15047–15061, 2011. doi:10.1364/OE.19.015047.

- [78] K.H. Su, Q.-H. Wei, X. Zhang, J.J. Mock, D.R. Smith, and S. Schultz. Interparticle coupling effects on plasmon resonances of nanogold particles. *Nano Letters*, 3(8):1087–1090, 2003. doi:10.1021/nl034197f.
- [79] T. Atay, J.-H. Song, and A.V. Nurmikko. Strongly interacting plasmon nanoparticle pairs: From dipole-dipole interaction to conductively coupled regime. *Nano Letters*, 4(9):1627–1631, 2004. doi:10.1021/nl049215n.
- [80] P.K. Jain, W. Huang, and M.A. El-Sayed. On the universal scaling behavior of the distance decay of plasmon coupling in metal nanoparticle pairs: A plasmon ruler equation. *Nano Letters*, 7(7):2080–2088, 2007. doi:10.1021/nl071008a.
- [81] M. Gluodenis and C.A. Foss. The effect of mutual orientation on the spectra of metal nanoparticle rod-rod and rod-sphere pairs. *Journal of Physical Chemistry B*, 106(37):9484–9489, 2002. doi:10.1021/jp014245p.
- [82] A.M. Funston, C. Novo, T.J. Davis, and P. Mulvaney. Plasmon coupling of gold nanorods at short distances and in different geometries. *Nano Letters*, 9(4):1651–1658, 2009. doi:10.1021/nl900034v.
- [83] D.P. Fromm, A. Sundaramurthy, P.J. Schuck, G. Kino, and W.E. Moerner. Gap-dependent optical coupling of single bowtie nanoantennas resonant in the visible. *Nano Letters*, 4(5):957–961, 2004. doi:10.1021/nl049951r.
- [84] O.L. Muskens, V. Giannini, J.A. Sánchez-Gil, and J. Gómez Rivas. Optical scattering resonances of single and coupled dimer plasmonic nanoantennas. *Optics Express*, 15(26):17736–17746, 2007. doi:10.1364/OE.15.017736.
- [85] E.M. Hicks, S. Zou, G.C. Schatz, K.G. Spears, R.P. Van Duyne, L. Gunnarsson, T. Rindzevicius, B. Kasemo, and M. Käll. Controlling plasmon line shapes through diffractive coupling in linear arrays of cylindrical nanoparticles fabricated by electron beam lithography. *Nano Letters*, 5(6):1065–1070, 2005. doi:10.1021/nl0505492.
- [86] B. Lamprecht, G. Schider, R.T. Lechner, H. Ditlbacher, J.R. Krenn, A. Leitner, and F.R. Aussenegg. Metal nanoparticle gratings: Influence of dipolar particle interaction on the plasmon resonance. *Physical Review Letters*, 84(20):4721–4724, 2000. doi:10.1103/PhysRevLett.84.4721.
- [87] N. Félidj, J. Aubard, G. Lévi, J.R. Krenn, G. Schider, A. Leitner, and F.R. Aussenegg. Enhanced substrate-induced coupling in two-dimensional gold

- nanoparticle arrays. *Physical Review B*, 66(24):245407, 2002. doi:10.1103/PhysRevB.66.245407.
- [88] L. Zhao, K. Lance Kelly, and G.C. Schatz. The extinction spectra of silver nanoparticle arrays: Influence of array structure on plasmon resonance wavelength and width. *Journal of Physical Chemistry B*, 107(30):7343–7350, 2003. doi:10.1021/jp034235j.
- [89] C.L. Haynes, A.D. McFarland, Van Duyne R.P. Zhao, L.L., G.C. Schatz, L. Gunnarsson, J. Prikulis, B. Kasemo, and M. Käll. Nanoparticle optics: The importance of radiative dipole coupling in two-dimensional nanoparticle arrays. *Journal of Physical Chemistry B*, 107(30):7337–7342, 2003. doi:10.1021/jp034234r.
- [90] N. Félidj, G. Laurent, J. Aubard, G. Lévi, A. Hohenau, J.R. Krenn, and F.R. Aussenegg. Grating-induced plasmon mode in gold nanoparticle arrays. *Journal of Chemical Physics*, 123(22):2140699, 2005. doi:10.1063/1.2140699.
- [91] B. Auguié and W.L. Barnes. Collective resonances in gold nanoparticle arrays. *Physical Review Letters*, 101(14):143902, 2008. doi:10.1103/PhysRevLett.101.143902.
- [92] R. Adato, A.A. Yanik, C.-H. Wu, G. Shvets, and H. Altug. Radiative engineering of plasmon lifetimes in embedded nanoantenna arrays. *Optics Express*, 18(5):4526–4537, 2010. doi:10.1364/OE.18.004526.
- [93] P. Albella. Private communication.
- [94] W. Rechberger, A. Hohenau, A. Leitner, J.R. Krenn, B. Lamprecht, and F.R. Aussenegg. Optical properties of two interacting gold nanoparticles. *Optics Communications*, 220(1-3):137–141, 2003. doi:10.1016/S0030-4018(03)01357-9.
- [95] C. Sönnichsen, B.M. Reinhard, J. Liphardt, and A.P. Alivisatos. A molecular ruler based on plasmon coupling of single gold and silver nanoparticles. *Nature Biotechnology*, 23(6):741–745, 2005.
- [96] B. Auguié, X.M. Bedaña, W.L. Barnes, and F.J. García de Abajo. Diffractive arrays of gold nanoparticles near an interface: Critical role of the substrate. *Physical Review B*, 82(15):155447, 2010. doi:10.1103/PhysRevB.82.155447.

- [97] S. Zou, N. Janel, and G.C. Schatz. Silver nanoparticle array structures that produce remarkably narrow plasmon lineshapes. *Journal of Chemical Physics*, 120(23):10871, 2004. doi:10.1063/1.1760740.
- [98] S. Zou and G.C. Schatz. Narrow plasmonic/photonic extinction and scattering line shapes for one and two dimensional silver nanoparticle arrays. *Journal of Chemical Physics*, 121(24):12606, 2004. doi:10.1063/1.1826036.
- [99] V.G. Kravets, F. Schedin, and A.N. Grigorenko. Extremely narrow plasmon resonances based on diffraction coupling of localized plasmons in arrays of metallic nanoparticles. *Physical Review Letters*, 101(8):087403, 2008. doi:10.1103/PhysRevLett.101.087403.
- [100] X.M. Bendaña and F.J. García de Abajo. Confined collective excitations of self-standing and supported planar periodic particle arrays. *Optics Express*, 17(21):18826–18835, 2009. doi:doi:10.1364/OE.17.018826.
- [101] M. Fox. *Optical properties of solids*. Oxford University Press, New York, 2008.
- [102] F. Neubrech. Private communication.
- [103] M.K. Gunde. Vibrational modes in amorphous silicon dioxide. *Physica B: Condensed Matter*, 292(3-4):286–295, 2000. doi:10.1016/S0921-4526(00)00475-0.
- [104] K.L. Kliewer and R. Fuchs. Optical modes of vibration in an ionic crystal slab including retardation. i. nonradiative region. *Physical Review*, 144(2):495–503, 1966. doi:10.1103/PhysRev.144.495.
- [105] K.L. Kliewer and R. Fuchs. Optical modes of vibration in an ionic crystal slab including retardation. ii. radiative region. *Physical Review*, 150(2):573–588, 1966. doi:10.1103/PhysRev.150.573.
- [106] J.C. Maxwell-Garnett. Colours in metal glasses, in metallic films, and in metallic solutions. II. *Philosophical Transactions of the Royal Society A*, 205:387–401, 1906. doi:10.1098/rsta.1906.0007.
- [107] D.A.G. Bruggeman. Berechnung verschiedener physikalischer Konstanten von heterogenen Substanzen. I. Dielektrizitätskonstanten und Leitfähigkeiten der Mischkörper aus isotropen Substanzen. *Annalen der Physik*, 416(7):636–664, 1935. doi:10.1002/andp.19354160705.

- [108] G. Han, D. Weber, F. Neubrech, I. Yamada, M. Mitome, Y. Bando, A. Pucci, and T. Nagao. Infrared spectroscopic and electron microscopic characterization of gold nanogap structure fabricated by focused ion beam. *Nanotechnology*, 22:275202, 2011. doi:10.1088/0957-4484/22/27/275202.
- [109] D. Weber. Preliminary studies for antenna-resonance enhanced Raman spectroscopy with excitation in the near-infrared spectral range. Diploma thesis, Heidelberg University, 2008.
- [110] J. Bochterle. Temperature dependence of the infrared-optical properties of gold nanostripes. Diploma thesis, Heidelberg University, 2010.
- [111] G. Binnig, C.F. Quate, and Ch. Gerber. Atomic force microscopy. *Physical Review Letters*, 56(9):930–933, 1986. doi:10.1103/PhysRevLett.56.930.
- [112] D. Sarid. *Scanning Force Microscopy*. Oxford University Press, New York, 1991.
- [113] E.P. Degarmo, J.T. Black, and R.A. Kohser. *Materials and Processes in Manufacturing*. Wiley, 9th edition, 2003.
- [114] T.C. Isabell, P.E. Fischione, C. O’Keefe, M.U. Guruz, and V.P. Dravid. Plasma cleaning and its applications for electron microscopy. *Microscopy and Microanalysis*, 5(2):126–135, 1999. doi:10.1017/S1431927699000094.
- [115] A.J.V Griffiths and T. Walther. Quantification of carbon contamination under electron beam irradiation in a scanning transmission electron microscope and its suppression by plasma cleaning. *Journal of Physics: Conference Series*, 241(1):012017, 2010. doi:10.1088/1742-6596/241/1/012017.
- [116] T.E. Everhart and R.F.M. Thornley. Wide-band detector for micro-microampere low-energy electron currents. *Journal of Scientific Instruments*, 37(7):246, 1960. doi:10.1088/0950-7671/37/7/307.
- [117] C. Ma. *Instructions for Use of LEO 1550VP Field Emission SEM with Oxford EDS and HKL EBSD*. California Institute of Technology, Pasadena, September 2003. URL: http://www.gps.caltech.edu/facilities/analytical/sem/LEOSEM_CIT_v2.pdf.
- [118] L. Reimer. *Scanning electron microscopy: Physics of image formation and microanalysis*. Springer, Berlin, Heidelberg, second edition, 1998.

Bibliography

- [119] S. Canovic, T. Jonsson, and M. Halvarsson. Grain contrast imaging in FIB and SEM. *Journal of Physics: Conference Series*, 126(1):012054, 2008. doi:10.1088/1742-6596/126/1/012054.
- [120] S.L. Flegler, J.W. Heckmann Jr., and K.L. Klomparens. *Scanning and Transmission Electron Microscopy. An Introduction*. W. H. Freeman and Company, New York, 1993.
- [121] J. Goldstein, D. Newbury, D. Joy, C. Lyman, P. Echlin, E. Lifshin, L. Sawyer, and J. Michael. *Scanning Electron Microscopy and X-Ray Microanalysis*. Springer, 2003.
- [122] T. Nagao. Private communication.
- [123] G. Han. Private communication.
- [124] A. Toma. Private communication.
- [125] F. Bartoli, R. Allen, L. Esterowitz, and M. Kruer. Auger-limited carrier lifetimes in HgCdTe at high excess carrier concentrations. *Journal of Applied Physics*, 45(5):2150, 1974. doi:10.1063/1.1663561.
- [126] R.L. Richardson, H. Yang, and P.R. Griffiths. Effects of detector nonlinearity on spectra measured on three commercial FT-IR spectrometers. *Applied Spectroscopy*, 52(4):572–578, 1998.
- [127] L. Fiedler, S. Newman, and S. Bakan. Correction of detector nonlinearity in Fourier transform spectroscopy with a low-temperature blackbody. *Applied Optics*, 44(25):5332–4340, 2005. doi:10.1364/AO.44.005332.
- [128] Korth Kristalle GmbH. URL: <http://www.korth.de>.
- [129] Heraeus. *Quartz Glass for Optics - Data and Properties*. 2007.
- [130] O. Humbach, H. Fabian, U. Grzesik, U. Haken, and W. Heitmann. Analysis of OH absorption bands in synthetic silica. *Journal of Non-Crystalline Solids*, 203:19–26, 1996. doi:10.1016/0022-3093(96)00329-8.
- [131] F.A. Johnson. Lattice absorption bands in silicon. *Proceedings of the Physical Society*, 73(2):265, 1959. doi:10.1088/0370-1328/73/2/315.

- [132] C.T. Kirk. Quantitative analysis of the effect of disorder-induced mode coupling on infrared absorption in silica. *Physical Review B*, 38(2):1255–1273, 1988. doi:10.1103/PhysRevB.38.1255.
- [133] G. Lucovsky, C.K. Wong, and W.B. Pollard. Vibrational properties of glasses: Intermediate range order. *Journal of Non-Crystalline Solids*, 59-60(2):839–846, 1983. doi:10.1016/0022-3093(83)90301-0.
- [134] P. Grosse, B. Harbecke, B. Heinz, R. Meyer, and M. Offenbergl. Infrared spectroscopy of oxide layers on technical Si wafers. *Applied Physics A: Materials Science & Processing*, 39(4):257–268, 1986. doi:10.1007/BF00617270.
- [135] R. Brendel and D. Bormann. An infrared dielectric function model for amorphous solids. *Journal of Applied Physics*, 71(1), 1992. doi:10.1063/1.350737.
- [136] A. Ulman. Formation and structure of self-assembled monolayers. *Chemical Reviews*, 96(4):1533–1554, 1996. doi:10.1021/cr9502357.
- [137] F. Schreiber. Structure and growth of self-assembling monolayers. *Progress in Surface Science*, 65:151–256, 2000. doi:10.1016/S0079-6816(00)00024-1.
- [138] C. Vericat, M.E. Vela, G.A. Benitez, J.A. Martin Gago, X. Torrelles, and R.C. Salvarezza. Surface characterization of sulfur and alkanethiol self-assembled monolayers on Au(111). *Journal of Physics: Condensed Matter*, 18(48):867–900, 2006. doi:10.1088/0953-8984/18/48/R01.
- [139] L.H. Dubois and R.G. Nuzzo. Synthesis, structure and properties of model organic surfaces. *Annual Review of Physical Chemistry*, 43:437–463, 1992. doi:10.1146/annurev.pc.43.100192.002253.
- [140] C.D. Bain and G.M. Whitesides. Modeling organic surfaces with self-assembled monolayers. *Angewandte Chemie, International Edition*, 1(4):110–116, 1989. doi:10.1002/anie.198905061.
- [141] R.T. Lee, P.E. Laibinis, J.P. Folkers, and G.M. Whitesides. Heterogeneous catalysis on platinum and self-assembled monolayers on metal and metal oxide surfaces. *Pure and Applied Chemistry*, 63(6):821–828, 1991. doi:10.1002/chin.199150320.

- [142] L. Häussling, H. Ringsdorf, F.J. Schmitt, and W. Knoll. Biotin-functionalized self-assembled monolayers on gold: Surface plasmon optical studies of specific recognition reactions. *Langmuir*, 7(9):1837–1870, 1991. doi:10.1021/la00057a001.
- [143] C.-M. Yam, C.-M. Pradier, M. Salmain, P. Marcus, and G. Jaouen. Binding of biotin to gold surfaces functionalized by self-assembled monolayers of cystamine and cysteamine: Combined FT-IRRAS and XPS characterization. *Journal of Colloid and Interface Science*, 235(1):183–189, 2001. doi:10.1006/jcis.2000.7362.
- [144] N. Nishi, D. Hobara, M. Yamamoto, and T. Kakiuchi. Chain-length-dependent change in the structure of self-assembled monolayers of n-alkanethiols on Au(111) probed by broad-bandwidth sum frequency generation spectroscopy. *Journal of Chemical Physics*, 118(4):1904–1911, 2003. doi:10.1063/1.1531098.
- [145] C. Naselli, J.F. Rabolt, and J.D. Swalen. Order-disorder transitions in Langmuir-Blodgett monolayers. I. Studies of two-dimensional melting by infrared spectroscopy. *Journal of Chemical Physics*, 82(4):2136–2140, 1985. doi:10.1063/1.448351.
- [146] S.M. Mendoza. *Exploiting molecular machines on surfaces*. PhD thesis, University of Groningen, Zernike Institute for Advanced Materials, 2007.
- [147] O. Dannenberger, M. Buck, and M. Grunze. Self-assembly of n-alkanethiols: A kinetic study by second harmonic generation. *Journal of Physical Chemistry B*, 103(12):2202–2213, 1999. doi:10.1021/jp9834331.
- [148] C.E.D. Chidsey and D.N. Loiacono. Chemical functionality in self-assembled monolayers: Structural and electrochemical properties. *Langmuir*, 6(3):682–691, 1990. doi:10.1021/la00093a026.
- [149] B. Kong, Y. Kim, and I.S. Choi. pH-dependent stability of self-assembled monolayers on gold. *Bulletin of the Korean Chemical Society*, 29(9):1843–1846, 2008.
- [150] Y. Li, J. Huang, R.T. McIver, and J.C. Hemminger. Characterization of thiol self-assembled films by laser desorption Fourier transform mass spectrometry.

- Journal of the American Chemical Society*, 114(7):2428–2432, 1992. doi:10.1021/ja00033a018.
- [151] N. Sandhyarani and T. Pradeep. Oxidation of alkanethiol monolayers on gold cluster surfaces. *Chemical Physics Letters*, 338(1):33–36, 2001. doi:10.1016/S0009-2614(01)00230-5.
- [152] Y. Zhang, R.H. Terrill, T.A. Tanzer, and P.W. Bohn. Ozonolysis is the primary cause of UV photooxidation of alkanethiolate monolayers at low irradiance. *Journal of the American Chemical Society*, 120(11):2654–2655, 1998. doi:10.1021/ja9714853.
- [153] M.H. Schoenfish and J.E. Pemberton. Air stability of alkanethiol self-assembled monolayers on silver and gold surfaces. *Journal of the American Chemical Society*, 120(18):4502–4513, 1998. doi:10.1021/ja974301t.
- [154] K. Hu and A.J. Bard. Use of atomic force microscopy for the study of surface acid-base properties of carboxylic acid-terminated self-assembled monolayers. *Langmuir*, 13(19):5114–5119, 1997. doi:10.1021/la9700782.
- [155] Y.-K. Kim, J.P. Koo, and J.S. Ha. Replacement of adsorbed alkanethiolate on Au with carboxyl-terminated thiol in solution: Effect of alkyl chain length. *Applied Surface Science*, 249(1-4):7–11, 2005. doi:10.1016/j.apsusc.2004.11.077.
- [156] M.C. Leopold, J.A. Black, and E.F. Bowden. Influence of gold topography on carboxylic acid terminated self-assembled monolayers. *Langmuir*, 18(4):978–980, 2002. doi:10.1021/la011683e.
- [157] G. Binnig and H. Rohrer. Scanning tunneling microscopy. *Surface Science*, 126:236–244, 1983.
- [158] E. Ito, K. Konno, J. Noh, K. Kanai, Y. Ouchi, K. Seki, and M. Hara. Chain length dependence of adsorption structure of COOH-terminated alkanethiol SAMs on Au(111). *Applied Surface Science*, 244(1-4):584–587, 2005. doi:10.1016/j.apsusc.2004.10.126.
- [159] K. Onuma, A. Oyane, T. Kokubo, G. Treboux, N. Kanzaki, and A. Ito. Nucleation of calcium phosphate on 11-mercaptopundecanoic acid self-assembled monolayer in a pseudophysiological solution. *Journal of Physical Chemistry B*, 104(50):11950–11956, 2000. doi:10.1021/jp002015p.

- [160] S.M. Mendoza, I. Arfaoui, S. Zanarini, F. Paolucci, and P. Rudolf. Improvements in the characterization of the crystalline structure of acid-terminated alkanethiol self-assembled monolayers on Au(111). *Langmuir*, 23(2):582–588, 2007. doi:10.1021/la0605539.
- [161] E. Hutter, D. Roy, and J. Fendler. Polarization modulated infrared reflection absorption (PM-IRRAS) spectroscopic and surface plasmon resonance (SPR) measurements of omega-mercaptopalanoic acid self-assembled monolayer (SAM) protonation equilibria. In *203rd Meeting - Paris, France - S1 - Nanostructured Thin Films: New Routes to Advanced Materials and Applications*, 2003.
- [162] L. Sun, R.M. Crooks, and A.J. Ricco. Molecular interactions between organized, surface-confined monolayers and vapor-phase probe molecules. 5. Acid-base interactions. *Langmuir*, 9(7):1775–1780, 1993. doi:10.1021/la00031a027.
- [163] H.C. Yang, D.L. Dermody, C. Xu, A.J. Ricco, and R.M. Crooks. Molecular interactions between organized, surface-confined monolayers and vapor-phase probe molecules. 8. Reactions between acid-terminated self-assembled monolayers and vapor-phase bases. *Langmuir*, 12(3):726–735, 1996. doi:10.1021/la9505226.
- [164] R. Arnold, W. Azzam, A. Terfort, and C. Wöll. Preparation, modification, and crystallinity of aliphatic and aromatic carboxylic acid terminated self-assembled monolayers. *Langmuir*, 18(10):3980–3992, 2002. doi:10.1021/la0117000.
- [165] R. Arnold. *Struktur und Ordnung selbstordnender Monolagen aliphatischer und aromatischer Thiole auf Goldoberflächen*. PhD thesis, Ruhr Universität Bochum, 2001.
- [166] C. Méthivier, B. Beccard, and C.M. Pradier. In situ analysis of a mercaptooundecanoic acid layer on gold in liquid phase, by PM-IRAS. Evidence for chemical changes with the solvent. *Langmuir*, 19(21):8807–8812, 2003. doi:10.1021/la0345789.
- [167] T. Buffeteau, B. Desbat, and J.M. Turllet. Polarization modulation FT-IR spectroscopy of surfaces and ultra-thin films: Experimental procedure and quantitative analysis. *Applied Spectroscopy*, 45(3):380–389, 1991.
- [168] R.G. Nuzzo, L.H. Dubois, and D.L. Allara. Fundamental studies of microscopic wetting on organic surfaces. 1. Formation and structural characterization of

- a self-consistent series of polyfunctional organic monolayers. *Journal of the American Chemical Society*, 112(2):558–569, 1990. doi:10.1021/ja00158a012.
- [169] Y.-T. Tao, W.-L. Lin, G.D. Hietpas, and D.L. Allara. Infrared spectroscopic study of chemically induced dewetting in liquid crystalline types of self-assembled monolayers. *Journal of Physical Chemistry B*, 101(47):9732–9740, 1997. doi:10.1021/jp972514z.
- [170] F. Neubrech. *Nanoantenna (tentative title)*, chapter "Surface-Enhanced Infrared Spectroscopy". Pan Stanford Publishing, Singapore, 2011.
- [171] A. Pucci, F. Neubrech, D. Weber, S. Hong, T. Toury, and M. Lamy de la Chapelle. Surface enhanced infrared spectroscopy using gold nanoantennas. *phys. stat. sol. (b)*, 247(8):2071–2074, 2010. doi:10.1002/pssb.200983933.
- [172] F. Neubrech, D. Weber, D. Enders, T. Nagao, and A. Pucci. Antenna sensing of surface phonon polaritons. *Journal of Physical Chemistry C*, 114(16):7299–7301, 2010. doi:10.1021/jp908921y.
- [173] S. Karim, M.E. Toimil-Molaes, F. Maurer, G. Miehe, W. Ensinger, J. Liu, T.W. Cornelius, and R. Neumann. Synthesis of gold nanowires with controlled crystallographic characteristics. *Applied Physics A: Materials Science & Processing*, 84(4):403–407, 2006. doi:10.1007/s00339-006-3645-6.
- [174] J. Liu, J.L. Duan, M.E. Toimil-Molaes, S. Karim, T.W. Cornelius, D. Dobrev, H.J. Yao, Y.M. Sun, M.D. Hou, D. Mo, Z.G. Wang, and R. Neumann. Electrochemical fabrication of single-crystalline and polycrystalline au nanowires: the influence of deposition parameters. *Nanotechnology*, 17(8):1922–1926, 2006. doi:10.1088/0957-4484/17/8/020.
- [175] D. Lin-Vien, N.B. Colthup, W.G. Fateley, and J.G. Grasselli. *The handbook of Infrared and Raman Frequencies of Organic Molecules*. Academic Press, Inc., San Diego, 1991.
- [176] D. Enders. *Surface Enhanced Infrared Absorption on Au Nanoparticle Films for Optical Biosensing*. PhD thesis, Heidelberg University, Kirchhoff Institut for Physics, 2005.
- [177] N. Camillone, C.E.D. Chidsey, G. Liu, and G. Scoles. Substrate dependence of the surface structure and chain packing of docosyl mercaptan self-assembled

- on the (111), (110), and (100) faces of single crystal gold. *Journal of Chemical Physics*, 98(5):4234, 1998. doi:10.1063/1.465030.
- [178] A. Lehmann. Theory of infrared transmission spectra of thin insulating films. *physica status solidi (b)*, 148(1):401–405, 1988. doi:10.1002/pssb.2221480138.
- [179] A. Pucci. IR spectroscopy of adsorbates on ultrathin metal films. *physica status solidi (b)*, 242(13):2704–2713, 2005. doi:10.1002/pssb.200541131.
- [180] J. Zuloaga and P. Nordlander. On the energy shift between near-field and far-field peak intensities in localized plasmon systems. *Nano Letters*, 11(3):1280–1283, 2011. doi:10.1021/nl1043242.
- [181] J. Kundu, F. Le, P. Nordlander, and N.J. Halas. Surface enhanced infrared absorption (seira) spectroscopy on nanoshell aggregate substrates. *Chemical Physics Letters*, 452(1-2):115–119, 2008. doi:10.1016/j.cplett.2007.12.042.
- [182] M. Lamy de la Chapelle and A. Pucci, editors. *Nanoantenna (tentative title)*. Pan Stanford Publishing, Singapore, not published yet.
- [183] H. Ibach and D.L. Mills. *Electron energy loss spectroscopy and surface vibrations*. Academic Press, Inc., New York, 1982.
- [184] M.G. Cottam and D.R. Tilley. *Introduction to surface and superlattice excitations*. Cambridge University Press, 2005.
- [185] R. Hillenbrand, T. Taubner, and F. Keilmann. Phonon-enhanced light-matter interaction at the nanometre scale. *Nature*, 418:159–162, 2002. doi:10.1038/nature00899.
- [186] N. Ocelic and R. Hillenbrand. Subwavelength-scale tailoring of surface phonon polaritons by focused ion-beam implantation. *Nature Materials*, 3:606–609, 2004. doi:10.1038/nmat1194.
- [187] U. Fano. Effects of configuration interaction on intensities and phase shifts. *Physical Review*, 124(6), 1961. doi:10.1103/PhysRev.124.1866.
- [188] Z. Chen, X. Li, A. Taflove, and V. Backman. Backscattering enhancement of light by nanoparticles positioned in localized optical intensity peaks. *Applied Optics*, 45(4):633–638, 2006. doi:10.1364/AO.45.000633.

- [189] V.E. Ferry, L.A. Sweatlock, D. Pacifici, and H.A. Atwater. Plasmonic nanostructure design for efficient light coupling into solar cells. *Nano Letters*, 8(12):4391–4397, 2008. doi:10.1021/nl8022548.
- [190] K. Yee. Numerical solution of initial boundary value problems involving Maxwell’s equations in isotropic media. *IEEE Transactions on Antennas and Propagation*, 14(3):302–307, 1966. doi:10.1109/TAP.1966.1138693.
- [191] A. Taflove. Application of the finite-difference time-domain method to sinusoidal steady state electromagnetic penetration problems. *IEEE Transactions on Electromagnetic Compatibility*, 22(3):191–202, 1980.
- [192] C. Sönnichsen. *Plasmons in metal nanostructures*. PhD thesis, LMU Munich, 2001.
- [193] C. Sönnichsen, T. Franzl, T. Wilk, G. von Plessen, and J. Feldmann. Drastic reduction of plasmon damping in gold nanorods. *Physical Review Letters*, 88(7):077402, 2002. doi:10.1103/PhysRevLett.88.077402.
- [194] F. Neubrech, T. Kolb, R. Lovrincic, G. Fahsold, A. Pucci, J. Aizpurua, T.W. Cornelius, M.E. Toimil-Molaes, R. Neumann, and S. Karim. Resonances of individual metal nanowires in the infrared. *Applied Physics Letters*, 89(25):253104, 2006. doi:10.1063/1.2405873.
- [195] U. Teschner and K. Hübner. IR-spectroscopic data of thin insulating films on semiconductors. New methods of interpretation and analysis. *physica status solidi (b)*, 159(2):917–926, 1990. doi:10.1002/pssb.2221590239.
- [196] D.W. Berreman. Infrared absorption at longitudinal optic frequency in cubic crystal films. *Physical Review*, 130(6):2193–2198, 1963. doi:10.1103/PhysRev.130.2193.
- [197] A. Pucci. *Lecture on thin films, Heidelberg University*, winter term 2002/2003.
- [198] R. Beerwerth. *FDTD simulation of infrared-optical properties of nanoantennas*. Bachelor’s thesis, Heidelberg University, 2011.
- [199] I.N. Bronstein and K.A. Semendjajew. *Taschenbuch der Mathematik*. B. G. Teubner Verlagsgesellschaft, Leipzig, 1989.
- [200] R. Hillenbrand. Private communication.

- [201] F. Keilmann and R. Hillenbrand. Near-field microscopy by elastic light scattering from a tip. *Philosophical Transactions of the Royal Society A*, 362(1817):787–805, 2004. doi:10.1098/rsta.2003.1347.
- [202] <http://www.neaspec.com>.
- [203] M. Schnell, A. García-Etxarri, A. J. Huber, K. Crozier, J. Aizpurua, and R. Hillenbrand. Controlling the near-field oscillations of loaded plasmonic nanoantennas. *Nature Photonics*, 3:287–291, 2009. doi:10.1038/nphoton.2009.46.
- [204] M. Schnell, A. García-Etxarri, J. Alkorta, J. Aizpurua, and R. Hillenbrand. Phase-resolved mapping of the near-field vector and polarization state in nanoscale antenna gaps. *Nano Letters*, 10(9):3524–3528, 2010. doi:10.1021/nl101693a.
- [205] N. Ocelic, A. Huber, and R. Hillenbrand. Pseudoheterodyne detection for background-free near-field spectroscopy. *Applied Physics Letters*, 89(10):101124, 2006. doi:10.1063/1.2348781.
- [206] S. Brandt and H.D. Dahmen. *Elektrodynamik - Eine Einführung in Experiment und Theorie*. Springer Verlag, Berlin, Heidelberg, 2005. doi:10.1007/b138039.
- [207] K.R. Brown and M.J. Natan. Hydroxylamine seeding of colloidal Au nanoparticles in solution and on surfaces. *Langmuir*, 14(4):729–728, 1998. doi:10.1021/la970982u.
- [208] K.R. Brown, L.A. Lyon, A.P. Fox, B.D. Reiss, and M.J. Natan. Hydroxylamine seeding of colloidal Au nanoparticles. 3. Controlled formation of conductive Au films. *Chemistry of Materials*, 12(2):314–323, 2000. doi:10.1021/cm980066h.
- [209] S. Meltzer, R. Resch, B.E. Koel, M.E. Thompson, A. Madhukar, A.A.G. Requicha, and P. Will. Fabrication of nanostructures by hydroxylamine seeding of gold nanoparticle templates. *Langmuir*, 17(5):1713–1718, 2001. doi:10.1021/la001170s.
- [210] C. Wang, J. Huang, J. Wang, C. Gu, J. Wang, B. Zhang, and J. Liu. Fabrication of the nanogapped gold nanoparticles film for direct electrical detection of DNA and EcoRI endonuclease. *Colloids and Surfaces B: Biointerfaces*, 69(1):99–104, 2009. doi:10.1016/j.colsurfb.2008.11.008.

- [211] G. Stremstoerfer, H. Perrot, J.R. Martin, and P. Cléchet. Autocatalytic deposition of gold and palladium onto n-GaAs in acidic media. *Journal of the Electrochemical Society*, 135(11):2881–2886, 1988. doi:10.1149/1.2095453.
- [212] D. Enders. Private communication.
- [213] T. Härtling, Y. Alaverdyan, A. Hille, M.T. Wenzel, M. Käll, and L.M. Eng. Optically controlled interparticle distance tuning and welding of single gold nanoparticle pairs by photochemical metal deposition. *Optics Express*, 16(16):12362–12371, 2008. doi:10.1364/OE.16.012362.
- [214] T. Härtling, Y. Alaverdyan, M.T. Wenzel, R. Kulloock, M. Käll, and L.M. Eng. Photochemical tuning of plasmon resonances in single gold nanoparticles. *Journal of Physical Chemistry C*, 112(13):4920–4924, 2008. doi:10.1021/jp711257y.
- [215] T. Härtling, A. Seidenstücker, P. Olk, A. Plettl, P. Ziemann, and L.M. Eng. Controlled photochemical particle growth in two-dimensional ordered metal nanoparticle arrays. *Nanotechnology*, 21(14):145309, 2010. doi:10.1088/0957-4484/21/14/145309.
- [216] K. Mallick, Z.L. Wang, and T. Pal. Seed-mediated successive growth of gold particles accomplished by UV irradiation: A photochemical approach for sizecontrolled sythesis. *Journal of Photochemistry and Photobiology A: Chemistry*, 140(1):75–80, 2001. doi:10.1016/S1010-6030(01)00389-6.
- [217] K. Kurihara, J. Kizling, P. Stenius, and J.H. Fendler. Laser and pulse radiolytically induced colloidal gold formation in water and in water-in-oil microemulsions. *Journal of the American Chemical Society*, 105(9):2574–2579, 1983. doi:10.1021/ja00347a011.
- [218] E. Gachard, H. Remita, J. Khatouri, B. Keita, L. Nadjjo, and J. Belloni. Radiation-induced and chemical formation of gold clusters. *New Journal of Chemistry*, 22(11):1257–1265, 1998. doi:10.1039/A8044445G.
- [219] T. Härtling. Private communication.
- [220] I. Alber. Private communication.

- [221] H. Wang and N.J. Halas. Plasmonic nanoparticle heterodimers in a semiembedded geometry fabricated by stepwise upright assembly. *Nano Letters*, 6(12):2945–2948, 2006. doi:10.1021/nl062346z.
- [222] F. Hao, Y. Sonnefraud, P. Van Dorpe, S.A. Maier, N.J. Halas, and P. Nordlander. Symmetry breaking in plasmonic nanocavities: Subradiant LSPR sensing and a tunable fano resonance. *Nano Letters*, 8(11):3983–3988, 2008. doi:10.1021/nl802509r.
- [223] C. Huang, X. Yin, and Y. Kong, L. Zhu. Interactions of nanorod particles in the strong coupling regime. *Journal of Physical Chemistry C*, 114(49):21123–21131, 2010. doi:10.1021/jp1074362.
- [224] L.S. Slaughter, Y. Wu, B.A. Willingham, P. Nordlander, and S. Link. Effects of symmetry breaking and conductive contact on the plasmon coupling in gold nanorod dimers. *ACS Nano*, 4(8):4657–4666, 2010. doi:10.1021/nn1011144.
- [225] M.-W. Chu, V. Myroshnychenko, C.H. Chen, J.-P. Deng, and F.J. Mou, C.-Y. García de Abajo. Probing bright and dark surface-plasmon modes in individual and coupled noble metal nanoparticles using an electron beam. *Nano Letters*, 9(1):399–404, 2009. doi:10.1021/nl803270x.
- [226] G. Volpe, S. Cherukulappurath, R.J. Parramon, G. Molina-Terriza, and R. Quidant. Controlling the optical near field of nanoantennas with spatial phase-shaped beams. *Nano Letters*, 9(10):3608–3611, 2009. doi:10.1021/nl901821s.
- [227] A.L. Koh, K. Bao, I. Khan, W.E. Smith, G. Kothleitner, P. Nordlander, S.A. Maier, and D.W. McComb. Electron energy-loss spectroscopy (EELS) of surface plasmons in single silver nanoparticles and dimers: Influence of beam damage and mapping of dark modes. *ACS Nano*, 3(10):3015–3022, 2009. doi:10.1021/nn900922z.
- [228] H. Yang, S.-C. Kobori, C.-L. He, M.-H. Lin, H.-Y. Chen, C. Li, M. Kanehara, T. Teranishi, and S. Gwo. Plasmon hybridization in individual gold nanocrystal dimers: Direct observation of bright and dark modes. *Nano Letters*, 10(2):632–637, 2010. doi:10.1021/nl903693v.

- [229] J.S. Huang, J. Kern, P. Geisler, P. Weinmann, M. Kamp, A. Forchel, P. Biagioni, and B. Hecht. Mode imaging and selection in strongly coupled nanoantennas. *Nano Letters*, 10(6):2105–2110, 2010. doi:10.1021/nl100614p.
- [230] G.C. Gazzadi and S. Frabboni. Fabrication of 5 nm gap pillar electrodes by electron-beam Pt deposition. *Journal of Vacuum Science and Technology B*, 23(2), 2005. doi:10.1116/1.1872015.
- [231] Ch. Santschi, M. Jenke, P. Hoffmann, and J. Brugger. Interdigitated 50 nm Ti electrode arrays fabricated using XeF₂ enhanced focused ion beam etching. *Nanotechnology*, 17(11):2722–2729, 2006. doi:10.1088/0957-4484/17/11/002.
- [232] K. Shigeto, M. Kawamura, A.Y. Kasumov, K. Tsukagoshi, K. Kono, and Y. Aoyagi. Reproducible formation of nanoscale-gap electrodes for single-molecule measurements by combination of FIB deposition and tunneling current detection. *Microelectronic Engineering*, 83(4-9):1471–1473, 2006. doi:10.1016/j.mee.2006.01.166.
- [233] T. Nagase, K. Gamo, T. Kubota, and S. Mashiko. Direct fabrication of nanogap electrodes by focused ion beam etching. *Thin Solid Films*, 499(1-2):279–284, 2006. doi:10.1016/j.tsf.2005.07.031.
- [234] A.A. Tseng. Recent developments in nanofabrication using focused ion beams. *Small*, 1(10):924–939, 2005. doi:10.1002/smll.200500113.
- [235] S. Reyntjens and R. Puers. A review of focused ion beam applications in microsystem technology. *Journal of Micromechanics and Microengineering*, 11:287–300, 2001.
- [236] D.B. Williams and C.B. Carter. *Transmission Electron Microscopy: A Textbook for Materials Science*. Springer, Germany, 2009. doi:10.1007/978-0-387-76501-3_1.
- [237] D. Vaughan, editor. *Energy-dispersive x-ray microanalysis. An Introduction*. NORAN Instruments, USA, 1999.
- [238] Measuring distances between atomic planes in high resolution TEM images. <http://rsbweb.nih.gov/ij/docs/examples/tem/>.

- [239] Y.Q. Fu and N.K.A. Bryan. Focused ion beam direct fabrication of microoptical elements: features compared with laser beam and electron beam direct writing. Published online, 2002. URL: <http://hdl.handle.net/1721.1/3904>.
- [240] V. Ignatova and I. Chakarov. Modeling of bombardment-induced diffusion and segregation during the self-sputtering of Ga^+ ions at SiO_2/Si interfaces. *Surface and Coatings Technology*, 158-159:281–287, 2002. doi:10.1016/S0257-8972(02)00184-6.
- [241] V. Ignatova, I. Chakarov, A. Torrisi, and A. Licciardello. Segregation of gallium at SiO_2/Si interfaces during sputtering with Ga^+ ions: experimental and computer simulation study. *Applied Surface Science*, 187(1-2):145–153, 2002. doi:10.1016/S0169-4332(01)00812-1.
- [242] O. Hunderi and R. Ryberg. Amorphous gallium - a free electron metal. *Journal of Physics F: Metal Physics*, 4(11):2096–2102, 1974. doi:10.1088/0305-4608/4/11/033.
- [243] I.N. Shklyarevskii, Y.Y. Bondarenko, and N.A. Makarovskii. Plasma resonance in granular gallium films deposited on rough NaCl and KCl single-crystal surfaces. *Optics and Spectroscopy*, 88(4):547–550, 2000. doi:10.1134/1.626836.
- [244] B. Bernert and P. Zacharias. Die optischen Konstanten von Silber-Gallium-Legierungen in der Nähe der Plasmafrequenz, Quantitativer Vergleich mit Energieverlustspektren von Elektronen. *Zeitschrift für Physik*, 241(3):205–216, 1971. doi:10.1007/BF01395329.
- [245] S. Walter and C.E. Jones. Infrared spectra of new acceptor levels in boron-doped and gallium-doped silicon. *Journal of Applied Physics*, 50(11):7258–7260, 1979. doi:10.1063/1.325806.
- [246] E. Burstein, G. Picus, B. Henvis, and R. Wallis. Absorption spectra of impurities in silicon-I: Group-III acceptors. *Journal of Physics and Chemistry of Solids*, 1(1-2):65–74, 1956. doi:10.1016/0022-3697(56)90012-9.
- [247] D. Han, D. West, X.-B. Li, S.-Y. Xie, H.-B. Sun, and S.B. Zhang. Impurity doping in SiO_2 : Formation energies and defect levels from first-principles calculations. *Physical Review B*, 82(15):155132, 2010. doi:10.1103/PhysRevB.82.155132.

- [248] F.M. Hoffmann. Infrared reflection-absorption spectroscopy of adsorbed molecules. *Surface Science Reports*, 3(2-3):107, 1983. doi:10.1016/0167-5729(83)90001-8.
- [249] Y.J. Chabal. Surface infrared spectroscopy. *Surface Science Reports*, 8(5-7):211–357, 1988. doi:10.1016/0167-5729(88)90011-8.
- [250] T. Sasaki, I.T. Bae, D.A. Scherson, B.G. Bravo, and M.P. Soriaga. Oxidation-state changes of molecules irreversibly adsorbed on electrode surfaces as monitored by in situ Fourier transform infrared reflection absorption spectroscopy. *Langmuir*, 6(7):1234–1237, 1990. doi:10.1021/1a00097a007.
- [251] J. Fan and M. Trenary. Symmetry and the surface infrared selection rule for the determination of the structure of molecules on metal surfaces. *Langmuir*, 10(10):3649–3657, 1994. doi:10.1021/1a00022a044.
- [252] H.A. Pearce and N. Sheppard. Possible importance of a metalsurface selection rule in the interpretation of the infrared spectra of molecules adsorbed on particulate metals; infrared spectra from ethylene chemisorbed on silica-supported metal catalysts. *Surface Science*, 59(1):205–217, 1976. doi:10.1016/0039-6028(76)90301-0.
- [253] O. Skibbe. *On the Influence of Surface Defects on the Molecular Vibrations of Ethene on the Copper(111) Surface: Investigations with Vibrational Spectroscopy Using Electrons and Infrared Light*. PhD thesis, Heidelberg University, Kirchhoff Institut for Physics, 2006.
- [254] T. Glaser. Infrared spectroscopy and photoluminescence measurements on emitter layers for organic light emitting devices. Diploma thesis, Heidelberg University, 2009.
- [255] M. Binder. *On infrared spectroscopy of thin films of the phosphorescent dye mer-Ir(cn-pmbic)₃*. PhD thesis, Heidelberg University, Kirchhoff Institut for Physics, 2009.
- [256] D. Enders. Oberflächenverstärkte infrarotabsorption von molekülen in flüssiger umgebung. Diplomarbeit, Universität Heidelberg, Kirchhoff-Institut für Physik, 2002.

- [257] G. Albert. *Herstellung und Charakterisierung polykristalliner Goldschichten zur Verwendung in der Nanolithographie*. Diploma thesis, Heidelberg University, 1995.
- [258] G. Albert. PVD-Beschichtungen, Silz, 2011. URL: <http://www.georg-albert-pvd.de>.
- [259] R. Frech and C.E. Wang. The i.r. and Raman spectra of CaCO₃ (aragonite). *Spectrochimica Acta Part A: Molecular Spectroscopy*, 36(10):915–919, 1980. doi:doi:10.1016/0584-8539(80)80044-4.
- [260] R. Wolke. Bachelor's thesis, Heidelberg University, 2011.
- [261] E.V. Blinkova and E.I. Eliseev. Dissolution of calcium carbonate in aqueous solutions of acetic acid. *Russian Journal of Applied Chemistry*, 78(7):1064–1066, 2005. doi:10.1007/s11167-005-0450-5.
- [262] J.-J. Max and C. Chapados. Isotope effects in liquid water by infrared spectroscopy. III. H₂O and D₂O spectra from 6000 to 0 cm⁻¹. *Journal of Chemical Physics*, 131(18):184505, 2009. doi:10.1063/1.3258646.
- [263] W. Kaiser, P.H. Keck, and C.F. Lange. Infrared absorption and oxygen content in silicon and germanium. *Physical Review*, 101(4):1264–1268, 1956. doi:10.1103/PhysRev.101.1264.
- [264] P. Echlin. *Handbook of Sample Preparation for Scanning Electron Microscopy and X-Ray Microanalysis*. Springer, 2009.
- [265] Bruker Optics, Ettlingen. *Hyperion user manual*, 3rd edition, 2010.
- [266] R. Tone. Infrared optical properties of porous nanoantennas. Bachelor's thesis, Heidelberg University, 2010.
- [267] Spectra Physics. *Reflecting Microscope Objectives*, 2004.
- [268] L. Schriver-Mazzuoli, A. Schriver, and A. Hallou. IR reflection absorption spectra of thin water ice films between 10 and 160 K at low pressure. *Journal of Molecular Structure*, 554(2-3):289–300, 2000. doi:10.1016/S0022-2860(00)00678-5.

- [269] J. Luo, K. Ying, and J. Bai. Savitzky-Golay smoothing and differentiation filter for even number data. *Signal Processing*, 85(7):1429–1434, 2005. doi: 10.1016/j.sigpro.2005.02.002.
- [270] Bruker Optics Ettlingen. Private communication.
- [271] R. Behrisch, editor. *Sputtering by Particle Bombardment*. Springer, Berlin, 1981.
- [272] C. S.-C. Yang, L.J. Richter, J.C. Stephenson, and K.A. Briggman. In situ, vibrationally resonant sum frequency spectroscopy study of the self-assembly of dioctadecyl disulfide on gold. *Langmuir*, 18(20):7549–7556, 2002. doi: 10.1021/1a0257790.

Appendices

A. Experimental Details

A.1. Lithographic Preparation at NIMS

Gold nanorods were prepared on floating zone¹ Si substrates with both sides being polished (except samples of series A with an unpolished, rough back side). Most of the wafers are covered with a natural silicon dioxide layer; its thickness (≈ 3 nm) was measured by ellipsometry [122]. In addition, series H was prepared on thermally oxidized silicon wafers which feature an oxide thickness of about 106 nm [123]. The geometrical dimensions of the samples are about $10 \times 15 \times 1$ mm³ for of series B to H and $19 \times 25 \times 0.5$ mm³ for series A. Figure A.1 schematically shows the different preparation steps of the EBL process. After cleaning the substrate's surface (1), a positive photoresist was spin coated on it (2). In this context, positive means that the portion of the photoresist which is exposed to the electron beam (3) becomes soluble to the photoresist developer and is therefore removed (4). Consequently, 5 – 10 nm titanium were evaporated as an adhesion layer followed by a 60 – 100 nm gold layer (5). Finally, the lift-off process was carried out to dissolve the metal coated photoresist (6). The preparation process according to the manufacturer (A. OHI, NIMS) can be found in [110].

¹The floating zone technique ensures a very low oxygen content in the silicon compared to the CZOCHRALSKI preparation process [263].

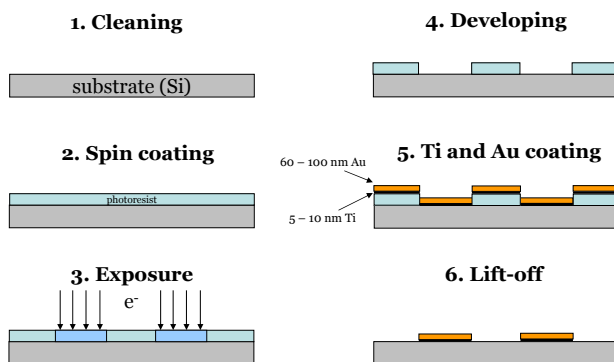


Figure A.1: Schematic representation of the individual preparation steps (see text).

A.2. Scanning Electron Microscopy

A.2.1. Carbon Contamination

Scanning over the sample with the electron beam for a long time leads to the deposition of carbon on the sample due to residual hydrocarbons in the gas phase of the sample chamber as well as on the sample surface. These contaminations can be detected with the In-lens detector due to its very high surface sensitivity [119]. Figures A.2a and A.2b show SEM images of a nanorod before and after the electron beam was scanned over a smaller area surrounding the nanorod. Clearly visible in Fig. A.2b is a dark rectangle which has emerged due to the focusing process. To exclude that the observed feature is due to charging effects, the same experiment was performed on the aluminum sample holder (not shown here) and similar results were obtained. In addition, the contamination area does not disappear as time goes by, as the image of Fig. A.2c, recorded one week after the image of Fig. A.2d, illustrates.

To remove the carbon contaminations, the sample was cleaned by an oxygen plasma at the Institute of Applied Physical Chemistry ($t = 30$ min, $p(\text{O}_2) = 0.4$ mbar, $P = 150$ W). Here, the ionized, low energy oxygen atoms of the plasma induce chemical reactions with the contamination species. In particular, hydrocarbon materials are converted into CO, CO₂, or H₂O and removed by the vacuum system [264]. And in fact, in the SEM image taken after the cleaning process (Fig. A.2d), nearly no contamination is observed. Note that the darker area, labeled as “new contamination” originates from a scan over the nanorod after the cleaning process. At a closer look, the contours of the formerly black rectangle can be seen. Now, this area appear brighter (“old contamination”) than the other substrate. Nevertheless, it was shown that oxygen plasma cleaning can be used to remove carbon contaminations from the sample.

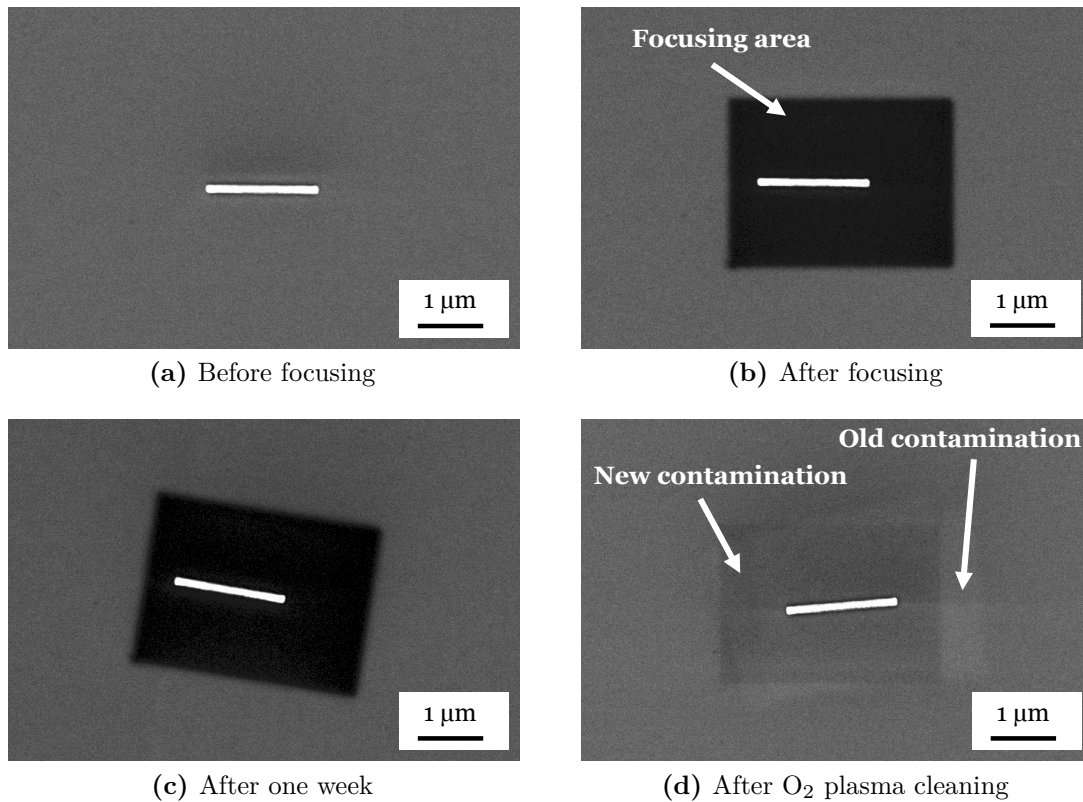


Figure A.2.: Series of SEM images of a nanorod ($L \approx 1.7 \mu\text{m}$) on sample Wb1. (a) shows the initial state before scanning and focusing. After 6 min of scanning, another image was recorded in (b). Subsequently, the sample was taken out of the SEM, stored for one week in a specimen container (at ambient conditions) and another image of the same rod was taken in (c). Finally, the sample was cleaned by an oxygen plasma and re-inserted into the SEM. (d) shows the rod after a quick scan over the nanorod at higher magnification. All images were recorded with the In-lens detector with the same settings of brightness and contrast. In all cases, an acceleration voltage of $U_{\text{acc}} = 3 \text{keV}$ was applied.

A.2.2. Brightness and Contrast

Figure A.3a shows SEM images of one and the same rod taken at with the same SEM and detector but different adjustments of brightness (B) and contrast (C). In the image taken with setting 1, a too high value of B is chosen so that the rod appears longer and wider than in the image taken with setting 2. Thus, differences in L up to $\Delta L = 30\text{nm}$ can arise depending on the adjustments of B and C.

This problem becomes obvious when results of L measured at different dates, and most likely different settings of B and C, are compared (see Fig. A.3b). Strong deviations depending on the date of the measurement were found. Note that for each measurement, at least three rods within the respective array were measured. Here, the deviations of L within one array were not exceeding 5 nm, which is indicated by the error bars. During the latest measurement series, all arrays were measured with the same settings similar to those of the images shown in Fig. 3.3. Nevertheless, the length difference between the actual measured value and the projected value plotted on the ordinate almost linearly increases with increasing projected length. To check whether this difference is not a measurement artifact due to a bad calibration of the SEM, one and the same sample was measured with two different SEMs.

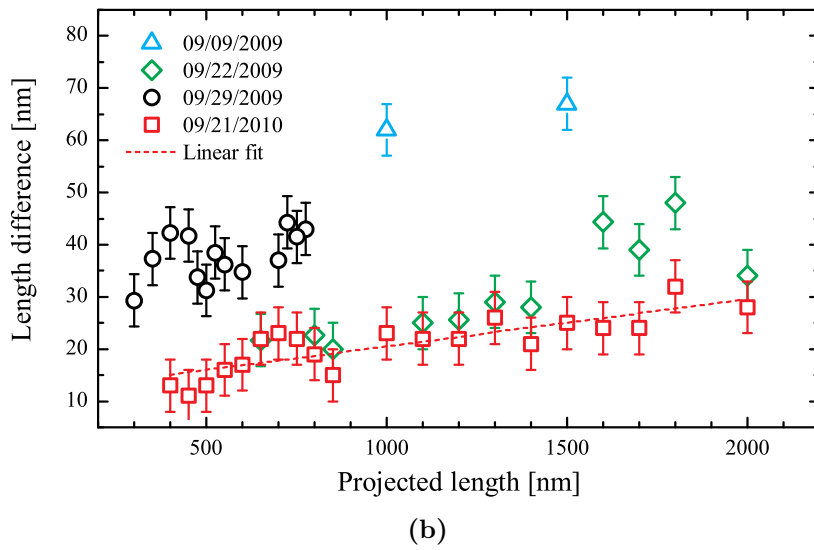
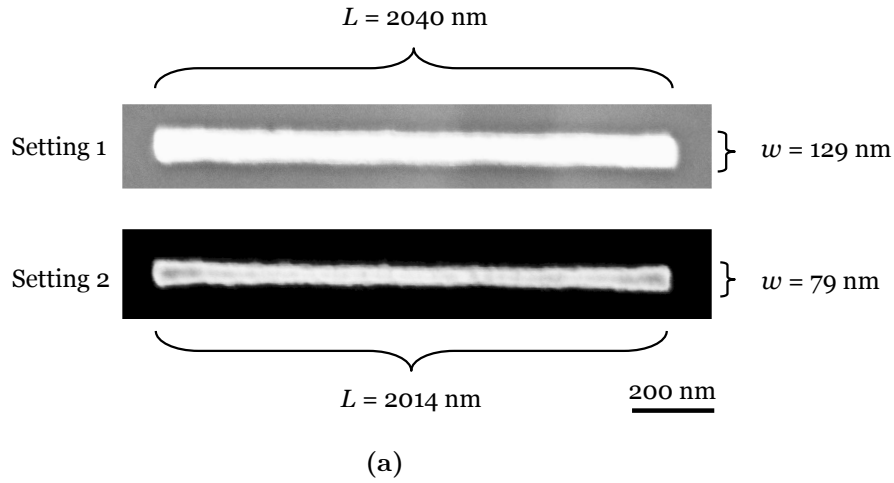


Figure A.3.: (a) SEM images of a nanorod on sample Wb1 ($L \approx 2 \mu\text{m}$) taken with the In-lens detector ($U_{\text{acc}} = 3 \text{keV}$). The settings of brightness and contrast differ for the two images: setting 1, (B/C) = (47 % / 43 %); setting 2, (B/C) = (44 % / 39 %). (b) On the ordinate, the length difference is plotted which is calculated by subtracting the projected value of L from the actually measured one. Data points on the same abscissa value originate from the *same* array of sample Wb3.

A. Experimental Details

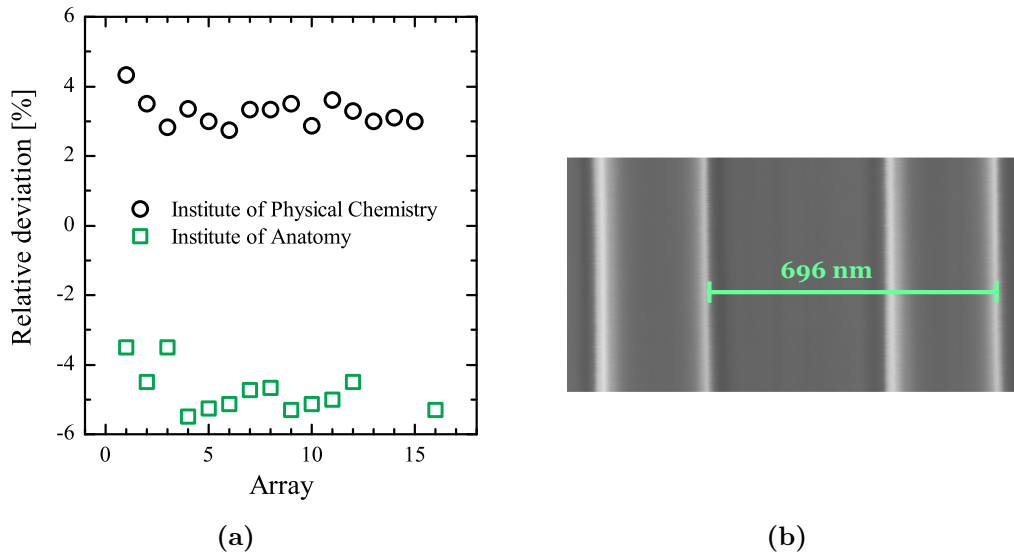


Figure A.4.: (a) Relative deviation of the length L (ratio between actually measured length and projected length) for several nanorod arrays on sample Wef1 measured with different microscopes. (b) SEM image of a calibration sample. The distance between the grooves should be (700 ± 0.5) nm.

A.2.3. Comparison between Different Microscopes

To clarify if the observed deviations between measured length and projected length arise from a bad calibration of the SEM, one and the same sample (Wef1) was also measured with a SEM of the Institute of Anatomy. Figure A.4a shows the relative deviations of the measured and the projected values. As already found for the nanorod arrays of sample Wb3 (see Fig. A.3b), the values of L measured with the SEM at the Institute of Applied Physical Chemistry (APC) are bigger than the projected values. Interestingly, measurements with the other SEM result in systematic smaller values of L . Hence, at least one of the SEMs has to be badly calibrated.

To check the calibration of the SEM of the APC, a calibration sample with grooves featuring a constant separation distance of 700 nm was investigated (see Fig. A.4b). The measured value of 696 nm is in good agreement with the manufacturer information and thus, it seems that the nanorods are really longer than they should be.

A.3. Microscopic Infrared Spectroscopy

A.3.1. Set-Up of the IR Microscope

Fig. A.1 shows a schematic drawing of the beam path inside the IR microscope. In total, there exist four different operating modes: the transmittance and reflectance mode which both can be operated either with visible or IR light. Two different visible light sources are installed: a light bulb (1) for reflectance and a LED (2) for transmittance measurements. The IR light source, the globar, is located inside the FT-IR spectrometer.

In reflectance mode, objective 6 is used to both focus and collect the IR light. The sample is brought into the focus by moving the xyz -table up and down. Two apertures (4 and 8) can be used to limit the IR spot size on the sample (see Fig. A.1). The IR polarizer can either be positioned before (23) or after (25) the light is reflected from the sample. In transmittance mode, objective 19 is used to focus the light whereas objective 6 collects the light. Aperture 17 can be used to limit the spot size of the beam before it passes the sample, aperture 8 after it passes the sample. The IR polarizer can be mounted in position 24 or 25, depending on whether the light should be polarized before or after it passes the sample.

The IR light is detected by a MCT detector (14a) while the visible image of the sample can be either recorded by a LCD camera (22) or directly observed through a binocular (11).

A.3.2. Schwarzschild Objective

A schematic drawing of the Schwarzschild objective is shown in Fig. A.6. Its description is taken from [267] and slightly modified:

The reflecting microscope objectives are fabricated from polished, electroless nickel. They are reverse Cassegrains, following the Schwarzschild design. Accordingly, they have zero chromatic, negligible coma, spherical and astigmatic aberrations. The objective is broadband coated with aluminum and MgF_2 overcoat. They are usable from 200 nm to 20 μm .

These reflecting microscope objectives have significant advantages over conventional (refractive type) microscope objectives. As there are no refracting elements, nor optical cement, the useful bandwidth is much greater. This is particularly important if good UV or IR performance is needed. This design also offers longer working distances and larger numerical apertures than do conventional microscope objectives.

A. Experimental Details

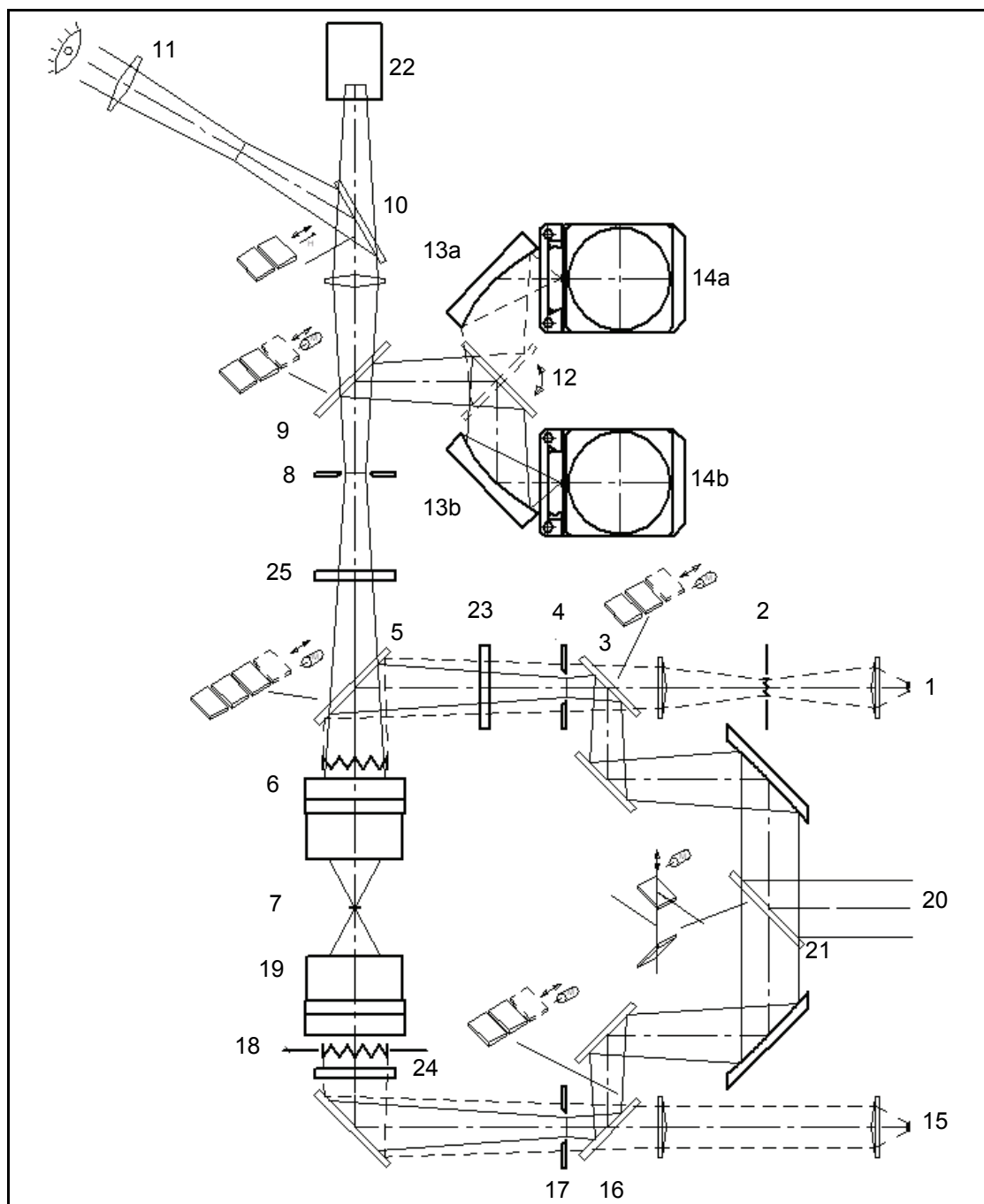


Figure A.5.: Schematic drawing of the beam path inside the IR microscope [265]. The components are explained in Tab. A.1.

No.	Component
1	Light source for visible light (reflectance mode)
2	Aperture for adjusting the KÖHLER illumination in reflectance mode
3	Motorized mirror with two adjustments: only visible or only IR light can pass
4	Aperture (optional), only for reflectance mode
5	Motorized mirror with two adjustments: transmittance or reflectance mode
6	Schwarzschild objective, see Fig. A.6
7	Sample
8	Aperture (above)
9	Motorized mirror with two adjustments: light is guided to the binocular eyepiece or to the camera, respectively, or light is guided to the MCT detector
10	Motorized mirror with two adjustments: light is guided to the binocular eyepiece or to the camera
11	Binocular eyepiece
12	In our set-up, we only have one MCT detector, therefore mirror 12 is fixed and the components 13b and 14 do not exist
13a	Mirror that guides the light to the detector
14a	Standard MCT detector
15	Light source for visible light in transmittance mode (LED, see [266])
16	Analogue to mirror 3
17	Aperture (below), only for transmittance mode
18	Aperture for adjusting the KÖHLER illumination in transmittance mode
19	Objective (adjustable in height) to maximize light intensity on the sample in transmittance mode
20	IR light beam coming from the spectrometer
21	Motorized mirror with three adjustments: IR light is guided either to transmittance or reflectance optic, light passes the IR microscope to reach the UHV chamber
22	LCD camera
23	Possible position for IR polarizer before passing sample (reflectance mode only)
24	Possible position for IR polarizer before passing sample (transmittance mode only)
25	Possible position for IR polarizer after passing sample

Table A.1.: Components shown in Fig. A.5.

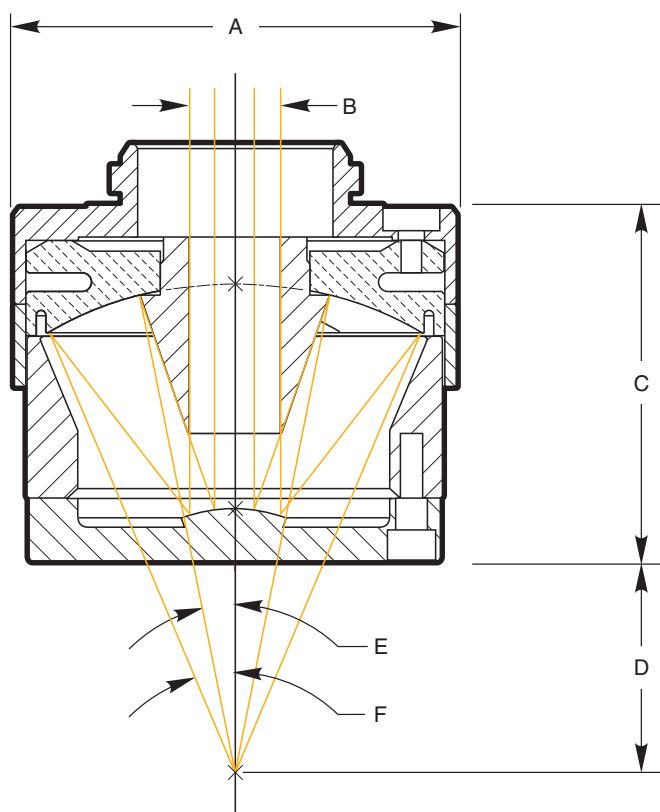


Figure A.6: Schematic drawing of the Schwarzschild objective (36-fold magnification, numerical aperture $NA = 0.5$). Dimensions given in mm: 49.3 (A), 5.3 (B), 33.5 (C), 10.4 (D). Angles: 10.3° (E) and 30° (F). Taken from [267].

The reflective objectives use all highly polished spherical metal mirrors. They are designed with two mirrors positioned to eliminate aberrations. The first mirror has a spherical concave surface with a center hole. The second mirror is small, with a spherical convex surface. The mirrors are coated with aluminum and magnesium fluoride. Reflection per surface of each mirror is 85% average in the UV-VIS, and 90% average in the IR, with a dip to 78% at 820 nm.

A.3.3. Non-Linearity of the MCT Detector

The non-linear behavior of the MCT detector in the IR microscope was characterized by measuring single channel spectra with different apertures. The measurements were performed with and without the non-linearity correction (NLC) option provided by the *OPUS* software. Figure A.7a shows the spectral intensity in dependence of the spot size on the sample in the focal plane. A linear behavior is observed for small spot sizes and thus small signal intensities. However, a deviation from the linear behavior (dotted straight line) is present with and without NLC for higher intensities. In Fig. A.7b, the saturation (compare Fig. A.11d) for measurements without NLC is plotted against the ADC count of the detector for two different

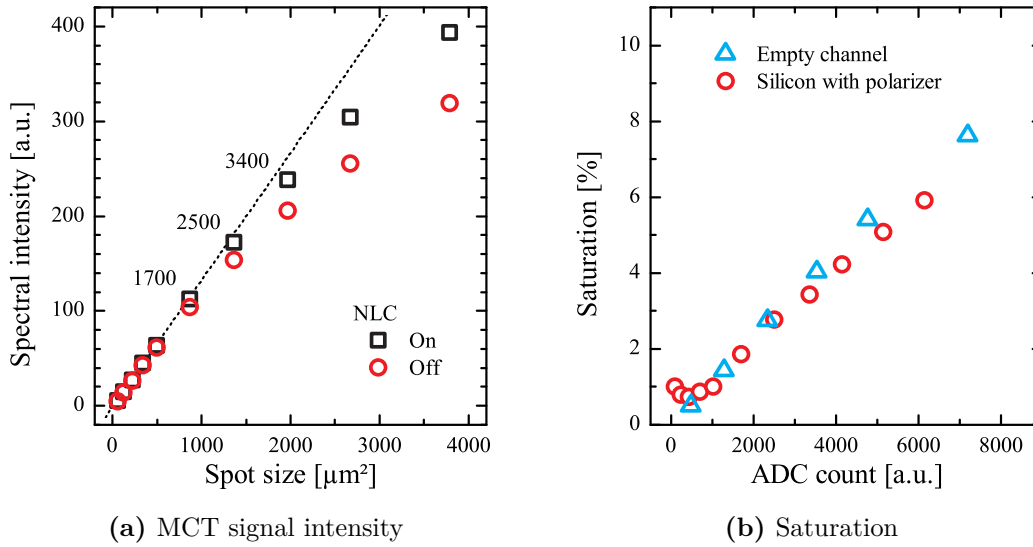


Figure A.7.: (a) Integrated area below the single channel spectrum from $\tilde{\nu}_1 = 650\text{cm}^{-1}$ to $\tilde{\nu}_2 = 8000\text{cm}^{-1}$ against the illuminated spot size $A_0 = \pi(D/2)^2$ with aperture diameter D for NLC on and off. The numbers in the figure indicate the ADC count of the corresponding measurement, which does not depend on NLC. The measurements were performed on a clean position on a silicon wafer and a polarizer was inserted in the beam path. (b) MCT detector's saturation against ADC count for two different measurement configurations. The open red symbols are same data as the one in (a).

measuring configurations. It can be concluded that the ADC count (not the aperture size) is the parameter that has to be controlled to avoid a non-linear response. From the data shown in Fig. A.7 follows that an ADC count of about 2500 should not be exceeded to maintain photometric accuracy.

A.3.4. Measurement Time of the MCT Detector

Prior to each measurement, the MCT detector has to be cooled with liquid nitrogen. When the detector is at room temperature before the filling is started, one can measure for at least 15 h. However, filling an already cooled detector results in a measurement time that can last even 20 h as Fig. A.8a shows.

A.3.5. Influence of Different Aperture Sizes

Choosing different aperture sizes influences the measured signal. In general, the bigger the aperture, the more intense is the detected signal which results in a better signal-to-noise ratio. However, aperture sizes have to be chosen corresponding to

A. Experimental Details

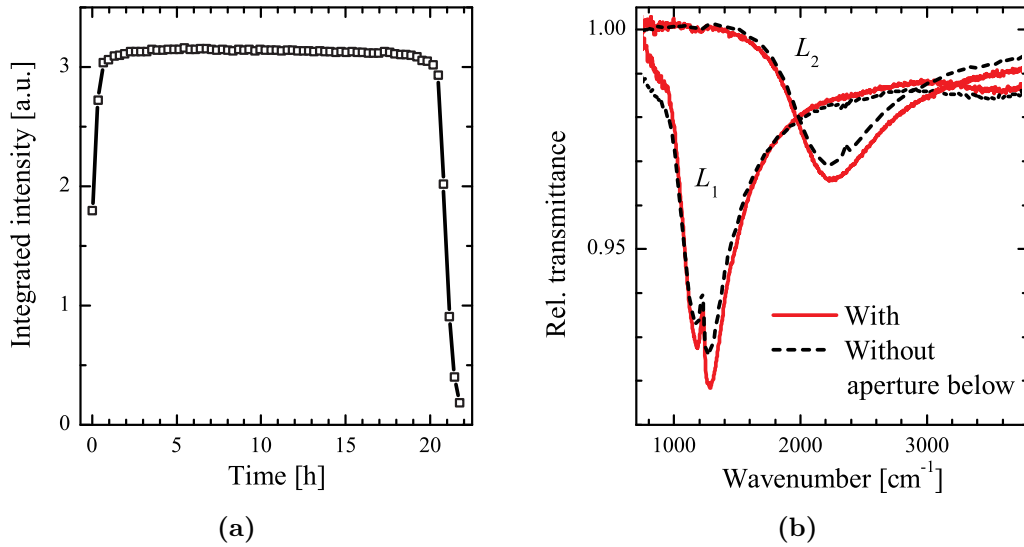


Figure A.8.: (a) Integrated single channel intensity between 1950 and 2050 cm^{-1} . The MCT detector was already cooled and refilled at $t = 0$. (b) Relative transmittance measurements of two different nanorod arrays on silicon ($L_1 \approx 1.4 \mu\text{m}$ and $L_2 \approx 775 \text{nm}$) with and without using an aperture below the sample ($\varnothing = 50 \mu\text{m}$). The aperture above was inserted in both cases and had a diameter of $33 \mu\text{m}$ in the focal plane. The total dimension of the arrays was $50 \times 50 \mu\text{m}^2$.

the overall size of the nanorod array that is to be measured. Most of the arrays investigated in this thesis have dimensions of $50 \times 50 \mu\text{m}^2$. Consequently, an aperture of $33 \mu\text{m}$ was chosen to ensure a homogeneous rod distribution inside the illuminated measuring spot if the sample position is defined in the middle of the array.

Figure A.3.5 shows relative transmittance spectra of two different nanorod arrays on silicon measured with a $33 \mu\text{m}$ -aperture above the sample. The difference between the solid red and the dashed black curves is that in the first case, an $50 \mu\text{m}$ -aperture below the sample was used which was omitted in the second case. Obviously, using an additional aperture increases the total signal strength of the plasmonic resonance. This is because less diffusely scattered light from the substrate reaches the detector in this configuration. However, signal-to-noise ratio slightly decreases since the overall intensity is reduced.

Note that this effect is only present as long as the dimension of the nanorod array is smaller than the illumination spot size without any apertures. For very large arrays (e.g. $4 \times 4 \text{mm}^2$ arrays investigated in [110]), adding an additional aperture shows no effect on the signal strength.

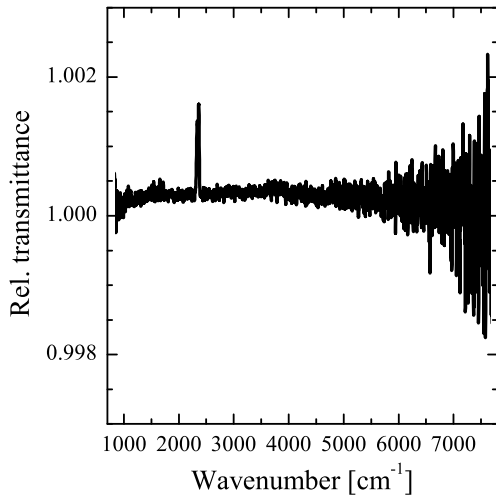


Figure A.9: 100%-line measured in the IR microscope with a pinhole having a diameter of 100 μm . The peak at around 2350 cm^{-1} originates from different CO_2 concentrations during sample and reference measurement.

A.3.6. Stability of the Apparatus

A simple way to test the stability is the acquisition of 100%-lines, i.e. taking relative transmittance spectra with sample and reference at the same position. In Fig. A.9, an example of a 100%-line measurement is shown. Obviously, the system seems to be quite stable since no major deviations from 100% exist. The very small absorption peak ($\approx 0.15\%$) at around 2350 cm^{-1} is due to slight changes of the CO_2 concentration in the optical beam path during the measurement. To provide a stable CO_2 concentration, a Plexiglas[®] box surrounding the whole sample stage was installed [266] and purged with CO_2 reduced and dried air. In Fig. A.10a, normalized single channel intensities before and after the installation of this purging box are shown. Apparently, the CO_2 concentration can almost be eliminated in case of purging (at least 1 h, see Sec. A.3.7). Even an open purging box already leads to a smaller CO_2 concentration compared to the case without box.

Another problem that may occur during the measurement is the formation of water ice on the MCT detector window due to a bad thermal insulation of the detector's dewar. Consequently, a broad water ice band in the range between 3100 and 3500 cm^{-1} [268] appears (see Fig. A.10b). New evacuation of the dewar generally solves this problem, as can be seen from the dashed black curve where the water ice band has vanished.

It turned out that mechanical instabilities heavily influence the stability. In Fig. A.11a, ten consecutive 100%-line measurements on a clean silicon substrate are shown. Obviously, big deviations up to 3% from the 100%-line exist. They seem to occur randomly and may cancel out if a sufficiently high number of scans is recorded.

A. Experimental Details

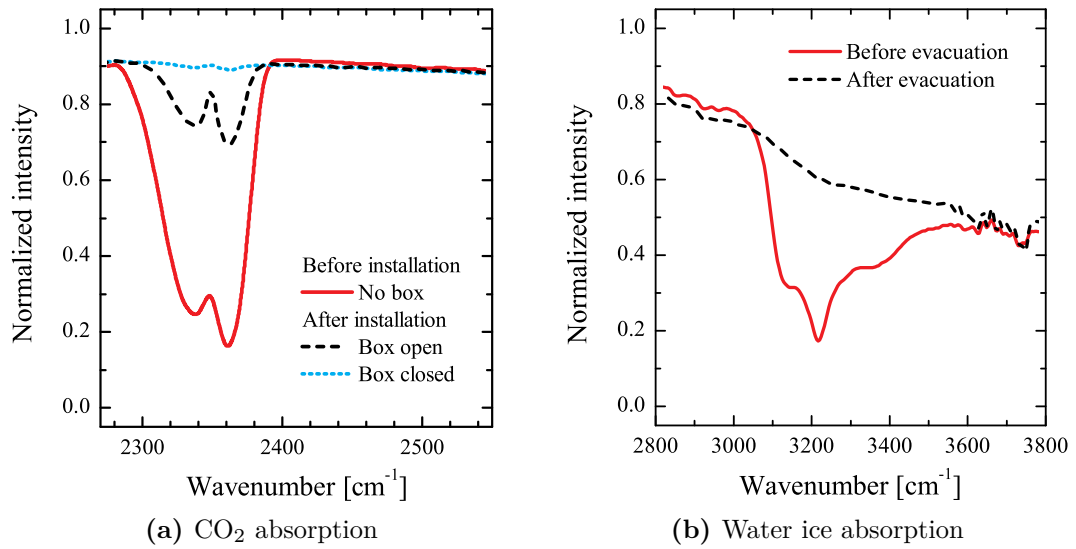
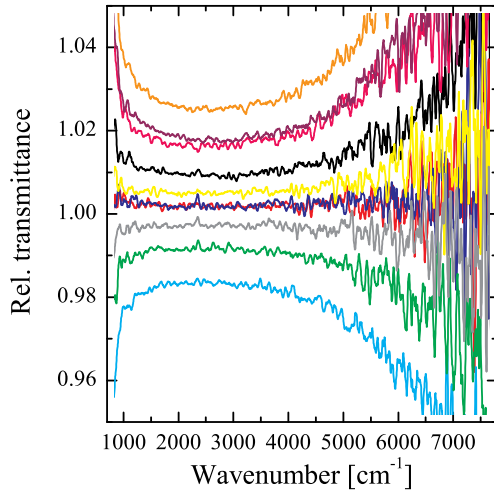


Figure A.10.: Single channel intensity normalized to spectrum’s apex in the range of (a) the CO₂ and (b) the water ice absorption band. A comparison before and after installation of the purging box is given in (a) whereas the spectra before and after the evacuation of the detector’s dewar are shown in (b).

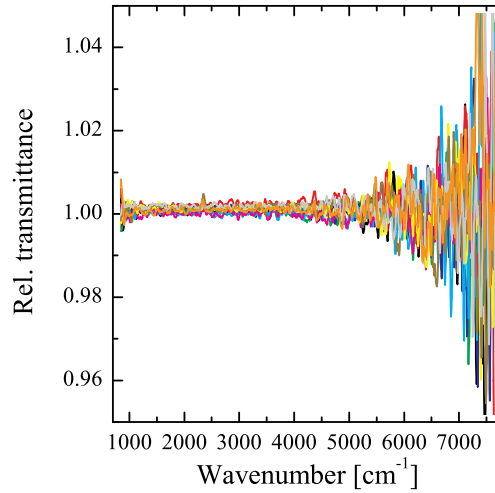
Nevertheless, it can happen that the measured baseline is shifted and slightly tilted with respect to the ideal 100%-line. In this case, the quantitative analysis of very low-intensity antenna resonances in the order of 1% or less is hampered. Interestingly, the fluctuations do not appear when the non-linearity correction (NLC) algorithm of the OPUS software² is switched off as demonstrated in Fig. A.11b. The appearance of the fluctuations can be explained by the fact that the algorithm projects low frequency fluctuations, which may be caused by external vibrations (e.g. vacuum pumps in the laboratory), onto the whole spectrum [270]. Consequently, the single channel spectrum is randomly “jumping up and down”, resulting in the observed fluctuations of Fig. A.11a.

Omitting the NLC impedes quantitative analyses since the measured intensity does not go linearly with the actual photon flux (see Sec. A.3.3). This is illustrated in Fig. A.11c where signals from nanoantennas on silicon are measured both in presence and in absence of the NLC algorithm. Obviously, the difference between the respective measurements is more pronounced for very intense signals. However, even for an antenna signal of around 3%, slight deviations are observed especially in the low and high wavenumber region. It is therefore very important to check

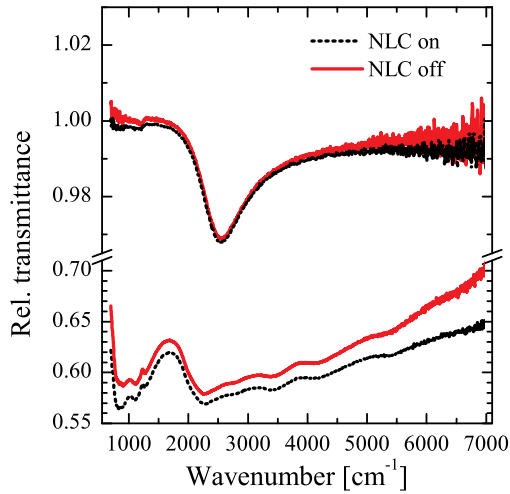
²This algorithm corrects the internal non-linear behavior of MCT detectors (see Sec. A.3.3) and is performed *before* the Fourier transform.



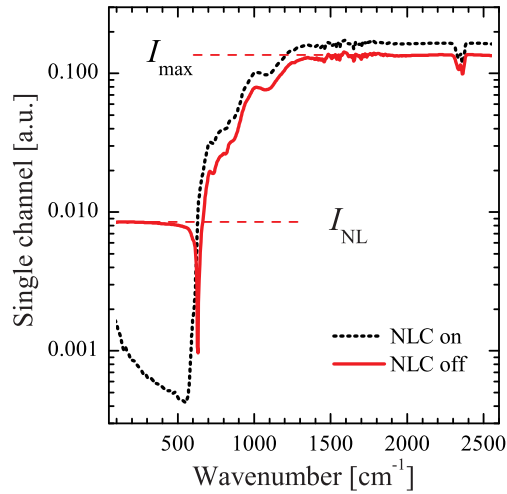
(a) Stability with NLC



(b) Stability without NLC



(c) Effect of NLC on rel. transmittance



(d) Effect of NLC on single channel

Figure A.11.: Ten consecutive 100%-line measurements (100 scans per spectrum) (a) with and (b) without applying NLC algorithm. The spectra are smoothed by using the SAVITZKY-GOLAY algorithm [269] (25 points). (c) Relative transmittance spectra of gold nanoantennas on silicon measured with and without NLC. (d) Single channel spectra of a silicon substrate with and without NLC. The non-physical energy response I_{NL} below 600 cm^{-1} has an intensity of about 6% of the spectrum's maximum I_{max} in the case of the solid red curve, which is an indication for detector saturation.

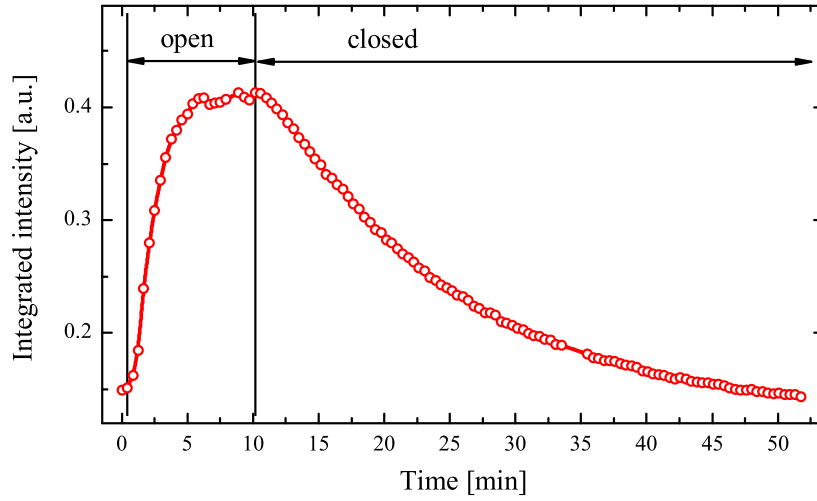


Figure A.12.: Integrated CO₂ intensity between 2290 and 2390 cm⁻¹ versus time. At $t \approx 1$ min, the purging box was opened and at $t \approx 10$ min, it was closed again.

whether the detector operates in the non-linear regime when the NLC is switched off. Any detected intensity I_{NL} in the frequency range below the cut-off region of the MCT detector ($\tilde{\nu} \lesssim 600 \text{ cm}^{-1}$, see Fig. A.11d) is a clear hint that the detector is saturated and that large signals cannot be interpreted quantitatively. In this context, the saturation of the detector, which is defined as the ratio between the response of the non-physical energy I_{NL} and the maximum I_{max} of the single channel spectrum (see Fig. A.11d), should be less than about 3 – 4% to maintain linear behavior and thus photometric accuracy of the detector [126] (see also Sec. A.3.3).

A.3.7. CO₂ Concentration Inside the Purging Box

Purging with dried and CO₂ reduced air contributes to stable measurement conditions. The influence of opening and closing the purging box is illustrated in Fig. A.12. The purging box was closed over night and opened at $t \approx 1$ min. After about 10 min, a stable concentration was reached. The dotted blue and dashed black curves in Fig. A.10a correspond to measurements at $t = 0$ and $t = 10$ min. After closing the purging box, one has to wait for about 50 min to reach the initial concentration. During this time, CO₂ absorption peaks in the relative transmittance spectra may arise (compare Fig. A.9).

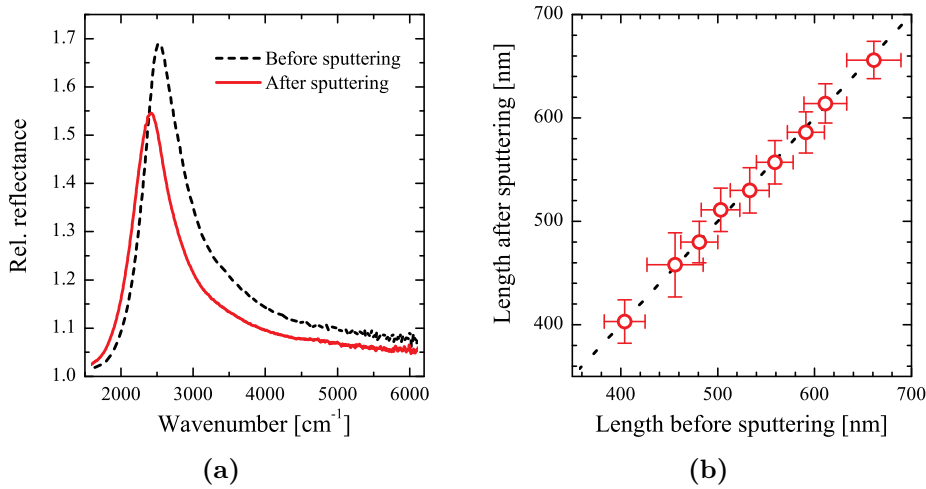


Figure A.13.: (a) Relative reflectance spectra of an array ($L \approx 0.65 \mu\text{m}$) before and immediately after argon-sputtering. (b) The ordinate shows the measured antenna length of the A1-arrays after sputtering versus the measured length before sputtering. Only minor deviations from the bisectrix (dotted black line) are present, indicating that the cleaning did not significantly modify the values of L (within the error of SEM measurement).

A.4. Argon-Sputtering

Sample Wa4 was sputtered with argon ions³ before the wet-chemical metal deposition experiment (Sec. 6.1) to remove dirt and the topmost layers of the sample to prepare a very clean surface, being mandatory for the experiment [212]. Ideally, any cleaning method should not alter the optical properties of the gold nanorods. However, a change of the resonance frequency after the cleaning process was observed for all investigated arrays, which is illustrated in Fig. A.13a. Possible reasons for the frequency shift could be changes of the geometrical parameters (longer L or smaller diameter D) or an increasing substrate polarizability. To identify geometrical modifications, SEM measurements were performed before and after sputtering. As a result, no significant changes in L (see Fig. A.13b) or w (not shown) were observed within the measurement error. Hence, modifications of the rod's geometry alone do not explain the induced spectral changes. Since the argon-sputtering method was not applied any more within this thesis, a detailed investigation of the spectral changes was not carried out.

³Sputtering is a physical process in which atoms are ejected from a solid bulk target material due to bombardment of with high energetic ions [271]. It is commonly used for thin-film deposition, etching and analytical techniques. Argon-sputtering was performed at the Kirchhoff Institute with the following parameters: $P = 500 \text{ W}$, $t = 1 \text{ min}$, $p \approx 1 \cdot 10^{-6} \text{ mbar}$ (before sputtering).

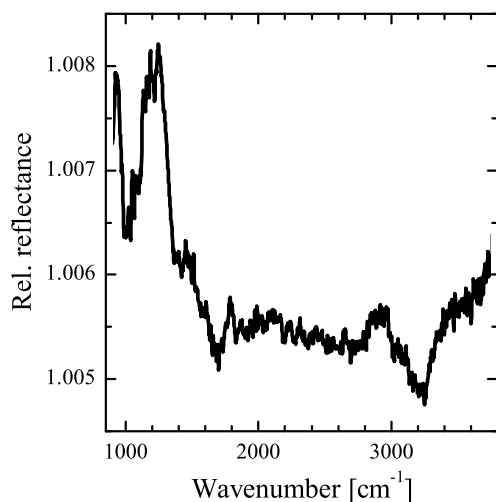


Figure A.14: Stability of the relative reflectance measurement (see text).

A.5. Measurement Stability of IRRAS

The reflectance spectrum is very sensitive to any displacement of the sample relative to the reflection unit. This is illustrated in Fig. A.14, where a relative reflectance measurement of a gold mirror versus the same gold mirror is shown. Between the sample and reference measurement, the vacuum inside the spectrometer was broken, the sample was unmounted and remounted again. The optimal result would be a horizontal 100 %-line since the same sample was measured in both cases. However, strong deviations are observed, especially in the low wavenumber region. Note that it is crucial that the gold mirror is fixed on the sample area in a reproducible way. Otherwise, the deviations become much stronger, being in the range of 1% or even more [109].

Moreover, strong fluctuations of the baseline are always present when spectra of *different* gold mirrors are related to each other since the mirrors are not completely identical. This can be seen in Fig. A.15, where relative reflectance measurements of a freshly prepared MUA monolayer (reference d-ODT) for different light polarizations are shown. Besides the fluctuations in the low wavenumber region, absorption peaks are observed in case of the p-polarized measurement. The two upwards pointing peaks at 2089cm^{-1} and 2194cm^{-1} are due to the d-ODT reference and can be attributed to the symmetric and antisymmetric CD_2 stretching vibration, respectively [272]. Furthermore, signals of MUA are clearly visible between 2800 and 3000cm^{-1} (CH_2 stretching vibrations). However, the interesting bands of MUA ($1200 - 1800\text{cm}^{-1}$) are located in a range with strong fluctuations of the baseline. Since the vibrational bands are not present in the s-polarized measurement due to the surface selection

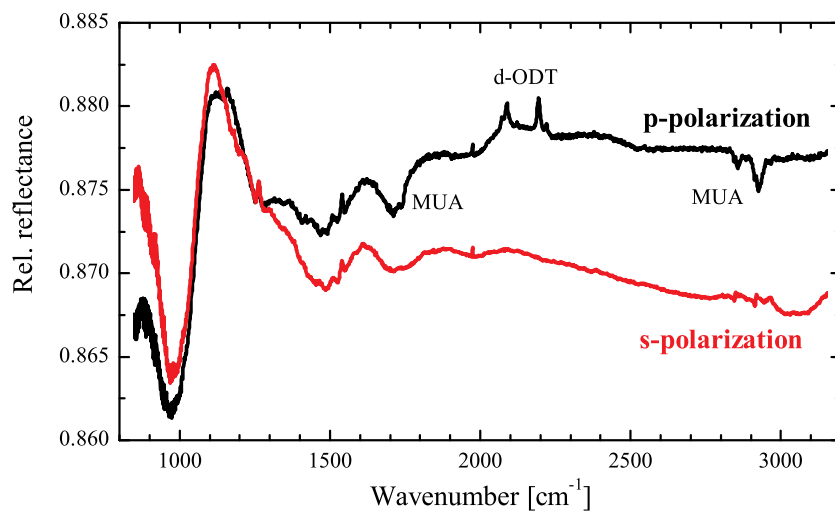


Figure A.15.: IRRAS spectra of a freshly prepared MUA monolayer on a smooth gold film versus a reference gold film covered by a d-ODT monolayer, measured with different light polarizations. The spectra were acquired with 3000 scans at a resolution of 2 cm^{-1} and no additional data treatment was applied.

rule, the normalized relative reflectance [see Eq. (7.1)] is calculated to reduce the baseline fluctuations. Spectrum (a) in Fig. 7.3 shows the resulting normalized relative reflectance spectrum of MUA, where a baseline correction with the help of the software OPUS was performed in addition to the normalization.

B. Various Spectra and Tables

Mode	$\tilde{\nu}_{\text{res}}$ [cm ⁻¹]	H	γ	Γ
SS	809.2	180.5	42.232	0.257
AS1 ^a	1064.8	630.9	0	26.075
AS1 ^b	1090.4	366.4	0.026	16.875
AS2	1173	434.8	138.059	0.471

Table B.1.: Fitting results of the resonance frequency $\tilde{\nu}_{\text{res}}$, oscillator strength H , damping γ and width Γ of the curve shown in Fig. 3.7.

B. Various Spectra and Tables

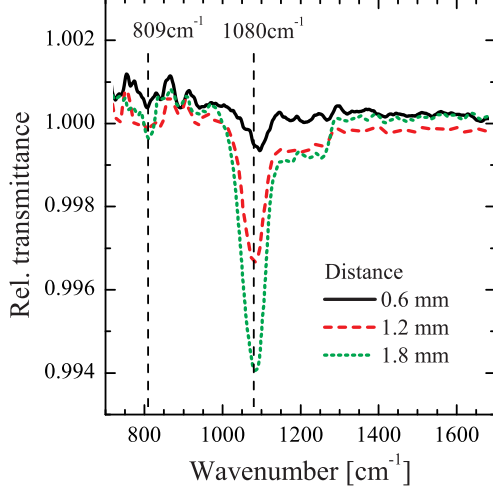


Figure B.1: Measurements on different bare substrate areas on a 106 nm oxide covered silicon wafer. The distances Δd between sample and reference are indicated. The observed peak at 1080 cm^{-1} grows in intensity as the distance increases, suggesting that the peak originates from slightly different layer thicknesses of the SiO_2 film (compare to Fig. 3.7). Since Δd for nanoantenna measurements is usually below $200\text{ }\mu\text{m}$, the substrate inhomogeneity should only have a minor influence on the relative transmittance measurement.

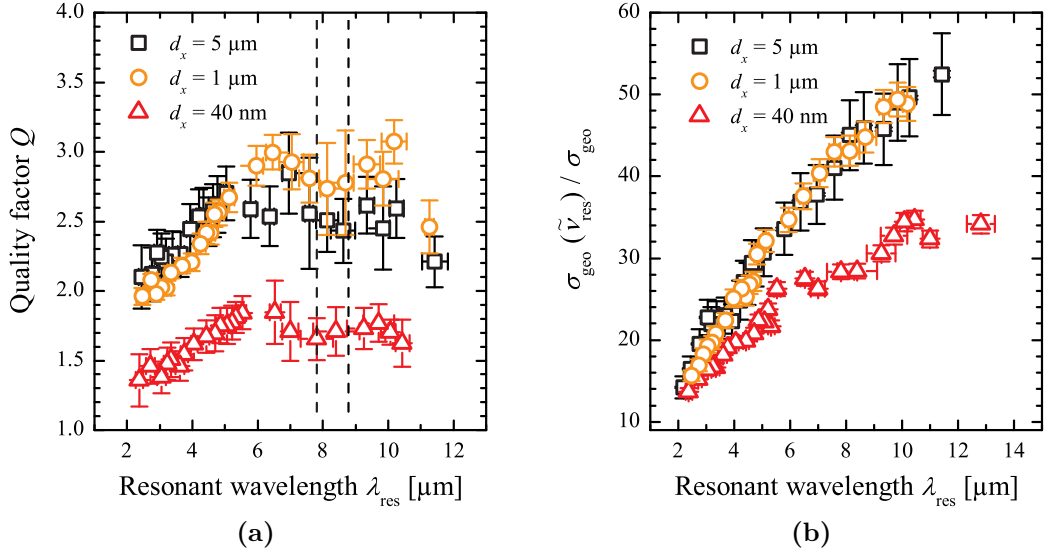


Figure B.2.: Behavior of (a) Q and (b) $\sigma_{\text{ext}}(\tilde{\nu}_{\text{res}})/\sigma_{\text{geo}}$ for nanorod arrays with different d_x ($w \approx 120\text{ nm}$, $h \approx 100\text{ nm}$, $d_y = 5\text{ }\mu\text{m}$). The vertical dashed lines in (a) indicate the range of the SiO_2 surface phonon-polariton which hampers the determination of Q , leading to the small valley.

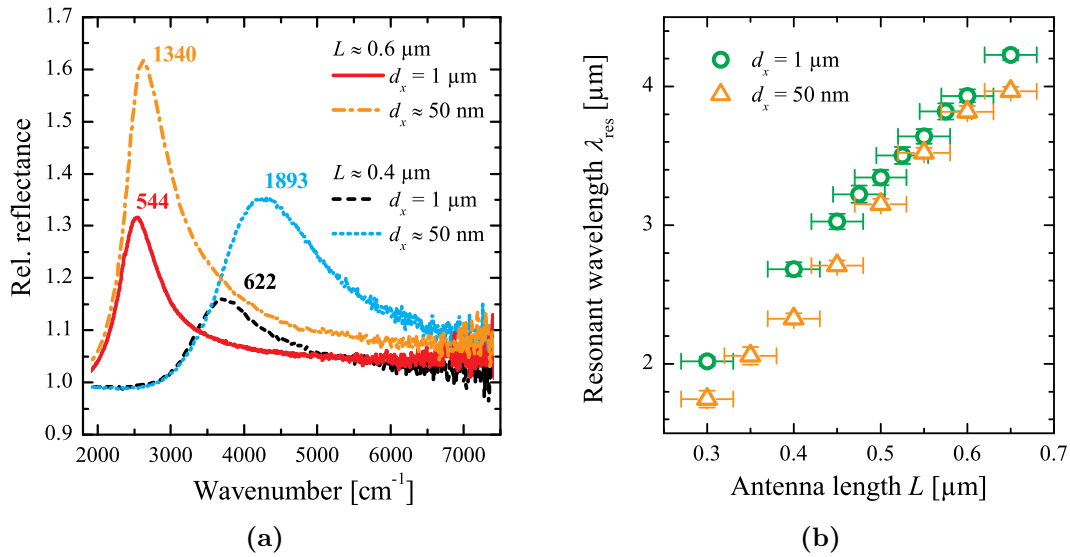


Figure B.3.: Mixed interaction. (a) Relative reflectance measurements of selected nanorod arrays on sample Wa4 ($w \approx 40$ nm, $h \approx 60$ nm, $d_y = 1$ μ m). The numbers indicate the quantities of rods that contribute to the signal. A shift to higher frequencies is observed for decreasing longitudinal distance d_x (for fixed rod length L), which is true for all investigated rod lengths as can be seen in (b).

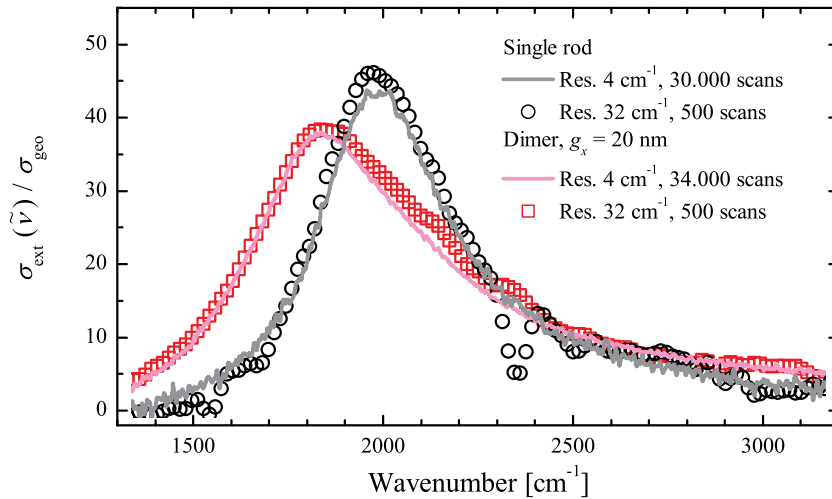


Figure B.4.: Extinction spectra of a single nanorod and a nanorod dimer with $g_x \approx 20$ nm on Antenna#19, each recorded with higher (solid curves, 8.3 μ m-aperture) and lower (open symbols, 16.7 μ m-aperture) resolution. The dip at around 2350 cm^{-1} in the spectrum with the open black circles originates from different CO_2 concentrations in the optical beam path during reference and sample measurement.

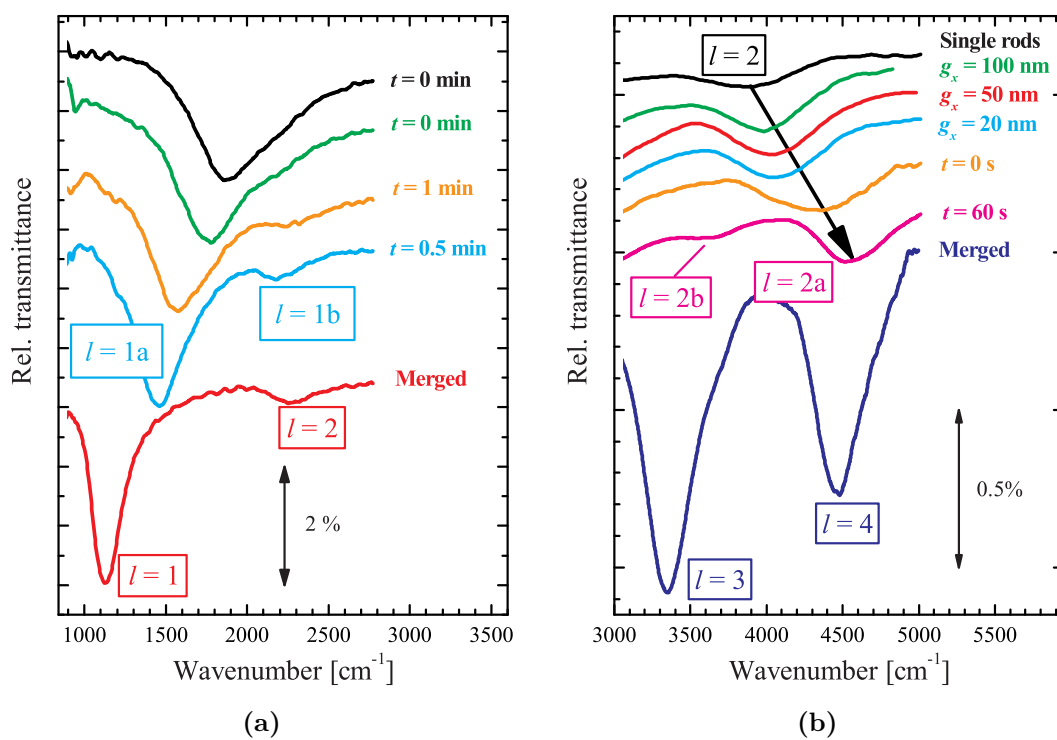


Figure B.5.: Relative transmittance spectra of photo-chemically grown nanorod dimers in the range of (a) the combinations of the $l = 1$ and (b) $l = 2$ modes of individual nanorods.

C. List of Publications

The following publications evolved directly from results presented in this thesis:

- **D. Weber**, P. Albella, P. Alonso-González, F. Neubrech, G. Han, T. Nagao, R. Hillenbrand, J. Aizpurua, and A. Pucci. *Longitudinal and transverse coupling in infrared gold nanoantenna arrays: long range versus short range interaction regimes*. Optics Express, 19(16): 15047–15061, 2011.
- G. Han, **D. Weber**, F. Neubrech, I. Yamada, M. Mitome, Y. Bando, A. Pucci, and T. Nagao. *Infrared spectroscopic and electron microscopic characterization of gold nanogap structure fabricated by focused ion beam*. Nanotechnology, 22: 275202, 2011.

Besides that, the author contributed to the following publications:

- F. Neubrech, **D. Weber**, D. Enders, T. Nagao, and A. Pucci. *Antenna sensing of surface phonon polaritons*. Journal of Physical Chemistry C, 114(16): 7299–7301, 2010.
- A. Pucci, F. Neubrech, **D. Weber**, S. Hong, T. Toury, and M. Lamy de la Chapelle. *Surface enhanced infrared spectroscopy using gold nanoantennas*. phys. stat. sol. (b), 247(8): 2071–2074, 2010.
- F. Neubrech, A. Garcia-Etxarri, **D. Weber**, J. Bochterle, H. Shen, M. Lamy de la Chapelle, G.W. Bryant, J. Aizpurua, and A. Pucci. *Defect-induced activation of symmetry forbidden infrared resonances in individual metallic nanorods*. Applied Physics Letters, 96(21): 213111, 2010.
- T. Nagao, G. Han, C.V. Hoang, J.-S. Wi, A. Pucci, **D. Weber**, F. Neubrech, V. M. Silkin, D. Enders, O. Saito, and M. Rana. *Plasmons in nanoscale and atomic-scale systems*. Science and Technology of Advanced Materials, 11(5): 054506, 2010.
- F. Neubrech, **D. Weber**, R. Lovrincic, A. Pucci, M. Lopes, T. Toury, and M. Lamy de La Chapelle. *Resonances of individual lithographic gold nanowires in the infrared*. Applied Physics Letters, 93(16): 163105, 2008.

D. Acknowledgments

At this point, I would like to thank everybody who supported me and, thus, contributed to the success of this thesis. Special thanks go to

- Prof. Dr. ANNEMARIE PUCCI for offering me the possibility to work in this interesting field of research and for being a great supervisor of my thesis,
- Prof. Dr. ALBRECHT WINNACKER for his willingness to be the second referee,
- Dr. FRANK NEUBRECH for great support during my whole PhD and for proof-reading the manuscript,
- all current and former members of the work group Pucci for being great colleagues, especially STEFFEN WETZEL for accompanying me from the first semester till the end of my PhD and the “nanoantenna people” Dr. FRANK NEUBRECH, JÖRG BOCHTERLE, and CHRISTIAN HUCK for fruitful discussions and experimental support,
- our scientific partners:
 - Dr. DOMINIK ENDERS, Dr. GUI HAN, and Dr. TADAAKI NAGAO for the preparation of lithographic gold nanorods on silicon as well as for FIB fabrication of nanogaps within the project DFG PU193/9-1 of the German Science Foundation,
 - Dr. ANDREA TOMA and Dr. ENZO DI FABRIZIO for the preparation of lithographic gold nanorods on calcium fluoride,
 - Dr. PABLO ALBELLA and Dr. JAVIER AIZPURUA for supplying me with valuable simulation results,
 - Dr. PABLO ALONSO-GONZALEZ and Dr. RAINER HILLENBRAND for performing s-SNOM measurements,
 - JULIA KATZMANN and Dr. THOMAS HÄRTLING for the fruitful cooperation and for the hospitalization into the photo-induced metal deposition technique,

D. Acknowledgments

- the Institute of Applied Physical Chemistry and the Institute of Anatomy of the Heidelberg University for offering me the possibility to perform SEM measurements,
- JANOSCH DEEG for plasma cleaning of the samples,
- DR. ANDREA SEEHUBER for providing deuterated octadecanethiol,
- and the Heidelberg Graduate School of Fundamental Physics for financial support.

Finally, I would like to thank my parents HANS and SIEGLINDE for supporting me in various ways during my thesis, my complete studies of Physics, and my whole life. Last but not least, I would like to thank HELENA for proof-reading the manuscript, getting through the stressful stages of the PhD, and for sharing her sorrows, happiness and life with me.

E. List of Abbreviations

2D	Two- <u>d</u> imensional
3D	Three- <u>d</u> imensional
AA	<u>A</u> cetic <u>a</u> cid
AFM	<u>A</u> tom <u>i</u> c <u>f</u> orce <u>m</u> icroscopy
AT-SAM	<u>A</u> lkanethiol-based <u>s</u> elf- <u>a</u> ssembled <u>m</u> onolayer
B&C	<u>B</u> rightness and <u>c</u> ontrast
BEM	<u>B</u> oundary <u>e</u> lement <u>m</u> ethod
BSE	<u>B</u> ack <u>s</u> cattered <u>e</u> lectron
CCD	<u>C</u> harge <u>c</u> oupled <u>d</u> evice
d-ODT	<u>D</u> euterated <u>o</u> cta <u>d</u> ecanethiol
DTGS	<u>D</u> euterated <u>t</u> riglycine <u>s</u> ulfate
EBL	<u>E</u> lectron <u>b</u> eam <u>l</u> ithography
EDX	<u>E</u> nergy- <u>d</u> ispersive <u>x</u> -ray
EtOH	Ethanol
FDTD	<u>F</u> inite- <u>d</u> ifference <u>t</u> ime- <u>d</u> omain
FIB	<u>F</u> ocused <u>i</u> on <u>b</u> eam
FK	<u>F</u> uchs- <u>K</u> liewer
FT-IR	<u>F</u> ourier <u>t</u> ransform <u>i</u> nfrared
IR	<u>I</u> nfrared
IRRAS	<u>I</u> nfrared <u>r</u> eflection <u>a</u> bsorption <u>s</u> pectroscopy

E. List of Abbreviations

LO	<u>L</u> ongitudinal <u>o</u> ptical
LSPR	<u>L</u> ocalized <u>s</u> urface <u>p</u> lasmon <u>r</u> esonance
MCT	<u>M</u> ercury <u>c</u> admium <u>t</u> elluride
MHDA	<u>M</u> ercapto <u>h</u> exa <u>d</u> ecanoic <u>a</u> cid
MUA	<u>M</u> ercapto <u>u</u> ndecanoic <u>a</u> cid
NAIRS	<u>N</u> anoantenna- <u>a</u> ssisted <u>i</u> nfrared <u>s</u> pectroscopy
NIMS	<u>N</u> ational <u>I</u> nstitute for <u>M</u> aterials <u>S</u> cience
ODT	<u>O</u> cta <u>d</u> ecanethiol
PM-IRRAS	<u>P</u> olarization <u>m</u> odulation IRRAS
SAM	<u>S</u> elf- <u>a</u> ssembled <u>m</u> onolayer
SEIRA	<u>S</u> urface- <u>e</u> nhanced <u>i</u> nfrared <u>a</u> bsorption
SEM	<u>S</u> canning <u>e</u> lectron <u>m</u> icroscopy
SERS	<u>S</u> urface- <u>e</u> nhanced <u>R</u> aman <u>s</u> cattering
SNOM	<u>S</u> cattering-type <u>n</u> ear-field <u>o</u> ptical <u>m</u> icroscopy
SPP	<u>S</u> urface <u>p</u> honon- <i>or</i> <u>p</u> lasmon- <u>p</u> olariton
SP	<u>S</u> urface <u>p</u> lasmon
STM	<u>S</u> canning <u>t</u> unneling <u>m</u> icroscopy
TEM	<u>T</u> ransmission <u>e</u> lectron <u>m</u> icroscopy
TO	<u>T</u> ransverse <u>o</u> ptical
UV	<u>U</u> ltravio <u>l</u> et
VPP	<u>V</u> olume <u>p</u> lasmon- <u>p</u> olariton
VP	<u>V</u> olume <u>p</u> lasmon

Index

- 100%-line, 203
- Aspect ratio, 10
- Atomic force microscopy, 27
- Back scattered electron detector, 28
- Bright mode, 15
- Dark mode, 15, 117
- Dielectric function, 5
 - Classical oscillator model, 19
 - Drude model, 6
 - Gold, 6
 - Ideal metal, 7
- Dispersion relation
 - Light, 5
 - Plasmon-polariton, 8
 - Surface plasmon-polariton, 8
 - Volume phonon-polariton, 20
 - Volume plasmon-polariton, 7
- Drude model, 6
- DTGS detector, 32
- Dwell time, 121
- Electromagnetic field enhancement, 13
- Electron beam lithography, 25, 191
- Enhancement factor, 42, 150
- Extinction coefficient, 5
- Fano profile, 47
- Finite-difference time-domain, 47
- Focused ion beam milling, 120
- Fourier transform IR spectroscopy, 4
- Fuchs-Kliewer mode, 22, 46, 66
- Hydroxylamine seeding, 92
- Ideal antenna, 11
- Ideal metal, 7
- Infrared microscope
 - Set-up, 31, 197
 - Stability, 203
- Infrared reflection absorption spectroscopy,
 - 42, 139
 - Stability, 208
- Infrared spectroscopy, 1, 3
- Interferogram, 4
- IR detectors, 32
- Lightning rod effect, 13
- Localized surface plasmon resonance, 9
- Longitudinal optical frequency, 19
- Longitudinal plasmon resonance, 10
- Longitudinal separation distance, 25
- MCT detector, 32
 - Measurement time, 201
 - Non-linearity, 200
- Mercaptoundecanoic acid, 38
- Metal deposition

Index

- Photo-induced, 96
 - Wet-chemical, 92
- Michelson interferometer, 4
- Microscopic IR spectroscopy
 - Measurement principle, 33
 - Stability, 203
- Mie scattering, 9
- Multiphonon absorption band, 36
- Nanoantenna, 2
- Nanoantenna-assisted IR spectroscopy,
 - 2, 41, 144
- Noise, 34
- NOVOTNY fit, 13
- NOVOTNY model, 12
- Phonon, 19
- Phonon-polariton, 19
- Photo-induced metal deposition, 96
- Plasma frequency, 6
 - Gold, 6
 - Gallium, 124
- Plasmon, 7
- Plasmonics, 1
- Polariton, 7
- Quality factor, 50
- Quasi-static approximation, 9
- Red-shift, 9
- Refractive index, 5
 - Complex, 5
- Relative reflectance, 33
 - Normalized, 141
- Relative shift of the resonance, 79
- Relative transmittance, 33
 - Normalized, 126
- Resonance frequency, 50
 - Normalized, 113
- Reststrahlen* band, 19
- Scan, 34
- Scanning electron microscopy, 28, 192
 - Detectors, 28
- Scattering rate, 6
 - Gold, 6
- Scattering-type near-field optical microscopy, 81
- Schwarzschild objective, 197
- Self-assembled monolayer, 37
- Skin depth, 7
- Surface phonon-polariton, 22
- Surface plasmon, 8
- Surface plasmon-polariton, 8
 - Localized, 9
- Surface selection rule, 139
- Surface-enhanced infrared absorption,
 - 1, 22
- Surface-enhanced Raman scattering, 1
- Thin-film surface phonon polariton, 46
- Transverse optical frequency, 19
- Transverse plasmon resonance, 10
- Transverse separation distance, 25
- Volume phonon-polariton, 20
- Volume plasmon, 7
- Volume plasmon-polariton, 7
- Wavenumber, 3
- Wet-chemical metal deposition, 92
- Yee cell, 48